

**ΠΑΝΕΠΙΣΤΗΜΙΟ ΑΘΗΝΩΝ**  
**ΤΜΗΜΑ ΦΥΣΙΚΗΣ**  
**ΤΟΜΕΑΣ ΠΥΡΗΝΙΚΗΣ ΦΥΣΙΚΗΣ & ΣΤΟΙΧΕΙΩΔΩΝ ΣΩΜΑΤΙΔΙΩΝ**

**ΑΝΑΖΗΤΗΣΗ ΤΟΥ ΧΕΙΡΑΛΙΚΟΥ ΚΡΙΣΙΜΟΥ ΣΗΜΕΙΟΥ**  
**ΤΗΣ ΑΔΡΟΝΙΚΗΣ ΥΛΗΣ ΣΤΙΣ ΣΧΕΤΙΚΙΣΤΙΚΕΣ**  
**ΣΚΕΔΑΣΕΙΣ ΙΟΝΤΩΝ**

**ΝΙΚΟΛΑΟΣ Ν. ΔΑΒΗΣ**  
**ΔΙΔΑΚΤΟΡΙΚΗ ΔΙΑΤΡΙΒΗ**

**ΑΘΗΝΑ 2015**



**UNIVERSITY OF ATHENS  
FACULTY OF PHYSICS  
DEPARTMENT OF NUCLEAR & PARTICLE PHYSICS**

**SEARCHING FOR THE CHIRAL CRITICAL POINT OF  
QUARK MATTER IN RELATIVISTIC ION COLLISIONS**

**NIKOLAOS N. DAVIS**

Ph.D. THESIS

ATHENS 2015



*Στη μνήμη της μητέρας μου*

*Rien ne se perd,  
rien ne se crée,  
tout se transforme...*



# Ευχαριστίες

Αρχικά, θα ήθελα να εκφράσω τις θερμές ευχαριστίες μου προς τον επιβλέποντά μου, αναπ. καθ. κ. Φώτη Διάκονο, ο οποίος με καθοδήγησε και με στήριξε καθ' όλη την πορεία της έρευνάς μου, όπως και πιο συγκεκριμένα κατά την εκπόνηση της παρούσας διατριβής, παρέχοντάς μου ανεκτίμητες πληροφορίες καθώς και ηθική υποστήριξη. Είμαι βαθύτατα ευγνώμων προς τον ομ. καθ. κ. Νικόλαο Αντωνίου, πρώτα και κύρια διότι οι παροτρύνσεις του υπήρξαν το έναυσμα και η έμπνευση για να ασχοληθώ με την αναζήτηση του κρισίμου σημείου της Χρωμοδυναμικής, καθώς και για την συνεχή και σταθερή υποστήριξη και τις συμβουλές που μου παρείχε καθ' όλη την επίπονη πορεία της έρευνάς μου, από τα πρώτα στάδια έως και την προσεκτική επιμέλεια της παρούσας διατριβής. Η παρούσα εργασία δεν θα είχε ποτέ καταστεί δυνατή χωρίς την συνεχή καθοδήγηση και την υποστήριξη και των δύο.

Θα ήθελα να ευχαριστήσω από καρδιάς τον Διευθυντή Ερευνών του ΕΚΕΦΕ “Δημόκριτος”, Δρ. Κωνσταντίνο Παπαδόπουλο, καθώς και τον ομ. καθ. κ. Απόστολο Παναγιώτου, οι οποίοι μου έδωσαν την δυνατότητα και την ευκαιρία να εργαστώ στο ερευνητικό περιβάλλον του CERN, και γενικά παρείχαν ουσιαστική αρωγή και συντονισμό στο αμοιβαίο θεωρητικό και πειραματικό εγχείρημα που οδήγησε στην παρούσα εργασία. Είμαι ευγνώμων προς την ομάδα του πειράματος NA61/NA49 γενικά, και συγκεκριμένα στον Δρ. Peter Seyboth και τον καθ. Marek Gazdzicki, που με καλωσόρισαν στους κόλπους του πειράματος NA61/SHINE και με καθοδήγησαν στην ανάλυση των δεδομένων του πειράματος NA49, όπως επίσης και στην αναπ. καθ. Katarzyna Grebieszkow η οποία με μεγάλη υπομονή με εκπαίδευσε και καθοδήγησε στη χρήση του λογισμικού της ανάλυσης και παρείχε πολύτιμη τεχνογνωσία σχετικά με τον ανιχνευτή συγκρούσεων βαρέων ιόντων του πειράματος NA49.

Κατά τη διάρκεια της εκπόνησης της παρούσας διατριβής, πολλοί συνάδελφοι και φίλοι με στήριξαν παρέχοντας επιστημονικές και τεχνικές συμβουλές. Θα ήθελα να ευχαριστήσω πιο συγκεκριμένα τον Δρ. Σταύρο Δημητρακούδη και τον Δρ. Παναγιώτη Καλοζούμη που μου παρείχαν υποστήριξη σε τεχνικά ζητήματα και θέματα παρουσίας κατά τη συγγραφή της διατριβής και κατά την οργάνωση της βιβλιογραφίας. Ευχαριστώ ακόμη θερμά τους συναδέλφους Θεοφάνη Γκούντρα και Λήλα Κουτσαντωνίου, και άλλους, υπερβολικά πολλούς για να αναφερθούν.

Τέλος, ένα μεγάλο ευχαριστώ στην οικογένεια μου, για την αμέριστη στήριξη και την ενθάρρυνσή τους στη διάρκεια της έρευνάς μου.

# Πρόλογος

Η παρούσα διδακτορική διατριβή πραγματεύεται τα χαρακτηριστικά της μετάβασης φάσης, την οποία υφίσταται η ισχυρώς αλληλεπιδρώσα ύλη, καθώς ένα σύστημα αδρονίων μεταβαίνει από συνθήκες χαμηλής θερμοκρασίας ( $T$ ) και βαρυονημικού δυναμικού ( $\mu_B$ ) (βαρυονικής πυκνότητας) προς υψηλότερες θερμοκρασίες και/ή πυκνότητες. Ένα φαινόμενο που παρουσιάζει ιδιαίτερο ενδιαφέρον σε ισχυρώς αλληλεπιδρώντα συστήματα είναι η (μερική) αποκατάσταση της χειραλικής συμμετρίας κατά τη μετάβαση από την ψυχρή αδρονική ύλη στο πλάσμα κουάρκ και γλουονίων (quark-gluon plasma, QGP). Με βάση υπολογισμούς από πρώτες αρχές (π.χ., επιχειρήματα από συμμετρία), καθώς και υπολογισμούς πλέγματος της Κβαντικής Χρωμοδυναμικής (ΚΧΔ), σε πεπερασμένη θερμοκρασία και βαρυονική πυκνότητα, υπάρχουν ισχυρές ενδείξεις ότι το αντίστοιχο διάγραμμα φάσεων περιλαμβάνει μια γραμμή αλλαγών φάσεως πρώτης τάξης σε χαμηλές θερμοκρασίες/υψηλές πυκνότητες, η οποία καταλήγει σε ένα κρίσιμο σημείο σε κάποια υψηλή θερμοκρασία και πεπερασμένη βαρυονική πυκνότητα.

Το κρίσιμο σημείο της ΚΧΔ έχει αποτελέσει αντικείμενο εκτενούς θεωρητικού και πειραματικού ενδιαφέροντος. Από θεωρητική σκοπιά, στην περιοχή συνθηκών του κρίσιμου σημείου, το σύστημα αναμένεται ότι υφίσταται μια μετάβαση φάσης δεύτερης τάξης, συνοδευόμενη από απειρισμό του χαρακτηριστικού μήκους συσχέτισης, μηδενισμό της αναμενόμενης τιμής της παραμέτρου τάξης (χειραλικό συμπύκνωμα), και κλιμάκωση των μακροσκοπικών μεγεθών σύμφωνα με καθολικούς νόμους δύναμης. Η προσέγγιση στο κρίσιμο σημείο συνδέεται επομένως με την εμφάνιση ενός συμπυκνώματος άμαζων (ή σχεδόν άμαζων) βαθμωτών σ-μποζονίων, τα οποία φέρουν τους χαρακτηριστικούς κβαντικούς αριθμούς του κενού. Πειραματικά, συνθήκες ικανές για το σχηματισμό θερμής και πυκνής αδρονικής ύλης αναπαράγονται τεχνητά σε πειράματα σύγκρουσης βαρέων ιόντων σε υψηλές ενέργειες, σε επιταχυντές όπως ο SPS του CERN, και ο εντοπισμός και η μελέτη του κρίσιμου σημείου της ΚΧΔ είναι ένας από τους στόχους παρόμοιων πειραμάτων (όπως π.χ. τα πειράματα NA49 και NA61 στο CERN). Είναι επομένως σημαντικό να εντοπιστεί η θέση του κρίσιμου σημείου στο διάγραμμα φάσεων της ΚΧΔ, καθώς και να αναζητηθούν πιθανά παρατηρήσιμα ίχνη της προσέγγισης συγκρούσεων βαρέων ιόντων στο κρίσιμο σημείο σε μελλοντικά

πειράματα.

Ανάμεσα στις κρίσιμες υπογραφές που έχουν προταθεί ως ενδείξεις προσέγγισης στο κρίσιμο σημείο είναι και διακυμάνσεις στην πυκνότητα των παραγόμενων σωματιδίων οι οποίες ακολουθούν νόμο δύναμης ως συνάρτηση της κλίμακας στο χώρο των ορμών, ένα φαινόμενο γνωστό ως σποραδική συμπεριφορά ή σποραδικότητα. Η παρούσα εργασία επικεντρώνεται πρωτίστως στη μελέτη των κρίσιμων διακυμάνσεων των βαρυονίων στο χώρο των εγκαρσίων ορμών.

Η διατριβή αποτελείται από έξι κεφάλαια, τα οποία δομούνται ως εξής:

Στο πρώτο κεφάλαιο, γίνεται μια σύντομη επισκόπηση της δομής και των συμμετριών της ύλης κουάρκ, όπως περιγράφεται από την Κβαντική Χρωμοδυναμική. Περιγράφουμε τα φαινόμενα του εγκλωβισμού και της ρήξης της χειραλικής συμμετρίας που λαμβάνουν χώρα κατά τη μετάβαση από το πλάσμα κουάρκ και γλουονίων σε υψηλές θερμοκρασίες στη συνήθη αδρονική ύλη στις χαμηλές θερμοκρασίες. Γίνεται μια σύντομη αναφορά στον μηχανισμό Higgs, και οδηγούμαστε στο συμπέρασμα ότι είναι υπεύθυνος για μικρό μόνο κλάσμα των μαζών των αδρονίων (μάζα ρεύματος). Συζητείται ο ρόλος της χειραλικής μετάβασης φάσης στην ερμηνεία του φάσματος των αδρονικών μαζών (μάζα συστατικού).

Στο δεύτερο κεφάλαιο, δίνεται μια εκτενέστερη περιγραφή του διαγράμματος φάσεων της ΚΧΔ, με ιδιαίτερη έμφαση στην περιοχή των σχετικά υψηλών θερμοκρασιών και χαμηλού χημικού δυναμικού όπου αναμένεται να εντοπιστεί το κρίσιμο σημείο της ΚΧΔ. Δίνεται μια σύνοψη των διαφόρων φάσεων και των συμμετριών τους, όπως προβλέπονται από αναλυτικούς και πλεγματολογικούς υπολογισμούς, για διάφορες περιοχές του φασικού διαγράμματος, και εξετάζονται τα διάφορα σενάρια που προκύπτουν για διαφορετικές μάζες κουάρκ και αριθμό γεύσεων. Εξηγείται ο ρόλος της αυθόρμητης ρήξης της χειραλικής συμμετρίας και συνδέεται με το χειραλικό συμπύκνωμα ως παράμετρος τάξης της χειραλικής μετάβασης φάσεως. Δίνεται μια σύνοψη των ενεργών θεωριών που περιγράφουν την φαινομενολογία του συμπυκνώματος κοντά στο κρίσιμο σημείο, καθώς και των κλάσεων παγκοσμιότητας στις οποίες ανήκουν. Τέλος, εξετάζουμε εν συντομία τις πλεγματολογικές θεωρίες που επιχειρούν να προσομοιώσουν αριθμητικά την χειραλική μετάβαση φάσεως και συζητούμε τις σχετικές τεχνικές. Δίνονται προβλέψεις των πλεγματολογικών θεωριών για την κρίσιμη θερμοκρασία, και συζητούνται οι προκλήσεις και οι περιορισμοί της επέκτασής τους σε πεπερασμένη βαρυονική πυκνότητα.

Το τρίτο κεφάλαιο εξετάζει σε βάθος τα γεωμετρικά χαρακτηριστικά του χειραλικού συμπυκνώματος. Δίνεται μια σύντομη επισκόπηση των χαρακτηριστικών των αλλαγών φάσης δεύτερης τάξης και της θεωρίας των κρίσιμων φαινομένων εν γένει. Καταδεικνύεται ότι ένα σύστημα που υφίσταται μετάβαση φάσεως δεύτερης τάξης παρουσιάζει στο κρίσιμο σημείο αναλλοiotητα κλίμακας και μορφοκλασματική αυτοομοiotητα, λόγω συσχετίσεων μακράς εμβέλειας, και επομένως η συμπεριφορά του μπορεί να περιγραφεί μέσω νόμων βάθμισης που χαρακτηρίζονται από λίγους κρί-

σιμους εκθέτες, οι οποίοι καθορίζονται από την κλάση παγκοσμιότητας στην οποία ανήκει η μετάβαση φάσης. Σκιαγραφείται η κατασκευή μιας ενεργού δράσης στην περιοχή του κρίσιμου σημείου, χρησιμοποιώντας το μοντέλο της μαγνήτισης ως χαρακτηριστικό παράδειγμα, αποσαφηνίζεται ο ρόλος της ως γεννήτρια συνάρτηση των συναρτήσεων συσχέτισης και γίνεται η σύνδεση ανάμεσα στους κρίσιμους εκθέτες και την μορφοκλασματική διάσταση των συστάδων σωματιδίων που σχηματίζονται στο κρίσιμο σημείο. Στη συνέχεια, μελετάται λεπτομερώς η χειραλική συμμετρία και παραμετροποιείται το χειραλικό συμπύκνωμα μέσω του βαθμωτού  $\sigma$  και του ψευδοβαθμωτού πιονικού πεδίου. Συζητούνται ενεργές θεωρίες αυθόρμητης ρήξης χειραλικής συμμετρίας 4ης και 6ης τάξης, και το κρίσιμο σημείο της KXΔ, σε πεπερασμένη βαρυνική πυκνότητα, συνδέεται με τη θεωρία του τρι-κρίσιμου σημείου 6ης τάξης. Τέλος, καταδεικνύεται ότι λόγω της αποσύζευξης του  $\sigma$ -πεδίου από το πεδίο των πιονίων, η αρμόζουσα κλάση παγκοσμιότητας του χειραλικού κρίσιμου σημείου είναι εκείνη του τρισδιάστατου μοντέλου Ising. Παρουσιάζεται η αντίστοιχη κλάση ενεργών δράσεων και ο ισοθερμικός κρίσιμος εκθέτης αναδύεται ως η κύρια ποσότητα που συνδέεται με την μορφοκλασματική γεωμετρία του συμπυκνώματος.

Το τέταρτο κεφάλαιο είναι μια εκτενής παρουσίαση των υπολογιστικών τεχνικών μέσω των οποίων επιτυγχάνεται η προσομοίωση του χειραλικού συμπυκνώματος μέσω στοχαστικών Monte-Carlo αλγορίθμων. Αρχικά, προσαρμόζουμε την ενεργό δράση του τρισδιάστατου μοντέλου Ising του βαθμωτού  $\sigma$ -πεδίου στην τυπική κυλινδρική γεωμετρία μιας σύγκρουσης βαρέων ιόντων και δείχνουμε ότι, κάτω από συγκεκριμένες προσεγγίσεις, μπορεί να επιμερισθεί σε ανεξάρτητες συνιστώσες στην ωκύτητα και τον εγκάρσιο χώρο. Χρησιμοποιούμε την προσέγγιση σαγματικού σημείου για να εξάγουμε λύσεις για τις δύο συνιστώσες χωριστά, και καταδεικνύεται ότι το χειραλικό συμπύκνωμα μπορεί να περιγραφεί ως συλλογή μορφοκλασματικών συστάδων στο καρτεσιανό γινόμενο της ωκύτητας με τον εγκάρσιο χώρο. Στη συνέχεια, συνάγουμε την αντίστοιχη μορφοκλασματική δομή στο χώρο των εγκαρσίων ορμών, και εισάγουμε την τεχνική των κανονικοποιημένων παραγοντικών ροπών (ανάλυση σποραδικότητας), με σκοπό να εξάγουμε την συνάρτηση συσχέτισης και τη μορφοκλασματική διάσταση του συστήματος στο χώρο των εγκαρσίων ορμών. Ακολούθως, παρουσιάζουμε την τεχνική των τυχαίων περιπάτων Lévy η οποία επιτρέπει την προσομοίωση μορφοκλασματικών συστάδων. Δίνεται μια λεπτομερής περιγραφή του αλγορίθμου Critical Monte Carlo (CMC), που μας επιτρέπει να προσομοιώσουμε κρίσιμες συστάδες  $\sigma$ -σωματιδίων (στο χώρο των εγκαρσίων ορμών/ωκύτητας) με τα επιθυμητά γεωμετρικά και φυσικά χαρακτηριστικά. Μια τροποποιημένη εκδοχή του αλγορίθμου CMC μας επιτρέπει να παράξουμε κρίσιμες συστάδες βαρυονίων, τις παραγοντικές ροπές των οποίων μπορούμε να συγκρίνουμε με εκείνες που προκύπτουν από την ανάλυση πειραματικών δεδομένων (κεφ. 5). Μέσω της ανάλυσης παραγοντικών ροπών, καθορίζουμε τη μορφοκλασματική διάσταση των συστάδων που παράγονται από το CMC, αποδεικνύοντας την αυτοσυνέπεια της προσομοίωσης. Τέλος, αντιμετωπίζο-

ντας το χειραλικό συμπύκνωμα ως παράδοξο ελκυστή με μορφοκλασματική διάσταση, εφαρμόζουμε την ανάλυση σποραδικότητας σε υποσύνολα του (ντετερμινιστικού) ελκυστή Ikeda, με σκοπό να εκτιμήσουμε κατά πόσον είναι εφικτή η ανακατασκευή ενός ελκυστή παρουσία ελλιπών δεδομένων και, πιθανώς, θορύβου.

Στο πέμπτο κεφάλαιο, δίνεται μια σύντομη επισκόπηση του πειράματος σύγκρουσης βαρέων ιόντων NA49 (SPS, CERN). Δίνεται μια σύνοψη των συνόλων πειραματικών δεδομένων που χρησιμοποιήσαμε στην ανάλυσή μας. Αφού δοθεί μια λεπτομερής περιγραφή των φίλτρων και των τεχνικών που χρησιμοποιήσαμε για να εξάγουμε τις εγκάρσιες ορμές των σωματιδίων από τα αρχικά δεδομένα, καθώς και για την ταυτοποίηση των πρωτονίων ανάμεσά τους, εξηγείται λεπτομερώς η μέθοδος της ανάλυσης σποραδικότητας των παραγοντικών ροπών στο χώρο των εγκαρσίων ορμών, μαζί με μια περιγραφή των τεχνικών που χρησιμοποιήθηκαν για την ενίσχυση του σήματος και την αφαίρεση του υποβάθρου. Στη συνέχεια, πραγματοποιείται μια ανάλυση σποραδικότητας των τελικών συνόλων δεδομένων, καθώς και μερικές Monte Carlo προσομοιώσεις (συμπεριλαμβανομένου του CMC του κεφ.4) σχεδιασμένες να προσομοιάζουν τις αντίστοιχες συγκρούσεις βαρέων ιόντων. Βασιζόμενοι στην πληροφορία που παρέχουν οι προσομοιώσεις, αξιολογούμε τις ενδείξεις για προσέγγιση στο κρίσιμο σημείο της ΚΧΔ και συζητούμε τα ζητήματα στατιστικών και συστηματικών σφαλμάτων που υπεισέρχονται στην ανάλυση.

Τέλος, στο έκτο κεφάλαιο, συνοψίζουμε τα αποτελέσματα της ανάλυσης και συζητούμε πιθανές μελλοντικές προοπτικές για την αναζήτηση και τον εντοπισμό του κρίσιμου σημείου της ΚΧΔ σε μελλοντικά πειράματα σύγκρουσης βαρέων ιόντων.

# Acknowledgements

I would like to express my warm gratitude towards my supervisor, Professor Fotis Diakonou, who firmly guided and supported me throughout my research, as well as the preparation and writing of this thesis, providing invaluable information and moral support. I am deeply grateful to Professor Emeritus Nikolaos Antoniou, first and foremost for inspiring me to work in the search of the critical point of QCD and, not least, for his constant and diligent support and counsel along the difficult road of my research, from the first stages up to the close scrutiny of this thesis. The present work would never have been possible without their guidance and support.

I would also like to thank NCSR “Democritos” Director of Research, Dr. Costas G. Papadopoulos, and Professor Emeritus Apostolos Panagiotou, for providing me with the means to work at CERN and in general for facilitating the joint theoretical and experimental effort that has resulted in the present analysis. I am grateful to the NA49/NA61 Collaborations in general, and in particular to Dr. Peter Seyboth and Professor Marek Gazdzicki, for welcoming me in the NA61/SHINE collaboration and guiding me in the analysis of NA49 experimental data, as well as to Associate Professor Katarzyna Grebieszko who introduced me to the data analysis software and process and provided me with much valuable expertise.

During my work, many colleagues and friends assisted me with scientific and technical advice. I would like to thank, in particular, Dr. Stavros Dimitrakoudis and Dr. Panayotis Kalozoumis for providing assistance in technical and stylistic matters during the writing of this thesis and organization of the bibliography, as well as many others, too numerous to mention.

Finally, special thanks goes to my family who stood by me, supporting and encouraging me throughout this work.



# CONTENTS

<b>Acknowledgements</b>	<b>ix</b>
<b>Abstract</b>	<b>1</b>
<b>Preface</b>	<b>3</b>
<b>1 Introduction</b>	<b>7</b>
1.1 Quantum Chromodynamics: Fundamental theory . . . . .	7
1.2 Apparent and actual symmetries of QCD . . . . .	8
1.3 Asymptotic freedom . . . . .	10
1.4 Confinement . . . . .	12
1.5 Chiral symmetry & chiral symmetry breaking . . . . .	13
<b>2 The phase diagram of QCD</b>	<b>17</b>
2.1 Introduction . . . . .	17
2.2 QCD phase structure . . . . .	18
2.2.1 Deconfinement and chiral restoration . . . . .	18
2.2.2 An outline of the QCD phase diagram . . . . .	19
2.3 QCD phase transition order parameters . . . . .	22
2.3.1 Polyakov loop and quark deconfinement . . . . .	22
2.3.2 Chiral condensate and dynamical breaking of chiral symmetry . . .	23
2.4 Chiral phase transition at finite temperature . . . . .	24
2.4.1 Ginzburg-Landau-Wilson analysis . . . . .	24
2.4.2 Lattice QCD simulations . . . . .	26
2.5 Chiral phase transition at finite baryon density . . . . .	28
2.5.1 Lattice QCD at low baryon density . . . . .	28
<b>3 Geometric characteristics of the Chiral Condensate</b>	<b>31</b>
3.1 Introduction . . . . .	31
3.2 First and second order phase transitions . . . . .	32

3.3	Critical exponents and scaling laws . . . . .	34
3.4	Long-range correlations . . . . .	36
3.4.1	Correlation functions . . . . .	36
3.4.2	Scale invariance, critical exponents and fractal dimension . . . . .	37
3.5	The chiral condensate as an order parameter . . . . .	39
3.5.1	The chiral phase transition . . . . .	39
3.5.2	$O(N)$ symmetry and its spontaneous breaking . . . . .	40
3.5.3	The $\sigma$ -model of QCD for $N_f = 2$ . . . . .	41
3.5.4	From $O(4)$ to the 3D-Ising model . . . . .	43
3.5.5	The 3D-Ising model effective action . . . . .	46
<b>4</b>	<b>Simulating the Chiral Condensate</b> . . . . .	<b>49</b>
4.1	Introduction . . . . .	49
4.2	Geometry . . . . .	50
4.2.1	The Ising model of magnetization . . . . .	50
4.2.2	3D Ising and Bjorken cascade . . . . .	51
4.3	Fractal clusters . . . . .	53
4.3.1	Magnetic clusters and critical fractality . . . . .	53
4.3.2	Saddle point approximation . . . . .	54
4.3.3	The baryon-number density as an alternative order parameter . . . . .	58
4.4	Fractal structure of clusters in transverse momentum space . . . . .	59
4.4.1	Density-density correlation function . . . . .	59
4.4.2	Inclusive distributions and intermittency . . . . .	62
4.5	Stochastic fractals and Lévy walks . . . . .	65
4.5.1	Generating stochastic fractals through random walks . . . . .	65
4.5.2	Distributions with finite and infinite variance. Lévy walks. . . . .	66
4.5.3	Cartesian products of Lévy walks. . . . .	70
4.6	Critical Monte Carlo (CMC) implementation . . . . .	71
4.6.1	The CMC algorithm . . . . .	71
4.6.2	Input parameter values . . . . .	73
4.6.3	The CMC algorithm for baryons . . . . .	76
4.7	The Chiral Condensate as an attractor . . . . .	79
<b>5</b>	<b>Analysis of NA49 experiment data sets</b> . . . . .	<b>85</b>
5.1	Introduction . . . . .	85
5.2	The NA49 experiment . . . . .	86
5.3	The analyzed data sets . . . . .	88
5.3.1	Event & track selection cuts . . . . .	89
5.3.2	Proton identification . . . . .	89
5.3.3	The $q_{inv}$ correlation function . . . . .	90

5.3.4	The $\Delta p_T$ correlation function	93
5.4	Transverse momenta analysis	93
5.4.1	Scaled factorial moments	93
5.4.2	Background subtraction	95
5.4.3	Statistical fluctuation handling	97
5.5	Results	101
5.5.1	NA49 datasets at maximum energy	101
5.5.2	CMC and EPOS simulation	110
5.5.3	Fluctuations at $\sqrt{s_{NN}} = 8.8$ GeV (40A GeV)	114
<b>6</b>	<b>Conclusions &amp; Future Prospects</b>	<b>115</b>
<b>A</b>	<b>Analytical calculation of mixed events</b>	<b>119</b>
A.1	The Problem	119
A.2	Assumptions	119
A.3	Expectation values for constant $L$	120
A.4	Expectation point and pair values per cell, for constant $L$	121
A.5	Weighing over event multiplicity distribution	121
A.6	General properties of $\langle F_{2,th}(M) \rangle$	122
A.7	Comparison of theoretical prediction to real mixed events	122
A.7.1	$F_{2,th}(M)$ of gaussian noise in $p_x, p_y$ (disjoint)	123
A.7.2	$F_{2,th}(M)$ for the actual mixed events in the “Si”+Si system	125
<b>B</b>	<b>Critical Monte Carlo code</b>	<b>127</b>
B.1	CMC code for $\sigma$	127
B.2	CMC code for protons	135
B.3	Numerical recipes auxiliary code	138
<b>C</b>	<b>Applied cuts for the NA49 data sets</b>	<b>145</b>
C.1	“Si”+Si, 158A GeV	145
C.2	“C”+C, 158A GeV	147
C.3	Pb+Pb low-intensity (00B), 158A GeV	151
C.4	Rapidity profiles and cuts for analyzed systems	157
	<b>Bibliography</b>	<b>159</b>



# List of Figures

2.1	Conjectured QCD Phase Diagram . . . . .	20
2.2	Critical points on QCD Phase Diagram . . . . .	21
2.3	Columbia Phase Diagram in $m_{u,d}-m_s$ space . . . . .	26
2.4	The pseudo-critical temperature in various lattice QCD simulations . . . . .	27
2.5	Evolution of Columbia plot with increasing $\mu_B$ . . . . .	29
3.1	The typical form of the O(N) potential, illustrated for the O(2) case. . . . .	40
3.2	Phase diagram of the $\phi^6$ model . . . . .	45
4.1	A sketch of the Bjorken inside-outside cascade scenario . . . . .	52
4.2	A random Lévy walk of 500,000 steps ( $D_F = 1.5$ ) . . . . .	68
4.3	Correlation function $C(R)$ vs distance scale $R$ for the Lévy walk in Fig.4.2 . . . . .	69
4.4	CMC Monte Carlo distributions (for $\sigma$ ) . . . . .	74
4.5	$\rho(p_x, p_y)$ one-particle distribution for CMC ( $\sigma$ ) . . . . .	75
4.6	$F_2(M)$ of transverse $\sigma$ momenta for CMC algorithm . . . . .	75
4.7	Proton multiplicity distribution for baryon-CMC . . . . .	77
4.8	Baryon-CMC Monte Carlo distributions ( $\phi, p_T$ ) . . . . .	78
4.9	$\rho(p_x, p_y)$ one-particle distribution for baryon-CMC (protons) . . . . .	78
4.10	$F_2(M)$ of transverse proton momenta for CMC-baryon algorithm . . . . .	79
4.11	The Ikeda attractor . . . . .	81
4.12	SSFMs $F_2(M)$ for the Ikeda attractor . . . . .	82
5.1	A schematic representation of the NA49 experiment . . . . .	86
5.2	Set up of the NA49 experiment . . . . .	87
5.3	$C(q_{inv})$ correlation function of proton pairs (“C”+C, “Si”+Si, Pb+Pb) . . . . .	91
5.4	$C(q_{inv})$ correlation function of proton pairs (high-intensity Pb+Pb) . . . . .	92
5.6	Effect of lattice displacement on SSFMs (sketch) . . . . .	98
5.7	SSFMs $F_2(M)$ on the Ikeda attractor, with and without lattice average . . . . .	99
5.8	SSFMs of protons in transverse momentum space for data & mixed events . . . . .	105
5.9	Correlator $\Delta F_2^{(e)}(M)$ for the moments in Fig. 5.8 . . . . .	106

5.10	Distribution $P(\phi_2)$ of bootstrap samples of $\phi_2$ (“C”+C, “Si”+Si, Pb+Pb) . . .	107
5.11	Fit errors $\delta\phi_2$ vs $\phi_2$ bootstrap values (“C”+C, “Si”+Si, Pb+Pb) . . . . .	108
5.12	Weighted $P(\phi_2)$ distribution of bootstrap samples (“C”+C, “Si”+Si, Pb+Pb)	109
5.13	SSFMs and $\Delta F_2^{(e)}(M)$ for baryon-CMC, compared to NA49 “Si”+Si . . . . .	111
5.14	Correlator $\Delta F_2^{(e)}(M)$ of protons for EPOS event generator and “Si”+Si . . . .	113
5.15	$C(q_{inv})$ distribution and $F_2(M)$ for Pb+Pb (00W) at 158A GeV . . . . .	114
A.1	Probability distribution function of momenta over the lattice (sketch) . . . .	120
A.2	Joint p.d.f. $\rho(p_x, p_y)$ for stochastic, normally distributed mixed events . . . .	123
A.3	Real and analytically predicted $F_2(M)$ of random (gaussian) mixed events	124
A.4	Joint p.d.f. $\rho(p_x, p_y)$ for the “Si”+Si dataset . . . . .	125
A.5	Real and analytically predicted $F_2(M)$ of mixed events for the “Si”+Si system	126
C.1	Summary of the “Si”+Si vertex cuts . . . . .	146
C.2	Normalized veto energy distribution for “Si”+Si . . . . .	146
C.3	$dE/dx$ vs $p_{tot}$ distributions for “Si”+Si . . . . .	148
C.4	Proton rapidity distributions for beam components in the “Si”+Si dataset .	148
C.5	Summary of the “C”+C 3mm vertex cuts . . . . .	150
C.6	Summary of the “C”+C 10mm vertex cuts . . . . .	150
C.7	Veto energy distributions for “C”+C . . . . .	151
C.8	Summary of the Pb+Pb vertex cuts . . . . .	152
C.9	Summary of the ntf-nto cuts in Pb+Pb . . . . .	153
C.10	Veto energy distribution for Pb+Pb . . . . .	154
C.11	Impact parameter ( $B_x, B_y$ ) cuts for Pb+Pb . . . . .	155
C.12	Effect of the zFirst cut on track selection in the X-Z plane, for Pb+Pb . . . .	155
C.13	Effect of the zLast cut on track selection in the X-Z plane, for Pb+Pb . . . .	156
C.14	Effect of the cut on number of points in the TPCs for Pb+Pb . . . . .	156
C.15	$dE/dx$ vs $p_{tot}$ distributions for Pb+Pb . . . . .	157
C.16	Normalized rapidity distribution for analyzed systems . . . . .	158

# Abstract

The chiral critical point of QCD is characterized by a second order phase transition. At its vicinity, the quark-antiquark chiral condensate vanishes and chiral symmetry is partially restored. This phase transition is accompanied by a divergence of the correlation length, which induces a self-similar fractal geometry in the condensate, and results in macroscopic observables following well-defined power-law scaling dictated by certain universality classes.

We use intermittency analysis of second scaled factorial moments (SSFMs) in transverse momentum space in order to detect power-law (self-similar) fluctuations in the density-density correlation function of baryons produced in relativistic ion collisions at SPS, CERN. Based on the saddle-point approximation, we develop a model of the effective actions describing the  $\sigma$ -condensate and baryon density at the vicinity of the critical point, as well as Monte-Carlo simulations that implement these models on a computer. We apply improved intermittency analysis to the simulated condensate as well as experimental data sets in order to determine the possible location of the QCD critical point on the  $T - \mu_B$  phase diagram. Adapting existing statistical techniques to intermittency analysis, we improve the quality of the signal and estimation of statistical and systematic uncertainties. By juxtaposing simulations with experiment, we estimate the level of contamination by non-critical components and the degree of approach of the system to the critical point.

We find evidence of critical fluctuations of the proton density in “Si”+Si collisions at the maximum energy of the NA49 experiment at CERN, SPS. Based on this evidence, we estimate that the critical point is around the vicinity of the freeze-out of the “Si”+Si system ( $T \sim 165$  MeV,  $\mu_B \sim 250$  MeV). We propose further intermittency analysis in the same neighborhood by future experiments probing the phase diagram of QCD, such as NA61/SHINE.



# Preface

The present doctoral thesis is concerned with the study of the characteristics of the phase transition undergone by strongly interacting matter, as a system of hadrons goes from states of low temperature ( $T$ ) and baryochemical potential ( $\mu$ ) (baryon density) towards higher temperatures and/or densities. A phenomenon of particular interest in strongly interacting systems is the (partial) restoration of chiral symmetry during the transition from cold hadronic matter to the Quark Gluon Plasma (QGP). Based on calculations from first principles (e.g. arguments from symmetry), as well as lattice calculations in Quantum Chromodynamics (QCD), at finite temperatures and densities, it is strongly suspected that the corresponding phase diagram exhibits a first order phase transition line at low temperatures/high densities, which terminates at a critical point at some high temperature and finite baryon density.

The critical point of QCD has been an object of much theoretical as well as experimental interest. From a theoretical viewpoint, at the vicinity of the critical point, the system is expected to undergo a second order phase transition, accompanied by a divergence of the characteristic correlation length scale, a vanishing expectation value of the order parameter (chiral condensate), and the scaling of macroscopic quantities according to universal power laws. Approach to the critical point is therefore linked with the appearance of a condensate of massless (or almost massless) scalar  $\sigma$ -bosons possessing the characteristic quantum numbers of vacuum. Experimentally, conditions capable of producing hot and dense hadronic matter are artificially reproduced in high energy heavy ion collision experiments in heavy ion colliders such as CERN SPS, and the discovery and study of the QCD critical point is one of the objectives of such experiments (e.g. the NA49 and NA61 experiments at CERN). It is therefore important to determine the location of the critical point in the phase diagram of QCD, as well as to search for possible observable traces of a collision's approach to the critical point in future experiments.

Among the critical signatures proposed as indicators of an approach to the critical point are fluctuations of the density of produced particles following a power-law as a function of momentum scale, a phenomenon known as intermittent behaviour, or intermittency. The present work is primarily concerned with the study of critical

fluctuations of baryons in transverse momentum space.

The thesis consists of six chapters, structured as follows:

In the first chapter, a brief overview is given of the structure and symmetries of quark matter, as described by Quantum Chromodynamics. We describe the phenomena of confinement and chiral symmetry breaking that take place during the transition from quark gluon plasma at high temperatures to the common hadronic matter at lower temperatures. A brief reference is given to the Higgs mechanism, leading to the conclusion that it only accounts for a small fraction of hadron masses (the quark “current” masses). The role of chiral phase transition in explaining hadron masses (through quark “constituent” masses) is discussed.

In the second chapter, a more detailed description of the QCD phase diagram is given, with particular emphasis to the region of relatively high temperature and low chemical potential where the critical point of QCD is expected to lie. A summary is given of the various phases, and their symmetries, predicted by analytical or lattice calculations, for different regions of the phase diagram, and the different scenarios, depending on the quark masses and number of flavors, are outlined. The role of chiral symmetry breaking is explained and it is connected to the chiral condensate as an order parameter of the chiral phase transition. A review is given of effective theories describing the phenomenology of the condensate near the critical point, as well as the universality classes to which they belong. Finally, we briefly examine lattice calculations that attempt to numerically simulate the chiral phase transition and discuss the related techniques. Lattice predictions of the critical temperature are given, and the challenges and limitations of expanding them to finite baryon density are discussed.

The third chapter examines in more depth the geometric characteristics of the chiral condensate. A brief overview is given of the characteristics of second order phase transitions and the theory of critical phenomena in general. It is shown that a system undergoing second order phase transition at the critical point exhibits scale invariance and fractal self-similarity, due to long-range correlations, and its behaviour can therefore be described through scaling laws characterized by a handful of critical exponents, dictated by the universality class to which the phase transition belongs. Construction of an effective action at the vicinity of the critical point is illustrated using the magnetization model as an example, its role as the generating functional of correlation functions is explained and a connection is made between critical exponents and the fractal dimension of clusters formed at the critical point. Subsequently, the chiral symmetry is examined in detail and the chiral condensate is parametrized through the scalar  $\sigma$  and pseudoscalar pion fields. Effective 4th and 6th order models of spontaneous chiral symmetry breaking are discussed, and the QCD critical point, at finite baryon density, is connected to 6th order tricritical point theory. Finally, it is shown that, due to the decoupling of  $\sigma$  from pion fields, the appropriate universality class of the chiral critical point is the 3D-Ising universality class. The corresponding effective action class is presented, and the

isothermal critical exponent emerges as the main characteristic connected to the fractal geometry of the condensate.

The fourth chapter is an extended discussion of computational techniques of simulating the chiral condensate through stochastic Monte-Carlo algorithms. First, we adapt the 3D-Ising effective action of the scalar  $\sigma$ -field to the typical cylindrical geometry of a heavy ion collision, and show that, under specific approximations, it can be partitioned into independent rapidity and transverse space components. The saddle point approximation is used to derive corresponding solutions for each case, and it is shown that the chiral condensate can be described by a collection of fractal clusters in rapidity  $\times$  transverse space. Consequently, we derive the corresponding fractal cluster structure in transverse momentum space, and introduce the technique of scaled factorial moment (intermittency) analysis in order to probe the correlation function and fractal dimension in transverse momentum space. Subsequently, the mathematical technique of Lévy walks is introduced, which allows the simulation of fractal clusters. A detailed description is given of the Critical Monte Carlo (CMC) algorithm, which enables us to simulate critical clusters of  $\sigma$  particles (in transverse momentum/rapidity space) with the desired physical and geometric properties. A modified version of the CMC algorithm also allows us to produce critical baryon clusters, the factorial moments of which we can compare to those of experimental data sets (chapter 5). Through scaled factorial moment (SFM) analysis, we determine the fractal dimension of clusters produced by the CMC, demonstrating the self-consistency of the simulation. Finally, viewing the chiral condensate as a strange attractor with a fractal dimension, we apply intermittency analysis to subsets of the (deterministic) Ikeda attractor in order to assess the feasibility of attractor reconstruction from sparse and, possibly noisy, data.

In the fifth chapter, a brief overview is given of the NA49 heavy ion collision experiment (SPS, CERN). A summary is presented of the experimental data sets used in this analysis. Following a detailed description of the filters, cuts, and techniques used to extract transverse momenta from the raw data, as well as identify protons, the method of intermittency analysis of factorial moments in transverse momentum space is explained in detail, along with a description of the tools employed for signal enhancement and background removal. An intermittency analysis is then performed on the resulting data sets, as well as a number of Monte Carlo simulations (including the CMC model detailed in Chapter 4) designed to model the corresponding ion collisions. Based on the insights provided by the simulations, we assess the evidence of approach to the QCD critical point and discuss the statistical and systematic uncertainties involved.

Finally, in the sixth chapter, we summarize the results of our analysis and discuss future prospects for the search and detection of the QCD critical point in future heavy ion collision experiments.



# CHAPTER 1

## INTRODUCTION

### **1.1 Quantum Chromodynamics: The Universe’s fundamental building block theory.**

Quantum Chromodynamics (QCD) is the theory that describes strong interactions, i.e. the interactions among “color charges”, the fundamental building blocks of matter, quarks, as well as the vector bosons that mediate that interaction, gluons. It therefore holds the key to understanding the structure of nuclear matter as we know it, as well as for the study of the primeval, extremely hot matter in the early Universe, and the super-dense state of matter forming in regions of intense gravitational fields, such as in the core of neutron stars.

From a theoretical viewpoint, QCD is a well-founded theory formulated within the context of Quantum Field Theory, its fundamental equations having been derived with extreme elegance and economy from a few general symmetry constraints, in particular the constraint to be symmetric (invariant) under local gauge transformations. Nevertheless, *solving* its fundamental equations, as well as applying the theory to actual physical systems occurring in nature, poses an extremely difficult open problem. The primary cause of difficulty is the fact that QCD is a *non-abelian* theory, i.e. a theory the mediating bosons (gluons) of which also carry charge, and therefore interact and entangle with each other. Furthermore, despite the fact that the (classical) QCD Lagrangian exhibits a multitude of symmetries, most of these symmetries are absent in the “real world”; they appear to be broken.

The most evident discrepancy between theory and observation is that the fundamental particles predicted by QCD, quarks and gluons, do not occur free in nature, but remain confined inside hadrons. Matter, in extreme conditions, organizes in color-singlet resonances. This confinement of quarks is not yet fully understood theoretically; nevertheless, it has been established by lattice calculations.

The main challenges posed by QCD are: reduction of the structure of nuclear matter

to the fundamental interactions of their elementary constituents, quarks and gluons; explanation of the observed spectrum of hadrons; and study of the behavior of QCD in extreme conditions of temperature and pressure. The latter, as already mentioned, is of the essence in the study of the early history of the Universe. Moreover, we have reasons to expect that in such extreme conditions, many of the symmetries that are broken in the normal conditions of nuclear matter are restored, which would result in significant simplification of the calculations involved.

The aforementioned problems can be approached in a multitude of ways, including the construction of analytical models, numerical approximation through lattice calculations, as well as the combination of analytical and numerical methods. Meanwhile, there are planned – and ongoing – heavy ion collision experiments, through which are reproduced the conditions of high temperature and baryon density that allow the deconfinement of the fundamental QCD degrees of freedom, the results of which are juxtaposed with the theoretical models. A multifaceted dialog with Nature is in progress.

## 1.2 Apparent and actual symmetries of QCD

The general, idealized form of the QCD Lagrangian density, for  $f$  distinct “flavors” of quarks, is given by [Wilczek, 2000]:

$$\mathcal{L} = -\frac{1}{4g^2} \text{tr} G^{\mu\nu} G_{\mu\nu} + \sum_{j=1}^f \bar{\psi}_j (i\mathcal{D}) \psi_j \quad (1.1)$$

where:

$$G_{\mu\nu} = \partial_\mu A_\nu - \partial_\nu A_\mu + i[A_\mu, A_\nu]$$

$$D_\mu = \partial_\mu + i A_\mu$$

$A_\mu$  are  $3 \times 3$  Hermitian, traceless matrices.  $g$  is the dimensionless coupling constant of QCD. Each spin-1/2 fermionic quark field  $\psi_j$  incorporates a 3-component color index (aside from its spinorial 4-vector index, of course).

Eq.(1.1) is in a sense general enough, as it leaves room for any given number of quark flavors  $f$ . At the same time, though, it is idealized, since all quarks are taken to be massless. We will address the consequences of adding a quark mass term later on.

The structure of eq.(1.1) is uniquely determined by a few very general axioms. These are the SU(3) gauge symmetry, along with the general principles of quantum field theory – special relativity, quantum mechanics and locality – as well as the constraint that it is renormalizable. Renormalizability forbids the presence of more complicated terms, such as, for example, an anomalous gluomagnetic moment term  $\propto \bar{q} \sigma^{\mu\nu} G_{\mu\nu} q$ .

The apparent symmetry of eq.(1.1) is:

$$\mathcal{G}_{\text{apparent}} = SU(3)^c \times SU(f)_L \times SU(f)_R \times U(1)_B \times U(1)_A \times \mathcal{R}_{\text{scale}}^+ \quad (1.2)$$

along with Poincare invariance and discrete C,P,T symmetries. The terms are, in order: local color symmetry, freedom to rotate left-handed quarks among themselves by an arbitrary angle, freedom to rotate right-handed quarks among themselves by an arbitrary angle, baryonic number conservation (= a common overall phase for all quark fields), axial baryonic number conservation (= equal and opposite phases for all left- and right- handed quark fields), and scale invariance.

The *chiral symmetries*,  $SU(f)_L \times SU(f)_R$ , arise because the only quark interaction terms, i.e. their minimal coupling to gluons, is common to all quark flavors and respects (conserves) helicity. These chiral symmetries are broken by the introduction of quark mass terms, since such terms couple different helicities. For quarks of nonzero, but equal masses, all that remains is a diagonal (vector) symmetry  $SU(f)_{L+R}$ , whereas if quark flavors have unequal nonzero masses, the symmetry breaks into a product of  $U(1)_S$  symmetries. Therefore, the choice  $m = 0$  is an axiom strengthening the symmetry.

Lastly, the term  $\mathcal{R}_{\text{scale}}^+$  implies that the only parameter in our theory,  $g$ , is dimensionless (in units where  $\hbar = c = 1$ , as usual). Therefore, the classical theory is invariant under variations of units of length, or equivalently, (inverse) mass units. Indeed, the action  $\int d^4x \mathcal{L}$  is scale invariant:

$$x^\mu \rightarrow \lambda x^\mu; A \rightarrow \lambda^{-1} A; \psi \rightarrow \lambda^{-1} \psi \quad (1.3)$$

The actual symmetry, on the other hand, that QCD exhibits in reality, is rather different than its apparent symmetry. It is as follows:

$$\begin{aligned} \mathcal{G}_{\text{actual}} &= SU(3)^c \times SU(f)_L \times SU(f)_R \times Z_A^f \times U(1)_B \\ &\quad \text{(asymptotic freedom, chiral anomaly)} \\ &\rightarrow SU(3)^c \times SU(f)_{L+R} \times U(1)_B \\ &\quad \text{(chiral condensate)} \\ &= SU(f)_{L+R} \times U(1)_B \\ &\quad \text{(confinement)} \end{aligned} \quad (1.4)$$

At the first step of this escalating reduction of symmetries, we find the symmetries that survive quantization. Scale invariance,  $\mathcal{R}_{\text{scale}}^+$ , of the classical Lagrangian totally vanishes, while  $U(1)_A$  symmetry (axial baryon number) is reduced to its discrete subgroup  $Z_A^f$ . In both cases, the cause is the dynamical character of vacuum in quantum theory, and the need to renormalize the theory with respect to its potential degrees of freedom. Breakdown of scale invariance is related to the dependence of the coupling constant

on the energy (equivalently, length) scale, asymptotic freedom and the dimensional transmutation of the coupling constant. Axial baryon number breaking is related to the triangular anomaly and instantons. Loss of these symmetries is ingrained in the very structure of quantum field theory.

At the second step are recorded the symmetries of the quantized lagrangian that are also symmetries of the ground state (the vacuum of the theory). These are reduced due to spontaneous symmetry breaking. That is, stable solutions to the equations possess fewer symmetries than the equations themselves. Chiral symmetry is lost, because of the appearance in the ground state of a *chiral condensate* of quarks and antiquarks of opposite helicities, which uniformly fills space. Thus, we are no longer free to independently rotate left- and right-handed components, leaving the condensate invariant. The fact that  $\pi$ -mesons (pions) have a much smaller mass compared to other mesons is due to their role as the Goldstone bosons of this spontaneous symmetry breaking.

Finally, in the third step, we recognize the fact that the local color gauge symmetry, which is the cornerstone in the construction of the QCD Lagrangian, is not immediately apparent in any observable physical system. During the construction of the Hilbert space of QCD, we restrict ourselves to gauge invariant states. Besides, we never observe any long-range color interactions, and observed particles are organized in singlet, never multiplet, color states. Quarks and gluons are “trapped” inside nuclear matter; this is the essence of the phenomenon of *confinement*.

Consequently, we will briefly examine the phenomena of asymptotic freedom and quark confinement, as well as the theoretical evidence for the existence and explanation of these phenomena.

### 1.3 Asymptotic freedom

According to quantum field theory, empty space behaves as a dynamical medium; it is filled with virtual particle-antiparticle pairs. Therefore, we expect to encounter, as with every dynamical medium, the familiar effects of polarization, paramagnetism and diamagnetism of the vacuum: a test charge polarizes its surrounding space, resulting in a dependence of its field strength on the distance from it (*charge screening*); the value of the observed charge is not the “bare” value appearing in the Lagrangian, but an “effective” value that changes as we probe the charge at different distances, or equivalently, at different energy scales. Thus, the coupling constant is not a true constant, but scales with energy (*running coupling constant*).

Asymptotic freedom is a special case of running coupling, for which the effective charge value, though finite at a given finite distance from it, weakens as we approach it until it vanishes. This amounts to *anti-screening*, an intuitively unexpected effect, since it is the exact opposite of electromagnetic charge-screening familiar to us. It can

be justified, however, if we recall that QCD is a *relativistic, non-abelian gauge theory*. Therefore:

- Being relativistic, magnetic terms are equally important to electric terms.
- Being a gauge theory, it incorporates vector bosons.
- Being non-abelian, these vector bosons carry charge, and their spins carry magnetic moments.

A spin's response to an external magnetic field is paramagnetic; spins tend to align with the field as to enhance it. In the case of QCD, this paramagnetic influence of virtual gluons wins over the normal screening caused by quarks. Let us imagine quarks surrounded by a "cloud" of virtual gluons. When we probe a quark at low energies (large wavelength), the wavelength "covers" many spins (gluons), and the effective charge is large. Conversely, at high energies (small wavelength), the wavelength covers only a few gluons, and the effective charge is decreased.

When the effective coupling constant has decayed enough, one can calculate perturbatively the charge (anti-)screening. For QCD, we get the following result for the running of the coupling constant:

$$\frac{dg(\epsilon)}{d \ln \epsilon} = \beta_0 g^3 + \beta_1 g^5 + \dots \quad (1.5)$$

where

$$\beta_0 = -\frac{1}{16\pi^2} \left( 11 - \frac{2}{3}f \right)$$

$$\beta_1 = \left( \frac{1}{16\pi^2} \right)^2 \left( 102 - \frac{38}{3}f \right)$$

where  $\epsilon$  is the energy scale, or equivalently the inverse length scale, for which the effective charge is defined. Therefore, for  $f \leq 16$  flavors, the effective coupling constant decreases to zero as the probing energy tends to infinity. This phenomenon is called *asymptotic freedom*. Taking only the first term, we see that the asymptotic behaviour can be approximated by:

$$\frac{1}{g(\epsilon)^2} = \frac{1}{g(1)^2} - \beta_0 \ln \epsilon \quad (1.6)$$

Asymptotic freedom facilitates calculations at higher energies; quarks then behave almost like free particles, since their color charge decays (conversely, electromagnetic charge is enhanced, thus revealing the presence of point-like sources of the electromagnetic field). Taking advantage of asymptotic freedom, we can predict the cross-sections

as well as the spatial topology of many processes, such as e.g.  $e^+e^-$  annihilation at high energies. These predictions are confirmed by numerous experiments. Unfortunately, these techniques limit us to the high energy region, while they are ineffectual where lower energy scales are involved.

The running of the coupling constant breaks the classical scale symmetry  $\mathcal{R}_{\text{scale}}^+$ , causing the so-called *dimensionalization* of the coupling constant: the coupling, which is classically a dimensionless, scale-invariant constant, in quantum theory becomes a function of energy scale, i.e. it boils down to a characteristic length or energy scale. Through eq.(1.5), we can indeed define a scale:

$$M = \lim_{\epsilon \rightarrow \infty} \epsilon e^{\frac{u}{\beta_0}} u^{\frac{\beta_1}{\beta_0^2}} \quad (1.7)$$

where

$$u \equiv \frac{1}{g(\epsilon)^2}$$

## 1.4 Confinement

One of the historical problems of QCD, which held back its acceptance, has been the phenomenon of quark confinement, i.e. the fact that we don't observe free quarks in nature. Specifically, among the experimentally detectable resonances we observe neither flavor-singlet, massless particles with long-range interactions, nor does the observed spectrum include SU(3) color singlets, nor, finally, do we see particles carrying the quantum numbers of pure quarks and gluons. Confinement, therefore, is well-documented in practice, but what can the theory tell us about it, and under what conditions can it be lifted?

A first argument, due to Amati and Testa, results directly from the Lagrangian, eq.(1.1). When the coefficient  $\frac{1}{g^2}$  tends to zero, i.e. when the coupling is strong enough, variation of the action with respect to the field  $A_\mu$  leads to a nullifying of color current and, therefore, the color density too; color has been confined, and with it, quarks. Therefore, low-frequency modes (large coupling constant) are confined, while high-frequency modes (small coupling constant) exhibit asymptotic freedom.

This model, however, is too crude: we have neglected higher-order derivative terms, which dominate when variations are too abrupt. For this reason, more refined models have been created, lattice gauge theories. In these models, we discretize space, taking care to preserve gauge symmetry. Discretization introduces a minimum lattice distance, in this way eliminating any ultraviolet divergences. This arbitrary cutoff needs to be canceled out, so that it doesn't affect resulting values. This is achieved through the introduction of ever smaller lattice constants, while at the same time we integrate over newly introduced degrees of freedom, in order to get a theory with the same physical

meaning. This process, which leads to the redefinition of the parameters of the theory, is called *renormalization*.

Leaving aside details, we note that perturbative calculations in lattice theory, in the case of strong coupling, taking only gluons into account (*pure glue*) and expanding the action in powers of  $1/g^2$ , where  $g$  is the (strong) coupling, lead to an estimate of the form of quark-antiquark potential. To this end, we define the action of the field  $A_\mu$  in the lattice as the trace of the product of transfer matrices, and we integrate over closed space-time paths (Wilson-Polyakov loops), at the spatial ends of which we have “implanted” a heavy quark-antiquark pair. The resulting potential has the form  $V(R) \propto R$ , i.e. it increases linearly with distance  $R$ , which means it is impossible to separate color charges indefinitely. Thus, the phenomenon of confinement is confirmed.

## 1.5 Chiral symmetry & chiral symmetry breaking

As was already mentioned, the classical QCD Lagrangian, eq.(1.1), is invariant under the independent rotation of left- and right-handed components of the massless quark fields:

$$q_L = \frac{1}{2}(1 - \gamma_5)q \quad ; \quad q_R = \frac{1}{2}(1 + \gamma_5)q \quad ; \quad \gamma_5 \equiv i\gamma_0\gamma_1\gamma_2\gamma_3 \quad (1.8)$$

Thus, the *helicity* (spin projection in the direction of particle momentum) of quarks is a conserved quantity, and therefore the baryon numbers of both left- and right-handed quarks are conserved – there are no transitions among the two helicities. We define:

$$B = B_L + B_R \quad ; \quad \Delta B = B_L - B_R \quad (1.9)$$

where  $B_L, B_R$  are the left and right baryon numbers. This independence of left- and right-handed degrees of freedom is known as the *chiral symmetry* of QCD.

At low temperatures in nature, however, the chiral symmetry is apparently broken. The reason is twofold:

- For massless quarks at low temperatures, quark-antiquark interaction leads to the spontaneous formation of a *chiral condensate* that violates chiral symmetry. In essence, the ground state (vacuum) of QCD does not respect the symmetry of the Lagrangian; the quantum vacuum is unstable with regards to chiral condensate formation:

$$\langle 0 | \bar{q}q | 0 \rangle \equiv \langle 0 | \bar{q}_L q_R + \bar{q}_R q_L | 0 \rangle,$$

Thus, only the total baryon number  $B = B_L + B_R$  is conserved, and we have quark pairs with  $\Delta B = \pm 2$ . This spontaneous symmetry breaking is completely analogous to the spontaneous magnetization of a ferromagnet below the Curie temperature.

- A non-zero mass term for quarks:

$$m_f \left( \bar{q}_L^f q_R^f + \bar{q}_R^f q_L^f \right)$$

couples left- and right-handed components, explicitly breaking chiral symmetry, and allowing transitions between helicities,  $L \leftrightarrow R$ , at a rate proportional to  $m_f$ . Thus,  $\Delta B$  is no longer conserved.

Quark	$\frac{Q}{e}$	Constituent mass (MeV)	Current mass (MeV)
$d$	$-1/3$	$\sim 350$	$3.5 \rightarrow 6.0$
$u$	$+2/3$	$\sim 350$	$1.5 \rightarrow 3.3$
$s$	$-1/3$	$\sim 550$	$104 \pm 30$
$c$	$+2/3$	$\sim 1800$	$1270 \pm 100$
$b$	$-1/3$	$\sim 4200$	$4200 \pm 100$
$t$	$+2/3$	$\sim 170 \times 10^3$	$(170 \pm 2) \times 10^3$

**Table 1.1:** Constituent and current masses of quarks

Even first generation quarks have small, nonzero current masses. However, these masses are only a fraction of the constituent masses they appear to have as parts of hadrons (see Table 1.1). Therefore, the phenomenon of confinement, in combination with spontaneous chiral symmetry breaking and condensate formation, account for most of the mass of (at least the light) hadrons in nature.

It is interesting to compare the role of chiral symmetry breaking to the Higgs mechanism. The scalar Higgs field is responsible, within the Standard Model, for the masses of the gauge vector bosons,  $W^\pm$  and  $Z$ , and through Yukawa couplings also for the non-zero current masses of quarks. In fact, the Higgs mechanism is based on the interplay of spontaneous symmetry breaking and gauge invariance, and thus has many similarities to chiral symmetry breaking. But in the case of light  $u$  and  $d$  quarks, the masses afforded through the Higgs mechanism are small enough that the chiral symmetry approximately holds. It is therefore only through spontaneous chiral symmetry breaking that the nucleons acquire 99% of their observed masses!

Let us briefly review the mechanism underlying chiral symmetry breaking: at low temperatures, and assuming for the moment zero  $u$  and  $d$  quark masses, the initial chiral symmetry spontaneously breaks down to its diagonal vector subgroup,

$$SU(2)_L \times SU(2)_R \rightarrow SU(2)_{L+R} \quad (1.10)$$

no longer allowing independent rotation of helicities. Thus, the chiral condensate is formed, breaking the symmetry of QCD equations. Since the condensate has to choose

an orientation, there is now a whole spectrum of rotationally equivalent ground states. The Nambu-Goldstone bosons that correspond to this rotational degree of freedom would be massless in the case of exactly zero quark masses. However, since  $u, d$  quarks have small masses, we look for an  $SU(2)_{L+R}$  isospin-triplet of light, scalar bosons,  $J^{PC} = 0^{-+}$  – and these turn out to be exactly the  $\pi^{\pm}$  and  $\pi^0$  pions. At the same time, the excitational degrees of freedom define an isoscalar-scalar *massive* field, the  $\sigma$ -field:

$$\sigma(\mathbf{x}) \sim \langle 0 | \bar{q}(\mathbf{x}) q(\mathbf{x}) | 0 \rangle \quad (1.11)$$

which is identified with the chiral condensate and plays the role of the order parameter of the chiral phase transition. In the following chapter, we explore in detail the nature of this phase transition, and the QCD phase diagram in general.



## CHAPTER 2

# THE PHASE DIAGRAM OF QCD

### 2.1 Introduction

As we mentioned in Chapter 1, the fundamental symmetries of QCD are broken in normal conditions of low temperature and pressure. On the other hand, evidence from heavy ion collision experiments, as well as models of the early Universe and study of astrophysical objects such as neutron stars, indicate that in extreme conditions of temperature and pressure, the fundamental degrees of freedom of QCD are restored: quarks are deconfined (asymptotic freedom), chiral symmetry is restored, and axial baryon number symmetry becomes increasingly accurate.

More specifically, starting at zero baryon density  $n_B$  and gradually increasing temperature, we go from a state of hadron gas (HG) to a plasma of weakly interacting quarks and gluons (quark-gluon plasma, QGP). On the other hand, if we increase baryon density at zero temperature, we first encounter nuclear matter and then superdense states, such as found in the core of neutron stars.

We therefore have good reason to believe that there are one or more phase transition lines separating the phases of QCD matter. Across those boundaries, QCD matter undergoes a *phase transition*; the nature (order) and classification of such phase transitions is the subject of much experimental, theoretical and computational study.

QCD in approximate thermal and chemical equilibrium is characterized by 2 external parameters, the temperature  $T$  and the baryon number density  $n_B$ . In the grand canonical ensemble, the quark chemical potential  $\mu_q = \mu_B/3$  may be introduced as a conjugate variable to the quark number density  $n_q = 3n_B$ .) Since the intrinsic scale of QCD is  $\Lambda_{\text{QCD}} \sim 200 \text{ MeV}$ , it would be conceivable that the QCD phase transition should take place around  $T \sim \Lambda_{\text{QCD}} \sim \mathcal{O}(10^{12})\text{K}$  or  $n_B \sim \Lambda_{\text{QCD}}^3 \sim 1 \text{ fm}^{-3}$ .

Heavy ion collision experiments worldwide allow us to produce hot and/or dense QCD matter and probe its properties. In particular, the Relativistic Heavy-Ion Collider (RHIC) at Brookhaven National Laboratory (BNL) has conducted experiments to create

hot QCD matter (quark-gluon plasma) by Au-Au collisions with the highest collision energy  $\sqrt{s_{NN}} = 200 \text{ GeV}$  [Stankus et al., 2009]. The Large Hadron Collider (LHC) at CERN will continue experiments along the same line with higher energies [Stankus et al., 2009; Abreu et al., 2007]. Exploration of a wider range of the QCD phase diagram with  $n_B$  up to several times of the normal nuclear matter density  $n_0 \simeq 0.17 \text{ fm}^{-3}$  may be carried out by low-energy scans in HIC at RHIC as well as at the future facilities such as the Facility for Antiproton and Ion Research (FAIR) at GSI, the Nuclotron-based Ion Collider Facility (NICA) at JINR and the Japan Proton Accelerator Research Complex (JPARC) at JAERI. Also at CERN, SPS experiments, such as NA49 and its continuation, the NA61 experiment, probe the relatively high-temperature and low (finite) baryochemical potential  $\mu_B$  in search of the QCD Critical point.

Turning to nature itself, the core conditions of stellar objects such as neutron stars would be ideal systems to probe for dense QCD matter at low temperature (see [Heiselberg and Hjorth-Jensen, 2000] for a review). For high enough baryon densities, weak coupling QCD analyses indicate that the QCD ground state forms a condensation of quark Cooper pairs, known as colour superconductivity (CSC). This is a much more complex pattern than that electron Cooper pairs in metallic superconductors, since quarks carry not just spin, but also the quantum numbers of color and flavor.

In this Chapter, we outline the current understanding of the QCD *phase diagram*, by which we mean the qualitative and quantitative information of where the boundaries (phase transition lines) that separate QCD matter phases lie, to what order they belong, as well as the physical characteristics of the phases they delimit. Each phase must be thought of as a system of strongly interacting matter at approximate chemical and thermal equilibrium. In what follows, we focus primarily on the relatively low baryon density and high temperature phase transition, and especially on the conjectured *QCD Critical Point*.

## 2.2 QCD phase structure

### 2.2.1 Deconfinement and chiral restoration

A preliminary picture of the QCD phase diagram in  $T$ - $n_B$  plane can be found in [Cabibbo and Parisi, 1975]. One can interpret Hagedorn's limiting temperature in the Statistical Bootstrap Model (SBM) [Hagedorn, 1965] as a critical temperature associated with a second-order phase transition into a new state of matter. It has also been recognized [Collins and Perry, 1975] that asymptotic freedom implies the existence of a phase of weakly interacting quark matter at large  $n_B$ .

Phase transitions of QCD matter are distinguished into *deconfinement* and *chiral restoration*:

- *Deconfinement* — An early model by [Hagedorn, 1985] uses a hadron resonance gas at finite temperature. The density of hadronic states (mostly mesons), a function of resonance mass  $m$  and the temperature  $T^{\text{H}} \simeq 0.19 \text{ GeV}$  known from the Regge slope parameter, has to be balanced against the Boltzmann factor  $\exp(-m/T)$  in the partition function. When  $T > T^{\text{H}}$ , the integration over  $m$  becomes singular, so that  $T^{\text{H}}$  plays a role of the limiting temperature (Hagedorn temperature) above which the hadronic description breaks down. This argument is applied to estimate the critical value of  $\mu_{\text{B}}$  as well. The density of baryonic states is balanced by the Boltzmann factor  $\exp[-(m_{\text{B}} - \mu_{\text{B}})/T]$ , leading to the limiting temperature  $T = (1 - \mu_{\text{B}}/m_{\text{B}})T_{\text{B}}^{\text{H}}$ . We see equivalently that the critical  $\mu_{\text{B}}$  at  $T = 0$  is given by  $m_{\text{B}}$  ( $\gtrsim 1 \text{ GeV}$ ).

The simple Bag Model, in which valence quarks are free except for the confining pressure of the “bag” (boundary), allows us to picture deconfinement as a gradual overlap of hadrons that leads to the dissolution of the bag at the Hagedorn temperature [Baym, 1979; Satz, 1998]. This naive image, however, needs to be supplemented by a more careful field-theoretical definition of the quark-deconfinement in QCD.

- *Chiral restoration* — As already mentioned in Chapter 1, QCD vacuum fluctuations are responsible for the generation of the non-perturbative quark *constituent* masses. In hot and dense quark matter, we expect quarks to become asymptotically free, acquiring their bare, *current* masses, and also restoring the chiral symmetry of QCD. One therefore expects to see a chiral phase transition. The QCD phase diagram at finite  $T$  and  $\mu_{\text{B}}$  has also been studied from the point of view of chiral symmetry [Hatsuda and Kunihiro, 1985]. The order parameter corresponding to the chiral phase transition is the chiral condensate,  $\langle \bar{\psi}\psi \rangle$  which takes a value about  $-(0.24 \text{ GeV})^3$  in the vacuum and sets a natural scale for the critical temperature of chiral restoration. In the chiral perturbation theory ( $\chi$ PT), the chiral condensate for two massless quark flavours at low temperature is known to behave as  $\langle \bar{\psi}\psi \rangle_T / \langle \bar{\psi}\psi \rangle = 1 - T^2/(8f_{\pi}^2) - T^4/(384f_{\pi}^4) - \dots$ , where  $f_{\pi}$  is the pion decay constant,  $f_{\pi} \simeq 93 \text{ MeV}$  [Gerber and Leutwyler, 1989].  $\chi$ PT only applies at low temperature; however, this is good evidence for the dissolution of the chiral condensate at finite temperature. At low baryon density, likewise, the chiral condensate decreases as  $\langle \bar{\psi}\psi \rangle_{n_{\text{B}}} / \langle \bar{\psi}\psi \rangle = 1 - \sigma_{\pi N} n_{\text{B}} / (f_{\pi}^2 m_{\pi}^2) - \dots$  [Drukarev and Levin, 1991; Cohen et al., 1992; Hatsuda and Lee, 1992] where  $\sigma_{\pi N} \sim 40 \text{ MeV}$  is the  $\pi$ - $N$  sigma term.

### 2.2.2 An outline of the QCD phase diagram

Fig.2.1 shows our current understanding of the QCD phase diagram. Various phases and features are shown, some more speculative than others. Our predictions can be said

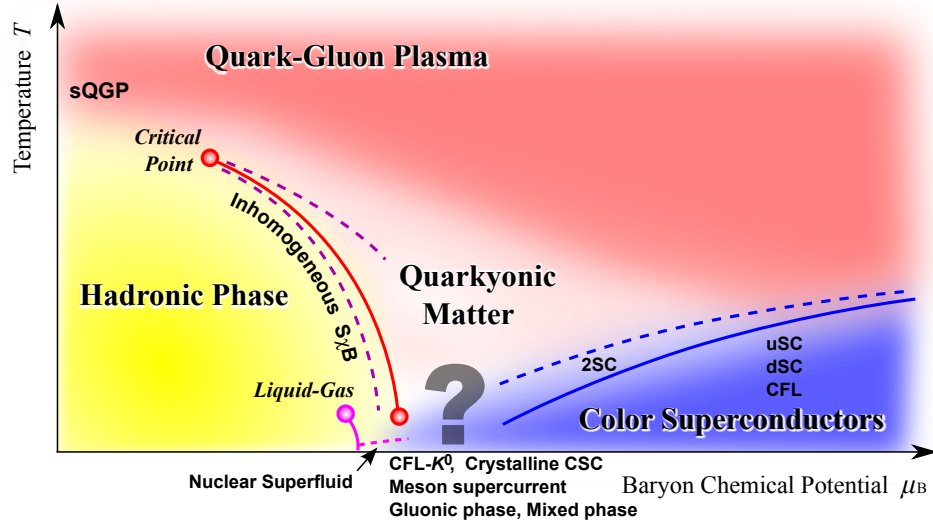


**Figure 2.1:** Conjectured QCD phase diagram with boundaries that define various states of QCD matter based on  $S\chi B$  patterns. Figure by [Fukushima and Hatsuda, 2011]

to be fairly accurate at finite  $T$  with small baryon density ( $\mu_B \ll T$ ) and at asymptotically high density ( $\mu_B \gg \Lambda_{\text{QCD}}$ ). In what follows, we take a closer look at key features of Fig.2.1.

**Hadron-quark phase transition at  $\mu_B = 0$ :** The phase transition from hadron gas to QGP at zero chemical potential has been studied through lattice numerical simulations. Results depend on the number of flavors and colors, [Svetitsky and Yaffe, 1982; Pisarski and Wilczek, 1984]. In the case of  $N_c = 3$  and  $N_f = 0$ , a 1st order phase transition is established through finite size lattice scaling [Fukugita et al., 1990], with a critical temperature of  $T_c \simeq 270 \text{ MeV}$ . For  $N_f > 0$  light flavors, analyses based on staggered fermion and Wilson fermion predict a crossover from HG to QGP for realistic  $u$ ,  $d$  and  $s$  quark masses [Aoki et al., 2006a; DeTar and Heller, 2009]. The pseudo-critical temperature  $T_{\text{pc}}$ , which characterizes the crossover location, is estimated to be within the range  $150 \text{ MeV} - 200 \text{ MeV}$ . For temperatures above  $T_{\text{pc}}$ , one may find strong correlations and pre-formed hadrons in QGP, at  $\mu_B = 0$  [Hatsuda and Kunihiro, 1985; Detar, 1985] as well as at  $\mu_B \neq 0$  [Kitazawa et al., 2002; Abuki et al., 2002; Nishida and Abuki, 2005].

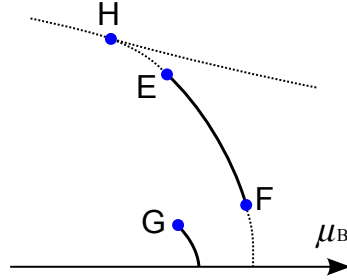


**Figure 2.2:** Characteristic points on the QCD phase diagram. E represents the so-called QCD critical point. F is another critical point induced by the quark-hadron continuity. G is the critical point associated with the liquid-gas transition of nuclear matter. H refers to a region which looks like an approximate triple point. Figure by [Fukushima and Hatsuda, 2011].

**QCD critical points:** Beyond the region  $\mu_B \sim T$ , lattice calculations are unreliable. However, effective chiral models suggest the existence of a *QCD critical point* at  $(\mu_B = \mu_E, T = T_E)$ , with a 1st order (crossover) phase transition for  $\mu_B > \mu_E$  ( $\mu_B < \mu_E$ ), for realistic values of  $u$ ,  $d$  and  $s$  quark masses [Asakawa and Yazaki, 1989; Barducci et al., 1989; Wilczek, 1992; Berges and Rajagopal, 1999] (see the point E in Fig.2.2). In the vicinity of the critical point, enhanced fluctuations are expected, which is why the search for the QCD critical point is of great experimental interest [Stephanov et al., 1998, 1999].

It is also possible that another critical point F exists, Fig.2.2, at a location  $(\mu_F, T_F)$ , in the lower- $T$  and higher- $\mu_B$  region. The existence and location of E and F depend crucially on the relative magnitude of the strange quark mass  $m_s$  and the typical values of  $T$  and  $\mu_B$  at the phase boundary.

**Liquid-gas phase transition of nuclear matter:** In the low  $T$  region of the plot, and around  $\mu_B = \mu_{NM} \simeq 924 \text{ MeV}$ , a non-vanishing nuclear matter baryon density starts to form. At the threshold  $\mu_B = \mu_{NM}$ , the density  $n_B$  varies between zero and the normal nuclear density  $n_0 = 0.17 \text{ fm}^{-3}$ , as droplets of nuclear matter start to form, in the manner of liquid-gas phase transition. This 1st order phase transition line ends up at a 2nd order phase transition critical point G, located at  $(\mu_G, T_G)$ , Fig.2.2. Low energy HIC experiments indicate that  $\mu_G \sim \mu_{NM}$  and  $T_G = 15 \sim 20 \text{ MeV}$  [Chomaz, 2004].

**Quarkyonic matter:** The Statistical Model, which assumes a thermally equilibrated gas of non-interacting mesons, baryons and resonances, defines a chemical freeze-out line. This line, although not a phase boundary, should lie close to the phase transition line. Mesons dominate thermal degrees of freedom for  $\mu_B \ll m_N$ , and baryons for

higher values of  $\mu_B$ . It is therefore likely that there is a point H, at  $(T_H, \mu_H)$ , around  $\mu_H = 350 \sim 400 \text{ MeV}$  and  $T_H = 150 \sim 160 \text{ MeV}$ , where the importance of baryons in thermodynamics surpasses that of mesons.

In the  $N_c = \infty$  limit, a finite baryon density arises, a cold, dense matter known as *quarkyonic matter*. For finite  $N_c$ , a remnant of a triple point remains, indicated by H in Fig.2.2.

**Colour superconductivity:** For  $\mu_B$  asymptotically large,  $\mu_B \gg \Lambda_{\text{QCD}}$ , we can use weak-coupling QCD methods in the analysis, and rely on knowledge of condensed matter physics, substituting quarks for electrons. We then get the analog of Cooper electron pairs, for low  $T$ , known as color superconductivity (CSC) [Rajagopal and Wilczek, 2000; Alford et al., 2008; Huang, 2010; Schmitt, 2010; Barrois, 1977; Bailin and Love, 1984].

## 2.3 QCD phase transition order parameters

### 2.3.1 Polyakov loop and quark deconfinement

The Polyakov loop which characterizes the deconfinement transition in Euclidean space-time is defined as [Polyakov, 1978; Susskind, 1979]

$$L(\mathbf{x}) = \mathcal{P} \exp \left[ -ig \int_0^\beta dx_4 A_4(\mathbf{x}, x_4) \right], \quad (2.1)$$

which is an  $N_c \times N_c$  matrix in color space. Here  $\beta$  is the inverse temperature  $\beta = 1/T$ , and  $\mathcal{P}$  represents the path ordering. We will use  $\ell$  to represent the traced Polyakov loop,

$$\ell = \frac{1}{N_c} \text{tr} L. \quad (2.2)$$

Under the center transformation group,  $Z(N_c)$  of  $SU(N_c)$ , the gauge field  $A_4$  receives a constant shift, and the traced Polyakov loop transforms as  $\ell \rightarrow z_k \ell$ . Because  $A_4^k$  remains periodic in  $x_4$ , such a non-periodic gauge transformation still forms a symmetry of the gauge action. This is called center symmetry [Svetitsky, 1986; Svetitsky and Yaffe, 1982]. The quark action explicitly breaks center symmetry, which only is an exact symmetry in the pure gluonic theory where dynamical quarks are absent or quark masses are infinitely heavy ( $m_q \rightarrow \infty$ ).

The expectation value of the Polyakov loop and its correlation in the pure gluonic theory can be written as [McLerran and Svetitsky, 1981; Nadkarni, 1986b,a]

$$\Phi = \langle \ell(\mathbf{x}) \rangle = e^{-\beta f_q}, \quad \bar{\Phi} = \langle \ell^\dagger(\mathbf{x}) \rangle = e^{-\beta f_{\bar{q}}}, \quad (2.3)$$

$$\langle \ell^\dagger(\mathbf{x}) \ell(\mathbf{y}) \rangle = e^{-\beta f_{q\bar{q}}(\mathbf{x}-\mathbf{y})}. \quad (2.4)$$

	Confined (Disordered) Phase	Deconfined (Ordered) Phase
Free Energy	$f_q = \infty$ $f_{\bar{q}q} \sim \sigma r$	$f_q < \infty$ $f_{\bar{q}q} \sim f_q + f_{\bar{q}} + \alpha \frac{e^{-m_M r}}{r}$
Polyakov Loop ( $r \rightarrow \infty$ )	$\langle \ell \rangle = 0$ $\langle \ell^\dagger(r)\ell(0) \rangle \rightarrow 0$	$\langle \ell \rangle \neq 0$ $\langle \ell^\dagger(r)\ell(0) \rangle \rightarrow  \langle \ell \rangle ^2 \neq 0$

**Table 2.1:** Behaviour of the expectation value and the correlation of the Polyakov loop in the confined and deconfined phases in the pure gluonic theory.

Here, the constant  $f_q$  ( $f_{\bar{q}}$ ) independent of  $\mathbf{x}$  is an excess free energy for a static quark (anti-quark) in a hot gluon medium. Also,  $f_{\bar{q}q}(\mathbf{x} - \mathbf{y})$  is an excess free energy for an anti-quark at  $\mathbf{x}$  and a quark at  $\mathbf{y}$ .

Table 2.1 summarizes the results of the Polyakov loop and its correlation for the potential between a quark and an anti-quark in the confined and deconfined phases (pure gluonic theory). In the confined phase, there can be no free quarks, and the potential increases linearly at long distance, ( $f_{\bar{q}q}(r \rightarrow \infty) \rightarrow \sigma r$  with  $r = |\mathbf{x} - \mathbf{y}|$ ). In the deconfined phase, on the other hand, the free energy of a single quark is finite, and the quark-antiquark potential is of the Yukawa type at long distance with a magnetic screening mass  $m_M$  [Arnold and Yaffe, 1995; Hart et al., 2000; Maezawa et al., 2010],

$$f_{\bar{q}q}(r \rightarrow \infty) \rightarrow f_{\bar{q}} + f_q + \alpha \frac{e^{-m_M r}}{r}, \quad (2.5)$$

where  $\alpha$  is a dimensionless constant.

### 2.3.2 Chiral condensate and dynamical breaking of chiral symmetry

In the QCD vacuum at  $T = \mu_B = 0$ , chiral symmetry is spontaneously broken, which is the source of hadron masses. The simplest choice of the order parameter for the chiral symmetry breaking is a bilinear form called the chiral condensate,

$$\langle \bar{\psi}\psi \rangle = \langle \bar{\psi}_R \psi_L + \bar{\psi}_L \psi_R \rangle, \quad (2.6)$$

where summation of color and flavor indices of the quark fields is implied. If the value of the chiral condensate is non-zero even after taking the limit of zero quark masses, chiral symmetry is spontaneously broken according to the pattern  $\mathcal{G} \rightarrow \mathcal{H}$  with

$$\mathcal{G} = \text{SU}(N_f)_L \times \text{SU}(N_f)_R \times \text{U}(1)_B \times \text{Z}(2N_f)_A \quad (2.7)$$

$$\mathcal{H} = \text{SU}(N_f)_V \times \text{U}(1)_B, \quad (2.8)$$

which leads to  $N_f^2 - 1$  massless Nambu-Goldstone bosons for  $N_f > 1$ . The  $U(1)_A$  symmetry in the classical level of the QCD Lagrangian is broken down explicitly to  $Z(2N_f)_A$  in the quantum level. Then, the  $U(1)_A$  current is no longer conserved ( $U(1)_A$  anomaly);

$$\partial_\mu j_5^\mu = -\frac{g^2 N_f}{32\pi^2} \epsilon^{\alpha\beta\mu\nu} F_{\alpha\beta}^a F_{\mu\nu}^a. \quad (2.9)$$

The right-hand side of the above relation is nothing but the topological charge density. Thus, gauge configurations with non-trivial topology are microscopically responsible for the  $U(1)_A$  anomaly. In other words, the  $U(1)_A$  current could be approximately conserved if the gauge configurations are dominated by topologically trivial sectors.

## 2.4 Chiral phase transition at finite temperature

The chiral phase transition at finite  $T$  with  $\mu_B = 0$  has been and is being extensively studied by the renormalization group method near the critical point à la Ginzburg-Landau-Wilson and by lattice-QCD simulations. Here, we give a brief overview of the results of these studies.

### 2.4.1 Ginzburg-Landau-Wilson analysis

If the phase transition is of second order or of weak first order, the free-energy functional, in terms of the order parameter field  $\Phi$ , can be expanded as a power series in  $\Phi/T_c$ . Large fluctuations of  $\Phi$  near the critical point are then handled by the renormalization group method. This is called the Ginzburg-Landau-Wilson approach. For chiral phase transitions in QCD, a suitable order parameter field is a  $N_f \times N_f$  matrix in flavor space,  $\Phi_{ij} \sim \langle \bar{\psi}_j (1 - \gamma_5) \psi_i \rangle$ . Under the flavour chiral rotation  $U(N_f)_L \times U(N_f)_R$ ,  $\Phi$  transforms as  $\Phi \rightarrow V_L \Phi V_R^\dagger$ . Then the Ginzburg-Landau free energy in three spatial dimensions ( $D = 3$ ) with full  $U(N_f)_L \times U(N_f)_R$  symmetry up to the quartic order in  $\Phi_{ij}$  becomes [Pisarski and Wilczek, 1984; Wilczek, 1992];

$$\Omega_{\text{sym}} = \frac{1}{2} \text{tr} \nabla \Phi^\dagger \nabla \Phi + \frac{a_0}{2} \text{tr} \Phi^\dagger \Phi + \frac{b_1}{4!} (\text{tr} \Phi^\dagger \Phi)^2 + \frac{b_2}{4!} \text{tr} (\Phi^\dagger \Phi)^2. \quad (2.10)$$

Temperature  $T$  dependence enters through the parameters  $a_0$ ,  $b_1$  and  $b_2$ . Note that  $\Omega_{\text{sym}}$  is bounded from below as long as  $b_1 + b_2/N_f > 0$  and  $b_2 > 0$  are satisfied. The renormalization group analysis of (2.10) on the basis of the leading-order  $\epsilon (= 4 - D)$  expansion leads to the conclusion that there is no stable IR fixed point for  $N_f > \sqrt{3}$  [Pisarski and Wilczek, 1984]. This implies that the thermal phase transition described by (2.10) is of the fluctuation-induced first order for two or more flavors.

In QCD, however, there is  $U(1)_A$  anomaly and the correct chiral symmetry is  $SU(N_f)_L \times SU(N_f)_R \times U(1)_B \times Z(2N_f)_A$  for  $N_f$  massless quarks. The lowest dimensional operator

	$N_f = 2$	$N_f \geq 3$
$U(1)_A$ symmetric ( $c_0 = 0$ )	Fluctuation-induced 1st order	1st order
$U(1)_A$ broken ( $c_0 \neq 0$ )	2nd order [O(4) universality]	1st order

**Table 2.2:** Order of the chiral phase transition conjectured from the chiral effective theory with massless  $N_f$  flavours with and without the  $U(1)_A$  anomaly.

which breaks  $U(1)_A$  symmetry explicitly while keeping the rest of chiral symmetry is the Kobayashi–Maskawa–’t Hooft (KMT) term [Kobayashi and Maskawa, 1970; Kobayashi et al., 1971; ’t Hooft, 1976b,a];

$$\Omega_{\text{anomaly}} = -\frac{c_0}{2} (\det \Phi + \det \Phi^\dagger). \quad (2.11)$$

The coefficient  $c_0$ , which is  $T$ -dependent in general, dictates the strength of  $U(1)_A$  anomaly.

For  $N_f = 3$  the KMT term becomes a cubic invariant in the order parameter. Hence,  $\Omega[\Phi] = \Omega_{\text{sym}} + \Omega_{\text{anomaly}}$  leads to the chiral phase transition of first order. For  $N_f = 2$ , on the other hand, the KMT term becomes a quadratic invariant. Also the chiral symmetry in this case is  $SU(2)_L \times SU(2)_R \cong SO(4)$ . Such an effective theory with  $O(4)$  symmetry has a Wilson-Fisher type IR fixed point as long as the coefficient of the quartic term of  $\Phi$  is positive. Therefore, *if* the chiral phase transition of massless  $N_f = 2$  QCD is of second order, its critical exponents would be the same as those in the 3D  $O(4)$  effective theory according to the notion of universality. In Table 2.2 we summarize the Ginzburg-Landau-Wilson analysis from the chiral effective theory [Pisarski and Wilczek, 1984].

In the real world, none of the quarks is exactly massless (see Table 1.1). It is therefore useful to have a phase diagram where quark masses are treated as external parameters, in analogy with an external magnetic field in a ferromagnet. Such a plot is called the Columbia plot [Brown et al., 1990], as shown in Fig.2.3, where the isospin degeneracy is assumed ( $m_u = m_d \equiv m_{ud}$ ). The first-order chiral transition and the first-order deconfinement transition at finite  $T$  are indicated by the left-bottom region and the right-top region, respectively. The chiral and deconfinement critical lines, which separate the first-order and crossover regions, belong to a universality class of the 3D  $Z(2)$  Ising model except for special points at  $m_{ud} = 0$  or  $m_s = 0$  [Gavin et al., 1994].

If the chiral transition is of second order for massless  $N_f = 2$  case, the  $Z(2)$  chiral critical line meets the  $m_{ud} = 0$  axis at  $m_s = m_s^{\text{tri}}$  (*tricritical point*) and changes its universality to  $O(4)$  for  $m_s > m_s^{\text{tri}}$  [Hatta and Ikeda, 2003]. The tricritical point at  $m_s = m_s^{\text{tri}}$  is a Gaussian fixed point of the 3D  $\phi^6$  model (that is, the critical dimension is not 4 but 3 at the tricritical point), so that the critical exponents take the classical (mean-field) values [Riedel and Wegner, 1972], which is confirmed in numerical studies of the chiral

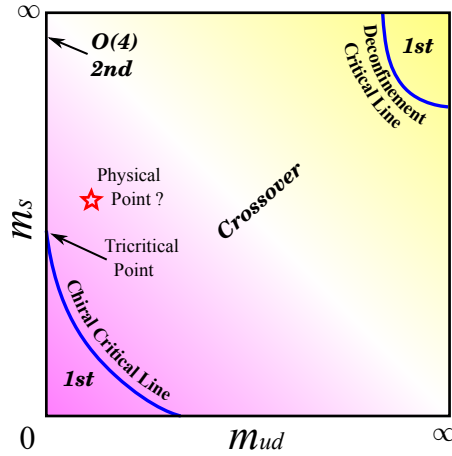


**Figure 2.3:** Schematic figure of the Columbia phase diagram in 3-flavour QCD at  $\mu_B = 0$  on the plane with the light and heavy quark masses. The  $U(1)_A$  symmetry restoration is not taken into account. Near the left-bottom corner the chiral phase transition is of first order and turns to smooth crossover as  $m_{ud}$  and/or  $m_s$  increase. The right-top corner indicates the deconfinement phase transition in the pure gluonic dynamics. Figure by [Fukushima and Hatsuda, 2011]

model [Schaefer and Wambach, 2007].

#### 2.4.2 Lattice QCD simulations

The critical properties arising from the analysis of section 2.4.1 are expected to be robust and universal. However, specific values for the critical temperature and the equation of state depend on the details of the microscopic theory. The only known way to obtain reliable information about the behavior of the microscopic dynamics is through simulations on a discretized lattice (lattice-QCD). In other words, we integrate functionally over a lattice with spacing  $a$ , and over a finite volume  $V$ , by the method of importance sampling. Consequently, in order to obtain physical results, independent of the particular simulation parameters, we have to take the continuum limit ( $a \rightarrow 0$ ), and then also go to the thermodynamic limit ( $V \rightarrow \infty$ ). Thus, adding to the inevitable statistical error due to importance sampling, we also introduce a systematic error due to the extrapolations in the limiting procedure.

There is also difficulty in reconciling lattice discretization with chiral symmetry for nearly massless fermions: the standard way to define light quarks on the lattice has been the Wilson fermion and the staggered fermion. More recently, the domain-wall fermion and overlap fermion have been proposed, which although theoretically more solid, are

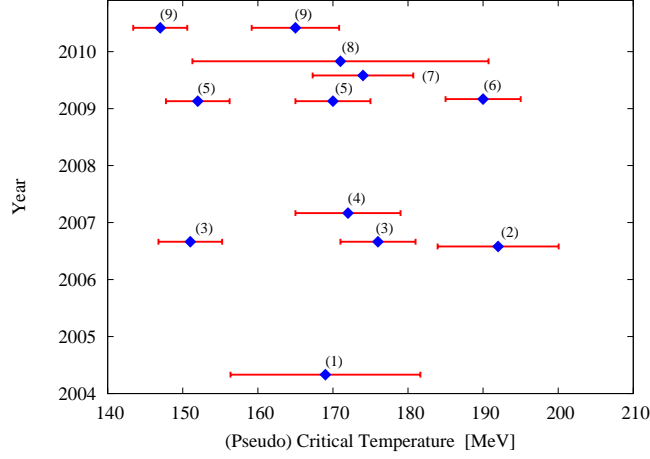


**Figure 2.4:** Determination of the pseudo-critical temperature  $T_{pc}$  for thermal QCD transition(s) from recent lattice QCD simulations. (1) 169(12)(4) MeV for 2 + 1 flavors in the asqtad action with  $N_t$  up to 8 determined by  $\chi_m/T^2$  (where  $\chi_m$  is the chiral susceptibility) [Bernard et al., 2005]. (2) 192(7)(4) MeV for 2 + 1 flavors in the p4fat3 staggered action with  $N_t$  up to 6 determined by  $\chi_m$  and  $\chi_L$  (where  $\chi_L$  is the Polyakov loop susceptibility) [Cheng et al., 2006]. (3) 151(3)(3) MeV and 176(3)(4) MeV for 2 + 1 flavors in the stout-link improved staggered action with  $N_t$  up to 10 determined by  $\chi_m/T^4$  and  $\chi_L$  respectively [Aoki et al., 2006b]. (4) 172(7) MeV for 2 flavors in clover improved Wilson action with  $N_t$  up to 6 determined by  $\chi_L$  [Maezawa et al., 2007]. (5) 152(3)(3) MeV and 170(4)(3) MeV for 2 + 1 flavors in the stout-link improved staggered action with  $N_t$  up to 12 determined by  $\chi_m/T^2$  and  $\chi_L$  respectively [Aoki et al., 2009]. (6) 185–195 MeV for 2 + 1 flavors in the asqtad and p4 actions with  $N_t$  up to 8 determined by  $\chi_m$  and  $\chi_L$  [Bazavov et al., 2009]. (7) 174(3)(6) MeV for 2 flavors in the improved Wilson action with  $N_t$  up to 12 determined by  $\chi_m$  and  $\chi_L$  [Bornyakov et al., 2010]. (8) 171(10)(17) MeV for 2 + 1 flavors in the domain-wall action with  $N_t = 8$  determined by  $\chi_m/T^2$  [Cheng et al., 2010]. (9) 147(2)(3) MeV and 165(5)(3) MeV for 2 + 1 flavors in the stout-link improved staggered action with  $N_t$  up to 16 determined by  $\chi_m/T^4$  and  $\chi_s/T^2$  (where  $\chi_s$  is the strange-quark susceptibility) [Borsányi et al., 2010]. Figure by [Fukushima and Hatsuda, 2011].

computationally more expensive to simulate. For various applications of lattice-QCD simulations to the system at finite  $T$  and  $\mu_B$ , see a recent review by [DeTar and Heller, 2009]

Finally, we note that based on finite-size scaling analysis with staggered fermion by [Aoki et al., 2006a], the thermal phase transition for realistic quark masses is likely a crossover, as indicated by the red star in Fig.2.3, but this should be confirmed by other fermion formalisms.

The (pseudo)-critical temperatures  $T_{pc}$  that result from different types of fermions and with different lattice spacings are summarized in Fig.2.4. Based on these data and their accompanying error bars, we adopt a conservative estimate at present;  $T_{pc} = 150\text{--}200\text{ MeV}$ . It has been clarified recently that improvement of the staggered action with less taste-symmetry breaking favours a smaller value of  $T_{pc} \lesssim 170\text{ MeV}$  [Borsányi et al., 2010; Bazavov and Petreczky, 2010].

## 2.5 Chiral phase transition at finite baryon density

We now take finite  $\mu_B$  into account, adding a third axis to the Columbia plot of Fig.2.3. As shown in Fig.2.5, there are two scenarios:

- (i). In the standard scenario (left), the first order region expands for increasing  $\mu_B$ , so that a point that belongs in the crossover region for  $\mu_B = 0$  undergoes a first order transition for all  $\mu_B > \mu_E$ , for some  $\mu_E \neq 0$ , and therefore we have in the  $\mu_B\text{--}T$  plot, for some choice of  $m_{u,d}$  and  $m_s$ , a first order transition line ending up at a critical point  $(\mu_E, T_E)$ .
- (ii). On the other hand, in the exotic scenario (right), the first order region shrinks with increasing  $\mu_B$ . In this case, if a physical point is in the crossover region for  $\mu_B = 0$ , it stays in the crossover region for finite  $\mu_B$ , and there is no critical point (at least for small  $\mu_B$ ), in the QCD  $\mu_B\text{--}T$  phase diagram.

In general, more complicated forms of the surface in Fig.2.5 are possible, which allow for multiple critical points.

### 2.5.1 Lattice QCD at low baryon density

The QCD partition function on the lattice, for  $\mu_q \neq 0$ , is given by:

$$Z(T, \mu) = \int [dU] \det[F(\mu_q)] \exp^{-\beta S_{YM}(U)}, \quad (2.12)$$

where  $U$  is the matrix-valued gauge field defined at the lattice links,  $\beta S_{YM}$  is the Yang-Mills action,  $\beta = 2N_c/g^2$ , and  $F(\mu_q) = D(\mu_q) + m_q$ , where  $m_q$  is the (positive) quark mass and  $D(\mu_q)$  is the Euclidean Dirac operator.

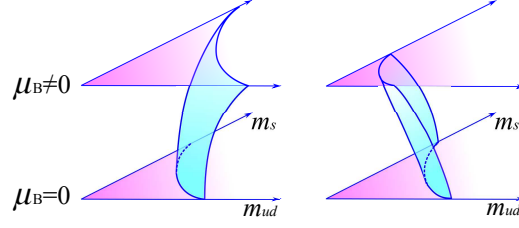


**Figure 2.5:** Schematic evolution of the Columbia plot with increasing  $\mu_B$  in the standard scenario (left) and the exotic scenario (right). Figure by [Fukushima and Hatsuda, 2011].

For  $\mu_q = 0$ ,  $\det[F(\mu_q)]$  is positive definite, and importance sampling works to evaluate (2.12). For  $\mu_q \neq 0$ , however,  $\det[F(\mu_q)]$  is no longer real, and we need to do a careful cancellation of positive and negative values; this is known as the *sign problem*, and its difficulty grows exponentially with increasing volume  $V$ .

In the following, we briefly mention some of the approaches used in simulations at finite  $\mu_q$ . Detailed reviews can be found at [Muroya et al., 2003; Ejiri, 2008; Lombardo et al., 2009].

- *Multi-parameter reweighting method* — Using reweighting, we can expand the expectation value of an operator  $\langle \mathcal{O} \rangle_{\mu_q}$ , given at  $\mu_q = 0$ , to  $\mu_q \neq 0$ . The method only works when  $\mu_q$  and the volume  $V$  are small.
- *Taylor expansion method* —  $\langle \mathcal{O} \rangle_{\mu_q}$  can be expanded in terms of  $\mu_q/T$ , for small  $\mu_q$ :

$$\langle \mathcal{O} \rangle_{\mu_q} = \sum_{n=0}^{\infty} c_n \left( \frac{\mu_q}{T} \right)^n,$$

This only makes sense within a radius of convergence, up to the closest singularity in the  $\mu_q$ - $T$  complex plane.

- *Imaginary chemical potential method* — For Imaginary  $\mu_q$ , denoted as  $\tilde{\mu}_q$ , the sign problem is gone, so we can perform calculations and go back to real  $\mu_q$  by analytic continuation. This method is only applicable within bounds set by singularities of periodicity.
- *Canonical ensemble method* — In the thermodynamic limit, the canonical ensemble, as a function of particle number  $N_q$ , is equivalent to the grand canonical ensemble, as a function of the chemical potential  $\mu_q$ . We can Fourier transform between the two by means of imaginary  $\mu_q$ . This only works for small volume  $V$ . Taking the

thermodynamic limit,  $V \rightarrow \infty$ , with  $n_q = N_q/V$  instead of  $N_q$  kept fixed, is a tricky procedure, and the order of the resulting phase transition depends on the way we approach this limit.

Demonstrating the existence or non-existence of the QCD critical point in the  $\mu_B$ - $T$  plane by lattice QCD simulations would be a very important achievement. Various attempts have been made, using the aforementioned approaches. One noteworthy approach is the idea to use the radius of convergence of a Taylor expansion in  $\mu_q/T$  (assuming convergence due to the singularity at the critical point) as an indication of its location.

In any case, the validity of such methods at finite baryon density is limited in the region  $\mu_q/T < 1$  at present, because of the sign problem. In conclusion, although some of the lattice-QCD simulations suggest the existence of the QCD critical point in  $\mu_B$ - $T$  plane, the results are to be taken with a grain of salt if it is predicted at large  $\mu_q/T$ .

## CHAPTER 3

# GEOMETRIC CHARACTERISTICS OF THE CHIRAL CONDENSATE

### 3.1 Introduction

In the previous chapter, we reviewed the evidence for the existence of a critical point in the QCD phase diagram, as the endpoint of a first order phase transition line, which separates the phases of Hadron Gas (HG) and Quark Gluon Plasma (QGP). The latter phase is characterized by a restored chiral symmetry, which is apparently broken in the hadron gas phase. We therefore concluded that the chiral phase transition can be described by means of an *order parameter*, which attains a non-zero expectation value in the broken symmetry phase, and is equal to zero in the symmetric phase. Such a suitable order parameter of the chiral phase transition is the expectation value of the chiral condensate.

In the vicinity of a second order transition critical point, the thermodynamics of the system undergoing phase transition is greatly simplified. The only relevant thermodynamic quantity is the order parameter. This is due to the divergence of the correlation length at the critical point: only long-wavelength features of the system matter. The system exhibits scale-invariance, which in turn means that all the relevant thermodynamic functions follow scaling laws with respect to the distance from the critical point.

It is therefore possible to describe a wide variety of very different systems employing only a handful of *universality classes*, since the critical exponents in the scaling laws depend only on the symmetries present and the dimensionality of space. Furthermore, the, in general, fractal geometry of a critical system can be quantitatively related to the set of critical exponents of the corresponding universality class. In the present chapter, we examine the universality class to which the QCD chiral phase transition belongs and we discuss the effective action that governs the behaviour and geometric characteristics of the chiral condensate in the vicinity of the QCD critical point.

### 3.2 First and second order phase transitions

We distinguish between two broad classes of phase transitions that exhibit rather different characteristics near the transition point. *First order* phase transitions are characterized by finite discontinuities in the main thermodynamic quantities (except for the free energy, which must be continuous across a phase transition line). In contrast, *second order* phase transitions are characterized by continuous, but non-analytic behaviour of thermodynamic quantities.

Near the transition point of a first order transition, the two phases are different enough that they have to be described by different expressions of the free energy. For a large, but finite volume, a first order phase transition is characterized by drastic and abrupt transitions from one phase to another; phase boundaries are sharp, and they give rise to hysteresis in the thermodynamic limit of infinite volume. In contrast, under similar circumstances, a second order phase transition point exhibits no jumps, and the partition function is analytic.

Non-analyticity arises only in the infinite volume limit. This suggests that, in order for a second order phase transition to take place, there must be present fluctuations of arbitrarily long-wavelength and low energy, since only such modes can survive and give a non-trivial contribution in the infinite volume limit – otherwise, the free energy is simply expressed as a sum of independent terms for small volumes. This means that the correlation length must tend to infinity at the transition point. From a particle physics viewpoint, this “translates” to massless particles, which are precisely the quanta of the aforementioned modes.

Following Landau and Wilson, we conclude that the fact that massless modes dominate the non-analytic part of thermodynamic functions near a second order phase transition allows us to make specific and accurate predictions about the behaviour of the system near the transition point, i.e. the critical behaviour of the system. The main idea is, as we have already mentioned, that symmetry and the dimensionality of space, along with the demand for massless modes, severely restrict the possible forms of effective action we can formulate, so that we may be able to find a unique action to fit our constraints. Thus, the divergent part of any given thermodynamic quantity at a second order transition with given symmetry and dimensionality of space is uniquely determined, regardless of microscopic theory details. This is the *universality* hypothesis.

Universality allows us to make predictions for the behaviour of complex systems, such as QCD near the critical point, by examining much simpler system models.

As a characteristic example, let us examine the 3D-Ising model for magnetization. We are interested in the divergent behaviour of thermodynamic quantities near a second order phase transition, where the magnetization is continuously reduced to zero from a non-zero value. As long as we focus on low-energy, long-wavelength modes, i.e. on slowly varying spatial variations of average magnetization, we can use a coarse-grained

description of the system. We therefore describe magnetization through a real valued, scalar field  $\phi(\mathbf{x})$  in three dimensions. We are interested in the singular behaviour of the partition function arising from  $\phi(\mathbf{x})$  fluctuations. In order to determine it, we must construct a proper “universal” theory in terms of the field  $\phi(\mathbf{x})$ .

Since we want to describe long-wavelength fluctuations, we write a Lagrangian including only lowest order  $\phi(\mathbf{x})$  terms and their derivatives. First of all, we need a quadratic term for the derivative of  $\phi$  in order to have spatial variations. We do not include a  $\phi^2$  term, since it would dominate the derivative term for long wavelengths. In other words, we assume a massless field. Due to the  $\phi \rightarrow -\phi$  symmetry (no external field), the next allowed term is  $\phi^4$ . Therefore, our test “Lagrangian” (i.e., the Hamiltonian in units of temperature,  $\mathcal{H}/T$ ), takes the form

$$\int d^3\mathbf{x} \mathcal{L} = \int d^3\mathbf{x} \left( (\partial\phi)^2 + \lambda\phi^4 \right) \quad (3.1)$$

By using simple dimensional analysis, we see that in order to have a dimensionless Lagrangian the field  $\phi$  must have a mass (inverse length) dimension of 1/2, and therefore  $\lambda$  must have dimensions of 1. Solely from dimensional analysis, we see that we do not get a scale invariant theory.

The problem is resolved through the process of *renormalization*: we define a cutoff at a high enough energy, as well as a renormalized value of the coupling constant at a finite energy scale, independent of the cutoff. Consequently, we let the cutoff go to infinity, and by a proper procedure, we finally recover a dimensionless coupling constant which is cutoff-independent. Another method consists of formulating the model in  $4-\epsilon$  dimensions, for small  $\epsilon$ , where the dimensionality of the coupling constant is small, and then extrapolating to  $\epsilon = 1$ , i.e. in three dimensions (dimensional regularization). We can therefore obtain in the end a scale invariant theory. Although such calculations are prohibitively difficult for QCD, thanks to universality we can obtain useful results by using much simpler models.

We turn now to a model capable of describing a first order phase transition. For the Ising model, we found that, in order to construct a scale invariant second order phase transition theory, mass terms must be dropped. It is reasonable to assume that the effective mass going into the Lagrangian is a function of the temperature,  $m^2 = m^2(T)$ , and therefore it goes to zero at a given temperature. Thus, the Lagrangian (3.1) is a special case of the more general

$$\int d^3\mathbf{x} \mathcal{L} = \int d^3\mathbf{x} \left( (\partial\phi)^2 + m^2(T)\phi^2 + \lambda\phi^4 \right), \quad (3.2)$$

which describes the fluctuations of magnetization not just at the critical transition temperature, but also nearby. This is evident for another reason: when  $m^2(T) < 0$ , the

field “favors” a configuration where  $\phi$  has a non-zero expectation value, whereas when  $m^2(T) > 0$  the expectation value is zero.

If we further assume that the system is placed in an external magnetic field  $H$ , the symmetry  $\phi \rightarrow -\phi$  is broken, allowing  $\phi$  and  $\phi^3$  terms. The  $\phi$  term can be absorbed, leaving the  $\phi^3$  and mass terms; the latter still goes to zero at the critical temperature. However, contrary to the previous model, this does not in general lead to a second order phase transition, since the presence of the  $\phi^3$  term causes the expectation value to jump to a new minimum for a non-zero (positive)  $m^2$  value. The special case where the cubic and square mass terms cancel out is only accessible if there is a second adjustable parameter, besides temperature. A so-called *tricritical point* then appears. In the phase plane, as we saw in the previous chapter, the tricritical point is the endpoint of a line of gradually weaker first order phase transitions.

Even if the mean field theory allows a second order phase transition, this will not occur unless there is a scale invariant theory representative of the universality class. The problem with mean field theory is that it ignores fluctuations, which however are vital. In order to recover in the end a scale invariant theory, the coupling constant must transform smoothly under renormalization group transformations towards the infrared (long-wavelength) limit. If this behaviour is absent, there will be no second order phase transition. Physically, what this means is that fluctuations in such cases grow arbitrarily large, leading to destructive rearrangements of the configuration, i.e. a first order phase transition. This is known as a *fluctuation-driven* first order phase transition.

Because they are characterized by finite discontinuities, first order phase transitions are robust against small perturbations. Thus, given a symmetry and an order parameter, whose variation from a non-zero to a zero value induces a first order phase transition, then according to the above, the phase transition will remain first order even if the symmetry is explicitly broken to a small extent. There will be no well-defined order parameter, and we therefore have to turn to a strictly symmetric variation of the theory in order to derive the necessity of the transition.

### 3.3 Critical exponents and scaling laws

Universality in the critical behaviour of various systems is quantified through the *critical exponents* of the corresponding universality class, i.e. the exponents describing the divergent component of measurable thermodynamic quantities near the critical temperature  $T_c$ . In the magnetization model, there are two relevant thermodynamic parameters describing the proximity of the system to the critical point: the reduced temperature,  $t \equiv (T - T_c)/T_c$ , where  $T_c$  is the critical temperature, and the magnetizing field  $H$ . Critical exponents are traditionally symbolized by the letters  $\alpha, \beta, \gamma, \delta, \eta$  and  $\nu$ , and are defined

as follows:

$$\text{Specific Heat: } C(T) \sim |t|^{-\alpha} \quad (3.3a)$$

$$\text{Order parameter: } \langle |\phi| \rangle \sim |t|^\beta \text{ (for } t < 0) \quad (3.3b)$$

$$\text{Susceptibility: } \chi \sim |t|^{-\gamma} \quad (3.3c)$$

$$\text{Equation of state (EoS): } \langle |\phi| \rangle (t = 0, H \rightarrow 0) \sim H^{1/\delta} \quad (3.3d)$$

(In the magnetization model, the role of order parameter is played by the magnetization  $M$ , whereas in QCD by the chiral condensate). Susceptibility describes the sensitivity of the order parameter to variations of the magnetizing field  $H$ . All of (3.3), except for (3.3d), are defined for the  $H = 0$  case.

The final two exponents refer to the *correlation function*, which expresses the spatial fluctuations of the order parameter and quantifies the correlation between remote sites, thus defining a characteristic ‘‘correlation length’’  $\xi$ , which diverges at the critical point. The correlation function is defined as follows:

$$\Gamma(\mathbf{r}) \equiv \langle \phi(\mathbf{r})\phi(\mathbf{0}) \rangle - \langle \phi(\mathbf{r}) \rangle \langle \phi(\mathbf{0}) \rangle \Rightarrow r^{-p} \exp(-r/\xi), \text{ at large distances} \quad (3.4)$$

whereas the integrated correlation function gives the susceptibility:

$$\chi = \frac{1}{k_B T} \int d^3\mathbf{r} \Gamma(\mathbf{r}) \quad (3.5)$$

The exponent  $\nu$  relates the correlation length  $\xi$  to the temperature:

$$\xi \sim |t|^{-\nu} \quad (3.6)$$

Finally, the exponent  $\eta$  is related to the so-called anomalous dimension, via the power-law  $p$  in the expression for the correlation function:

$$p = d - 2 + \eta, \quad (3.7)$$

where  $d$  is the dimensionality of space.

The six critical exponents defined above are not independent; they are related to each other through the following four scaling laws [Huang, 1987]:

$$\begin{aligned} \text{Fisher: } & \gamma = \nu(2 - \eta) \\ \text{Rushbrooke: } & \alpha + 2\beta + \gamma = 2 \\ \text{Widom: } & \gamma = \beta(\delta - 1) \\ \text{Josephson: } & \nu d = 2 - \alpha \end{aligned} \quad (3.8)$$

Thus, determining the values of any two critical exponents, e.g.  $\eta$  and  $\nu$ , and the dimensionality  $d$  of space, uniquely determines the rest of the critical exponents too.

Exponent	TH	EXPT	MFT	TRICR	ISING2	ISING3	HEIS3
$\alpha$		0–0.14	0	1/2	0	0.12	$-0.19 \pm 0.06$
$\beta$		0.32–0.39	1/2	1/4	1/8	0.31	$0.38 \pm 0.01$
$\gamma$		1.3–1.4	1	1	7/4	1.25	$1.44 \pm 0.04$
$\delta$		4–5	3	5	15	5	$4.82 \pm 0.05$
$\nu$		0.6–0.7	1/2	1/2	1	0.64	$0.73 \pm 0.02$
$\eta$		0.05	0	0	1/4	0.05	$0.03 \pm 0.01$
$\alpha + 2\beta + \gamma$	2	$2.00 \pm 0.01$	2	2	2	2	2
$(\beta\delta - \gamma)/\beta$	1	$0.93 \pm 0.08$	1	1	1	1	
$(2 - \eta)\nu/\gamma$	1	$1.02 \pm 0.05$	1	1	1	1	1
$(2 - \alpha)/\nu d$	1		4/d	3/d	1	1	1

**Table 3.1:** Critical exponents and scaling law values corresponding to various universality classes. TH: theoretical values (from scaling laws); EXPT: experimental values (from a variety of systems); MFT: mean field theory; TRICR: tricritical point; ISING $d$ : Ising model in  $d$  dimensions; HEIS3: classical Heisenberg model,  $d = 3$  [Bagnuls et al., 1987]. Adapted from [Huang, 1987]

## 3.4 The role of long-range correlations at the critical point

### 3.4.1 Correlation functions

Let us consider a general statistical system, for example the magnetization model. If we are interested in a coarse-grained description of it (and near a critical point, that is typically all we are interested in), its partition function can be given as a functional of a slowly varying field  $\chi(\mathbf{x})$ :

$$Z = \int \mathcal{D}\chi e^{-S[\chi]}, \quad S[\chi] = \beta\mathcal{H}[\chi] \quad (3.9)$$

where  $\beta$  is the inverse temperature and  $\mathcal{H}$  is the Hamiltonian corresponding to the system. Typically,  $S[\chi]$  is given by:

$$S = \int d^3\mathbf{x} \left\{ \frac{1}{2} |\nabla\chi(\mathbf{x})|^2 + V_{eff}[\chi] \right\}, \quad (3.10)$$

where  $V_{eff}[\chi]$  is some effective potential.

The field  $\chi(\mathbf{x})$  is subject to thermal and quantum fluctuations. In order to quantify them, we can define expectation values for  $\chi(\mathbf{x})$ , as well as for functions of  $\chi(\mathbf{x})$  at various points. These are computed as weighted integrals:

$$\langle \chi(\mathbf{x})\chi(\mathbf{y}) \rangle = Z^{-1} \int \mathcal{D}\chi \chi(\mathbf{x})\chi(\mathbf{y}) e^{-S[\chi]} \quad (3.11)$$

If now we define an external field,  $H(\mathbf{x})$ , linearly coupled to  $\chi(\mathbf{x})$ , we can generalize  $Z$  to a functional  $Z[H]$  taking the form:

$$Z[H] = \int \mathcal{D}\chi \cdot \exp \left\{ -S[\chi] + \int d^3\mathbf{x} \chi(\mathbf{x}) H(\mathbf{x}) \right\} \quad (3.12)$$

Eq.(3.12) allows us to define the functional  $W[H]$ :

$$W[H] \equiv \ln Z[H], \quad (3.13)$$

which is closely related to the thermodynamic *free energy potential*. Indeed, the functional derivatives of  $W[H]$  with respect to the external field  $H$  are the *connected correlation functions*:

$$\frac{\delta W}{\delta H(\mathbf{x})} = \langle \chi(\mathbf{x}) \rangle \equiv \phi(\mathbf{x}) \quad (3.14)$$

$$\frac{\delta^2 W}{\delta H(\mathbf{x}) \delta H(\mathbf{y})} = \langle \chi(\mathbf{x}) \chi(\mathbf{y}) \rangle - \langle \chi(\mathbf{x}) \rangle \langle \chi(\mathbf{y}) \rangle \quad (3.15)$$

with (3.14) giving the average density of the field at  $\mathbf{x}$ , and (3.15) giving the density-density correlation function,  $\Gamma(\mathbf{x} - \mathbf{y})$ , (eq.3.4).

Finally, the effective action,  $\Gamma_{eff}[\phi]$ , is defined in terms of the average density  $\phi(\mathbf{x})$ , via a Legendre transformation of  $W[H]$ :

$$\Gamma_{eff}[\phi] \equiv -W[H] + \int d^3\mathbf{x} \phi(\mathbf{x}) H(\mathbf{x}) \quad (3.16)$$

$\Gamma_{eff}[\phi]$  is easier to handle than  $W[H]$ , and we can extract the relevant physical observables from it. It is related to the free energy by the following formula:

$$\mathcal{F} = T \Gamma_{eff} - T \int d^3\mathbf{x} \phi_{eq}(\mathbf{x}) H(\mathbf{x}), \quad (3.17)$$

where  $\phi_{eq}$  is the equilibrium value of the field, and  $H(\mathbf{x})$  is a function of  $\phi_{eq}(\mathbf{x})$ :

$$\frac{\delta \Gamma_{eff}}{\delta \phi(\mathbf{x})} = H(\mathbf{x}) \quad (3.18)$$

### 3.4.2 Scale invariance. The relation of critical exponents and fractal dimensions.

At the critical point of a second order phase transition, the correlation length  $\xi \rightarrow \infty$ . (3.4) then suggests that the correlation function follows a power-law,  $\Gamma(\mathbf{r}) \sim r^{-p}$ . In

other words, there is no characteristic length scale in the physical system; it exhibits *scale invariance*, which means all physical quantities are invariant under a scale transformation.

Scale-invariant mathematical functions are known as *homogeneous functions*:

$$f(b^{D_q} q) = b^{D_f} f(q) \quad (3.19)$$

where  $b$  is the rescaling factor,  $x \rightarrow x/b$ . If in a critical system we define the free energy density,  $g = \frac{G}{kTV}$ , as a function of reduced temperature  $t$  and reduced external field  $h = \frac{H}{kT}$ , we expect to get a scaling form [Huang, 1987]:

$$g(h, t) = b^{-d} g(b^{D_h} h, b^{D_t} t), \quad (3.20)$$

where  $d$  is the dimensionality of space. This result – a generalized version of Widom's scaling form – stems from the fact that the free energy density has an energy (inverse length) dimension of  $d$ . As we saw in the previous section, the free energy is the generating functional of the density-density correlation functions. Therefore, the power-law, scale invariant form of the free energy is reflected in the behaviour of all thermodynamic variables, which transform under scale transformations, each with a characteristic and generally fractal dimension.

We can relate the fractal dimensions  $D_h, D_t$  to the set of critical exponents, (3.3). Since the correlation length  $\xi$  is the only relevant length scale near the critical point, we get from (3.6)

$$D_t = 1/\nu \quad (3.21)$$

Setting  $b^{D_t} t \sim 1 \Rightarrow b \sim t^{-1/D_t}$ , we can express Widom's scaling form as:

$$g(h, t) = |t|^{d/D_t} \mathcal{G}\left(\frac{h}{|t|^{D_h/D_t}}\right) \quad (3.22)$$

Differentiating (3.22) with respect to  $h$  and  $t$ , and using the definitions (3.3) of critical exponents, we obtain:

$$D_h = \frac{d \cdot \delta}{\delta + 1} \quad (3.23)$$

which relates the fractal dimension  $D_h$  to the isothermal critical exponent  $\delta$  and the dimensionality  $d$  of space. The rest of the critical exponents can also be related to  $D_h, D_t$  via the scaling laws (3.8).

Eq.(3.23) is crucial for understanding the geometry of the chiral condensate. It tells us that, at the critical temperature, the order parameter, i.e. the chiral condensate, organizes in structures (clusters) that have a fractal dimension of  $D_h$ . If we can therefore measure the fractal dimension of critical clusters in configuration or momentum space, we can determine the isothermal critical exponent  $\delta$ , and obtain information about the universality class to which the chiral phase transition belongs.

## 3.5 The chiral condensate as an order parameter

### 3.5.1 The chiral phase transition

As we have already seen, massless QCD possesses the chiral symmetry, which means fermionic fields are invariant under independent rotation of their left and right components. In particular, we can define the chiral transformation operator as  $U_5 \equiv \exp(-g_5 \gamma^5 \frac{\tau_i \epsilon_i}{2})$ , where  $\tau_i$  are the isospin generators (Pauli matrices),  $\epsilon_i$  are the rotation angles and  $g_5$  is a coupling constant. The chiral transformation of a spinor is then:

$$\psi' = U_5 \psi \quad (3.24)$$

whereas

$$\bar{\psi}' = \bar{\psi} U_5 \quad (3.25)$$

Therefore, the kinetic term of the QCD Lagrangian is invariant under (3.24-3.25), whereas the mass term is not:

$$m \bar{\psi}' \psi' = m \bar{\psi} U_5 U_5 \psi \neq m \bar{\psi} \psi \quad (3.26)$$

It follows that high-temperature ( $T > T_c$ ) deconfined QCD, where quarks are approximately massless, is almost chirally symmetric, whereas the acquisition of quark mass that occurs in the chiral condensate  $\langle \bar{q}q \rangle$  breaks the chiral symmetry at  $T < T_c$ .

There is evidence [Pisarski and Wilczek, 1984; Wilczek, 1992] that the chiral phase transition is a second order phase transition with an order parameter  $M_j^i = \langle \bar{q}_L^i q_{Rj} \rangle$ , and that the pion corresponds to the Nambu-Goldstone (almost) massless boson related to the spontaneous chiral symmetry breaking. However, this symmetry breaking also predicts a massless Goldstone boson for baryon number symmetry, which is absent. We can get around this problem, for two flavor QCD [Wilczek, 1992], by postulating that the order parameter  $M$  transforms as:

$$M \rightarrow VMU^+ \quad (3.27)$$

where  $V, U$  are unitary left and right transformation matrices with a positive determinant and equal phases. We then get an  $SU(2) \times SU(2) \equiv O(4)$  symmetry, where  $O(4)$  is an isomorphic group. We therefore conclude that the chiral phase transition belongs to the same universality class as an  $O(4)$  isotropic Heisenberg magnet in 3 dimensions. Using the Pauli matrices  $\tau$ , the order parameter can be written as:

$$M = \sigma + i\pi\tau, \quad (3.28)$$

where  $\sigma = \langle \bar{q}_i q^i \rangle$  is the scalar and  $\pi = \langle \bar{q}_i \gamma_5 \tau q^i \rangle$  is the isovector component. We can therefore parametrize the order parameter of the chiral phase transition as a 4-vector

$\phi = (\sigma, \boldsymbol{\pi})$ , where the transformations (3.27) are simple  $O(4)$  rotations in the internal 4-dimensional isospin space. The pattern of chiral symmetry breaking,  $SU(2)_L \times SU(2)_R \rightarrow SU(2)_{L+R}$  then translates to  $O(4) \rightarrow O(3)$ , in terms of the  $\phi$ -field.

### 3.5.2 $O(N)$ symmetry and its spontaneous breaking

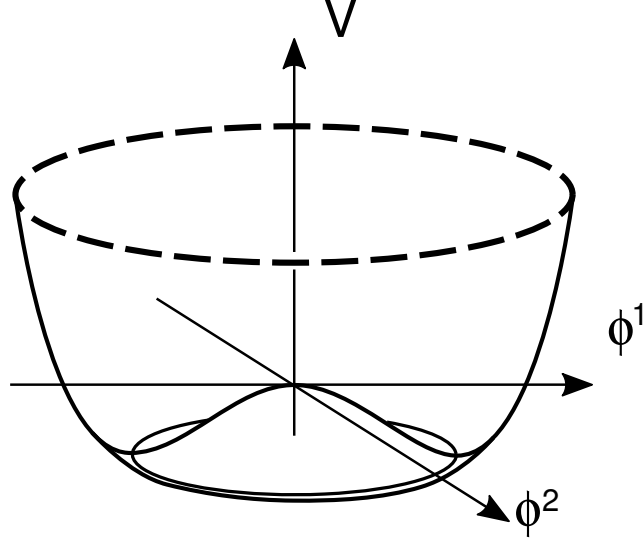


**Figure 3.1:** The typical form of the  $O(N)$  potential, illustrated for the  $O(2)$  case.

The  $O(4)$  symmetry group mentioned in the previous section is a special case of the  $O(N)$  group of rotations in  $N$ -dimensional real space. The elements  $R$  of  $O(N)$  are  $N \times N$  orthogonal matrices. A model obeying this symmetry is the  $\sigma$ -linear model, whose Lagrangian is [Peskin-Schroeder]:

$$\mathcal{L} = \frac{1}{2}(\partial_\mu \phi^i)^2 + \frac{\mu^2}{2}(\phi^i)^2 - \frac{\lambda}{4}[(\phi^i)^2]^2 \quad (3.29)$$

where  $\phi^i(x)$  are  $N$  real scalar fields,  $\mu^2$ ,  $\lambda$  coupling constants, and  $i = 1, \dots, N$ .  $\mathcal{L}$  is invariant under the transformation  $\phi^i \rightarrow R^{ij}\phi^j$ , where  $R^{ij}$  are the elements of the  $R$  matrix. The constant fields  $\phi_0^i$  that minimize the potential of (3.29) satisfy  $(\phi_0^i)^2 \equiv u = \frac{\mu^2}{\lambda}$ . The values  $u$  are the vacuum expectation values of the  $\phi(x)$  field. Fig.3.1 shows the typical form of such a potential for  $N = 2$ .

We can now define a set of transformed fields:

$$\phi^i(x) = (\pi^k(x), u + \sigma(x)), \kappa = 1, \dots, N - 1 \quad (3.30)$$

Then, (3.29) can be written in terms of the  $\phi^i(\mathbf{x})$  fields, (3.30), therefore:

$$\begin{aligned} \mathcal{L} = & \frac{1}{2}(\partial_\mu \pi^k)^2 + \frac{1}{2}(\partial_\mu \sigma)^2 - \frac{1}{2}(2\mu^2)\sigma^2 - \sqrt{\lambda}\mu\sigma^3 - \sqrt{\lambda}\mu(\pi^k)^2\sigma - \frac{\lambda}{4}\sigma^4 \\ & - \frac{\lambda}{2}(\pi^k)^2\sigma^2 - \frac{\lambda}{4}[(\pi^k)^2]^2 \end{aligned} \quad (3.31)$$

The Lagrangian (3.31) is not invariant under  $O(N)$ , to which we refer as *spontaneous symmetry breaking* due to vacuum excitation. We see from (3.31) that the mass terms for the  $\pi(\mathbf{x})$  field have vanished, whereas the  $\sigma(\mathbf{x})$  field has acquired a mass of  $\sqrt{2}\mu$ . This spontaneous symmetry breaking has given rise to  $N - 1$  massless  $\pi(\mathbf{x})$  fields and a massive  $\sigma(\mathbf{x})$  field. This is compatible with the Goldstone theorem, and we therefore identify the  $\pi(\mathbf{x})$  fields as the Goldstone bosons.

Expanding the potential  $V(\phi)$  around the minimum, we obtain:

$$V(\phi) = V(\phi_0) + \frac{1}{2}(\phi - \phi_0)^\alpha (\phi - \phi_0)^\beta \left( \frac{\partial^2}{\partial \phi^\alpha \partial \phi^\beta} V \right)_{\phi_0} + \dots \quad (3.32)$$

where the first derivative vanishes at the minimum. The second term is thus a mass term:

$$m_{ab}^2 = \left( \frac{\partial^2}{\partial \phi^\alpha \partial \phi^\beta} V \right)_{\phi_0} \quad (3.33)$$

where the elements  $m_{ab}$  in 3.33 are the mass matrix  $M$  elements. Given that non-zero second partial derivatives in the potential occur along the radial direction (Fig.3.1), it follows that the fields  $\sigma(\mathbf{x})$  oscillate in the radial direction. The same figure shows the ‘‘rim’’ of the potential, where the azimuthal second derivatives vanish; the massless  $\pi(\mathbf{x})$  fields oscillate along this direction.

Obviously, due to the degeneracy of minima along this  $(N - 1)$ -dimensional line, the  $O(N - 1)$  symmetry of these  $N - 1$  massless fields still holds.

### 3.5.3 The $\sigma$ -model of QCD for $N_f = 2$

The  $\sigma$ -model consists of an isodoublet, zero-mass fermion field,  $\psi$ , coupled to a triplet of pseudoscalar pions  $\pi$  and a scalar  $\sigma$  field. The corresponding Lagrangian takes the form [Itzykson and Zuber, 1985]:

$$\mathcal{L} = \mathcal{L}_s + c\sigma \quad (3.34)$$

where

$$\mathcal{L}_s = \bar{\psi} \left[ i\gamma^\mu \partial_\mu + g(\sigma + i\pi\tau\gamma_5) \right] \psi + \frac{1}{2}[(\partial\pi)^2 + (\partial\sigma)^2] - \frac{\mu^2}{2}(\sigma^2 + \pi^2) - \frac{\lambda}{4}(\sigma^2 + \pi^2)^2 \quad (3.35)$$

and

$$c = -f_\pi m_\pi^2 \quad (3.36)$$

We will show that the  $\mathcal{L}_s$  part is invariant under chiral transformation, represented by  $SU(2) \times SU(2)$  for  $N_f = 2$ . We have already mentioned the chiral invariance of the kinetic term,  $\bar{\psi} i \partial^\mu \gamma_\mu \psi$ . Furthermore, we have:

$$\bar{\psi}(\sigma + i\pi\tau\gamma_5)\psi = \bar{\psi}_L(\sigma + i\pi\tau)\psi_R + \bar{\psi}_R(\sigma - i\pi\tau)\psi_L \quad (3.37)$$

where  $\psi_L = \frac{1}{2}(1 - \gamma_5)\psi$  and  $\psi_R = \frac{1}{2}(1 + \gamma_5)\psi$ . Using (3.28), we obtain:

$$\bar{\psi}(\sigma + i\pi\tau\gamma_5)\psi = \bar{\psi}_L M \psi_R + \bar{\psi}_R M^+ \psi_L \quad (3.38)$$

Taking the U,V matrices and the transformation equations:

$$\begin{aligned} \psi_R &\rightarrow U \psi_R, & \bar{\psi}_R &\rightarrow \bar{\psi}_R U^+ \\ \psi_L &\rightarrow V \psi_L, & \bar{\psi}_L &\rightarrow \bar{\psi}_L V^+ \end{aligned}$$

as well as (3.27) and its conjugate,  $M^+ = U M^+ V^+$ , (3.38) gives:

$$\begin{aligned} \bar{\psi}_L M \psi_R + \bar{\psi}_R M^+ \psi_L &\rightarrow \bar{\psi}_L V^+ V M U^+ U \psi_R + \bar{\psi}_R U^+ U M^+ V^+ V \psi_L \\ &= \bar{\psi}_L M \psi_R + \bar{\psi}_R M^+ \psi_L \end{aligned}$$

i.e. the coupling term  $\bar{\psi} M \psi$  is chirally invariant.

The last three terms in  $\mathcal{L}_s$  take the form:

$$\frac{1}{2} \partial M \partial M^+ - \frac{\mu^2}{2} M M^+ - \frac{\lambda}{4} (M M^+)^2 \quad (3.39)$$

and are thus of the form (3.29) for  $N = 4$ , invariant under  $O(4)$ , which as we have mentioned is isomorphic to  $SU(2) \times SU(2)$ .

In summary, the  $\sigma$ -model couples the order parameter meson fields,  $M = (\sigma, \pi)$ , to a massless fermion field  $\psi$  in a chiral-invariant way.

However, the invariance of the total Lagrangian (3.34) is broken by the linear term,  $f_\pi m_\pi^2 \sigma$ . Therefore, the pion's mass breaks chiral symmetry, which is restored in the limit of zero pion mass.

The linear symmetry breaking term induces a non-zero vacuum expectation value,  $\langle 0 | \sigma | 0 \rangle = u \neq 0$ , for the quantum  $\sigma$ -field. Defining a perturbation field  $\sigma'$  around  $u$ , where  $\sigma = u + \sigma'$ ,  $\mathcal{L}$  takes the form:

$$\begin{aligned} \mathcal{L} &= \bar{\psi} \left[ i \partial^\mu \gamma_\mu + g u + g(\sigma' + i\pi\tau\gamma_5) \right] \psi + \frac{1}{2} \left[ (\partial\pi)^2 + (\partial\sigma')^2 \right] - \frac{1}{2} (\mu^2 + 3\lambda u^2) \sigma'^2 \\ &\quad - \frac{1}{2} (\mu^2 + \lambda u^2) \pi^2 - \lambda u \sigma' (\sigma'^2 + \pi^2) - \frac{\lambda}{4} (\sigma'^2 + \pi^2)^2 \\ &\quad + \sigma' (c - \mu^2 u - \lambda u^3) \end{aligned} \quad (3.40)$$

There are three noteworthy features in (3.40):

1. The mass degeneracy of  $M$  is lifted, since its components acquire different masses:

$$m_\pi^2 = \mu^2 + \lambda u^2 \quad (3.41a)$$

$$m_\sigma^2 = \mu^2 + 3\lambda u^2 \quad (3.41b)$$

2. Fermions also acquire mass:

$$m_N = -gu \quad (3.42)$$

3. A coupling appears,  $\sigma'\pi\pi$ .

If we demand that the vacuum excitation give a zero  $\sigma'$  expectation value, i.e.  $\langle 0|\sigma'|0\rangle = 0$ , then the linear term in (3.40) vanishes:

$$c - \mu^2 u - \lambda u^3 = 0 \quad (3.43)$$

Then, eqs. (3.36), (3.42) and (3.43) give:

$$m_N = gf_\pi \quad (3.44)$$

a result which is compatible with observation [Itzykson and Zuber, 1985].

Furthermore, in the limit  $c \rightarrow 0$ , it follows from (3.43) for  $\mu^2 < 0$  that:

$$u^2 = -\frac{\mu^2}{\lambda} \quad (3.45)$$

which is in agreement with  $(\sigma, \pi)$  being a Goldstone mode vacuum excitation value. On the other hand, (3.41a) and (3.45) give  $m_\pi = 0$ , i.e. we get the three massless Nambu-Goldstone pions predicted by the  $O(4)$  symmetry breaking.

In summary, the  $\sigma$ -model incorporates 2-flavor QCD chiral phase transition within the global Goldstone symmetry breaking mechanism through the vacuum excitation of the scalar  $\sigma$ -field.

### 3.5.4 From $O(4)$ to the 3D-Ising model

We now focus on the Landau-Ginzburg form of the free energy, in 3 dimensions, corresponding to the scalar meson part of the  $\sigma$ -model Lagrangian, (3.34), for massless  $N_f = 2$  QCD at zero chemical potential:

$$\mathcal{F} = \int d^3x \left[ \frac{1}{2} \partial^i \phi \partial_i \phi + \frac{\mu^2}{2} \phi^2 + \frac{\lambda}{4} \phi^4 \right] \quad (3.46)$$

where  $\phi$  is a 4-component scalar field.  $\mu^2$  is the renormalized mass, and is a function of temperature. Below the critical temperature,  $\mu^2 < 0$ , whereas above it  $\mu^2 > 0$ . Symmetry breaking gives us  $\langle \sigma \rangle \neq 0, \langle \pi \rangle = 0$  below the critical temperature.

This model has been studied extensively for arbitrary number of components  $n$  and spatial dimension  $d$ , and the existence of an infrared-stable renormalization group (RG) solution has been established for  $n = 4, d = 3$  [Pisarski and Wilczek, 1984; Rajagopal and Wilczek, 1993].

As we explained in section 3.3, in the vicinity of the critical temperature, the critical exponents of the corresponding universality class can be calculated. In this case, the universality class is the  $O(4)$  symmetry class of the Heisenberg magnetic (spin) model for  $d = 3$ . Critical exponents have been calculated via perturbation theory [Bagnuls et al., 1987]. The results are shown in the last column of Table 3.1.

We saw in the previous chapter that adjusting the mass  $m_s$  of the strange quark can turn a second order to a first order transition for  $\mu_B = 0$  (see the Columbia plot, Fig.2.3). The *tricritical point* is defined as the point in the  $T - m_s$  plot for which this shift in phase transition order occurs.

Adding a third, massive quark influences the renormalization process of the coupling constants  $\mu^2, \lambda$ . Shifting  $\mu^2$  simply shifts the critical temperature  $T_c$ , however, if  $\lambda$  becomes negative, the free energy (3.46) must be expanded beyond  $\phi^4$ -order and up to  $\phi^6$ -order. For  $\lambda > 0$  we still get a second order phase transition, but for  $\lambda < 0$  the transition turns into first order. The value of  $m_s$  where  $\lambda = 0$  represents the tricritical point.

The tricritical point also belongs to a universality class, namely that of the Landau-Ginzburg  $\phi^6$ -model, which is directly renormalizable in 3 dimensions. Its critical exponents can therefore be extracted through mean field theory (MFT), and are shown in Table 3.1 (TRICR column).

Therefore, for large enough  $m_s$  values, the specific heat  $C(T)$  is discontinuous, whereas for  $T = T_c$  it is divergent.

If we ascribe small masses to the  $u, d$  quarks, the first order transition, being robust, survives, whereas the second order transition turns into a smooth analytic continuation (this is analogous to placing a ferromagnet in a small external magnetic field; the Curie anomaly at the critical temperature is removed, and the magnetization varies smoothly with temperature). A tricritical point remains in the  $T - m_s$  phase diagram, however; it belongs to the universality class of the 3D-Ising model.

Although it is not possible to vary the mass  $m_s$  experimentally, we can equivalently vary the baryochemical potential  $\mu_B$  [Stephanov et al., 1998]. We can keep the physical value of  $m_s$  while varying the chemical potential  $\mu_B$ , and the tricritical point reappears in the  $T - \mu_B$  phase diagram, with an effective  $\phi^6$  potential of the general form:

$$\Omega_{eff} = \Omega_0(T, \mu_B) + \frac{1}{2}a(T, \mu_B)\phi^2 + \frac{1}{4}b(T, \mu_B)\phi^4 + \frac{1}{6}c(T, \mu_B)\phi^6 - h\phi, \quad c > 0 \quad (3.47)$$

where the coefficient  $h$  is proportional to the current quark mass [Berges and Rajagopal, 1999]. The coefficients  $a$  and  $b$  are both zero at the tricritical point, and are assumed to be linear in  $(T - T_c)$  and  $(\mu - \mu_c)$ . The phase diagram predicted by the tricritical  $\phi^6$  model is shown in Fig.3.2. The second order phase transition line is given by  $a = 0$ ,  $b > 0$ , and the first order transition line by  $b^2 = 16ca/3$ ,  $b < 0$ .

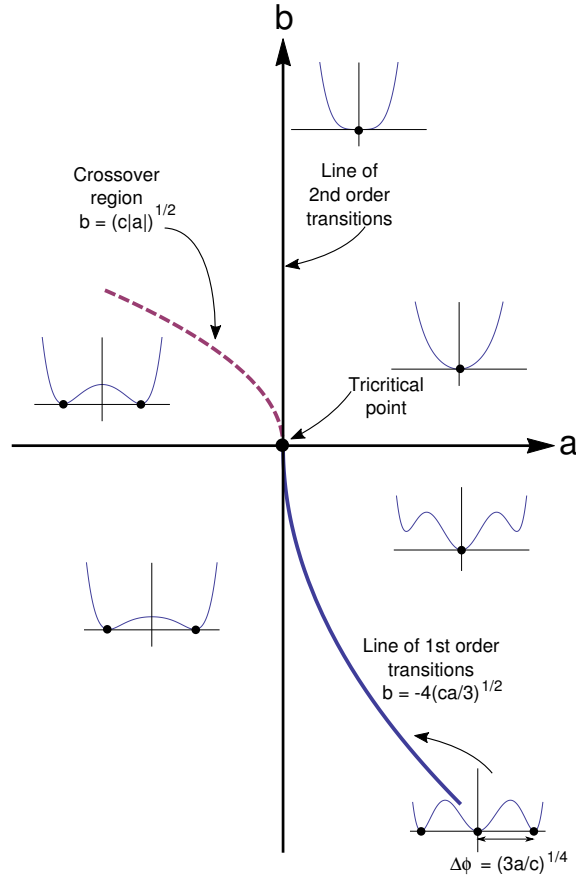


**Figure 3.2:** A sketch of the phase diagram of the  $\phi^6$  model in the mean field approximation. In the plot,  $a$  is the coefficient of  $\phi^2$  and  $b$  the coefficient of  $\phi^4$  in the Landau effective potential  $\Omega_{eff}$ , (3.47). Also shown are the first order transition line (solid line), and the crossover region (dashed line). The inset plots show the form of the effective potential in different regions.

Once again, the effect of small quark masses on the  $T - \mu_B$  phase diagram is to replace the line of second order phase transitions with a smooth crossover, leaving only the first order transition line, terminating at an ordinary critical point. At this critical

point, one degree of freedom, associated with the magnitude of  $\phi$ , becomes massless. On the other hand, pions remain massive, since the chiral symmetry is explicitly broken. The transition therefore belongs to the same universality class as the 3D-Ising model [Berges and Rajagopal, 1999], and the order parameter is identified as the expectation value of the scalar  $\sigma$ -field condensate.

### 3.5.5 The 3D-Ising model effective action

Let us consider the form of the microscopic action for a  $\phi^4$ -theory in 3 dimensions, for a 3D-Ising model. In such a case, the order parameter is a scalar field with only one component:

$$S = \int d^3x \left[ \frac{1}{2} |\nabla\phi|^2 + \frac{1}{2} m^2 \phi^2 + \lambda \phi^4 \right] \quad (3.48)$$

An effective action can be defined from (3.48), and more generally from microscopic actions through *renormalization group* transformations, which consists of integrating out all microscopic degrees of freedom, along with appropriate renormalization of the coupling constants in order to retain physical meaning. The resulting effective action takes the Ginzburg-Landau-Wilson form:

$$S_{eff} = \int d^3x \left[ \frac{1}{2} Z_\phi^{-1} |\nabla\phi|^2 + V_{eff}(\phi) \right] \quad (3.49)$$

In order to calculate  $S_{eff}$  for a theory, knowledge of the effective potential  $V_{eff}(\phi)$ , as well as the field renormalization factor  $Z_\phi$ , is required. Tsypin numerically simulated the 3D-Ising model on a  $14^3 - 58^3$  cubic lattice with periodic boundary conditions [Tsypin, 1994]. He found that a Wilson-renormalized [Huang, 1987] test effective potential of the form:

$$V_{eff} = r\phi^2 + u\phi^4 \quad (3.50)$$

cannot agree with the numerical simulation results. He therefore added a  $\phi^6$ -term, resulting in an effective potential:

$$V_{eff} = r\phi^2 + u\phi^4 + w\phi^6 \quad (3.51)$$

Therefore, the effective Lagrangian (3.49) takes the form:

$$\mathcal{L}_{eff} = \frac{1}{2} Z_\phi^{-1} |\nabla\phi|^2 + r\phi^2 + u\phi^4 + w\phi^6 \quad (3.52)$$

The presence of a  $\phi^6$  term is also justified by Wilson's method for dimensions  $d > 4$ , through the renormalization process [Huang, 1987]. The parameters  $r, u, w$  are determined through a fitting procedure to the simulated distribution  $P(\phi)$  of the mean

$\phi$ -field on the lattice. The parameter  $Z_\phi$  can be calculated by the value of the propagator in momentum space:

$$G_2(\mathbf{p}) = \langle \phi(\mathbf{p})\phi^*(\mathbf{p}) \rangle, \quad \phi(\mathbf{p}) = \frac{1}{\sqrt{N}} \sum_{\mathbf{x}} \phi_{\mathbf{x}} e^{i\mathbf{p}\mathbf{x}} \quad (3.53)$$

which, for small momentum  $p$ , behaves as:

$$G_2(\mathbf{p})^{-1} = Z_\phi^{-1} p^2 + 2r \quad (3.54)$$

The effective Lagrangian, (3.52), in terms of renormalized field:

$$\phi_R = Z_\phi^{-1/2} \phi \quad (3.55)$$

becomes

$$\mathcal{L}_{eff} = \frac{1}{2} |\nabla \phi_R|^2 + \frac{1}{2} m^2 \phi_R^2 + m g_4 \phi_R^4 + g_6 \phi_R^6 \quad (3.56)$$

where

$$m = \sqrt{2Z_\phi r}, \quad g_4 = \frac{Z_\phi^2 u}{\sqrt{2Z_\phi r}}, \quad g_6 = Z_\phi^3 w \quad (3.57)$$

For the parameters  $g_4, g_6$ , the Monte Carlo simulation gives:

$$\begin{aligned} g_4 &= 0.97 \pm 0.02 \\ g_6 &= 2.05 \pm 0.15 \end{aligned} \quad (3.58)$$

Therefore, by replacing  $\mathcal{L}_{eff}$  by (3.52) into  $S_{eff}$ , we get

$$\begin{aligned} S_{eff} &= \int d^3 \mathbf{x} \left[ \frac{1}{2} Z_\phi^{-1} |\nabla \phi|^2 + r \phi^2 + u \phi^4 + w \phi^6 \right] \\ &= Z_\phi^{-1} \int d^3 \mathbf{x} \left[ \frac{1}{2} |\nabla \phi|^2 + Z_\phi (r \phi^2 + u \phi^4 + w \phi^6) \right] \end{aligned} \quad (3.59)$$

At the critical point, where  $m \rightarrow 0$ , and therefore by (3.57)  $r = u = 0$ , the critical effective action becomes:

$$S_{eff,cr} = Z_\phi^{-1} \int d^3 \mathbf{x} \left[ \frac{1}{2} |\nabla \phi|^2 + \hat{w} \phi^6 \right] \quad (3.60)$$

where

$$\hat{w} = Z_\phi w = Z_\phi^{-2} g_6 \quad (3.61)$$

The appearance of a  $\phi^6$  term in the effective potential makes the connection to the theory of the tricritical point of phase transitions mentioned in the previous section, thus allowing the description of various universality classes that predict tricritical points

by effective actions of the form  $S_{eff}$  and  $S_{eff,cr}$ . Apart from the 3D-Ising universality class, the  $O(4)$  model at the critical QCD point with  $m_u \simeq m_d \simeq 0$  and  $m_s \leq m_s^*$  is such a theory. The most general form of the  $O(N)$  symmetry, as shown in [Reuter et al., 1993], predicts for its effective action a  $\phi^6$  term, due to the small value of the anomalous dimension ( $\eta \simeq 0.034$ ).

## CHAPTER 4

# SIMULATING THE CHIRAL CONDENSATE

### 4.1 Introduction

We saw in the previous chapter that, according to the theory of critical phenomena, a system undergoing a second order phase transition exhibits, exactly at the critical temperature  $T = T_c$ , a divergent correlation length  $\xi$ ; in other words, there appear fluctuations of the order parameter with a scale invariant structure. This scale invariance “overshadows” the microscopic dynamics of the system, allowing for an effective description of a variety of very diverse systems through simple, coarse-grained models that belong to a few universality classes. In general, the symmetries and dimensionality of the system suffice for it to be classified into a universality class.

As we explained in sections 3.5.4 and 3.5.5, there are arguments, based on perturbative QCD as well as numerical simulations, that the QCD chiral critical point belongs to the 3D Ising universality class; in that case, the order parameter of the transition is the expectation value of the  $\sigma$ -field condensate. In a heavy ion collision, the  $\sigma$ -condensate should form at the critical temperature and its modes, the  $\sigma$ -particles, remain massless as long as the critical temperature endures. As the system expands and freezes out, the  $\sigma$  mass should attain a small, non-zero value, at the vicinity of the critical point.

The fact that the fluctuations of the order parameter at the critical point are self-similar implies the formation of *fractal clusters* in space [Mandelbrot, 1982; Stinchcombe, 1988]. Given the universality class (and the dimensionality of space), the fractal dimension of such clusters can be related to the critical exponents that characterize the singular behavior of thermodynamic variables of the system, and in particular with the isothermal critical exponent  $\delta$  that characterizes the system’s EoS.

In this chapter, we model the expected geometry of the chiral  $\sigma$  condensate near the QCD critical point, using a 3D Ising effective action, we discuss instanton-like solutions to the model and finally, we present a Monte Carlo that simulates the chiral  $\sigma$  condensate.

## 4.2 The 3D Ising model in the geometry of heavy ion collisions

### 4.2.1 The Ising model of magnetization

The simplest scalar field model is the spin-1/2 Ising model of magnetization, which is the standard “toy model” for formulating the effective action of single and multiple component scalar fields. The described system consists of a collection of spins  $\sigma_i$ , each of which can take one of two discrete values, +1, -1 (“up” and “down”, respectively), and which are placed on the nodes  $i$  of a lattice in space. Spins interact with each other, as well as with an external uniform magnetic field  $h$ , via the Hamiltonian:

$$\frac{H}{k_B T} = - \sum_{\langle ij \rangle} J_{ij} \sigma_i \sigma_j - h \sum_i \sigma_i, \quad (4.1)$$

where the summation is over nearest neighbor pairs of spins,  $\langle ij \rangle$ , and  $h$  is a constant external magnetic field (divided by the system temperature).  $J_{ij}$  is usually a constant  $J$  for nearest neighbor pairs, and zero for all other pairs. The system’s partition function then becomes:

$$Z = \sum_{\{\sigma_i\}} \exp \left\{ J \sum_{\langle ij \rangle} \sigma_i \sigma_j + h \sum_i \sigma_i \right\}, \quad (4.2)$$

where the summation is over all possible configurations  $\{\sigma_i\}$  of spins. Since we are interested in the behavior of the system near the critical point, it is enough to take into account the slow, long-wavelength fluctuations. We can therefore replace the lattice of spins with a slowly varying, scalar field  $\phi(x)$  in space, and the system’s Hamiltonian with an integral of the effective action over all space, which takes the form:

$$\begin{aligned} S_{eff} &= \int d^3x \left\{ \frac{1}{2} \partial_\mu \phi \partial^\mu \phi + V_{eff}(\phi) - h(x)\phi(x) \right\}, \\ V_{eff} &= r\phi^2 + (\text{higher order terms}), \end{aligned} \quad (4.3)$$

which is just the effective action (3.49) with an interaction term added. The fluctuations of the field have been taken into account by the gradient terms, and the  $\phi^2$  coefficient  $r$  is a function of temperature. Once we have an expression for action as a field functional, we can proceed with calculating the partition function, as follows:

$$Z = \int \mathcal{D}[\phi] e^{-S_{eff}[\phi]}, \quad (4.4)$$

where  $\mathcal{D}[\phi]$  implies summation over all (coarse-grained) configurations of the field  $\phi$  in space. To calculate the action, and therefore the partition function, we need to know

the form of the effective potential  $V_{eff}(\phi)$ . As we explained in section 3.5.5, Monte Carlo calculations in the 3D Ising model have been conducted, and the most significant order terms and coefficients have been determined. It turns out [Tsypin, 1994] that the  $\phi^6$  term plays the most crucial role at the critical point.

### 4.2.2 Adapting the 3D Ising model to the Bjorken cascade scenario of colliding nuclei

Assuming that the freeze-out temperature of a system of colliding nuclei is not very far from the critical,  $T_f \simeq T_c$ , the structure of the  $\sigma$ -condensate can be satisfactorily described by the 3D Ising effective action for  $T = T_c$ :

$$\Gamma_c[\sigma] = T_c^{-1} \int d^3\mathbf{x} \left[ \frac{1}{2}(\nabla\sigma)^2 + g T_c^4 (T_c^{-1}\sigma)^{\delta+1} \right], \quad (4.5)$$

where  $\delta$  is the isothermal critical exponent and  $g$  is a dimensionless coupling constant. The  $\sigma$  field has dimensions  $[\sigma] \sim [\text{length}]^{-1}$ . The parameters  $(g, \delta)$  are universal and express the equation of state (EoS) at the critical point:  $\delta\Gamma_c/\delta\sigma \sim g\sigma^\delta$  (see 3.18, 3.3d). For the 3D Ising universality class, the corresponding values are  $\delta \approx 5$ , due to the small value of the anomalous dimension [Berges et al., 1996], and  $g \approx 1.5 - 2.5$  [Tsypin, 1994; Berges et al., 1996].

Consequently, we must write the action 4.5 in a form that expresses the geometry of a system of colliding nuclei. We adopt the Bjorken inside-outside cascade scenario for the expansion of quark-gluon plasma: just after collision, a ‘‘central plateau’’ is formed, containing quarks and gluons in (local) thermal equilibrium, Fig.4.1. This system is considered to expand smoothly enough, so that it remains locally in equilibrium, and is described by an ensemble of locally inertial observers in relative motion to each other, following local plasma flow. All relevant thermodynamic quantities are functions of proper time,  $\tau$ . Dynamical evolution can be modeled by a succession of hyperboloid, space-like surfaces in the  $t-z$  plane (where  $z$  is the axis of collision), and flat surfaces in the transverse directions. This structure persists for about  $\sim 10 - 20$  fm/c, after which time hadrons form (mostly pions).

In order to describe the above geometry, we switch from Cartesian to hyperbolic ‘‘polar’’ coordinates of rapidity and proper time,  $(\xi, \tau)$ , so that the longitudinal coordinate corresponding to a co-moving inertial observer becomes  $dx_{\parallel} = \tau d\xi$ . To describe the clusters that form at  $T = T_c$ , we must integrate the longitudinal coordinate across the critical hyperbola  $\tau = \tau_c$ . We therefore obtain the following expression for the effective

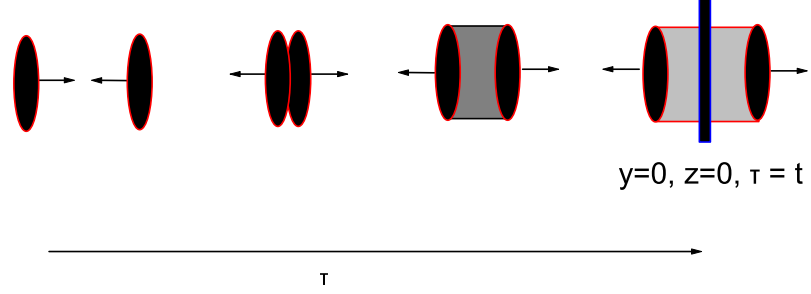


**Figure 4.1:** A sketch of the Bjorken inside-outside cascade scenario

action  $\Gamma_c[\sigma]$  as we approach the critical temperature:

$$\Gamma_c[\sigma] = \frac{1}{C_A} \int_{\Delta} d\xi \cosh \xi \int_{S_{\perp}} d^2 x_{\perp} \left[ \frac{1}{2 \cosh^2 \xi} \left( \frac{\partial \sigma}{\partial \xi} \right)^2 + \frac{\tau_c^2}{2} (\nabla_{\perp} \sigma)^2 + g T_c^4 C_A^2 (T_c^{-1} \sigma)^{\delta+1} \right], \quad (4.6)$$

where  $\Delta$  is the rapidity range,  $S_{\perp}$  is the transverse cross-section of the system and  $C_A = \tau_c / \beta_c$ .

Since we treat the system as an ensemble of local inertial observers, we can replace in (4.6) the full range  $\Delta$  of rapidity with a thin slice  $\Delta\xi$  around a local observer. Lorentz invariance allows us to freely select the center  $\xi$  of this slice. For convenience, we set  $\xi = 0$  and  $\Delta\xi \ll 1$ , so that we can set  $\cosh \xi \approx 1$ .

The system's geometry is cylindrical ( $3D \rightarrow 1D_{\xi} \otimes 2D_{R_{\perp}}$ ), with symmetry axis  $z$ , the collision direction. We want to examine configurations of the field that follow this geometry; we therefore separate the effective action, (4.6), by first projecting onto the rapidity direction, obtaining:

$$\Gamma_c^{(1)}[\hat{\sigma}] = g_1^{(1)} \int_{\Delta\xi} d\xi \left[ \frac{1}{2} \left( \frac{\partial \hat{\sigma}}{\partial \xi} \right)^2 + g_2^{(1)} (\hat{\sigma}^2)^{\frac{\delta+1}{2}} \right], \quad (4.7)$$

where we have defined, for clarity, the coefficients:

$$g_1^{(1)} = \frac{\pi R_{\perp}^2}{\beta_c \tau_c}, \quad g_2^{(1)} = g C_A^2, \quad (4.8)$$

$\Delta\xi$  is a slice of rapidity around a local observer at  $\xi = 0$ , and  $R_\perp$  is the transverse radius of the system at  $T = T_c$ , while  $\hat{\sigma}$  indicates a dimensionless  $\sigma$ -field ( $\hat{\sigma} = T_c^{-1} \sigma$ ).

Then, we project independently onto the transverse space directions, obtaining:

$$\Gamma_c^{(2)}[\hat{\sigma}] = g_1^{(2)} \int_{\perp} d^2 x_{\perp} \left[ \frac{1}{2} (\nabla_{\perp} \hat{\sigma})^2 + g_2^{(2)} (\hat{\sigma}^2)^{\frac{\delta+1}{2}} \right] \quad (4.9)$$

where now

$$g_1^{(2)} = C_A \Delta, \quad g_2^{(2)} = g \quad (4.10)$$

and  $\Delta$  is the full range of rapidity. The full 3D cluster is constructed as a cartesian product of the fractal clusters of rapidity & transverse configuration space, and is compatible with the longitudinal expansion of the system.

## 4.3 Fractal clusters

### 4.3.1 Magnetic clusters and critical fractality

It is instructive to examine the characteristics of the configuration of magnetization during the transition to the critical point, since it illustrates the relation between the fractal dimension of a system and experimentally measurable critical exponents.

At the critical point  $T = T_c$ , the total magnetization of a (theoretically infinite) system goes to zero, i.e., the difference between the volumes of areas of “up” and “down” spin, divided by the total volume tends to zero. However, since the correlation length  $\xi \rightarrow \infty$ , it follows from the correlation function,  $\Gamma(r) \sim r^{-p} e^{-r/\xi}$ , that there should arise clusters of opposite spin at arbitrarily large scales, that are also characterized by self-similarity (they look the same at all scales). Due to this fact, in any finite region, however large, the total magnetization is never strictly zero. Instead, the difference  $\Delta$  between “up” and “down” regions will depend on the linear size  $L$  of the region, according to the law:

$$\Delta(L) \propto L^{d_F} \quad (4.11)$$

where  $d_F$  is the fractal dimension of the set defined by the difference of regions of opposite spin.

In the case where the system is just below the critical temperature  $T_c$ , (4.11) is only valid for scales below the correlation length ( $L < \xi$ ), whereas for regions larger than the correlation length,  $L > \xi$ , magnetization smoothly shifts into trivial scaling, following the dimensionality  $d$  of embedding space.

We can use this transition to link, through a general theoretical argument, the fractal dimension  $d_F$  with the critical exponents of the magnetic system (and, owing to universality, with the critical exponents of any critical system) [Stinchcombe, 1988]. Let us

assume that  $T$  is just below  $T_c$ , so that the correlation length  $\xi$  is large but finite. Then, for a large enough system, i.e.  $L \gg \xi$ , the normalized magnetization will be given by

$$M \equiv \Delta(L)/L^d \propto t^\beta \propto \xi^{-\beta/\nu}, \quad (4.12)$$

according to eq.(3.3b) and (3.6). (4.12) ought to reproduce eq.(4.11) for  $L \ll \xi$ . A usual form of transition law that links the two asymptotic regimes,  $L \gg \xi$ ,  $L \ll \xi$ , through a function of the dimensionless ratio  $L/\xi$ , is

$$\Delta(L) = L^{d_F} f(\xi/L), \quad (4.13)$$

where  $f$  is a function with the property  $f(\infty) = \text{const.}$  and  $f(x) \sim x^{d_F-d}$  for small  $x$ . Comparing eqs.(4.12) and (4.13), we are led to:

$$d_F = d - \beta/\nu. \quad (4.14)$$

(4.14) links the fractal dimension of the magnetization clusters with the critical exponents. Using the four scaling laws, eqs.(3.8), that arise solely by virtue of scale invariance of a critical system, we can recast (4.14) in a more useful form, as a function of the isothermal critical exponent and dimensionality of space:

$$d_F = d - \frac{d}{\delta+1} = \frac{\delta d}{\delta+1} \quad (4.15)$$

Eq.(4.15) will show up again, when we examine saddle point solutions to the  $\sigma$ -field. We had obtained the same result, through scale-invariance of the free energy, for the dimension  $D_h$  connected with the external conjugate field  $h$ , in (3.23). It is therefore not coincidental, but a consequence of the general theory of critical phenomena.

### 4.3.2 The saddle point approximation to the partition function of the $\sigma$ -field.

We saw in section 4.2.2 that the 3D Ising effective action can be partitioned into independent rapidity and transverse configurations ((4.7) and (4.9), respectively). The partition function of the system<sup>1</sup>:

$$Z_c = \int \mathcal{D}[\sigma] e^{-\Gamma_c[\sigma]} \quad (4.16)$$

is only meaningful if we determine which states contribute, at equilibrium, and assign measures to them. We postulate a density matrix that is diagonal with respect to the

---

<sup>1</sup>From here on, we omit the ‘‘hat’’ ( $\hat{\sigma}$ ) for brevity, and will simply write  $\sigma$  for the dimensionless sigma field.

coherent states that correspond to the eigenstates of the field operators  $\sigma(x)$ , and are composed of superpositions of all particle states. Then, the average multiplicity  $\langle n \rangle$  of  $\sigma$  in a volume  $V$  within the system is given by:

$$\langle n \rangle = \int \mathcal{D}[\sigma] \left[ \int_V d^2 \mathbf{x}_\perp d\xi \sigma^2(\mathbf{x}_\perp, \xi) \right] e^{-\Gamma_c[\sigma]} / \int \mathcal{D}[\sigma] e^{-\Gamma_c[\sigma]} \quad (4.17)$$

Next, we need to define statistical weights  $\mathcal{D}[\sigma]$  for summing over states in (4.17). To this end, we note again that we are looking for solutions describing *clusters*, i.e. subsystems of the total volume for which the order parameter is greater than or equal to a minimum cutoff value. In our case, the order parameter is the total multiplicity of sigmas within a volume, or the ‘‘mass’’ contained within a volume, as defined by the squared  $\sigma$ -field. We work with *open* clusters, i.e., no boundary condition is imposed, which is a realistic condition unless we are too close to the boundary of the entire system.

We first examine the simpler 1D-case (rapidity). For large values of the action:

$$g_1^{(1)} = \frac{\pi R_\perp^2}{\beta_c \tau_c} \gg 1, \quad (4.18)$$

the sum over configurations in the partition function (4.16) is dominated by the so-called *saddle point configurations*. Following the methodology detailed in [Antoniou et al., 1998], we find the instanton-like solutions to the classical equations of motion:

$$\ddot{\sigma} - (\delta + 1)g_2^{(1)}\sigma^\delta = 0 \quad (4.19)$$

which are classified by their total energy,

$$E = \frac{1}{2}\dot{\sigma}^2 - g_2^{(1)}|\sigma|^{\delta+1} \quad (4.20)$$

and their central point  $\xi_0$ .

It is evident that any given solution with energy  $E$  contributes a suppressive factor  $e^{-E\Delta\xi}$  to (4.16), and therefore the only significant contribution comes from solutions with almost zero energy. We can then write down analytically this family of solutions, in closed form

$$\sigma(\xi) = \left[ \frac{\sqrt{2}}{(\delta - 1)\sqrt{g_2^{(1)}}} \right]^{\frac{2}{\delta-1}} |\xi - \xi_0|^{-\frac{2}{\delta-1}}. \quad (4.21)$$

The effective action, as a function of the range  $\Delta\xi$ , takes the form

$$\Gamma_c(\Delta\xi; \xi_0) = 2g_1^{(1)}g_2^{(1)} \int_{\Delta\xi} [\sigma(|\xi - \xi_0|)]^{\delta+1} d\xi. \quad (4.22)$$

It is clear from the form of (4.21) that the field attains very large values near  $\xi_0$ , and therefore that the area close to  $\xi_0$  contributes almost nothing to the partition function. We therefore impose the constraint  $\Delta\xi \ll \xi_0$  to the summed family of solutions, i.e. we only include those solutions where the size of the instanton is much larger than the size of the local system. As a result, the field is practically constant within the narrow slice  $\Delta\xi$ :

$$\sigma \approx \left[ \frac{\sqrt{2}}{\xi_0 \sqrt{g_2^{(1)}} (\delta - 1)} \right]^{\frac{2}{\delta-1}}. \quad (4.23)$$

We now picture the critical system as an ensemble of such clusters, of all sizes  $\Delta\xi$ . The partition function results as a summation of all instanton-like solutions that correspond to different  $\xi_0$ , with the proper weight function for every  $\xi_0$ . In order to define the range of integration  $d\xi_0$ , we introduce an extensive variable  $M$  that characterizes the configuration of the field within the cluster, whose average depends on the size of the cluster. Specifically, we choose the quantity  $M = \int_0^{\Delta\xi} [\sigma(x)]^2 dx$ , which, according to (4.17) gives the multiplicity  $\langle n(\Delta\xi) \rangle = \left\langle \int_0^{\Delta\xi} [\sigma(x)]^2 dx \right\rangle$  of  $\sigma$  within the cluster  $\Delta\xi$ . In the sum, we include those values of  $\xi_0$  that correspond to field configurations that give average values of  $M$  larger than a minimum value  $\mu$ . Based on (4.17) and (4.22), the expectation value turns out to be:

$$\begin{aligned} \left\langle \int_0^{\Delta\xi} [\sigma(x)]^2 dx \right\rangle &= \frac{A^2 \left( \frac{\delta-1}{\delta-3} \right)}{Z} \int_{\Delta\xi}^{(A^2 \Delta\xi / \mu)^{\frac{\delta-1}{4}}} d\xi_0 \xi_0^{-\frac{\delta+1}{\delta-1}} \left[ \xi_0^{\frac{\delta-3}{\delta-1}} - (\xi_0 - \Delta\xi)^{\frac{\delta-3}{\delta-1}} \right] \\ &\times \exp \left\{ -G_1 \frac{\delta-1}{\delta+3} \left[ (\xi_0 - \Delta\xi)^{-\frac{\delta+3}{\delta-1}} - \xi_0^{-\frac{\delta+3}{\delta-1}} \right] \right\}, \end{aligned} \quad (4.24)$$

where  $G_1 \equiv 2g_1^{(1)} g_2^{(1)} A^{\delta+1}$  and  $A = \left[ \left( g_2^{(1)} / 2 \right) (\delta - 1)^2 \right]^{-\frac{1}{\delta-1}}$ .

It can be shown analytically [Antoniou et al., 1998] that, for  $G_1 \gg 1$ , we can define three different regions with respect to the behavior of the right-hand integral in (4.24):

$$\begin{aligned} \Delta\xi \ll \Delta_d, & \quad \langle n(\Delta\xi) \rangle \sim \text{const.}, \\ \Delta_d \ll \Delta\xi \ll \Delta_u, & \quad \langle n(\Delta\xi) \rangle \sim (\Delta\xi)^{\frac{\delta-1}{\delta+1}}, \\ \Delta\xi \gg \Delta_u, & \quad \langle n(\Delta\xi) \rangle \sim (\Delta\xi)^{\frac{\delta-5}{\delta-1}}, \end{aligned} \quad (4.25)$$

where

$$\Delta_d \equiv A^{-2 \frac{\delta+1}{\delta-1}} G_1^{\frac{2}{\delta-1}} \mu^{\frac{\delta+1}{\delta-1}}, \quad \Delta_u \equiv G_1^{\frac{\delta-1}{\delta+3}} \quad (4.26)$$

define lower ( $\Delta_d$ ) and upper ( $\Delta_u$ ) size bounds for a cluster centered at  $\xi = 0$ .

Therefore, a fractal structure of critical clusters is revealed, with a dimension

$$d_F^{(1)} = \frac{\delta - 1}{\delta + 1} \quad (4.27)$$

in the range  $\Delta_d \ll \Delta\xi \ll \Delta_u$ . We note that, due to the self-similar structure of the system, the behavior described arises either by examining the scaling of the  $\sigma$  multiplicities as a function of varying distance from the cluster center or, equivalently, by examining the multiplicities of clusters of different size  $\Delta\xi$ , provided of course their size remains within limits of the aforementioned range.

We now turn our attention to the transverse profile of the system, which is described by (4.9). Quite analogously to (4.25), we find:

$$\begin{aligned} R \ll R_d, & \quad \langle n_{\perp}(R) \rangle \sim \text{const.}, \\ R_d \ll R \ll R_u, & \quad \langle n_{\perp}(R) \rangle \sim R^{2\frac{\delta-1}{\delta+1}}, \\ R \gg R_u, & \quad \langle n_{\perp}(R) \rangle \sim R^{2-\frac{4}{\delta-1}}, \end{aligned} \quad (4.28)$$

where

$$R_d = \beta_c G_2^{\frac{1}{2\delta}} A_2^{-\frac{\delta+1}{2\delta}} \mu^{\frac{\delta+1}{2\delta}} \pi^{-\frac{\delta+1}{2\delta}}, \quad R_u = \beta_c G_2^{\frac{\delta-1}{4}} \quad (4.29)$$

with

$$G_2 = 2\pi g_1^{(2)} g_2^{(2)} A_2^{\delta+1} \left( \frac{\delta+3}{4} \right) \quad \text{and} \quad A_2 = ((g_2^{(2)}/4)(\delta-1)^2(\delta+1))^{-\frac{1}{\delta-1}}. \quad (4.30)$$

And, similarly to (4.27), we conclude from (4.28) that fractal clusters form in transverse space with dimension

$$d_F^{(2)} = \frac{2(\delta-1)}{\delta+1} \quad (4.31)$$

in the range  $R_d \ll R \ll R_u$ .

The scaling laws, eqs.(4.25) and (4.28), can be generalized to other extensive variables: for example, if instead of averaging  $\sigma^2$  over a cluster, we take the field average,  $\left\langle \int_0^R \sigma(\mathbf{x}_{\perp}) d\mathbf{x}_{\perp} \right\rangle$ , we obtain clusters in transverse space with fractal dimension  $d'_F = 2\delta/(\delta+1)$ , for  $R_d \ll R \ll R_u$  [Antoniou et al., 1998]. This is in agreement with our earlier result for the scaling of magnetization at the critical point, eq.(4.15), for  $d = 2$ , which we arrived at via general critical theory arguments. This is only to be expected, as the field average over a region corresponds precisely to the total magnetization of the region.

### 4.3.3 The baryon-number density as an alternative order parameter

There are other possible order parameters of the critical phase transition besides the  $\sigma$ -field average (and powers of it). In a finite-density medium, a coupling exists between the  $\sigma$ -condensate and the net baryon number density,  $n_B(\mathbf{x})$ , which induces critical fluctuations in the latter. Specifically, the critical fluctuations of the chiral condensate are transferred to the net proton density, as well as the densities of protons and anti-protons separately, through the coupling of protons with the isospin-zero  $\sigma$ -field [Hatta and Stephanov, 2003].

In the vicinity of the QCD critical point, we can again employ an effective action belonging to the 3D-Ising universality class to describe the net baryon density fluctuations [Antoniou et al., 2006]:

$$\Gamma_c[n_B] = T_c^{-5} g^2 \int d^3 \mathbf{x} \left[ \frac{1}{2} |\nabla_{\perp} n_B|^2 + G g^{\delta-1} T_c^8 |T_c^{-3} n_B|^{\delta+1} \right], \quad (4.32)$$

where  $G$  is a universal, dimensionless coupling with a value  $G \simeq 1.5 - 2$ ,  $g$  is a non-universal dimensionless constant, and the baryon number density  $n_B(\mathbf{x})$  has dimension  $\sim [T_c]^3$ , resulting in a dimensionless action.

Again, taking into account the cylindrical geometry of a nuclear collision, we can replace the longitudinal coordinate  $x_{\parallel}$  with the space-time rapidity  $y$ , therefore taking the integration measure in rapidity,  $dx_{\parallel} = \tau_c \cosh y dy$ , where  $\tau_c$  is the formation time of the critical point. In a central rapidity region of size  $\delta y$ , we can assume boost-invariant configurations  $n_B(y, \mathbf{x}_{\perp})$ , defining the same 2-dimensional density  $\rho_B(\mathbf{x}_{\perp})$  in transverse configuration space,

$$n_B(\mathbf{x}_{\perp}) = \frac{\rho_B(\mathbf{x}_{\perp})}{2\tau_c \sinh(\delta y/2)} \quad (4.33)$$

Integrating in rapidity, and rescaling  $\mathbf{x}_{\perp}$  and  $\rho_B$  to dimensionless quantities:

$$\begin{aligned} \mathbf{x}_{\perp} &\rightarrow T_c \mathbf{x}_{\perp} \\ \rho_B &\rightarrow T_c^{-2} \rho_B, \end{aligned} \quad (4.34)$$

We obtain from (4.32) the dimensionless effective action in transverse space:

$$\Gamma_c[\rho_B] = C g^2 \int d^2 \mathbf{x}_{\perp} \left[ \frac{1}{2} |\nabla_{\perp} \rho_B|^2 + G (gC)^{\delta-1} \rho_B^{\delta+1} \right], \quad (4.35)$$

where  $C \equiv (T_c \tau_{\text{eff}})^{-1}$ ,  $\tau_{\text{eff}} \equiv 2\tau_c \sinh(\delta y/2)$ .

If we now define the order parameter of the system as the density  $\rho_B$  integrated over the volume of a transverse space cluster of radius  $R$ ,  $\langle n_B(R) \rangle \equiv \int d^2 \mathbf{x}_{\perp} \rho_B(\mathbf{x})$ , we obtain, following saddle-point approximation, section 4.3.2:

$$\langle n_B(R) \rangle \sim R^{d_F^{(B)}}, \quad R_d^{(B)} \ll R \ll R_u^{(B)} \quad (4.36)$$

where  $d_F^{(B)} = \frac{2\delta}{\delta+1}$  is the fractal dimension in transverse configuration space, and  $R_d^{(B)}$ ,  $R_u^{(B)}$ , are lower and upper size bounds for the clusters, whose values depend on the coupling constants:

$$\begin{aligned} g_1^{(B)} &\equiv Cg^2 \\ g_2^{(B)} &\equiv G(gC)^{\delta-1} \end{aligned} \quad (4.37)$$

Specifically, if we define, as in eq.(4.30),  $G_2^{(B)}$  and  $A_2^{(B)}$  in the same manner as  $G_2$  and  $A_2$ , we obtain for the lower and upper bounds:

$$R_d^{(B)} = \beta_c G_2^{(B)\frac{1}{2\delta}} A_2^{(B)-\frac{\delta+1}{2\delta}} \mu^{\frac{\delta+1}{2\delta}} \pi^{-\frac{\delta+1}{2\delta}}, \quad R_u^{(B)} = \beta_c G_2^{(B)\frac{\delta-1}{4}} \quad (4.38)$$

## 4.4 Fractal structure of clusters in transverse momentum space

### 4.4.1 Transition to transverse momentum space: The density-density correlation function

The fundamental measure quantifying correlations in a critical system is the *density-density correlation function* (see eq.3.4). Let us consider a point  $\mathbf{x}_0$ , belonging to a fractal set of dimension  $d_F$  which is embedded in  $d$ -dimensional space. For the sake of simplicity, and without loss of generality, let us set  $\mathbf{x}_0 = \mathbf{0}$ . Then, the density-density correlation function is defined as the conditional probability,  $C(\mathbf{x}|\mathbf{x}_0) \equiv C(\mathbf{x}-\mathbf{x}_0)$  of finding a fractal set point at  $\mathbf{x}$ , given that  $\mathbf{x}_0$  belongs to the set. For an isotropic fractal of mass dimension  $d_F$ , the number (“mass”) of points within a neighborhood of one of its points  $\mathbf{x}_0$  follows a power-law  $M(R) \sim R^{d_F}$ , where  $R = |\mathbf{x} - \mathbf{x}_0|$  is the distance from  $\mathbf{x}_0$ . It can then be shown [Vicsek, 1989] that the density-density correlation function at  $\mathbf{x}_0$  follows a power-law  $C(\mathbf{x} - \mathbf{x}_0) \sim |\mathbf{x} - \mathbf{x}_0|^{d_F-d} = R^{d_F-d}$ , where  $d$  is the embedding space dimension. Thus, for a system of critical  $\sigma$ -clusters, based on the fractal structure, eqs.(4.25), (4.28), the density-density correlation function in configuration space (rapidity  $\otimes$  transverse space) follows a power law:

$$C(\xi, \mathbf{x}_\perp) = \langle \rho(\xi, \mathbf{x}_\perp) \rho(0, \mathbf{0}) \rangle \sim |\xi|^{-\frac{2}{\delta+1}} \left| \frac{\mathbf{x}_\perp}{\beta_c} \right|^{-\frac{4}{\delta+1}} \quad (4.39)$$

where, due to translational symmetry, the behaviour around any point of the set is the same as for  $(0, \mathbf{0})$ . Similarly, for critical baryon-number density clusters in transverse space, we obtain:

$$C_B(\mathbf{x}_\perp) = \langle \rho_B(\mathbf{x}_\perp) \rho_B(\mathbf{0}) \rangle \sim \left| \frac{\mathbf{x}_\perp}{\beta_c} \right|^{-\frac{2}{\delta+1}} \quad (4.40)$$

The density-density correlation function in transverse space is a useful tool, because the fluctuations of the  $\sigma$ -field in transverse configuration space, contrary to those in rapidity space, are not directly observable. All we can observe are production rates of particles in transverse momentum space. It is therefore necessary to translate our description of the structure of critical clusters from transverse configuration to transverse momentum space. In terms of the density-density correlation function, this is achieved, as usual, through a Fourier transform.

Let us first understand how the one-particle density, i.e. the field, or a power of the field, transforms to momentum space. The one-particle density,  $\rho(\mathbf{x})$ , has a representation  $\tilde{\rho}(\mathbf{k})$  in momentum space, given in terms of creation/annihilation operators:

$$\tilde{\rho}(\mathbf{k}) = \int d^d \mathbf{x} e^{-i\mathbf{k}\mathbf{x}} \rho(\mathbf{x}) \quad ; \quad \tilde{\rho}(\mathbf{k}) = \sum_{\mathbf{p}} a_{\mathbf{p}}^* a_{\mathbf{p}+\mathbf{k}}, \quad (4.41)$$

where  $\mathbf{k}$  is the momentum transfer in a process  $\mathbf{p} \rightarrow \mathbf{p} + \mathbf{k}$ , and  $\tilde{\rho}(\mathbf{k})$  is associated with the amplitude of the process. For critical processes, only the limit  $\mathbf{k} \rightarrow 0$  is relevant, and taking the average over events for multiparticle production, we get:

$$\langle \tilde{\rho}(\mathbf{k} = \mathbf{0}) \rangle = \int d^d \mathbf{x} \langle \rho(\mathbf{x}) \rangle = \sum_{\mathbf{p}} \langle a_{\mathbf{p}}^* a_{\mathbf{p}} \rangle = \sum_{\mathbf{p}} \langle n_{\mathbf{p}} \rangle \quad (4.42)$$

or

$$\langle \tilde{\rho}(\mathbf{k} = \mathbf{0}) \rangle = \langle n \rangle$$

where  $n_{\mathbf{p}}$  is the particle number operator, and  $\langle n \rangle$  the average particle multiplicity over the set of events. Using the representation (4.41), the density-density correlation function has the following Fourier transform:

$$\langle \tilde{\rho}^*(\mathbf{k}) \tilde{\rho}(\mathbf{k}) \rangle = \int d^d \mathbf{x} e^{-i\mathbf{k}\mathbf{x}} \langle \rho(\mathbf{x}) \rho(\mathbf{0}) \rangle \quad (4.43)$$

and, in terms of creation/annihilation operators:

$$\langle \tilde{\rho}^*(\mathbf{k}) \tilde{\rho}(\mathbf{k}) \rangle = \sum_{\mathbf{p}, \mathbf{p}'} \langle a_{\mathbf{p}+\mathbf{k}}^* a_{\mathbf{p}} a_{\mathbf{p}'}^* a_{\mathbf{p}'+\mathbf{k}} \rangle \quad (4.44)$$

When (4.44) is viewed as an operator acting on a multiparticle state of the system, terms with  $\mathbf{p} \neq \mathbf{p}'$  vanish in the summation, as a result of the successive action of creation/annihilation operators. Therefore, we obtain for the Fourier transform of the density-density correlation function:

$$\langle \tilde{\rho}^*(\mathbf{k}) \tilde{\rho}(\mathbf{k}) \rangle = \sum_{\mathbf{p}} \langle a_{\mathbf{p}+\mathbf{k}}^* a_{\mathbf{p}} a_{\mathbf{p}}^* a_{\mathbf{p}+\mathbf{k}} \rangle = \sum_{\mathbf{p}} \langle n_{\mathbf{p}+\mathbf{k}} (n_{\mathbf{p}} - 1) \rangle \quad (4.45)$$

Eq.(4.45) shows that the Fourier transform of the density-density correlation function measures the number of pairs of points in momentum space that differ by  $\mathbf{k}$  in their momenta. Therefore, in the infrared limit  $|\mathbf{k}| \rightarrow 0$ , it represents the divergent part of the pair correlation function  $\tilde{C}(\mathbf{k})$  in momentum space:

$$\lim_{|\mathbf{k}| \rightarrow 0} \langle \tilde{\rho}^*(\mathbf{k}) \tilde{\rho}(\mathbf{k}) \rangle = \lim_{|\mathbf{k}| \rightarrow 0} \tilde{C}(\mathbf{k}) \sim |\mathbf{k}|^{\tilde{d}_F - d}, \quad (4.46)$$

where  $\tilde{d}_F$  is the fractal dimension of the set of particles in momentum space. The relationship between  $d_F$  and  $\tilde{d}_F$  can be extracted via the Fourier transform in (4.43). By simple dimensional analysis, we conclude  $\tilde{C}(\mathbf{k}) \sim |\mathbf{k}|^{-d_F}$ . Schematically, the transition from configuration to momentum space is given by the chain:

$$d_F \xrightarrow{C(\mathbf{x}, \mathbf{0})} |\mathbf{x}|^{d_F - d} \xrightarrow[\text{transform}]{\text{Fourier}} |\mathbf{k}|^{-d_F} = |\mathbf{k}|^{\tilde{d}_F - d} \xrightarrow{\tilde{C}(\mathbf{k})} \tilde{d}_F = d - d_F \quad (4.47)$$

Applying the transform for transverse momentum space ( $d = 2, \mathbf{k} = \mathbf{p}_T$ ), we obtain:

$$\tilde{C}(\mathbf{p}_T) \sim \int d^2 \mathbf{x}_\perp e^{i \mathbf{p}_T \cdot \mathbf{x}_\perp} C(\mathbf{x}_\perp, \mathbf{0}) \quad (4.48)$$

where  $C(\mathbf{x}_\perp, \mathbf{0})$  is the density-density  $\sigma$  correlation function for the projection in transverse configuration space of a critical cluster centered at  $\mathbf{x}_0 = \mathbf{0}$ , and  $\tilde{C}(\mathbf{p}_T)$  is the corresponding density-density correlation function in transverse momentum space. Setting  $R = |\mathbf{x}_\perp|$ , and inserting

$$C(R, 0) \sim R^{-\frac{2}{\kappa}} \quad (4.49)$$

in (4.48), where  $\kappa \equiv \frac{\delta+1}{2}, (\delta+1)$  for  $\sigma$  (baryons) respectively, we obtain from Fourier-transforming:

$$\tilde{C}(\mathbf{p}_T) \sim \int d^2 \mathbf{x}_\perp e^{i \mathbf{p}_T \cdot \mathbf{x}_\perp} C(\mathbf{x}_\perp, \mathbf{0}) = \int dR \cdot R \cdot R^{-\frac{2}{\kappa}} \int d\theta e^{i p_T R \cos \theta} \quad (4.50)$$

and, by the variable substitution  $z \equiv p_T \cdot R$ , we get

$$\tilde{C}(\mathbf{p}_T) \sim p_T^{-2 \frac{\kappa-1}{\kappa}} \int dz \cdot z \cdot z^{-\frac{2}{\kappa}} \int d\theta e^{i z \cos \theta} \quad (4.51)$$

we are thus led to the following power-laws for the density-density correlation functions in transverse momentum space:

$$\begin{aligned} \tilde{C}(\mathbf{p}_T) &\sim |\mathbf{p}_T|^{-2 \frac{(\kappa_\sigma - 1)}{\kappa_\sigma}} = |\mathbf{p}_T|^{-2(\delta-1)/(\delta+1)} \\ \tilde{C}_B(\mathbf{p}_T) &\sim |\mathbf{p}_T|^{-2 \frac{(\kappa_B - 1)}{\kappa_B}} = |\mathbf{p}_T|^{-2\delta/(\delta+1)}. \end{aligned} \quad (4.52)$$

#### 4.4.2 Inclusive q-particle distributions. Intermittency and factorial moments in transverse momentum space.

In order to study the fractal distribution of particle multiplicities in transverse momentum space, we employ statistical tools used in heavy ion collisions to study the many-particle states of strongly interacting particles produced. Such tools are the *inclusive q-particle distributions*: their integrated form, over phase space domains, provides us with the expected multiplicities of particles, as well as their fluctuations.

Specifically, we define the (symmetrized) inclusive q-particle distribution  $\rho_q$  [De Wolf et al., 1996]:

$$\rho_q = \sigma_{tot}^{-1} d\sigma_q(p_1, \dots, p_q) / \prod_{i=1}^q dp_q, \quad (4.53)$$

where  $\sigma_q(p_1, \dots, p_q)$  is the inclusive cross-section for q particles possessing momenta  $p_1, \dots, p_q$ , regardless of the presence and exact position of any other produced particles (i.e., we have integrated over all possible distributions of other particles). The variable  $p_i$  stands for the collection of all necessary parameters that determine the location of the i-th particle in phase space.  $\sigma_{tot}$  is the total cross section of the process under study.

In the case of identical particles, integrating (4.53) in a domain  $\Omega$  of momentum phase space gives:

$$\int_{\Omega} dp_1 \dots \int_{\Omega} dp_q \rho_q(p_1, \dots, p_q) = \langle n(n-1) \dots (n-q+1) \rangle, \quad (4.54)$$

where  $n$  is the multiplicity of identical particles in  $\Omega$  for a given collision event, and brackets denote averaging over the set of all events.

In order to extract statistically significant results given the limited statistics provided by experiment, it is necessary to subdivide the phase space  $\Omega$  into “cells” of volume  $\delta\Omega$ , and average (4.54) over cells. Important conclusions can be drawn by inspecting how multiplicities scale as a function of the size (equivalently, the number) of cells in momentum space.

Let us consider such a cell  $\Omega_m$  in phase space, having a volume of  $\delta\Omega$ . The total phase space, of volume  $\Omega$ , is partitioned into  $M^D$  non-overlapping cells of the same volume  $\delta\Omega$ . Evidently,  $\Omega = M^D \delta\Omega$ , where  $D$  is the dimensionality of phase space. Let  $n_m$  be the multiplicity of particles in the m-th cell  $\Omega_m$ . We can then define several different kinds of moments that average over cells.

The *Scaled Factorial Moments* (SFMs), also known as *vertical moments*, are defined as

[Bialas and Peschanski, 1986, 1988]:

$$\begin{aligned}
F_q^V(M) &\equiv \frac{1}{M^D} \sum_{m=1}^{M^D} \frac{\langle n_m(n_m-1)\dots(n_m-q+1) \rangle}{\langle n_m \rangle^q} \\
&\equiv \frac{1}{M^D} \sum_{m=1}^{M^D} \frac{\int_{\delta\Omega} \rho_q(p_1, \dots, p_q) \prod_{i=1}^q dp_i}{\left( \int_{\delta\Omega} \rho_1(p) dp \right)^q} \\
&\equiv \frac{1}{M^D (\delta\Omega)^q} \sum_{m=1}^{M^D} \int_{\delta\Omega} \frac{\rho_q(p_1, \dots, p_q) \prod_{i=1}^q dp_i}{(\bar{\rho}_m)^q},
\end{aligned} \tag{4.55}$$

where all  $p_i$  belong to the domain  $\delta\Omega$  and  $\langle n_m \rangle \equiv \bar{\rho}_m \delta\Omega \equiv \int_{\delta\Omega} \rho_1(p) dp$ .

We can also define *horizontal factorial moments* [Bialas and Peschanski, 1986, 1988]:

$$F_q^H(M) = \frac{\left\langle \frac{1}{M^D} \sum_{m=1}^{M^D} n_m(n_m-1)\dots(n_m-q+1) \right\rangle}{\left\langle \frac{1}{M^D} \sum_{m=1}^{M^D} n_m \right\rangle^q}, \tag{4.56}$$

where we first average over phase space cells and subsequently over the collection of events (denoted by angle brackets,  $\langle \dots \rangle$ ). The horizontal and vertical moments coincide in the case of a single phase space cell,  $M = 1$ . Vertical moments are locally normalized, and are therefore sensitive only to fluctuations within each cell, and not to fluctuations of the overall shape of the one-particle distribution. In contrast, horizontal moments are sensitive to the form of the one-particle distribution and also depend on the correlations between cells.

What form do factorial moments  $F_q(M)$  take as a function of size (number) of cells  $\delta\Omega$  ( $M$ )? That depends on the way points are distributed in phase space, and is intimately related to the possible fractality of the set they form. If the set of points possesses some characteristic length scale, we expect  $F_q(\delta\Omega) \rightarrow \text{const.}$  as  $\delta\Omega \rightarrow 0$ . If, on the contrary, the set is characterized by scale invariance (as is typically the case for a critical system), then the factorial moments will follow a scaling law, i.e. they will be invariant under rescaling (change of cell size):

$$F_q(\delta) = (\Delta/\delta)^{\phi_q} F_q(\Delta), \quad \phi_q > 0 \tag{4.57}$$

where  $\Delta, \delta$  are two different cell size scales and the exponent  $\phi_q$  is a function of the fractal dimension of the set of points.

In the context of particle physics, *intermittency* is defined as self-similarity of the many-particle states spectrum, when it is examined at different scales. As we have seen,

this implies that the factorial moments  $F_q(\delta\Omega)$  follow a power-law with regards to cell size:

$$F_q(\delta\Omega) \propto (\delta\Omega)^{-\phi_q}, \quad \delta\Omega \rightarrow 0. \quad (4.58)$$

The exponent  $\phi_q > 0$  is a constant for given  $q$  and is called the *intermittency index*. The form of (4.58) implies that the inclusive distributions  $\rho_q$ , as well as the density correlation functions  $C_q$ , are divergent in the infinitesimal distance limit  $\delta\Omega \rightarrow 0$  in momentum space. This is easier to understand if we recall that the density-density correlation function  $C_2$  merely expresses the conditional probability, defined in eqs.(4.39,4.40), that a point is found at  $\mathbf{x}$  given that  $\mathbf{0}$  belongs to the set. Intermittency arises in a critical system due to the fact that the density-density correlation function follows a power-law. Indeed, according to the usual conditional probability law, we can express the 2-particle density as:

$$\rho_2(p_1, p_2) = C_2(p_1|p_2) \cdot \rho_1(p_2), \quad (4.59)$$

where  $C_2(p_1|p_2) = C_2(|p_1 - p_2|) \propto |p_1 - p_2|^{-f_2}$  is the probability density of finding a set point in the vicinity of  $p_1$ , given that  $p_2$  belongs to the set, and the exponent  $f_2$  is derived from the power-law the density-density correlation function follows.  $\rho_1$  is the prior probability density of finding a set point in a volume  $\delta\Omega$ , and is a constant for homogeneous fractals, i.e. the probability is proportional to  $\delta\Omega$ . Based on the above, as well as the definitions of factorial moments, (4.56),(4.55), we can relate the exponent  $f_2$  of the density-density correlation function to the intermittency index of the second scaled factorial moments (SSFMs)  $F_2(\delta\Omega)$ :

$$F_2(\delta\Omega) \propto \frac{(\delta\Omega) \cdot (\delta\Omega)^{\frac{D-f_2}{D}}}{(\delta\Omega)^2} \propto (\delta\Omega)^{-\frac{f_2}{D}} \propto (M^{-D})^{-f_2/D} \propto M^{f_2}, \quad (4.60)$$

where  $D$  is the dimensionality of embedding space. In the case of transverse momentum space, we have  $D = 2$ ,  $f_2 = 2 \frac{\kappa-1}{\kappa}$ , eq.(4.52), and therefore:

$$F_2(M) \sim \left(M^2\right)^{\frac{\kappa-1}{\kappa}} \quad (4.61)$$

where  $M^2$  is the number of cells in 2D space. It is  $M^2 \sim (\delta\Omega)^{-1}$ , and referring to (4.58) we see that  $\phi_2 = \frac{\kappa-1}{\kappa}$ .

It can be shown more generally [De Wolf et al., 1996], for a fractal or multi-fractal set, that the intermittency index  $\phi_q$  is related to the fractal dimension of the set as:

$$D \cdot \phi_q = (q-1) \cdot d_q, \quad (4.62)$$

where  $d_q$  is the *anomalous dimension* of the set, obtained by subtracting the *Rényi dimension*,  $D_q$ , from the topological dimension  $D$  of embedding space:

$$d_q = D - D_q \quad (4.63)$$

The Rényi dimension  $D_q$  generalizes the concepts of fractal “mass” dimension  $d_F$ , information dimension and correlation dimension. In the case of a mono-fractal, we can take  $D_q$  as identical to the “mass” dimension  $d_F$ .

We therefore conclude that, when critical, the factorial moments  $F_q(M)$  follow intermittent power-laws of the form:

$$F_q(M) \propto (M^D)^{(q-1)\frac{D-D_q}{D}} \quad (4.64)$$

with

$$\phi_q = (q-1)\frac{D-D_q}{D} \quad (4.65)$$

## 4.5 Stochastic fractals and Lévy walks

### 4.5.1 Generating stochastic fractals through random walks

We now seek methods by which we can numerically *simulate* fractal clusters in transverse configuration (or momentum) space. The problem reduces to that of numerically producing a set of points, representing critical particles in momentum space, which should exhibit self-similarity possessing the desired fractal dimensionality.

It is relatively simple to produce, via iterated algorithms, *deterministic* fractal sets with self-similar structure; however, such sets are excessively regular and uniform, and therefore cannot satisfactorily simulate a critical system, which only possesses self-similarity in a statistical sense, i.e. in the distribution of fractal measures averaged over a large number of generated configurations. We ought to use an algorithm that produces stochastic (random) fractals, employing pseudorandom number generators coupled with a proper iterative process. The produced fractal sets also need to be (statistically) uniform and isotropic, i.e. to look the same, on average, from every point and in every orientation.

This can be achieved through the technique of *random walks*: We start at some point in space (for illustrative purposes, let us imagine we are working on the plane,  $D = 2$ , and start at the origin,  $\mathbf{x}_0 = \mathbf{0}$ ) and randomly select a direction, with uniform probability. Next, we take a step in the direction chosen. The step length is also chosen at random from a given probability (density) distribution. We thus reach a new point,  $\mathbf{x}_1$ . Iteration of this process of consecutive steps produces a set of points  $\mathbf{x}_i$ ,  $i = 1, \dots, N$  on the plane. Since every step is independent from the ones preceding it (such a series is called a “Markov chain”), the process has no “memory”, and the set should look the same from each of its points, in the limit  $N \rightarrow \infty$ . (Of course, for any finite number of steps, the points near the initial and last step possess a privileged place, but for a large enough set, or a large ensemble of such sets, the condition holds for the majority of points).

Although such a set possesses translational and rotational symmetry, it is not necessarily self-similar, i.e. it does not in general possess (non-trivial) scale invariance with a fractal dimension  $D_F < D$ , where  $D$  is the dimensionality of embedding space. This feature of the set depends on the choice of the step probability distribution  $\rho(r)$ , which gives the probability density of taking a step with a length between  $r$  and  $r + dr$ ,  $0 < r < \infty$ .

In the matter of step distribution functions, the mathematical property of *infinite divisibility* plays a crucial role. A probability distribution function (more precisely, a family of functions) is said to be infinitely divisible when, for every random variable  $X$  following the distribution and for every positive integer  $n$ , there exist  $n$  independent identically distributed (i.i.d.) random variables,  $X_1, \dots, X_n$ , following identical distributions (not necessarily the same as  $X$ ), such that their sum follows the distribution of  $X$ . Intuitively, infinite divisibility means that we can indefinitely subdivide the steps of a random walk, approaching the continuous time limit (“Brown motion”).

Infinite divisibility by itself is not sufficient for scale invariance. In order for that to hold, the step distribution must also be *stable*. A distribution  $F$  is said to be stable when, for every two i.i.d. random variables  $X_1, X_2$  following  $F$ , and for every two coefficients  $c_1, c_2$ , there exists a coefficient  $c$  and a random variable  $X_3$ , also following  $F$ , such that:  $c_1 X_1 + c_2 X_2 = c X_3$  [Shlesinger et al., 1995]. A stable distribution can therefore be “rescaled”, subdivided in an arbitrary number of copies of itself.

Stable distributions belong to classes, characterized by the parametrization of the characteristic functions of each distribution [Shlesinger et al., 1995]. The relevant parameter,  $\alpha$ , takes values in the interval  $0 < \alpha \leq 2$ . Notable examples of stable distributions are the Gaussian ( $\alpha = 2$ ), Cauchy ( $\alpha = 1$ ), etc.

The importance of a distribution’s stability lies in the fact that it defines a simple scaling law: if time (number of steps) is multiplied by a factor of  $\lambda$ , and length scale by a factor of  $\lambda^{1/\alpha}$ , we get a rescaled copy of the original walk. It is easy to see from this fact, that the parameter  $\alpha$ , i.e. the class where the distribution belongs, controls the dimensionality of the set produced by the random walk.

#### 4.5.2 Distributions with finite and infinite variance. Lévy walks.

If the random walk step follows a distribution with finite variance, then the Central Limit Theorem applies, and asserts that the total displacement (vector sum of steps) after  $N$  steps follows, for large enough  $N$ , a Gaussian (normal) distribution, with a mean of  $\mu(N) = N \mu$  and a variance of  $\sigma^2(N) = N \sigma^2$ , where  $\mu, \sigma^2$  the mean and variance of one step, respectively. Thus, the endpoint on a random walk at the  $N$ -th step is found on average at a distance  $R(N) \sim \sqrt{N}$  from the origin. Therefore, the average

---

<sup>2</sup>To be sure, classes require more parameters to be fully characterized. Here, we focus solely on  $\alpha$ , since it is intimately connected to the dimensionality of the fractal set produced by the random walk.

number of points within a radius  $R$  centered at a point in the set scales as  $\langle N(R) \rangle \sim R^2$ , which means that a Gaussian random walk fills the plane in the limit  $N \rightarrow \infty$  (“mass” dimension  $d = D = 2$ ).

A set produced by such a random walk possesses only trivial self-similarity. In order to produce fractal sets with a dimensionality strictly less than their embedding space, we must perform random walks the steps of which follow distributions with infinite variance. If our distribution tends asymptotically to zero for large  $r$  as  $\rho(r) \sim r^{-(1+\gamma)}$ ,  $0 < \gamma < 2$ , then the step variance is infinite. A generalized Central Limit Theorem then asserts that, after a large number of steps, the distance from the origin will tend to a Lévy distribution. The specific choice of Lévy distribution depends on the value of the exponent  $\gamma$ . Since Lévy distributions also have infinite variance, the random walk set of points will possess non-trivial self-similarity. We can picture that by realizing that if, for example, we merge every 50 steps, we get a set of points with the exact same characteristics as when we merge every 500, or any other number, of steps, in other words we get *the same structure at different scales*.

Such a random walk is called a *Lévy walk*, or *Lévy flight*. The fractal dimension of the set produced by it is  $D_F \simeq \gamma$ . In order to obtain a well-defined, self-similar structure, this fractal dimension needs to be strictly smaller than the embedding space dimension,  $\gamma < D$ . Moreover, the demand that total probability be normalizable to unity introduces the additional constraint  $\gamma > D - 1$  (thus, on the plane we have  $1 < \gamma < 2$ ). In practice, we perform a Lévy walk by setting up the step algorithm such that the probability of selecting a step of length  $\Delta r$  larger than  $\Delta r_0$  is [Mandelbrot, 1982]:

$$Pr(\Delta r > \Delta r_0) = \begin{cases} 1, & \text{for } \Delta r_0 < \Delta r_d \\ C \Delta r_0^{-D_F}, & \text{for } \Delta r_d \leq \Delta r_0 \leq \Delta r_u \\ 0, & \text{for } \Delta r_0 > \Delta r_u \end{cases} \quad (4.66)$$

where  $\Delta r_d, \Delta r_u$  are cutoffs that define a lower and upper scale for the set, respectively, and  $C$  is a normalization constant. The cutoffs define a range of scales within which the set possesses fractal self-similarity, and they are imposed by practical considerations: a computer can only produce (pseudo)random numbers within a finite range of values. It is evident that while in theory the step size can lie in the range  $0 < r < \infty$ , in practice the distribution has to be cut off at some value, so as to prevent overflow<sup>3</sup>.

Fig.4.2 shows the results of a random walk of 500,000 steps, with a fractal dimension of  $D_F = 1.5$ , at various scales. The development of clusters of points is apparent in the picture. Most steps are very small, but due to the infinite step variance, some steps are large, and the random walk leaps from one cluster to another (only the

<sup>3</sup>As is evident from the definition (4.66), a single  $C$  value cannot satisfy both cutoffs; there is necessarily a discontinuity in  $Pr(\Delta r > \Delta r_0)$ , either at the lower cutoff, or the upper (or both). However, for small (large) enough cutoff values, this discontinuity can be arbitrarily small.

endpoints of steps are drawn, not the connecting segments). We notice, in the successive magnifications of the walk, the self-similarity of the clusters.

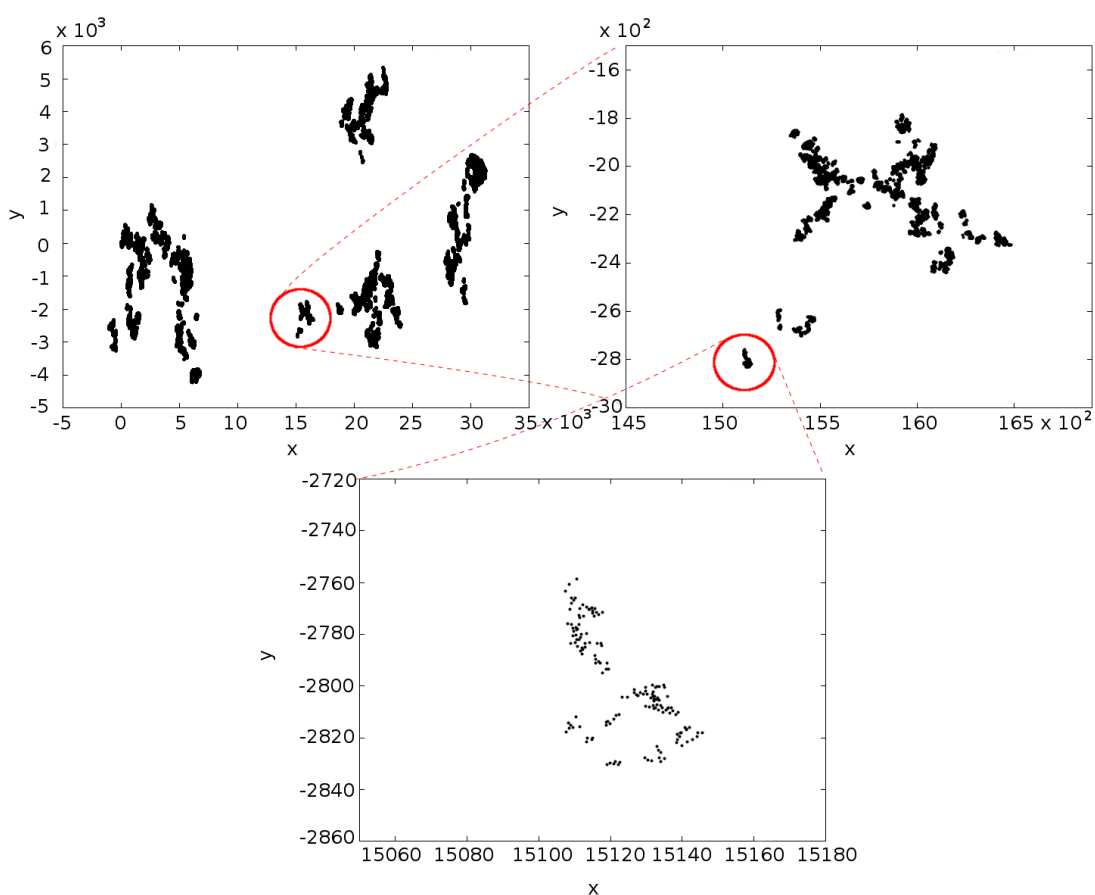


**Figure 4.2:** A random Lévy walk of 500,000 steps, corresponding to a dimension of  $D_F = 1.5$ . The top left image shows the whole set produced by the walk. The top right image is a magnification of a cluster within the set, and the bottom image is a further magnification of a sub-cluster, at a zoom factor of about 200 : 1. The “grain size” of the walk is only apparent in the final magnification.

Fig.4.3 is a plot of the *correlation function*  $C(R)$  versus the distance scale  $R$ .  $C(R)$  is

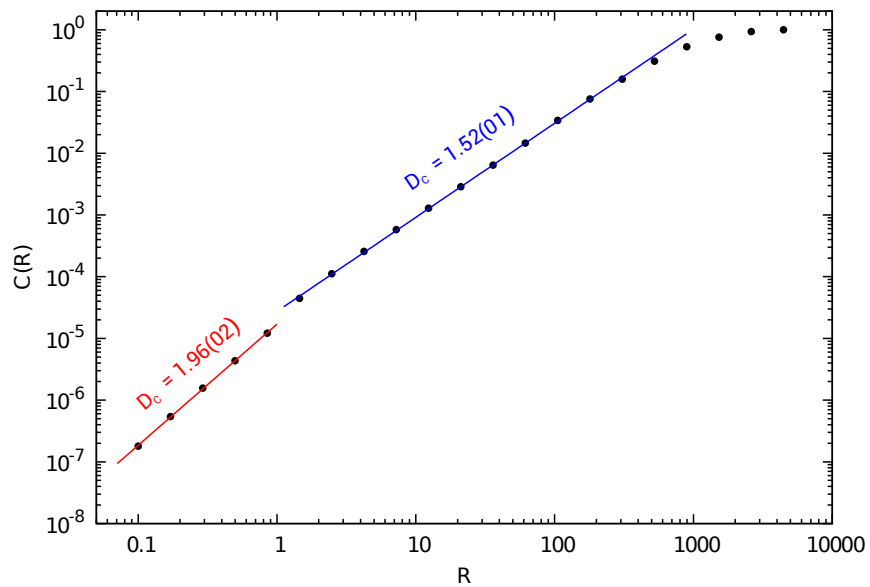


**Figure 4.3:** The correlation function  $C(R)$  vs distance scale  $R$ , for a subset of 80,000 successive points belonging to the Lévy walk in Fig.4.2. In the central region, the correlation dimension  $D_C$ , estimated by fitting the log-log plot, is approximately equal to the fractal exponent  $D_F = \gamma$  used in the construction of the set. In scales smaller than the lower cutoff of the Lévy step size,  $D_C \approx D = 2$ , and the set fills the plane.

a measure of the distribution of distances among points in the set, and is defined as:

$$C(R) = \frac{2}{N(N-1)} \sum_{\substack{i,j \\ i < j}} \Theta(R - |\mathbf{x}_i - \mathbf{x}_j|), \quad (4.67)$$

where  $\Theta$  is the step function and  $|\mathbf{x}_i - \mathbf{x}_j|$  are all the sets of distances in the set,  $i, j = 1, \dots, N$ . For a fractal set of points,  $C(R)$  is expected to scale as  $C(R) \sim R^{D_C}$ , where  $D_C$  is the *correlation dimension* of the set. We expect  $D_F \simeq D_C$  [Grassberger and Procaccia, 1983].

As can be seen in Fig.4.3, the log-log plot of  $C(R)$  does not possess an exactly linear form; however, its central area is well approximated by a straight line with a slope around 1.5. At very long distances, we observe a saturation of  $C(R)$ , since we reach the borders of the set. Remarkably, at very small distances, smaller than the minimum step size  $\Delta r_d$ , we get excellent linearity, but with a dimensionality corresponding to that of embedding space. This behavior – two almost linear regimes connected by a sharp transition at a “knee” – is reminiscent of the behavior of the instanton solutions to the 3D-Ising effective action, eq.(4.28). The linearity of  $\log C(R)$  can be enhanced, if proper lower and upper cutoffs are selected, which is a matter of some empirical experimentation. For the set depicted in Fig.4.2, we have set  $\Delta r_d = 1$ ,  $\Delta r_u = 1 \times 10^4$ .

### 4.5.3 Cartesian products of Lévy walks.

We've seen that a random Lévy walk with a step distribution of  $Pr(\Delta r > \Delta r_0) \sim r_0^{-\gamma}$ ,  $1 < \gamma < 2$ , embedded in a space of dimension  $D \geq 2$ , produces a stochastic fractal set of dimension  $D_F = \gamma$ . However, we sometimes need to produce fractal sets with  $D_F < 1$  on the plane. In such cases, we resort to the following trick: we produce 2 independent random walks,  $\mathcal{A}$  and  $\mathcal{B}$ , embedded in one dimensional spaces ( $D_1 = D_2 = 1$ ), with:

$$\begin{aligned} (\mathcal{A}) : Pr(\Delta x > \Delta x_0) &\sim \Delta x_0^{-D_{F_1}}, \quad D_{F_1} < 1 \\ (\mathcal{B}) : Pr(\Delta y > \Delta y_0) &\sim \Delta y_0^{-D_{F_2}}, \quad D_{F_2} < 1 \end{aligned}$$

Embedding in 1D space then leads to fractal sets with dimensions  $D_{F_1}, D_{F_2} < 1$ . Consequently, we form the cartesian product:

$$(\mathcal{A})_{D_{F_1}} \otimes (\mathcal{B})_{D_{F_2}} : x_i \otimes y_i \rightarrow (x_i, y_i) \in E_2,$$

i.e., we form pairs of coordinates using as elements the points of the 2 independent walks. It can be proven that the resulting set of points in the plane has a dimensionality equal to the sum of dimensions of the 1D Lévy walks,  $D_{F_{\mathcal{A} \otimes \mathcal{B}}} = D_{F_1} + D_{F_2}$ .

## 4.6 Critical Monte Carlo (CMC) implementation

### 4.6.1 The CMC algorithm

Let us now examine how the techniques of section 4.5 can be applied in the simulation of the critical  $\sigma$ -condensate. First of all, the simulation is implemented in momentum space. As we have seen in section 4.4.1, we can transport the properties of critical geometry from configuration to momentum space via a Fourier transform in transverse space. Our simulation is an adaptation of the *Critical Monte Carlo* (CMC) algorithm [Antoniou et al., 2001], with a few modifications in input parameters. The code implementation, in Fortran 90, can be found in Appendix B.

As was explained in section 4.2.2, the cluster geometry is cylindrical, i.e. it is formed as a cartesian product in rapidity  $\otimes$  transverse momentum space. In simulating an event, the algorithm begins by determining the number and distribution, in phase space, of the clusters corresponding to the  $\sigma$ -condensate. We recall that the number of clusters is determined by the overall size of the critical system, whereas the multiplicity of  $\sigma$  within each cluster depends on the values of the coupling constants appearing in the free energy expression of the system at the critical point.

The input parameters to the algorithm determining the  $\sigma$ -distribution are:

- The transverse size of the system,  $R_\perp$
- The total rapidity range,  $\Delta$
- The proper timescale,  $\tau$
- The critical temperature,  $T_c$
- The coupling constant  $g$  in the effective action for the 3D-Ising model, and
- The isothermal critical exponent  $\delta$ .

Once we have determined the values of these parameters, we can calculate the size of a cylindrical  $\sigma$ -cluster, i.e. its radius  $|\Delta\mathbf{p}_\perp|$  in transverse momentum space and its width  $2\Delta_u$  in rapidity. These are given by:

$$\begin{aligned}\Delta_u &= G_1^{(\delta-1)/(\delta+3)} \\ |\Delta\mathbf{p}_\perp| &= (4\pi C_A \Delta g)^{-\frac{1}{10}} \beta_c^{-1}\end{aligned}\tag{4.68}$$

$\Delta_u$  derives from eq.(4.26).  $|\Delta\mathbf{p}_\perp|$  is determined by  $R_d$ , eq.(4.29), where we have used the value  $\delta = 5$ .

The number of  $\sigma$ -clusters in transverse (configuration or momentum) space, as well as the corresponding number of clusters in rapidity space, are given by:

$$\begin{aligned} N_{//} &= \frac{\Delta}{2\Delta_u} = \frac{2\Delta\tau}{\sqrt{\pi}R_{\perp}} \left(\frac{g}{2}\right)^{1/4} \\ N_{\perp} &= \left(\frac{R_{\perp}}{R_u}\right)^2 = \left(\frac{12\sqrt{6g}R_{\perp}}{\pi\Delta\tau}\right)^2 \end{aligned} \quad (4.69)$$

Finally, the multiplicity of  $\sigma$  within each cluster can be estimated as:

$$\langle n_{cl} \rangle = \frac{\Gamma\left(\frac{3}{\delta+1}\right)}{\Gamma\left(\frac{1}{\delta+1}\right)} \left(\frac{V}{V_0}\right)^{(\delta-1)/(\delta+1)}, \quad (4.70)$$

where  $V = 2\pi R_u^2 \Delta_u$  and  $V_0 = \beta_c^2 \sqrt{2gC_A}$ .

Consequently, cluster centers must be appropriately distributed in phase space. In rapidity, we generate as already mentioned  $N_{//}$  clusters, the center positions of which are treated as random variables, uniformly distributed in the range  $[0, \Delta]$ . In transverse momentum space, the centers of the  $N_{\perp}$  clusters follow an exponential distribution:

$$f(\mathbf{p}_T) = \frac{2}{\pi \langle p_T \rangle^2} e^{-2p_T / \langle p_T \rangle}, \quad (4.71)$$

under the constraint that the total transverse momentum of cluster centers vanishes:

$$\sum_{i=1}^{N_{\perp}} \mathbf{p}_{T,i} = \mathbf{0}. \quad (4.72)$$

$\langle p_T \rangle$  is the mean transverse momentum, which we approximate by  $\langle p_T \rangle \approx 2T_c$ .

After the cluster centers have been positioned, a number of  $\sigma$  particles are produced, with the appropriate mean multiplicity per cluster. At this point, we implement the Lévy walk technique described in section 4.5, with a suitable plug-in value for the dimension  $d_F$ . In rapidity, we stochastically produce the particles corresponding to a cluster using a 1D Lévy walk with  $d_F^{(1)} = \frac{\delta-1}{\delta+1} = 2/3$ , eq.(4.27). The resulting set does not, in general, have the correct center and size. By exploiting the self-similarity of the system, we can produce the desired set by rescaling the original set and positioning it around the correct center. The resulting multiplicities within each cluster depend on the positions of the neighboring cluster centers. Therefore, the distribution of cluster centers in rapidity determines the total multiplicity  $N_{\sigma}$  of  $\sigma$  particles within an event.

Additionally, to each transverse momentum cluster there correspond  $N_{\sigma}/N_{\perp}$   $\sigma$ -particles, distributed according to the power-law in eq.(4.28). If we Fourier-transform

eq.(4.31), this translates to a fractal dimension of  $\tilde{d}_F^{(2)} = \frac{4}{\delta+1} = 2/3 < 1$  in transverse momentum space. In order to construct this set, we resort to the cartesian product Lévy walk technique described earlier: we produce independent sets for the coordinates  $p_x, p_y$  by implementing walks of dimension 1/3 embedded in 1D space, and then we take their cartesian product.

We therefore obtain two sets of variables in phase space: a set  $S_T$  of  $N_\sigma$  pairs of transverse momenta,  $\{(p_{x_1}, p_{y_1}), \dots, (p_{x_{N_\sigma}}, p_{y_{N_\sigma}})\}$ , and a set  $S_\xi$  of  $N_\sigma$  rapidity values,  $\{\xi_1, \dots, \xi_{N_\sigma}\}$ . The  $\sigma$ -particle content of a critical event following the underlying cylindrical geometry is then produced by a one-to-one, random combination of the elements of  $S_T$  with those of  $S_\xi$ .

Finally, for every produced particle, we change variables from the triplet  $\{p_{x_i}, p_{y_i}, \xi_i\}$  to the corresponding  $\{p_{x_i}, p_{y_i}, p_{z_i}\}$ , where  $p_z = \sqrt{p_x^2 + p_y^2} \cdot \sinh \xi$ , where we have set  $m_\sigma = 0$ , since we assume  $T = T_c$ .

#### 4.6.2 Input parameter values

Consequently, we must select realistic values for the input parameters of the CMC algorithm. The following table summarizes the input parameters and their selected values:

Parameter	$T_c$ (MeV)	$R_\perp$ (fm)	$\Delta$	$\tau$ (fm)	$\delta$	$g$
Value	163	8	6	11	5	2

Of these parameters,  $\delta$  and  $g$  are fixed by the 3D-Ising universality class at  $\delta \approx 5$  and  $g \approx 2$ , respectively. The rapidity range is selected to be compatible with SPS conditions (Si+Si collisions, NA49 experiment). The aforementioned values for  $R_\perp$  and  $g$  lead to a value of  $R_u \approx 5$  fm, which results in the formation of 2 clusters in transverse momentum space. Taking into account the fact that  $\Delta_u \approx 0.32$ , we obtain 9 clusters in the projection in rapidity space. Therefore, we expect 18 critical clusters to form in total, based on the cylindrical evolutionary scenario.

In Fig.4.4, we show the distribution of simulated  $\sigma$  particles in rapidity and transverse momentum space, as well as the multiplicity distribution of  $\sigma$ . As expected, the profiles in rapidity and azimuthal angle are approximately flat, while  $p_T$  follows an exponential distribution (in 2D). The one-particle joint distribution in  $\{p_x, p_y\}$  is shown in Fig.4.5. Finally, the second scaled factorial moment,  $F_2(M)$ , as a function of bin size  $M$  in transverse momentum space is shown in Fig.4.6 for a set of 150,000 events. The resulting intermittency index,  $\phi_2 = 0.690(2)$ , is within 5% of the theoretically expected value of  $\phi_{2,\sigma} = 2/3$ , confirming the self-consistency of the CMC algorithm.

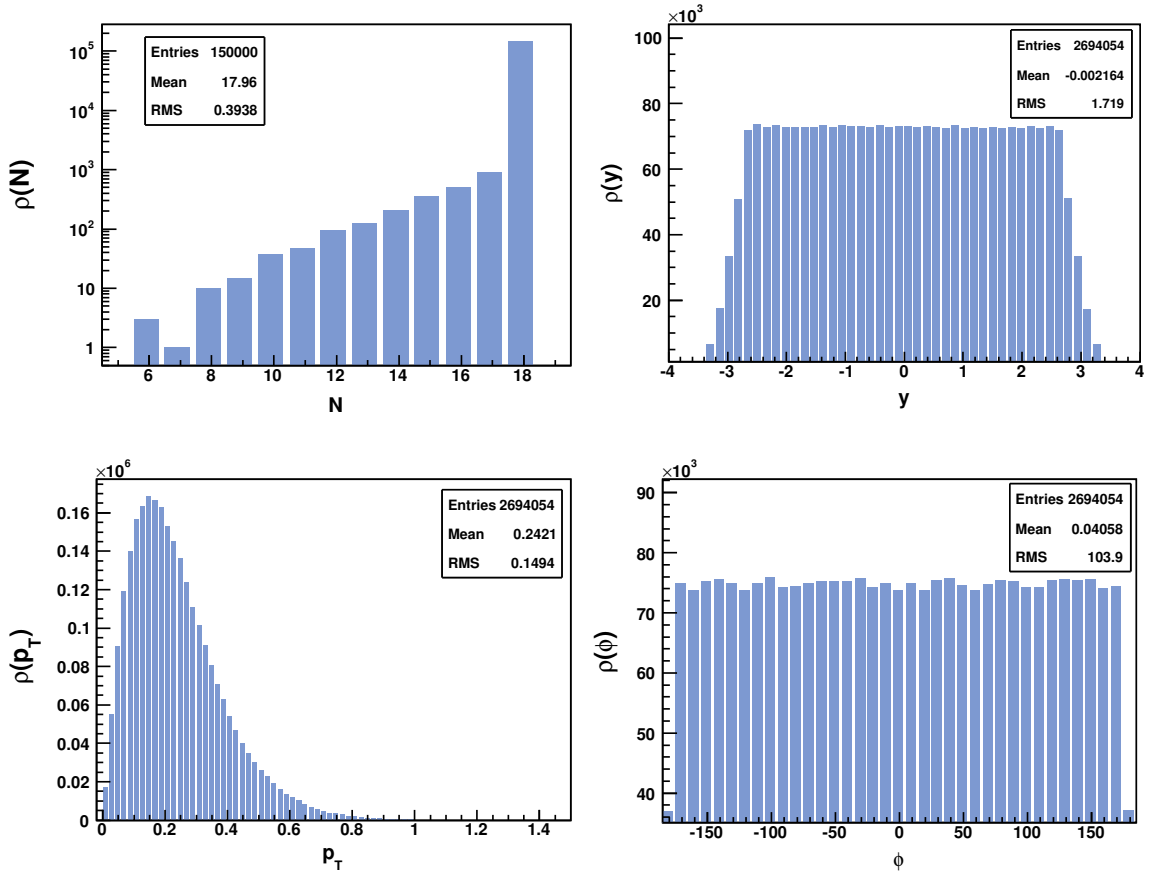


**Figure 4.4:** The results of a 150,000 event run of CMC with typical input parameter values. Top left: event multiplicity distribution of  $\sigma$ . Top right: rapidity distribution. Bottom left: Transverse momentum ( $p_T$ ) distribution. Bottom right: Azimuthal angle ( $\phi$ ) distribution.

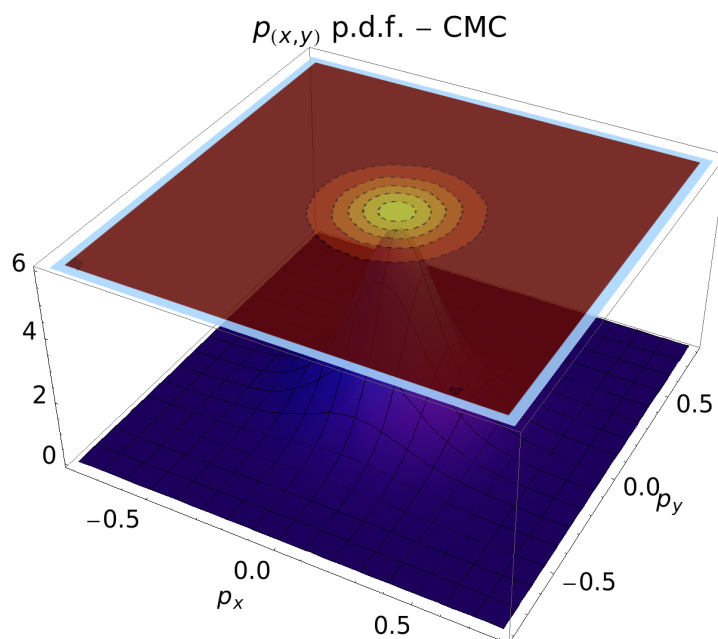


**Figure 4.5:**  $\rho(p_x, p_y)$  one-particle distribution for 150,000 events generated by the CMC algorithm.

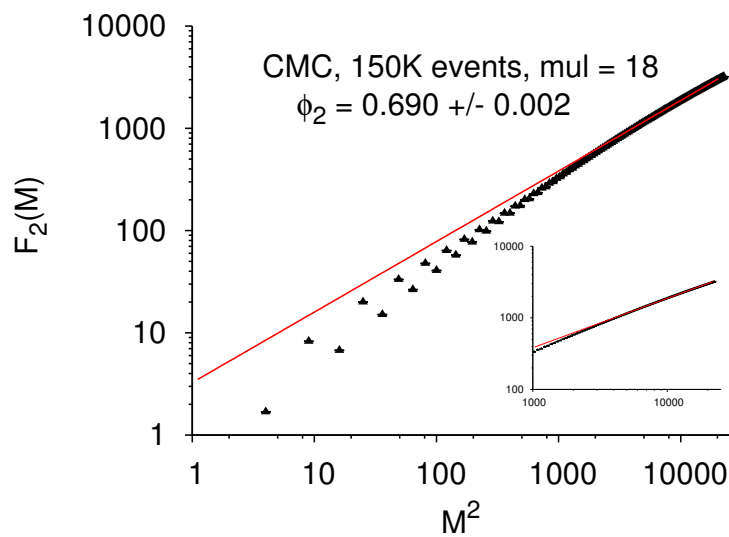


**Figure 4.6:** The SSFM  $F_2(M)$  of transverse  $\sigma$  momenta and the corresponding (fitted) intermittency index  $\phi_2$  ( $M^2 > 6000$ ) for 150,000 events generated by the CMC algorithm.

### 4.6.3 The CMC algorithm for baryons

We have seen how the CMC algorithm can simulate critical  $\sigma$ -clusters at the vicinity of the chiral critical point, assuming that the order parameter of the system is the average multiplicity of  $\sigma$  particles in a cluster, which is proportional to  $\sigma^2(\mathbf{x})$ . Similarly, we can generate baryon clusters by adopting the net baryon number multiplicity, proportional to  $\rho_B(\mathbf{x})$ , as an order parameter. This, according to section 4.3.3, leads to the formation of clusters where the net baryon multiplicity scales according to (4.36), with  $\tilde{d}_F^{(B)} = \frac{2\delta}{\delta+1}$  being the fractal dimension in transverse configuration space. By performing a Fourier transform of the density-density correlation function, as detailed in section 4.4.1, we obtain the corresponding fractal dimension in transverse momentum space,

$$\tilde{d}_F^{(B)} = \frac{D}{\delta+1} = \frac{1}{3}, \quad (4.73)$$

for  $D = 2, \delta = 5$ .

We can adapt the CMC algorithm in order to simulate critical baryon clusters. Several simplifying assumptions are made, compared to “vanilla” CMC:

- We simulate only transverse momentum space, ignoring rapidity.
- We concentrate on protons and ignore anti-protons. This is based on the expectation that proton and anti-proton densities, separately, follow the scaling law (4.36), and that in the experimental data sets we study, anti-proton multiplicity is much lower than proton multiplicity.
- Only one cluster per event is produced, as the Cartesian product of two Lévy walks of  $\tilde{d}_F^{B,1} = 1/6$ , in transverse momentum space. The cluster center position is randomized per event, following a uniform distribution with specified widths in  $p_x, p_y$  (in later versions of the algorithm, an exponential distribution for cluster centers was provisionally tried).
- The proton multiplicity per event is also a plug-in parameter, set to follow specified average and variance values. Since the cluster is produced as the cartesian product of two walks of equal length, the total event multiplicity is always the square of a natural number. Therefore, to achieve the correct multiplicity distribution, we adjust the probabilities for producing multiplicities  $N_p = 1, 4, 9, \dots$  accordingly. A typical proton multiplicity distribution is shown in Fig.4.7.

In summary, the modified CMC algorithm is governed by only 5, empirically adjusted input parameters:

- The lower and upper bounds of 1D Lévy walks in momentum space,  $p_{\min}$  and  $p_{\max}$ .

- The average proton multiplicity  $\langle p \rangle$ , and the corresponding variance  $\Delta\langle p \rangle$ .
- A range  $\Delta p_0$ , so that cluster centers are produced uniformly in  $[-\Delta p_0, \Delta p_0]$ .

The following table summarizes the typical values for the input parameters:

Parameter	$p_{\min}$ (MeV)	$p_{\max}$ (MeV)	$\langle p \rangle$	$\Delta\langle p \rangle$	$\Delta p_0$ (MeV)
Value	0.5	500	3.1	1.6	800

The code implementation for CMC baryon, in Fortran 90, can be found in Appendix B.

The distributions in  $\phi$  and  $p_T$  for the proton CMC algorithm are shown in Fig.4.8a,b. We observe that, due to the use of a cartesian product of 1D walks, the azimuthal angle distribution is not uniform. The two-dimensional distribution  $\rho(p_x, p_y)$  is shown in Fig.4.9. Clearly, the algorithm does a poor job of simulating the cylindrical geometry of a heavy ion collision. However, the scaling properties of the power-law, eq.(4.36) are adequately represented even in this crude adaptation of CMC. This is evident in Fig.4.10, where we have plotted  $F_2(M)$  of CMC-baryon for 150,000 events in transverse momentum space. The estimated intermittency index  $\phi_2 = 0.836(1)$  is in excellent agreement with the theoretically expected value  $\phi_{2,B} = 5/6$ .

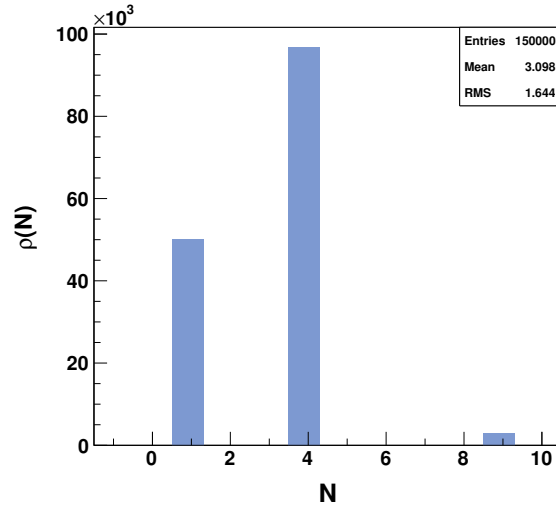


**Figure 4.7:** Proton multiplicity distribution for 150,000 events generated by the baryon-CMC algorithm.

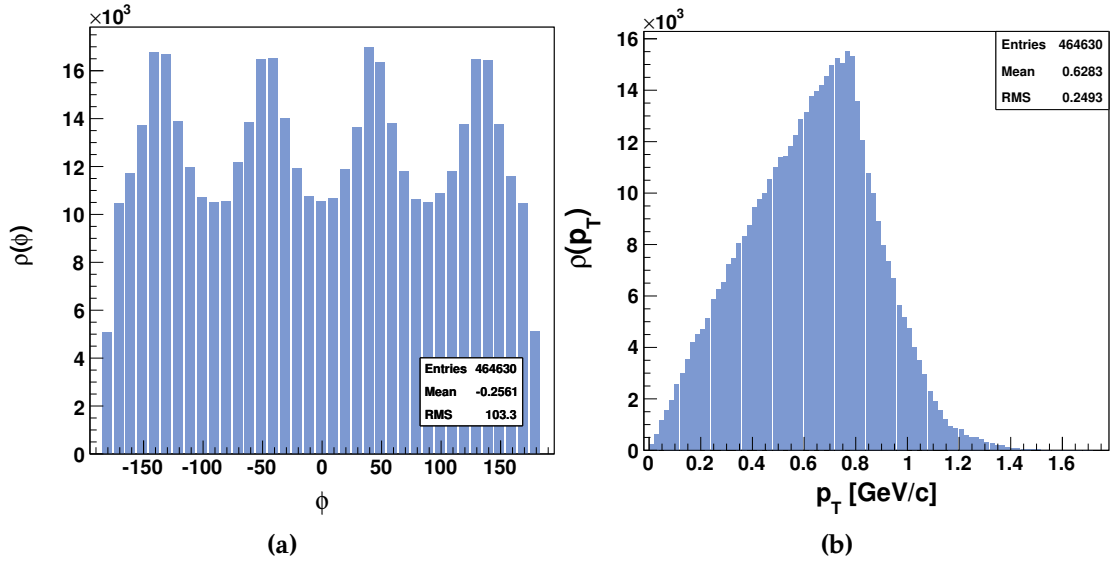


**Figure 4.8:** The distributions of (a)  $\phi$  and (b)  $p_T$  for 150,000 events generated by the baryon-CMC algorithm.

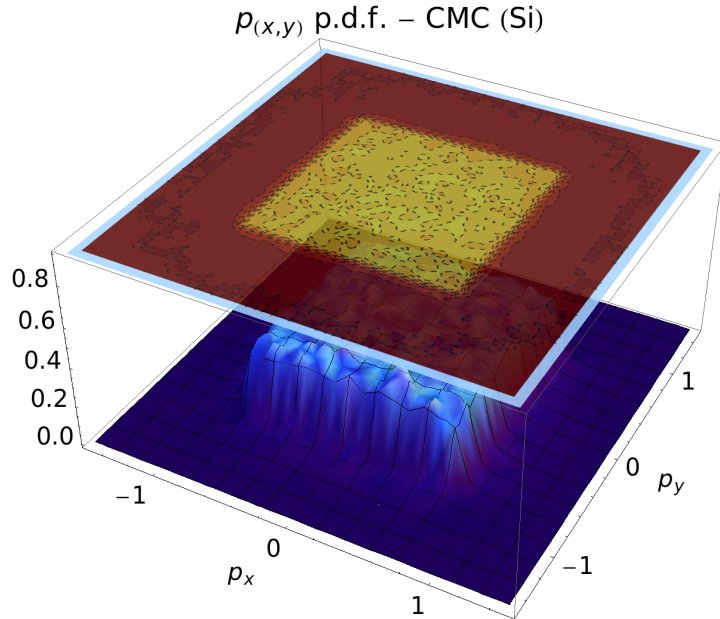


**Figure 4.9:**  $\rho(p_x, p_y)$  one-particle distribution for 150,000 events generated by the baryon-CMC algorithm.

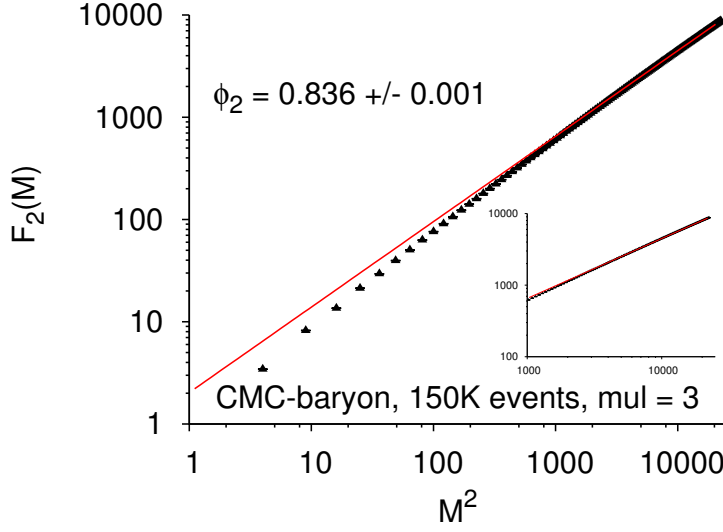


**Figure 4.10:** The SSFM  $F_2(M)$  of transverse proton momenta and the corresponding (fitted) intermittency index  $\phi_2$  ( $M^2 > 6000$ ) for 150,000 events generated by the CMC-baryon algorithm.

## 4.7 The Chiral Condensate as an attractor

The CMC algorithm presented in the previous sections simulates the geometry of  $\sigma$  and baryon clusters that characterize the chiral condensate by means of random Lévy walks. We have seen that the correlation dimension of a sufficiently long Lévy walk can be numerically calculated, and that it is usually a good approximation to the fractal dimension used to construct the walk. However, a typical event produced by the CMC algorithm contains very little structure that is only statistically connected to the fractal dimension of the underlying process. The same is true of any one heavy ion collision event, especially if the multiplicity is low.

Most of the information about fractality lies in the collection of events as a whole; in order to extract it, we must calculate a cumulative statistical quantity at various scales. Such quantities are in fact the Scaled Factorial Moments (SFMs) introduced in section 4.4.2, and in particular the Second Scaled Factorial Moment (SSFM),  $F_2(M)$ , as a function of the number of cells  $M$  in transverse momentum space.

The underlying fractal structure of the chiral condensate can be viewed as a strange attractor, and the points in individual events as sections of orbits that belong to it. In order to illustrate how factorial moment analysis can reveal the structure of the chiral condensate, let us attempt a similar reconstruction of a deterministic fractal of known dimensionality: the *Ikeda map*.

The Ikeda map is a two-dimensional non-linear map defined by the iterative equations

$$\begin{aligned}x_{n+1} &= u(x_n \cos t_n - y_n \sin t_n) + 1 \\y_{n+1} &= u(x_n \sin t_n + y_n \cos t_n)\end{aligned}\tag{4.74}$$

where

$$t_n = a - \frac{b}{1 + x_n^2 + y_n^2}\tag{4.75}$$

For  $u \geq 0.6$ , the system possesses a chaotic attractor, i.e. a set of points to which all orbits converge, provided they start in a (non-zero measure) region, the *basin of attraction*. For our simulation, we choose the set of parameters:

$$a = 0.4 \quad , \quad b = 6.0 \quad , \quad u = 0.9$$

which are well within the chaotic regime. For the above set of parameters, the Ikeda attractor has a fractal mass dimension of approximately:

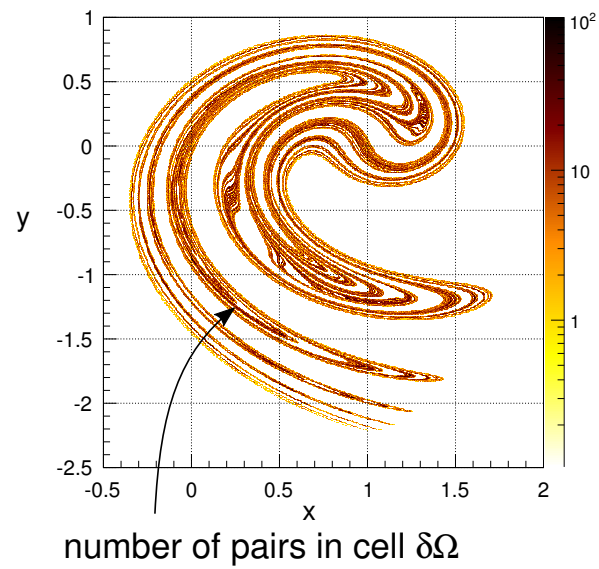
$$d_F^I \simeq 1.7$$

Fig.4.11 shows a density plot of 500,000 points on the Ikeda attractor (after an initial transient). In order to simulate the structure of a set of high energy collision events, we follow a long orbit on the attractor and we collect the set of produced points into events of a given average multiplicity,  $\langle n \rangle = \lambda$ . Event multiplicities follow the poisson distribution. We want to avoid immediate correlations between points within an event, leaving only their correlation as parts of the overall structure of the attractor. To this end, we take a random number of iterative steps between the points we record, which we choose to be a random integer, uniform in the [10, 110] range. This minimum gap of 10 steps is sufficient for the points to “forget” their correlation as parts of a single orbit, a conclusion supported by calculations of the correlation function of the time series of points on an orbit.

We have tried two different groupings of points into events: in the first case, we record 20,000 events of an average multiplicity  $\lambda = 50$ , whereas on the second case we record 200,000 events with a lower average multiplicity  $\lambda = 3$ . The goal is to assess how much information needs to be present in an individual event in order to reconstruct the fractal structure of the attractor.

Consequently, we proceed to calculate the SSFMs  $F_2(M)$  of the produced data sets, as a function of cell size  $\delta\Omega$ . According to the analysis of section 4.4.2, and in particular eq.(4.65) with  $q = 2$ ,  $D = 2$ , the intermittency index  $\phi_2^I$  of the SSFMs on the Ikeda attractor has an expected value of:

$$\phi_2^I = \frac{D - d_F^I}{D} = \frac{2 - 1.7}{2} \simeq 0.15.\tag{4.76}$$



**Figure 4.11:** Density plot of 500,000 points on the Ikeda attractor. Color map illustrates the density of points in various locations on the attractor. In an intermittency analysis, we sample a long orbit and count the number of pairs of points in cells of a given size  $\delta\Omega$ .

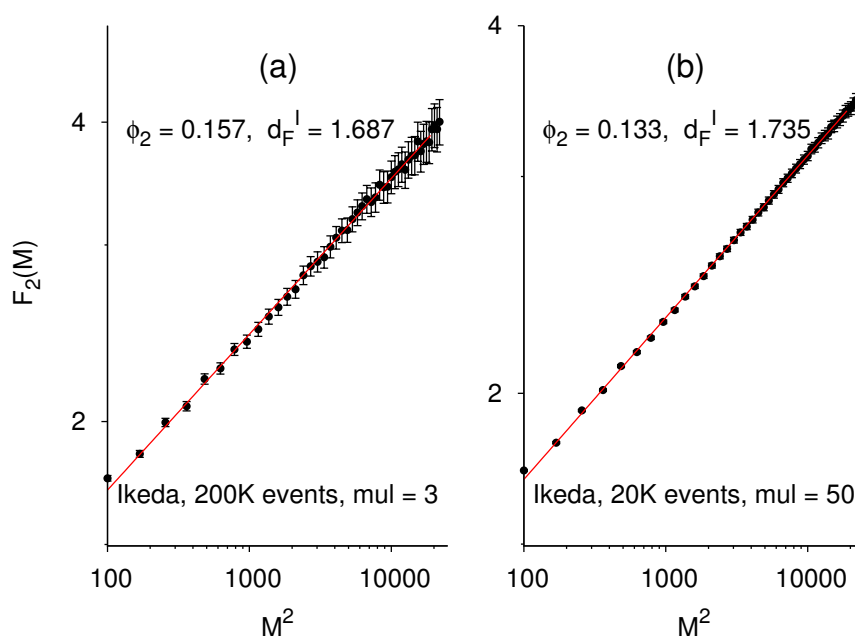


**Figure 4.12:** SSFMs  $F_2(M)$  of (a) 200,000 events with  $\langle n \rangle = 3$ , and (b) 20,000 events with  $\langle n \rangle = 50$  as a function of number of bins  $M$ , on the Ikeda attractor. A log-log fit,  $\log F_2(M) = C + \phi_2^I \cdot \log(M^2)$ , was performed for both cases. The corresponding mass dimension  $d_F^I$  is shown alongside  $\phi_2^I$ .

Fig.4.12 shows the results of the intermittency analysis on the Ikeda attractor. We observe that in both cases the log-log plot shows excellent linearity. Statistical errors are larger for the  $\langle n \rangle = 3$  set, although the statistics (number of events) is ten times larger than in the  $\langle n \rangle = 50$  case. On the other hand, the small multiplicity set has an intermittency index closer to the theoretically expected value of  $\phi_2^I = 0.15$ .

Both sets give an intermittency index value within 10% of the theoretically expected. We conclude that the reconstruction of a fractal attractor through factorial moment analysis is feasible. By extension, the fractal geometry of the chiral condensate is accessible by intermittency analysis, to the extent that it can be approximated by a monofractal in transverse momentum space.



## CHAPTER 5

# ANALYSIS OF NA49 EXPERIMENT DATA SETS

### 5.1 Introduction

As we have already mentioned, the chiral condensate,  $\langle \bar{q}q \rangle$ , is the order parameter of the chiral phase transition. Therefore, finding suitable observables [Stephanov et al., 1998, 1999; Stephanov, 2009; Fujii, 2003; Gazdzicki et al., 2011; Antoniou et al., 2001, 2005, 2006] that are connected to its fluctuations is essential in order to detect the QCD critical point (CP) in heavy ion collision experiments. The quantum state carrying the quantum numbers as well as the critical properties of the chiral condensate is the isoscalar  $\sigma$ -field,  $\sigma(x)$ . In a heavy ion collision experiment, it is possible for the vacuum state fluctuations that lead to chiral condensate formation to occur, however the latter is unstable and will decay mainly into pions, at time scales characteristic of the strong interaction. The critical properties of the condensate are transferred to detectable pion pairs,  $\pi^+\pi^-$ , with invariant mass just above their production threshold [Antoniou et al., 2005].

In a finite-density medium, there is also a coupling between the chiral condensate and the net baryon density, that induces critical fluctuations in the latter [Fukushima and Hatsuda, 2011; Gavin, 1999; Antoniou et al., 2000, 2010; Hatta and Ikeda, 2003; Stephanov, 2004, 2005]. Specifically, the critical fluctuations of the chiral condensate are transferred to the net proton density, as well as the densities of protons and anti-protons separately, through the coupling of protons with the isospin-zero  $\sigma$ -field [Hatta and Stephanov, 2003]. Thus, detecting the QCD CP through observing fluctuations in the proton density is a very promising strategy.

In the present chapter, we describe the data extraction and analysis of proton density fluctuations in experimental data sets acquired in the NA49 heavy ion collision experiment (CERN SPS). By the application of suitable cuts, we select the most central events (low % centrality = small impact parameter), and subsequently we identify those tracks, in momentum space, which to a high confidence level, belong to protons produced dur-

ing collision. Special care is taken during the particle identification of protons among other particles produced during the collision. Subsequently, we proceed to calculate the factorial moments of selected tracks in transverse momentum space and check for critical signatures in the results.

## 5.2 A brief overview of the NA49 experiment

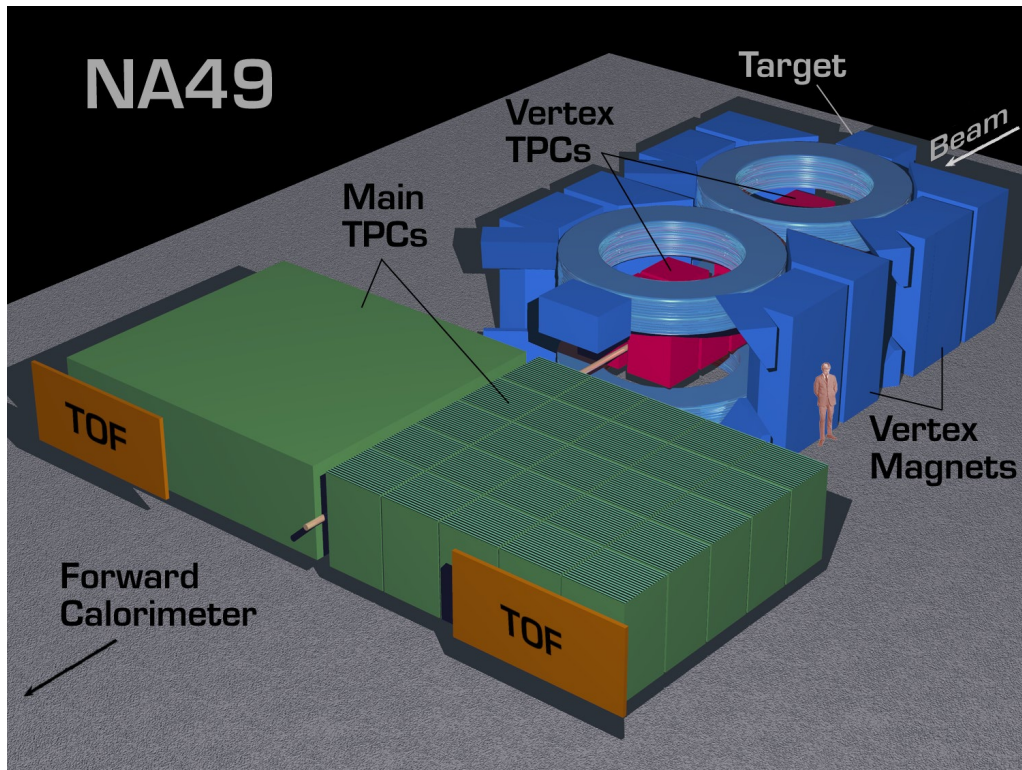


**Figure 5.1:** A schematic representation of the hadronic detector of the NA49 experiment (SPS CERN).

The NA49 experiment is a fixed-target, heavy ion collision experiment at CERN SPS, focusing on the study of charged hadrons and neutral strange particles, in search for the QCD deconfinement transition and the QCD critical point. A schematic representation of its main hadronic detector is shown in Fig.(5.1).

The overall experimental setup of NA49 is shown in Fig.(5.2), along with the possible alternative arrangements for different beam and target definitions [Afanasiev et al., 1999]. The main detectors are four large-volume time projection chambers (TPC's).

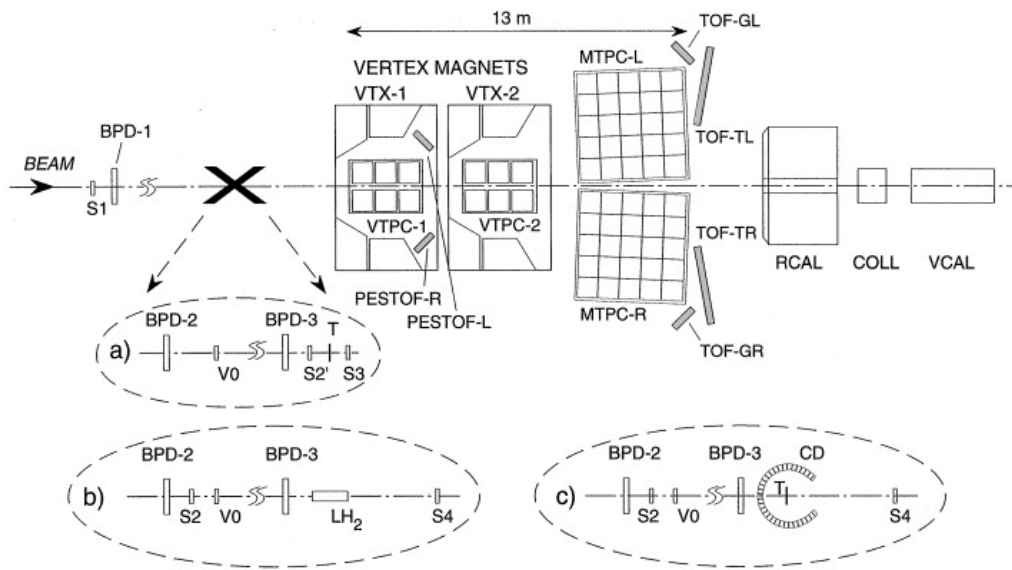


**Figure 5.2:** Set-up (not to scale) of NA49 experiment with different beam definitions and target arrangements for (a) Pb+Pb, (b) p+p and (c) p+A collisions. The target position is at the front face of the first Vertex Magnet (VTX-1). Figure by [Afanasiev et al., 1999].

Of these, the two vertex TPC's (VTPC-1, VTPC-2) are located just behind the target T, within the magnetic field of two superconducting dipole magnets, allowing for separation of positively and negatively charged tracks, as well as measuring particle momenta. The two remaining TPC's (MTPC-L, MTPC-R), positioned behind the magnets at either side of the beam, are optimized for precise measurement of ionizing energy loss  $dE/dx$ , used for particle identification. Additionally, four time of flight (TOF) scintillator detector arrays are placed behind the MTPC's in groups of two. These provide supplementary information on particle mass, used for particle identification. The Ring Calorimeter (RCAL), placed 18m behind the target, after the MTPC's, was initially installed for the NA5 SPS experiment. It is used to measure neutral particle production in the projectile hemisphere in p+p and p+A collisions. In Pb+Pb collisions, it provides information on transverse energy production rates and event anisotropy. The veto calorimeter (VCAL) determines the centrality of collisions by measuring the energy deposited by projectile spectators. The calorimeter is placed behind a collimator (COLL) which adjust the geometrical acceptance of VCAL so that only spectators reach it. Finally, three beam position detectors (BPD-1, BPD-2, and BPD-3) are used to measure the  $x$  and  $y$  coordinates of each beam particle at the target. Alternatively, the primary vertex position can be reconstructed as the common point of intersection of all reconstructed tracks. An extensive description of the NA49 experimental setup and tracking software can be found in [Afanasiev et al., 1999].

### 5.3 The analysed data sets of the NA49 experiment

The analysed data sets were recorded during the NA49 heavy ion collision experiment (A+A collisions). Most sets were acquired at the maximum CERN SPS energy, of  $158A$  GeV ( $\sqrt{s_{NN}} = 17.3$  GeV), with the exception of a Pb+Pb dataset at  $40A$  GeV ( $\sqrt{s_{NN}} = 8.8$  GeV). For the analysis we used the most central collisions (12%, 12%, 10%) of carbon ("C"), silicon ("Si") and lead (Pb) nuclei, on C (2.4% interaction length), Si (4.4%) and Pb (1%) targets, respectively. The "C" beam as defined by the online trigger and offline selection was a mixture of ions with charge  $Z = 6$  and  $7$  (intensity ratio 69:31); the "Si" beam of ions with  $Z = 13, 14$  and  $15$  (intensity ratio 35:41:24) [Anticic et al., 2011a]. The event statistics amounted to 150k events for "C"+C, 166k events for "Si"+Si, and 330k events for Pb+Pb (after appropriate cuts). We also analysed a 200k Pb+Pb high-intensity dataset ( $158A$  GeV), subsequently rejected due to ambiguities in the intermittency analysis, as well as 360k of the 12.5% most central Pb+Pb events at  $\sqrt{s_{NN}} = 8.8$  GeV<sup>1</sup>. A summary of the analysed data sets is given in Table 5.1. A detailed list of cuts is given in Appendix C.

---

<sup>1</sup>In the case of the "C" and "Si" systems, statistics at  $\sqrt{s_{NN}} = 8.8$  GeV were insufficient for the purposes of an intermittency analysis.

### 5.3.1 Event & track selection cuts

Event and track selection cuts were based on the standard cuts used in the NA49 experiment, as detailed in Anticic et al. [2011b].

Specifically, event selection included cuts on the ion components of the beam (in the case of “C” and “Si”). Each beam component provided us with a separate data set. Throughout the analysis, we found little variation in the overall profiles of individual components within each beam. In order to enhance statistics, we merged all components in one final set per beam. Additionally, we applied cuts on the quality and position of the reconstructed primary vertex of tracks in the selected events.

The final selection of tracks in each event also included quality checks: we required a minimum number of reconstructed points on each track, as well as a maximum impact parameter for each reconstructed track. It was also necessary to minimize the number of possible *split tracks* that may contaminate the data: fragments of a track mistakenly identified as two separate tracks of very similar momenta. In order to exclude such tracks, we have only accepted tracks for which the ratio of number of measured points to estimated maximum number of points in the TPCs exceeds 55%. It is nevertheless possible that some split tracks remain after the cuts. In the following, we discuss methods of dealing with such tracks.

We also applied a cut on the total momenta  $p_{tot}$  of candidate protons (via a  $dE/dx$  cut, detailed in the next section). Finally, we restricted our analysis in the mid-rapidity region, since it is established that the density of the fireball formed during collision is approximately constant in rapidity in this phase space region [Antoniou et al., 2006].

### 5.3.2 Proton identification via $dE/dx$

Proton identification [Anticic et al., 2011b] was performed via the measurement of particle energy loss  $dE/dx$  in the gas of the time projection chambers. The inclusive  $dE/dx$  distribution for positively charged particles in each reaction was fitted in 10 bands of momentum  $p$  to a sum of contributions  $f^\alpha(dE/dx, p)$  from different particle species  $\alpha$  with  $\alpha = \pi, K, p, e$ . The probability  $P$  for a track with energy loss  $x_i$  and momentum  $p_i$  of being a proton is then given by:

$$P = f^p(x_i, p_i) / (f^\pi(x_i, p_i) + f^K(x_i, p_i) + f^p(x_i, p_i) + f^e(x_i, p_i)) \quad (5.1)$$

The value of  $P$  for proton candidates had to exceed 80% for the “C”+C and “Si”+Si systems and 90% for Pb+Pb, where event multiplicities are higher and permit higher purity.

### 5.3.3 The $q_{inv}$ correlation function

In order to study the critical fluctuations of proton density in transverse momentum space, it is first necessary to remove non-critical contributions to the proton-proton density correlation function. These include: (a) a statistical background of dynamically uncorrelated protons, (b) the possible presence of split or merged tracks, and (c) unwanted proton-proton correlations due to Coulomb repulsion and Fermi-Dirac statistics. (a) is taken care of by the subtraction of mixed events. However, (b) and (c) require us to study the distribution of the relative four-momenta of proton pairs:

$$q_{inv} = \frac{1}{2} \sqrt{-(p_1 - p_2)^2} \quad (5.2)$$

where  $p_1, p_2$  are all the possible combinations of proton 4-momenta in our final track & event selection. The associated correlation function  $C(q_{inv})$  is the ratio of true to mixed event pairs for all studied systems.

The  $q_{inv}$  correlation function is expected from theoretical predictions [Koonin, 1977] to develop a dip in the low  $q_{inv}$  region due to Fermi-Dirac statistics and Coulomb repulsion, followed by a maximum around 20 MeV/c which should become more pronounced with decreasing size of the colliding nuclei.

In Fig.5.3 are shown the correlation functions  $C(q_{inv})$  for all studied systems, in the range  $q_{inv} \in [0, 120] \text{ MeV}/c$ . It is clear that, while the profiles of “C”+C, “Si”+Si and low-intensity Pb+Pb sets agree with the theoretical predictions, the high-intensity Pb+Pb data set exhibits an anomalous  $C(q_{inv})$  peak at very low  $q_{inv}$ . This is an indication of possible contamination of the set by merged/split tracks, which could seriously compromise the intermittency analysis.

If the anomalous Pb+Pb peak is due to split/merged tracks, it can be treated by application of a lower cutoff on the track pair distance at the mid-plane of the MTPC, for both data and mixed event pairs, as described in [Appelshauser et al., 1999]. In Fig.5.4, the  $C(q_{inv})$  distribution for high-intensity Pb+Pb is shown, before and after a 2 cm cut in pair distance. The cut disposes of the anomalous peak. However, information on track distance was not available for all studied datasets, and there could be other possible causes of the anomalous peak in Pb+Pb. For this reason, we have refrained from drawing definite conclusions from intermittency analysis of the high-intensity Pb+Pb dataset, focusing instead on the low-intensity Pb+Pb dataset.

Furthermore, based on the profiles of Fig.5.3, we have imposed an additional  $q_{inv} \geq 25 \text{ MeV}/c$  cutoff to all 3 data sets, throughout the intermittency analysis that follows. This should have the effect of removing unwanted non-critical correlations. The uniform application of the cutoff also allows us to better compare intermittency results in all studied systems.

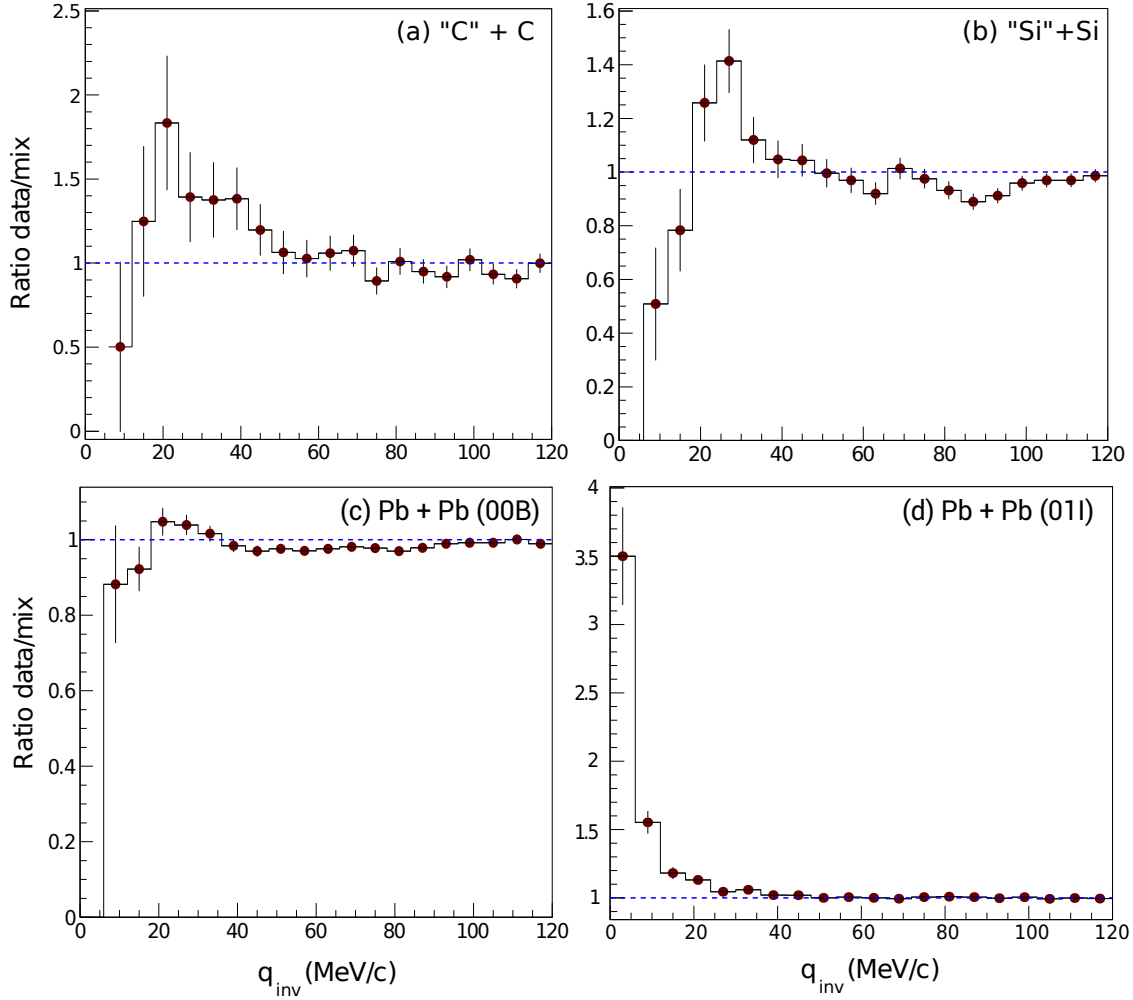


**Figure 5.3:** The  $C(q_{inv})$  correlation function of proton pairs (ratio of pairs from real and mixed events) at midrapidity ( $-0.75 < y_{CM} < 0.75$ ) for the most central collisions of (a) "C"+C (centrality 12%), (b) "Si"+Si (centrality 12%), (c) low-intensity Pb+Pb (centrality 10%) and (d) high-intensity Pb+Pb (centrality 12%) at  $\sqrt{s_{NN}} = 17.3$  GeV.

A	“C”+C	“Si”+Si	Pb+Pb (01I)	Pb+Pb (00B)	Pb+Pb (00W)
# Bootstrap Samples	1000				
Rapidity range	$-0.75 \leq y_{CM} \leq 0.75$				
# lattice positions	11 ( $2 \times 5$ + central)				
Lattice range (GeV)	$[-1.529, 1.471] \rightarrow [-1.471, 1.529]$				
Beam Energy	158 A GeV			40 A GeV	
$\sqrt{s_{NN}}$	17.3 GeV			8.8 GeV	
Centrality range	0 $\rightarrow$ 12%		0 $\rightarrow$ 10%		0 $\rightarrow$ 7%
# events	148 060	165 941	200 758	329 789	359 397
$\langle p_{data} \rangle$ (after cuts)	$1.6 \pm 0.9$	$3.1 \pm 1.7$	$10.8 \pm 3.7$	$9.12 \pm 3.15$	$12.0 \pm 3.5$

**Table 5.1:** Summary of the analysed data sets of the NA49 experiment. In the case of C and Si, beams were a mixture of multiple constituent ions: “C” = C,N , “Si”+Si = Si,Al,P, whereas we have merged components per beam in order to improve statistics, since we have found little differentiation in their profiles. Average event multiplicities,  $\langle p_{data} \rangle$ , refer to protons.

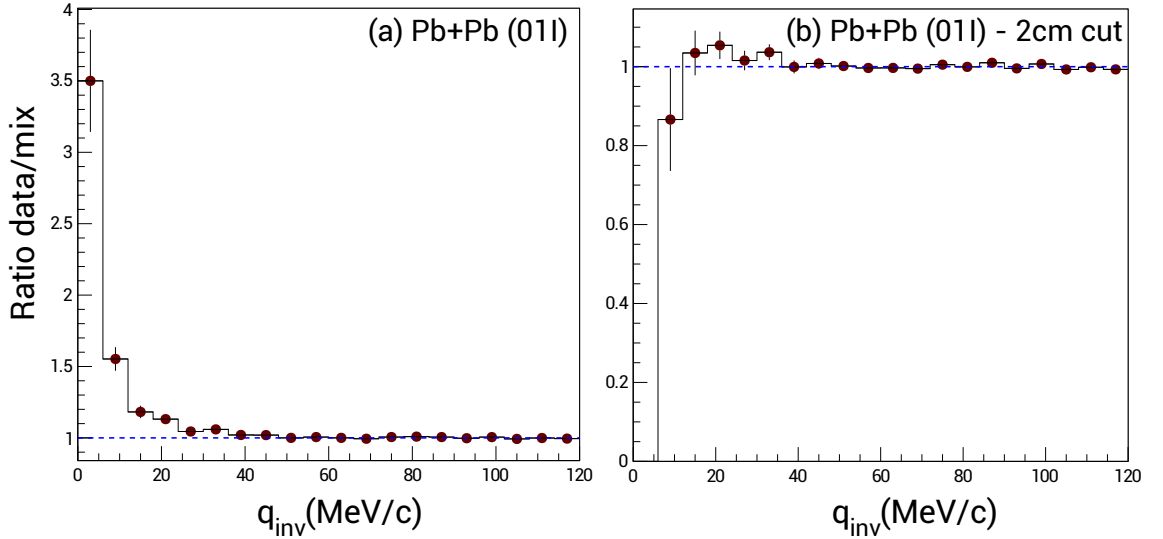


**Figure 5.4:** The  $C(q_{inv})$  correlation function of proton pairs (ratio of pairs from real and mixed events) at midrapidity ( $-0.75 < y_{CM} < 0.75$ ) for the most central collisions of high-intensity Pb+Pb (centrality 12%) at  $\sqrt{s_{NN}} = 17.3$  GeV, (a) before and (b) after applying a 2cm pair distance cut in the mid-plane of MTPC.

### 5.3.4 The $\Delta p_T$ correlation function

Before we proceed with the intermittency analysis of the NA49 experimental data sets, it would be interesting to examine more evidence of the presence of significant correlations among protons in transverse momentum space. The  $q_{inv}$  distribution reveals correlations between tracks in 4D-momentum space, which is not enough to guarantee strong correlations in  $p_T$ . We therefore look for strongly correlated pairs of protons in the low relative  $p_T$  region, i.e. for proton tracks that are close in transverse momentum space. To this end, we calculate the distribution in  $\Delta p_T$ :

$$\Delta p_T \equiv \frac{1}{2} \sqrt{(p_{X_1} - p_{X_2})^2 + (p_{Y_1} - p_{Y_2})^2}, \quad (5.3)$$

i.e. the difference in  $p_T$  of protons in the pairs, as well as the associated correlation function. The results of the calculation are shown in Fig.5.5, where we also plotted the  $\Delta p_T$  distribution for a simulated CMC data set corresponding to a critical system mixed with 99% random proton tracks (see section 5.5.2). We see from Fig.5.5 that “C”+C and Pb+Pb data sets do not exhibit significant correlations in the low  $\Delta p_T$  region, whereas “Si”+Si shows a peak at low  $\Delta p_T$ , which is comparable to the behaviour of the simulated CMC dataset. The peak in low  $p_T$  in “Si”+Si and CMC is evidence of a singularity in  $p_T \rightarrow 0$ , which further strengthens the claim that the “Si”+Si freeze-out occurs close to the chiral critical point in the QCD phase diagram.

## 5.4 Analysis of proton transverse momenta

### 5.4.1 Scaled factorial moments as a technique for probing the density-density correlation function

We saw in 4.4.2 that the scaled factorial moments can provide us with valuable information about the presence of critical fluctuations in a data set. In particular, if the density-density correlation function exhibits a power-law scaling, the corresponding factorial moments will show intermittent behaviour, i.e. they will also follow a power-law with regards to cell size  $\delta\Omega$ ; the power-law exponent, called the intermittency index, is related to the fractal dimension of the set via eq.(4.65). Thus, intermittency provides us with a “signature” of criticality.

Specifically, in our analysis we use the Second Scaled Factorial Moments (SSFMs) in transverse momentum space, which give the distribution of pairs of particles at different momentum scales. We work with horizontal factorial moments; therefore our method is not sensitive to local fluctuations within a cell, since we average over cells, but only to fluctuations of the one-particle distribution function, and to scaling. In the case of

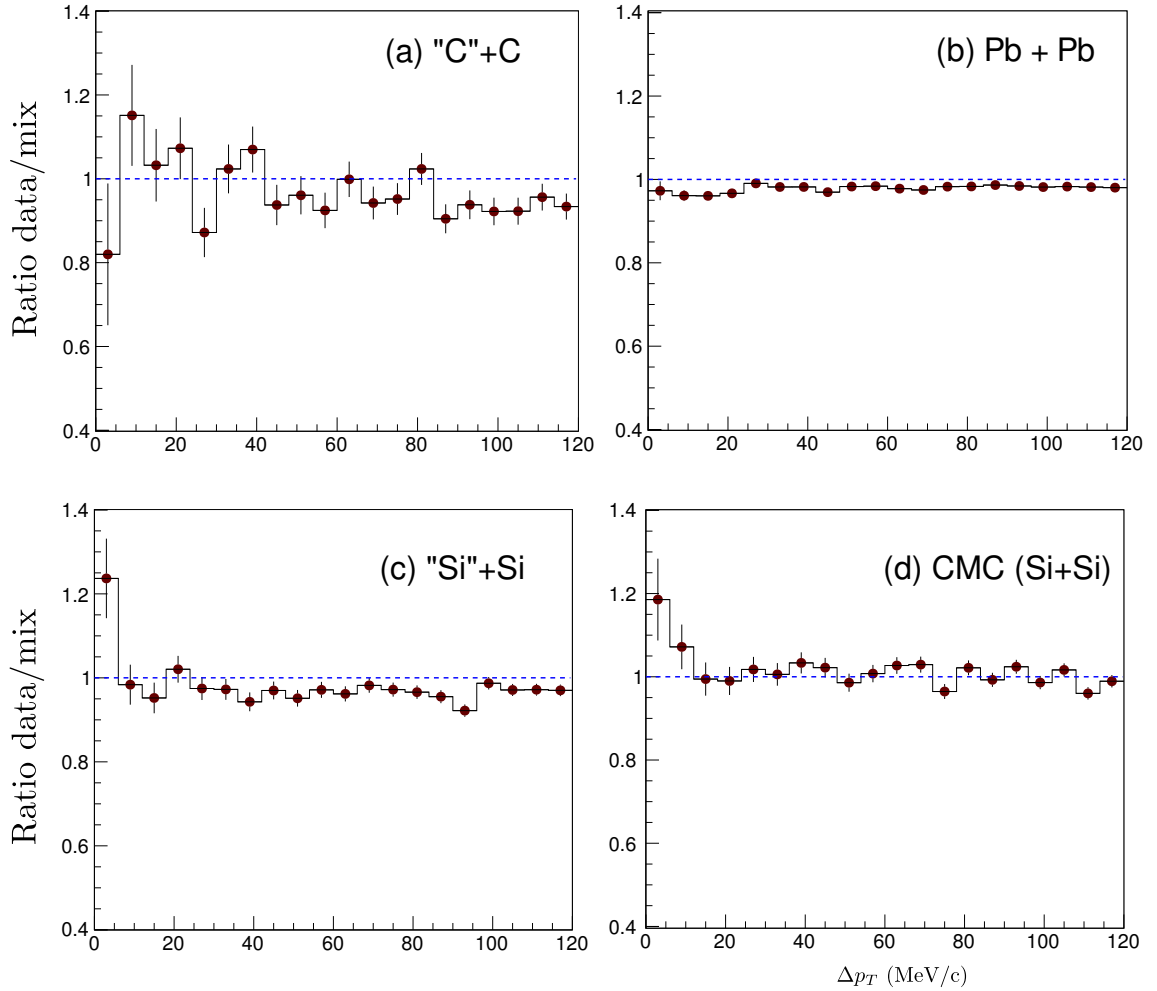


**Figure 5.5:** The  $C(\Delta p_T)$  correlation function of proton pairs (ratio of pairs from real and mixed events) at midrapidity ( $0.75 < y_{CM} < 0.75$ ) for the most central collisions of (a) "C"+C (centrality 12%), (b) low-intensity Pb+Pb (centrality 10%), (c) "Si"+Si (centrality 12%), at  $\sqrt{s_{NN}} = 17.3$  GeV, as well as for (d) CMC simulated Si+Si events (99% noise).

limited statistics, however, and especially for low multiplicity events, arbitrary positioning of cell borders can distort the profile of correlations. In the following sections, we describe in detail a method of coping with this issue.

If we set  $q = 2$ ,  $D = 2$  in (4.56), we get the SSFMs:

$$F_2^H(M) = \frac{\left\langle \frac{1}{M^2} \sum_{m=1}^{M^2} n_m (n_m - 1) \right\rangle}{\left\langle \frac{1}{M^2} \sum_{m=1}^{M^2} n_m \right\rangle^2} \quad (5.4)$$

If there is scale-invariance, as is the case for a critical system, then the factorial moments  $F_2(M)$  for  $M \gg 1$  should follow a power-law as a function of cell size:

$$F_2(M) \propto (M^2)^{\phi_2} \quad (5.5)$$

where the intermittency index  $\phi_2$  is related to the power-law exponent of the density-density correlation function via (4.61). In the case we examine, of baryonic fluctuations in a critical system which freezes out exactly at the chiral critical point,  $\kappa = \kappa_B = \delta + 1 = 6$ , and therefore  $\phi_{2,cr} = \frac{5}{6}$ , as determined by the universality class that governs the critical properties of QCD [Antoniou, Diakonov, Kapoyannis, and Kousouris, 2006].

### 5.4.2 Background subtraction – Mixed events

Eq.(5.5) for  $F_2(M)$  scaling is only valid in the case of a pure critical system. In an actual experiment, however, even assuming the freeze-out of the system occurs right at the critical point, events will always be contaminated by a background of non-critical protons coming from various processes, alongside critical tracks, as well as, unavoidably, particles falsely identified as protons. The presence of this background will result in the distortion of the profile of factorial moments, leading to a modification of  $\phi_2$  values and/or deterioration of power-law behavior, (eq. 5.5) [Antoniou et al., 2005; Anticic et al., 2010].

In order to recover the power-law behavior, we first of all make the assumption that multiplicities in each cell can be divided into background and critical contributions,  $n = n_b + n_c$ . We can then reformulate the numerator in eq.(5.4) as:

$$\langle n(n-1) \rangle = \langle n_c(n_c-1) \rangle + \langle n_b(n_b-1) \rangle + 2\langle n_b n_c \rangle \quad (5.6)$$

where the term  $\langle n_c(n_c-1) \rangle$  corresponds to the average number of critical pairs,  $\langle n_b(n_b-1) \rangle$  are the background pairs and  $\langle n_b n_c \rangle$  is a mixed term. (For brevity, we omit the sum over cells and the cell index – they are implied by the brackets,  $\langle \dots \rangle$ ). The mixed term in

eq.(5.6) vanishes when  $\langle n_b \rangle \rightarrow 0$  or  $\langle n_c \rangle \rightarrow 0$ , since the corresponding joint probability acquires a  $\delta$ -function singularity in the limiting cases. We can thus quite generally express the mixed term in eq.(5.6) as  $\langle n_b n_c \rangle = \langle n_b \rangle \langle n_c \rangle f_{bc}$ , where  $f_{bc}$  is a finite quantity. In general,  $f_{bc}$  cannot be further determined. Dividing both sides of eq.(5.6) by  $\langle n \rangle^2$  (which is proportional to  $(M^2)^{-2}$  for large  $M$ ), we obtain:

$$\Delta F_2(M) = F_2^{(d)}(M) - \lambda(M)^2 F_2^{(b)}(M) - 2\lambda(M)(1 - \lambda(M)) f_{bc} \quad (5.7)$$

The correlator,  $\Delta F_2(M) = \langle n_c(n_c - 1) \rangle / \langle n \rangle^2$  contains the critical contribution. The right hand side of eq. (5.7),  $F_2^{(d)}(M)$  is the SSFM of the original data set,  $\lambda(M) = \langle n_b \rangle / \langle n \rangle$  is a measure of contamination by non-critical protons and  $F_2^{(b)}(M) = \langle n_b(n_b - 1) \rangle / \langle n_b \rangle^2$  is the SSFM of the background. Note that for  $M \gg 1$  the ratio  $\lambda$  becomes almost independent of  $M$  and can be identified as the fraction of non-critical protons in the considered ensemble. By construction, the correlator  $\Delta F_2(M)$  possesses the same  $M^2$  dependence as the SSFM of the critical component ( $\Delta F_2(M) \sim M^{2\phi_{2,cr}}$ ) of the data for  $M \gg 1$ , since the background contribution to the two-particle correlations is removed.

Two special cases of Eq.(5.7) merit discussion:

1. When the background dominates, i.e. when  $\lambda \lesssim 1$ , we can neglect the third term in Eq.(5.7), which is equivalent to omitting the cross-term in Eq.(5.6). The theoretical justification of this approach is non-trivial. It is however empirically justified by simulations employing the CMC model, discussed in Chapter 4. In section 5.5, where we compare CMC results for protons with experimental data, the validity of this approach will be further clarified.
2. When the freeze-out of the considered system occurs very close to the chiral critical point, one expects the background contribution to become very small, so that  $\lambda \gtrsim 0$  for  $M \gg 1$  and the correlator  $\Delta F_2(M)$  practically coincides with  $F_2^{(d)}(M)$ .

By comparing the level  $F_2^{(d)}(M)$  of the SSFM of the original data with that of CMC simulated data which have been contaminated with random background at various levels (see section 5.5), we conclude (as will become apparent) that  $\lambda \geq 0.98$ , meaning that the first of the above mentioned cases holds at a very good approximation – the background dominates.

We can therefore apply the technique of producing mixed events from the original data set in order to simulate the background and estimate  $F_2^{(b)}(M)$  in Eq.(5.7), assuming that the background consists of uncorrelated particles in transverse momentum space.

The mixed events technique consists in randomly combining tracks originating from different events in the original data set. All tracks have equal probability of being selected, the only constraint being that no two particles coming from the same original

event can be placed in the same mixed event. Therefore, mixed events exclude by construction all dynamical correlations between tracks, leaving only random correlations (however, they make no distinction between *critical* and *non-critical* correlations). By construction, mixed event multiplicities are identical to the initial set multiplicities,  $\langle n \rangle_{mixed} = \langle n \rangle$ . Moreover,  $F_2^{(m)}(M) \simeq F_2^{(b)}(M)$ , since we use scaled factorial moments.

In conclusion we approximate, from here on, the correlator as the difference of the SSFMs of the original data set and the estimated SSFMs of the mixed events:

$$\Delta F_2^{(e)}(M) \simeq F_2^{(d)}(M) - F_2^{(m)}(M) \quad (5.8)$$

Finally, we have found that in order to have a satisfactory statistical convergence in the mixed event moments, we need far greater statistics (typically, 10-fold) compared to the original data. This is a computationally intractable approach. For this reason, we have developed a technique for analytically calculating an estimator of  $F_2^{(m)}(M)$  from the one-particle p.d.f.s of transverse momenta in the original data set in phase space cells (higher-order distributions, e.g. of pairs, are not needed in this calculation, since we have eliminated correlations by construction in the mixed events). A detailed working-out of the calculations is presented in Appendix A.

### 5.4.3 Statistical fluctuation handling – Lattice averaging and Bootstrapping

As we have already mentioned, the limited statistics of some of our data sets, as well as the small event multiplicity and the presence of noise in the data encumber the statistical analysis of factorial moments and make it error prone and vulnerable to spurious correlations. It is therefore essential firstly, to have a reliable estimate of the statistical fluctuations and errors involved in our calculations and secondly, to minimize or eliminate if possible the various sources of systematic error.

We calculate the SSFMs of proton transverse momenta in a lattice of cells within a domain  $\mathcal{D} = [-p_{x,max}, p_{x,max}] \otimes [-p_{y,max}, p_{y,max}]$ , where  $p_{x,max} = p_{y,max} = 1.5 \text{ GeV}/c$ . The plane  $(p_x, p_y)$  is perpendicular to the beam direction. This domain in momentum space is partitioned in  $M = 1 \dots 150$  cells per  $p_T$  direction. This upper (lower) bound in cell number (size) is imposed by the experimental resolution  $\delta p_T \gtrsim 5 \text{ MeV}/c$  [Toy, 1997]. For  $M_{max} = 150$ , minimum cell size is  $20 \text{ MeV}/c$ , well above the experimental resolution.

In a typical intermittency analysis, the lattice position remains fixed, and the number of subdivisions (cells) is the only adjustable parameter. Cell boundary lines are therefore arbitrary, which can result in the occasional splitting of pairs of points at distances smaller than the bin size. This can lead to artificial bin-to-bin fluctuations of the distribution of pairs, a serious effect, especially when the mean multiplicity of events is small (Fig. 5.6).

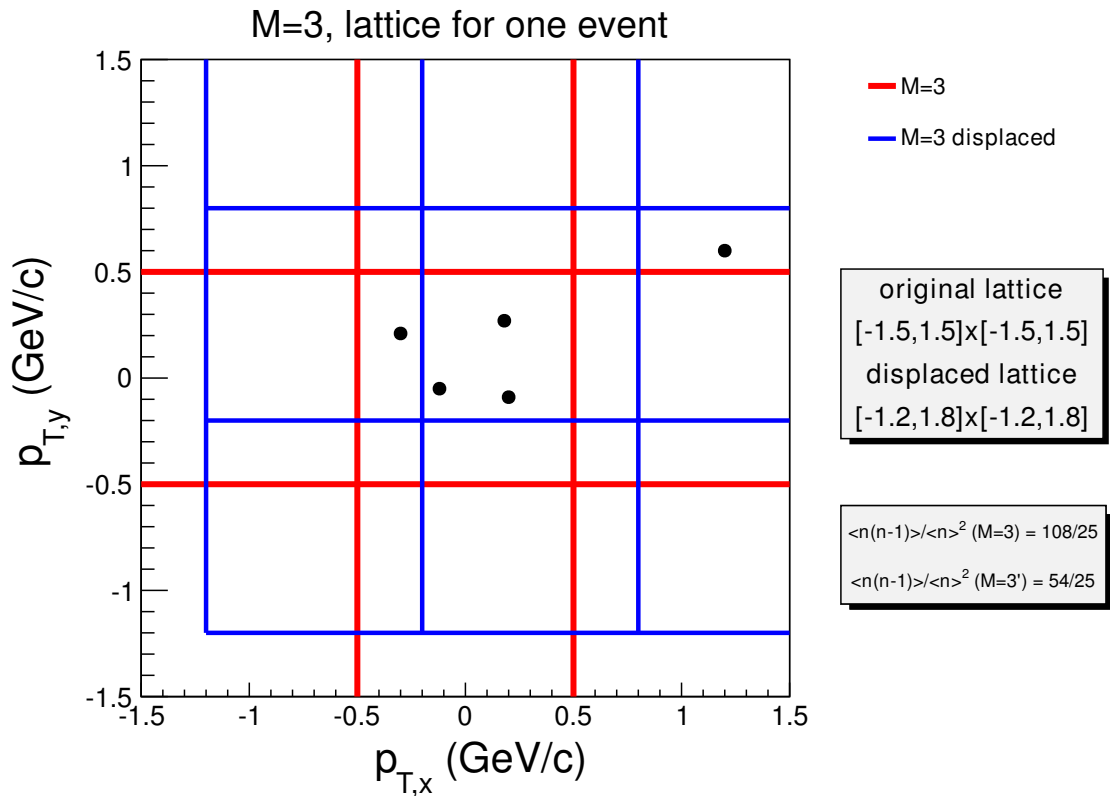


**Figure 5.6:** The effect of lattice displacement on the calculated SSFM value of one event. Points at distances smaller than the bin size can be split apart or grouped together, depending on the (arbitrary) lattice boundary positioning. Averaging over several displaced lattice positions compensates for that effect.

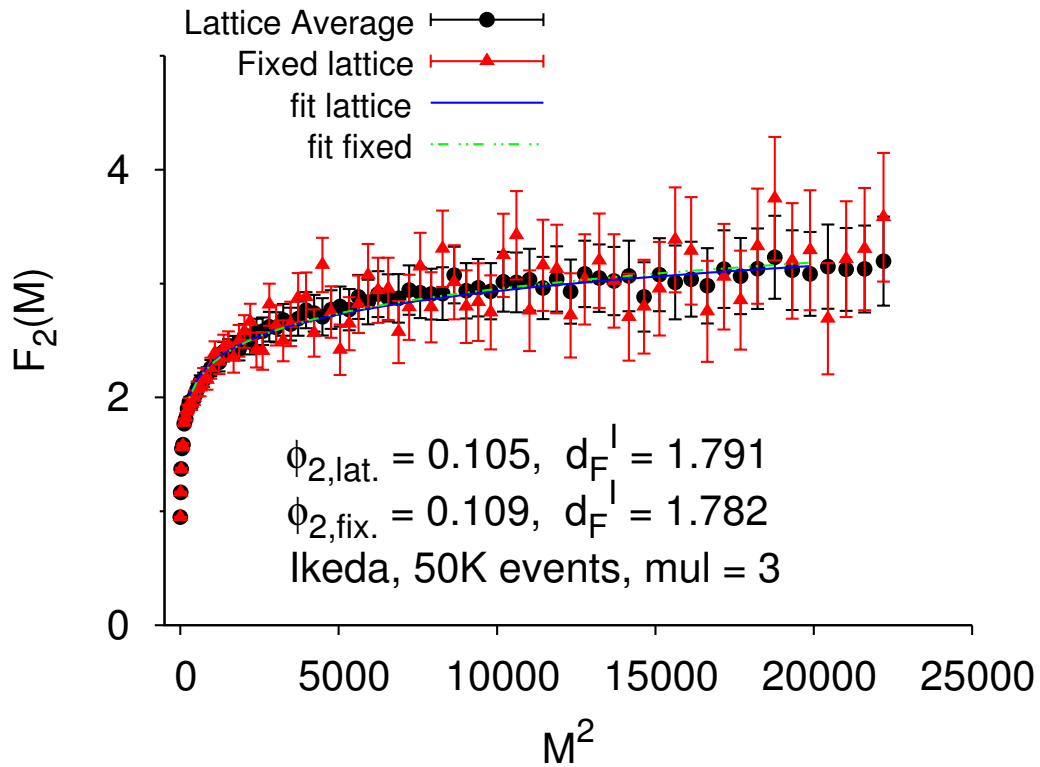


**Figure 5.7:** SSFMs  $F_2(M)$  of 50,000 events with  $\langle n \rangle = 3$  as a function of number of bins  $M$ , on the Ikeda attractor. The black circles (red triangles) correspond to lattice averaged (fixed lattice) moments. The solid blue (dashed green) line represents a log-log power-law fit to the lattice averaged (fixed lattice) set of moments.

In order to compensate for this effect, we have developed the lattice averaging technique. Factorial moments are calculated for several, slightly displaced, positions of the whole lattice, followed by averaging of SSFMs over all lattice positions; thus we obtain a lattice averaged  $\Delta F_2(M)$  value. Maximum lattice displacement is  $\pm 30 \text{ MeV}/c$ . This process leads to significant smoothing of  $\overline{\Delta F_2(M)}$ . Moreover, the variance  $\sigma\left(\Delta F_2^{(\ell)}(M)\right)$  with respect to lattice positions provides us with an estimate of the statistical uncertainties of  $\Delta F_2(M)$ .

The effect of lattice averaging on SSFM calculation is further illustrated in Fig.5.7, where once again we use the Ikeda attractor as a gauging tool for intermittency analysis. The SSFMs of 50,000 low-multiplicity events have been calculated with and without the use of lattice averaging. It can be seen that lattice average has little effect on the fitted intermittency index value  $\phi_2$ ; its main effect lies in the smoothing of moments, which in the lattice averaged set are more closely clustered around their mean value, per  $M$ .

An additional source of fluctuations, qualitatively different from lattice position, arises from statistical fluctuations of factorial moments between different data sets. In a critical condensate simulation (see Ch.4), such fluctuations can be estimated via production and analysis of multiple data sets, followed by calculating a suitable measure of dispersion (standard deviation, confidence interval, etc.). Instead, in the analysis of real experimental data, where we only have one data set at our disposal, our options include:

1. Randomly partitioning the original data set into subsets and studying SSFM fluctuations among them. This is a feasible method only when there is adequate statistics (large enough number of events), which unfortunately is not the case with most of the data sets we have studied.
2. Estimating SSFM fluctuations via the fluctuations of point and pair event-by-event distributions in the original data set, using error propagation. This method is generally applicable, even with low statistics. However, estimation of derived quantity fluctuations, such as of the SSFMs, becomes computationally harder the more complex those quantities get, and is laden with approximations due to error propagation. We therefore run the risk of a biased error estimation.
3. Finally, using the method of statistical bootstrap, or resampling, [Efron, 1979; Hesterberg, Moore, Monaghan, Clipson, and Epstein, 2005], which has the advantage of being applicable at low statistics without giving biased results, contrary to error propagation. Bootstrapping consists in constructing new data sets of the same size as the original data set. This is achieved by randomly sampling, with replacement, whole events from the original dataset (with uniform probability), so

that in the new samples some events are of necessity duplicated, while others are omitted. When a sufficient number of resampled events,  $N_s$ , has been produced in this manner, we can proceed as we would in a simulation: we calculate the variance  $\sigma(\Delta F_2^{(s)}(M))$  of SSFMs across bootstrap samples, which provides us with an estimate of the statistical error [Metzger, 2004] of factorial moments. Furthermore, by fitting eq.(5.5) to  $\Delta F_2^{(s)}(M)$  separately for each bootstrap sample, we can have an estimate of the probability distribution  $P(\phi_2)$  of the intermittency index  $\phi_2$ .

In the present analysis, we chose bootstrapping as the most suitable method, whereas we have experimented with partitioning into subsets whenever our statistics was large enough to allow it. We have also calculated, for all analysed systems, the SSFM fluctuations via error propagation, and have found them to be in good agreement with bootstrapping. The main advantage of bootstrapping lies in that it allows effortless and unbiased derivation of fluctuations of all kinds of derived quantities, such as the distribution  $P(\phi_2)$  of the intermittency index. For this reason, it was our final choice in this analysis.

## 5.5 Results

### 5.5.1 Intermittency analysis of NA49 datasets at maximum collision energy

By applying the methodology described in section 5.4, we calculated the factorial moments (eq.5.4) for the “C”+C, “Si”+Si and Pb+Pb datasets (Table 5.1), as well as for the corresponding sets of mixed events. Results are shown in Fig. 5.8. We notice that in the case of the “Si”+Si system, Fig. 5.8(b), factorial moments of data are clearly above corresponding ones for mixed events for large values of  $M^2$ . The difference between the two is an increasing function of number of cells  $M^2$ , a typical feature of intermittency. This is evidence for considerable correlations among the protons produced. However, due to low statistics in the case of “Si”+Si,  $F_2(M)$  values for data, as estimated by bootstrap, are accompanied by large statistical errors. In the case of the “C”+C and Pb+Pb systems, Figs. 5.8(a),(c), respectively, both data and mixed event factorial moments saturate (level out) for large  $M^2$ , and they almost totally overlap, especially in the large  $M^2$  region, a fact suggesting absence of intermittency in these systems.

Consequently, we can use eq.5.8 in order to estimate the correlator  $\Delta F_2^{(e)}(M)$  for each of the aforementioned systems, by subtracting mixed event moments from data moments. Results are shown in Fig. 5.9. In the case of “Si”+Si, Fig. 5.9(b), we observe intermittent behavior for  $M^2 > 6000$ . We have therefore used this value as a threshold of  $M^2$  ( $M_{min}^2$ ) in all our fits. The intermittency index  $\phi_2$  for each of the three examined

systems is determined via a power-law fit<sup>2</sup> on the corresponding correlator  $\Delta F_2^{(e)}(M)$ ,

$$\Delta F_2^{(e)}(M; \mathcal{C}, \phi_2) = e^{\mathcal{C}} \cdot (M^2)^{\phi_2} \quad (5.9)$$

where the parameter  $\mathcal{C}$  corresponds to the power-law constant. The “C”+C and Pb+Pb systems, Fig. 5.9(a), as we have already mentioned, do not exhibit intermittent behavior; all the same, we calculate an intermittency index for all 3 systems for the sake of completeness.

Table 5.2 summarizes the values and corresponding errors of  $\phi_{2,PF}$  resulting from fitting the three analysed systems. A weighted fit was performed in each case to the original data set, the weights calculated using the bootstrap error. However, this analysis cannot be considered statistically robust: the non-linear fit parameter error gives a misleadingly small estimate for the  $\phi_2$  variance, especially in the “Si”+Si system, where  $\Delta F_2^{(e)}(M)$  errors are large. For this reason, we supplement our analysis with an assessment of systematic and statistical uncertainties of  $\phi_2$ . Specifically:

1. As we have already mentioned (section 5.4.3), the statistical bootstrap method allows us to calculate the distribution  $P(\phi_2)$  of  $\phi_2$  in our bootstrap samples, by performing a power-law fit for each sample. This provides us with an estimate of  $\phi_2$  statistical fluctuations due to event by event statistical fluctuation of factorial moments.

Fig. 5.10 shows the  $P(\phi_2)$  distributions for all four systems. With the exception of the Pb+Pb high-intensity system, we observe that they are highly asymmetric. For this reason, the mean value and standard deviation of  $\phi_2$  are not suitable estimators of, correspondingly, central tendency and dispersion [Good and Hardin, 2012]. Instead, we choose the median as a measure of central tendency, and a suitable confidence interval (C.I.) around the median as a measure of dispersion. Specifically, we choose the interval bracketed by the 1/6 and 5/6 percentiles, as it corresponds to a 67% confidence level, or approximately one standard deviation ( $1\sigma$ ) in the case of a normal distribution. Table 5.2 shows the values of  $\phi_{2,B}$  and corresponding asymmetric errors  $\delta\phi_{2,B}$  for all four systems.

2. The values of  $\Delta F_2^{(e)}(M)$  for different  $M$  are not independent; they are correlated due to the fact that the same points in momentum space are used to calculate factorial moments in all scales. It is reasonable to assume (and a direct calculation of correlations confirms) that correlation between moments for two scales  $M$  and  $N$  is a rapidly decreasing function of the “distance”  $|M - N|$  [Metzger, 2004].

---

<sup>2</sup>A linear fit to a log-log plot turns out to be unsuitable in this case, both because it distorts the form of correlator errors, as well as due to the fact that negative values of the correlator appear in some samples, due to the small differences between data and mixed event moments.

Unfortunately, attempts to incorporate information about correlations in the fit itself, by performing a correlated fit, fail due to instabilities in the convergence of such fits to a solution [Michael, 1994].

We therefore approach this problem in a different way: firstly, the bootstrap method described above, incorporates fluctuations of  $\phi_2$  due to binning correlations. This only provides indirect evidence, however, so we resort additionally to the *sparse binning* (SB) technique. The latter consists in performing  $\Delta F_2^{(e)}(M)$  fits only for non-consecutive  $M$  values, and subsequently studying the variation in the value of  $\phi_2$  as we increase the minimum distance  $\delta M$  used. Since correlations weaken with increasing distance  $\delta M$ , uncorrelated fits become increasingly better approximations, and we can estimate an average value,  $\phi_{2,SB}$ , as well as a corresponding error  $\delta\phi_{2,SB}$ , using the average value and the standard deviation of sparse binning values, correspondingly. We use intervals of  $\delta M = 2 \rightarrow 8$ , as well as all possible shifts obtainable from the original set of  $M$  values for any given  $\delta M$  interval. Results are presented in Table 5.2, and show that uncorrelated fits are in good agreement with  $\phi_{2,SB}$ , and that systematic errors are relatively small, with the exception of the low-intensity Pb+Pb dataset.

3. The threshold value,  $M_{min}^2$ , above which  $\Delta F_2^{(e)}(M)$  is assumed to follow a power-law, is not strictly defined; it emerges empirically based on inspection of the behavior of  $F_2^{data}(M)$ ,  $F_2^{mix}(M)$ , Fig. 5.8, as well as the quality of fits on  $\Delta F_2^{(e)}(M)$ . A sensible lower bound is practically dictated by the constraint that data and mixed event moments don't overlap for  $M$  above the threshold, a criterion that is only met by the "Si"+Si dataset in the cases we have studied. We examine the dependence of  $\phi_2$  values on  $M_{min}^2$  for all studied systems, by performing a scan of  $\phi_2$  values as  $M_{min}^2$  varies in the [6000, 12000] interval, in steps of 1000. Table 5.2 shows the mean value  $\phi_{2,M^2}$  and the standard deviation  $\delta\phi_{2,M^2}$  of the resulting scan values.
4. The purity level of protons in our data sets. As we have mentioned in section 5.3.2, we can only identify particles as (candidate) protons at a certain confidence level. This level corresponds to 90% purity for the Pb+Pb systems and 80% purity for "C"+C and "Si"+Si systems, where proton multiplicities are significantly lower. Unfortunately, it was not feasible to increase purity for the one system, "Si"+Si, that exhibits intermittency, while at the same time maintaining sufficient event multiplicity for an intermittency analysis. However, a weaker background of particles is expected for the "C"+C and "Si"+Si systems compared to Pb+Pb, which possibly compensates for the lower threshold of purity.

Going through Table 5.2, we firstly note that uncorrelated power-law fits are in fairly

A	$M_{min}^2 = 6\ 000$				$M_{min}^2$ scan <sup>†</sup>
	$\phi_{2,PF}$	$\phi_{2,SB}$	$\phi_{2,B}^*$	$\phi_{2,Bw}^*$	$\phi_{2,M^2}$
“C”+C	-2.70(70)	-2.20(70)	$-0.9^{+1.1}_{-4.1}$	$0.12^{+0.32}_{-0.47}$	-3.00(80)
“Si”+Si	0.95(05)	0.95(10)	$0.96^{+0.38}_{-0.25}$	$0.85^{+0.22}_{-0.17}$	0.84(12)
Pb+Pb (01I)	0.48(06)	0.47(15)	$0.49^{+0.45}_{-0.46}$	$0.49^{+0.25}_{-0.24}$	0.46(06)
Pb+Pb (00B)	$2.1 \pm 1.2$	$2.0 \pm 0.8$	$1.1^{+1.5}_{-0.6}$	$0.74^{+0.31}_{-0.33}$	$0.2 \pm 1.2$

\* 67% C.I. †  $M_{min}^2 \in [6\ 000, 12\ 000]$

**Table 5.2:** Summary of intermittency analysis results for the “C”+C, “Si”+Si and Pb+Pb systems at  $\sqrt{s_{NN}} = 17.3$  GeV in mid-rapidity. Values of the intermittency index  $\phi_2$  are given for the case of uncorrelated fit to the original sample ( $\phi_{2,PF}$ ), for sparse binning ( $\phi_{2,SB}$ ), and confidence intervals via the bootstrap method ( $\phi_{2,B}$ ,  $\phi_{2,Bw}$ ). Finally, the range of values is shown for a threshold scan in  $M^2$ .

good agreement with sparse binning values for all studied systems, a fact reinforcing our confidence in simple power-law fits. The scan in  $M_{min}^2$ , on the other hand, reveals significant variability in intermittency index values  $\phi_2$ , especially in the case of “Si”+Si. Although there is marginal overlap of  $\phi_{2,M^2}$ ,  $\phi_{2,PF}$  and  $\phi_{2,SB}$  intervals, the mean  $\phi_{2,M^2}$  value is significantly displaced compared to the  $M_{min}^2 = 6000$  threshold value.

By far the most significant contribution to the statistical variability of  $\phi_2$  comes from the bootstrap distributions,  $\delta\phi_{2,B}$ . In the case of the high-intensity Pb+Pb system, the distribution is almost symmetric, however the variance is large. On the contrary, in the “Si”+Si case, the distribution is highly asymmetric, with a long tail extending far in the large  $\phi_2$  value region.

The long  $P(\phi_2)$  tails appearing in the “C”+C, “Si”+Si, as well as the low-intensity Pb+Pb systems are to some extent an artifact of ill-defined  $\phi_2$  values, due to the fact that data and mixed event moments overlap to a significant extent, with the data moments for some bootstrap samples sometimes even being below mixed event values, as can be seen in Fig. 5.8. Thus, the correlator attains negative values, that throw the fit towards extreme, unphysical intermittency index values, in order to accommodate such points (eq.5.9 clearly shows that a power-law fit can never pass through a negative point). The pathological case of extreme  $\phi_2$  values is clearly illustrated in Fig. 5.11, where the estimated  $\delta\phi_2$  fit errors are plotted against  $\phi_2$  fit values. It can be seen that extremal values are accompanied by much larger errors than values close to the median.

A much more accurate picture of bootstrap variation can be obtained via a *weighted distribution* of  $\phi_2$  sample values. Each sample fit is assigned a *weight* based on its fit

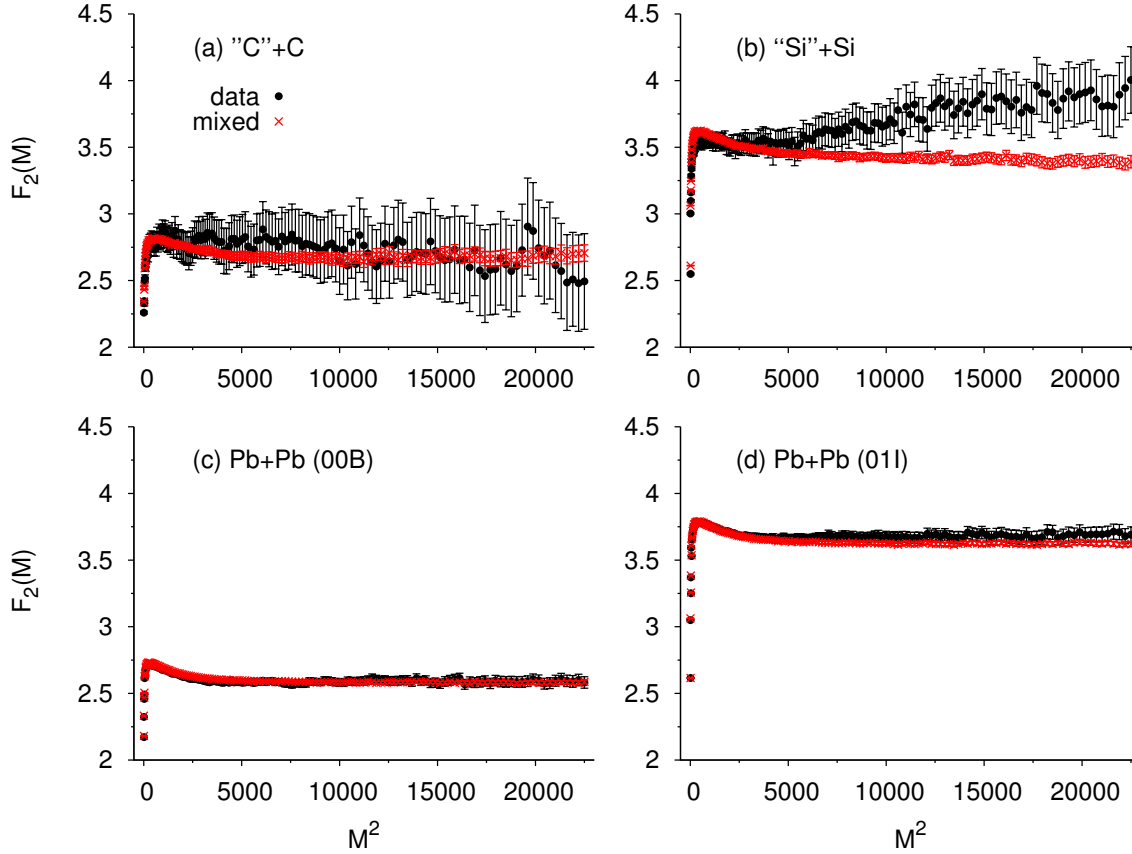


**Figure 5.8:** SSFMs of proton density in transverse momentum space at midrapidity ( $-0.75 < y_{CM} < 0.75$ ) for the most central collisions of (a) “C”+C, (b) “Si”+Si, (c) Pb+Pb (low-intensity), and (d) Pb+Pb (high intensity) at  $\sqrt{s_{NN}} = 17.3$  GeV (158 A GeV). The circles (crosses) represent SSFMs  $F_2(M)$  of data (mixed events) respectively. A cutoff of  $q_{inv} \geq 25$  MeV/c was applied to all data sets. Plotted values correspond to the lattice average of  $F_2(M)$ . Error bars were obtained by the bootstrapping method.

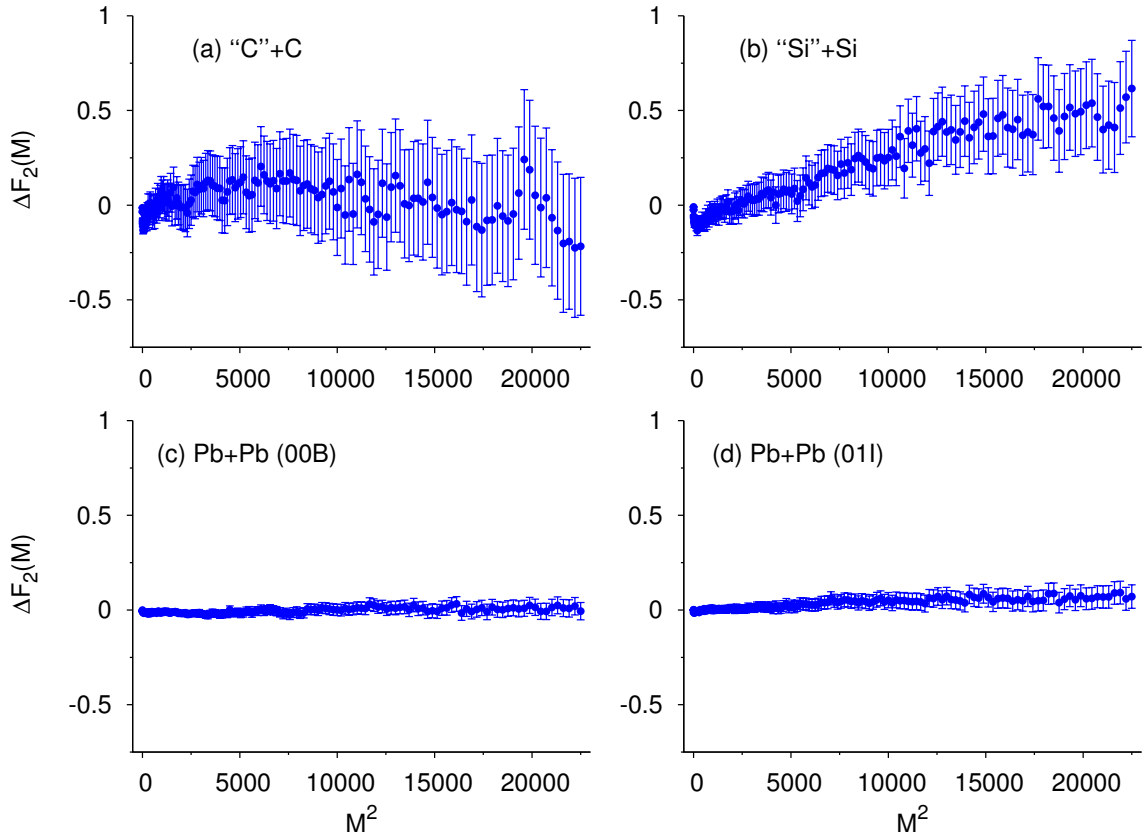


**Figure 5.9:** The estimated correlator  $\Delta F_2^{(e)}(M)$  corresponding to the moments of Fig. 5.8, for the most central collisions of (a) "C"+C, (b) "Si"+Si, (c) Pb+Pb (low-intensity), and (d) Pb+Pb (high intensity) at  $\sqrt{s_{NN}} = 17.3$  GeV (158 A GeV). Error bars were obtained by the bootstrapping method.

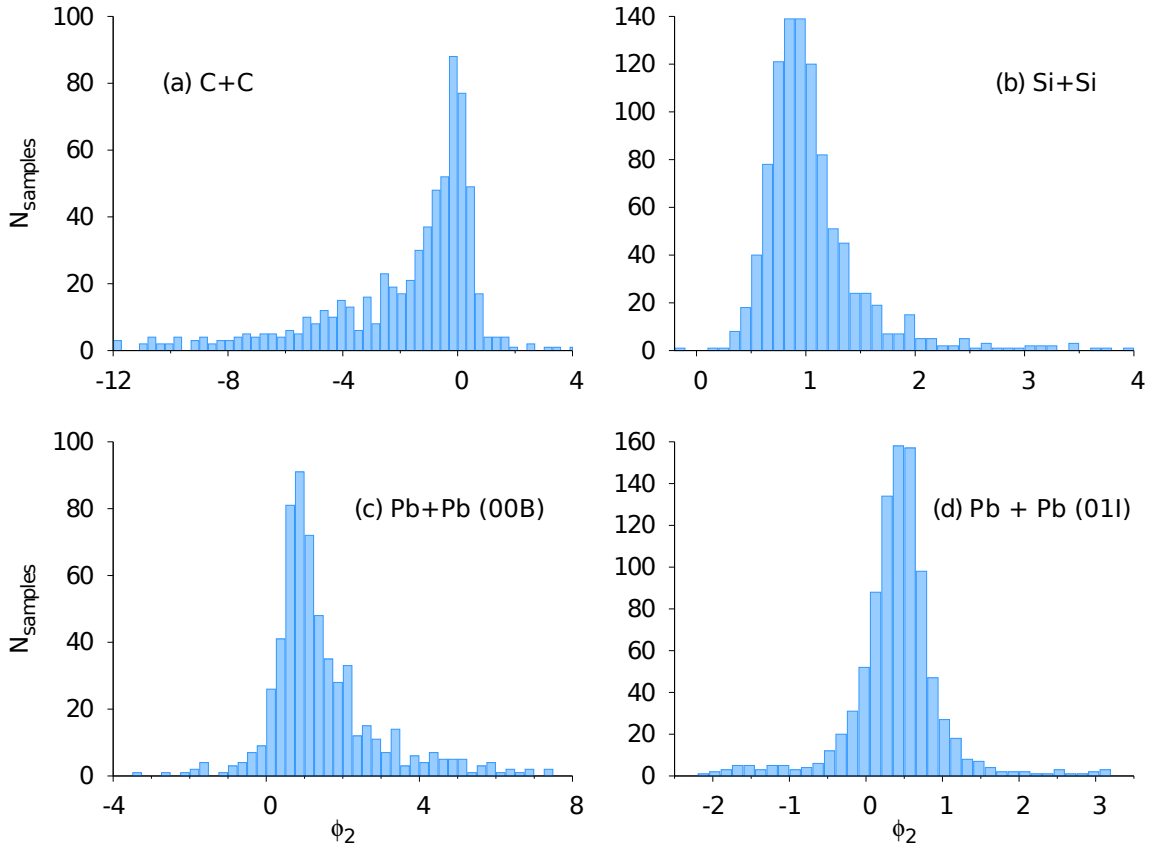


**Figure 5.10:** The distribution  $P(\phi_2)$  obtained applying the statistical bootstrap method to the calculation of the intermittency index  $\phi_2$  for the (a) “C”+C, (b) “Si”+Si, (c) low-intensity Pb+Pb, and (d) high-intensity Pb+Pb systems. In each case, 1000 bootstrap samples were used, at midrapidity ( $-0.75 < y_{CM} < 0.75$ ), at  $\sqrt{s_{NN}} = 17.3$  GeV.

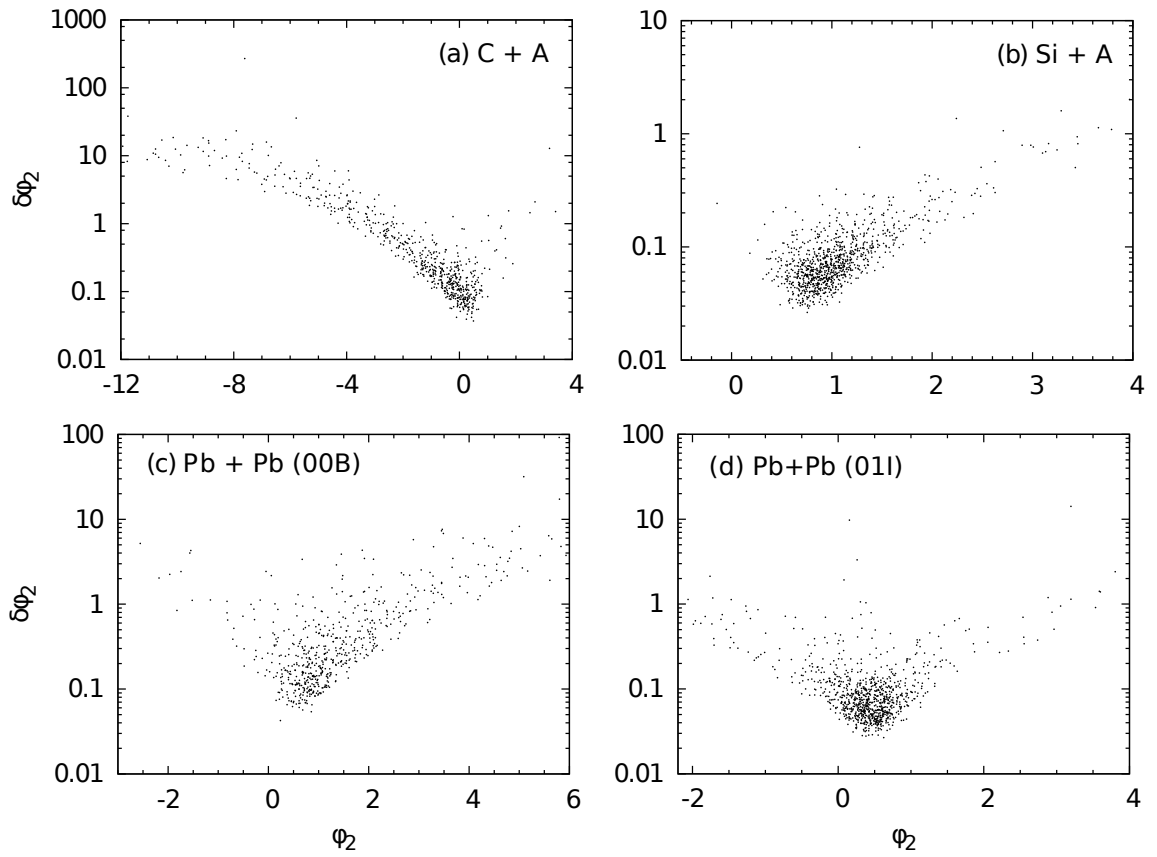


**Figure 5.11:** Estimated  $\delta\phi_2$  fit errors vs  $\phi_2$  fit values, for  $N_B = 1000$  bootstrap samples, in (a) “C”+C, (b) “Si”+Si, (c) low-intensity Pb+Pb, and (d) high-intensity Pb+Pb systems.

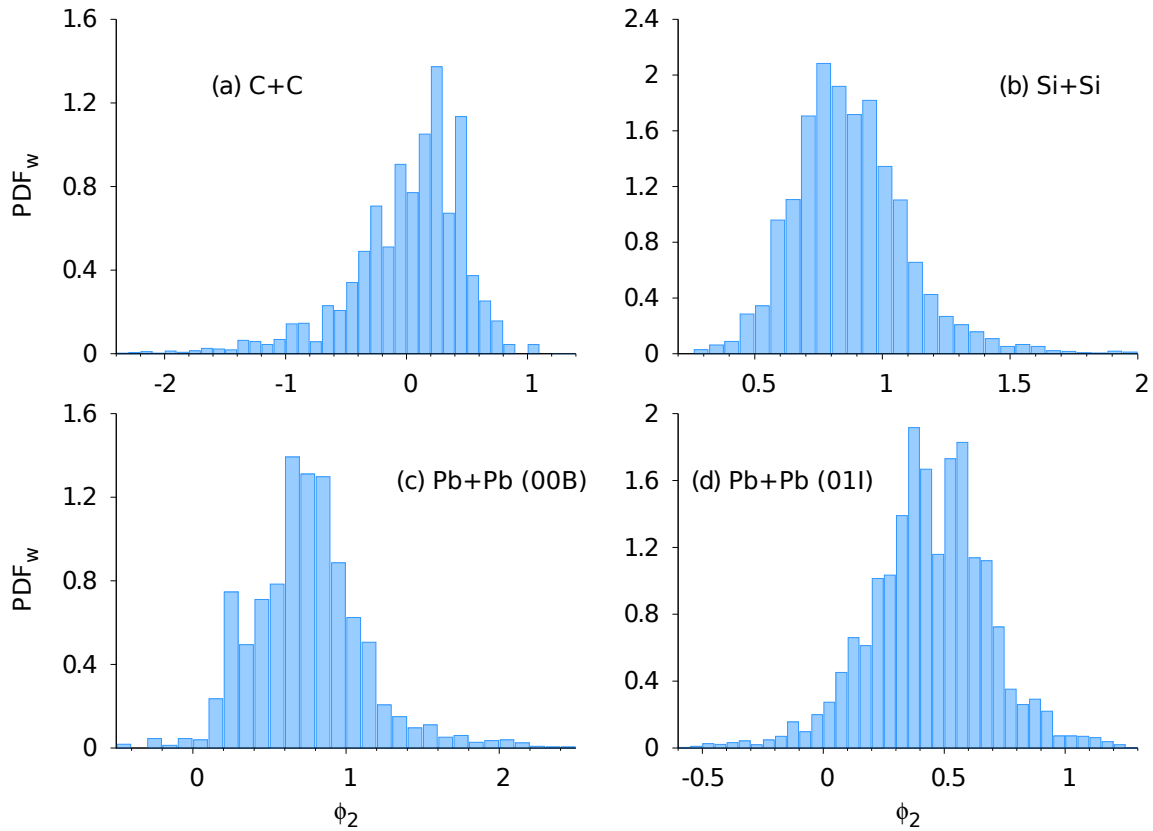


**Figure 5.12:** The distribution  $P(\phi_2)$  of bootstrap samples, weighted by their  $\delta\phi_2$  error, in (a) “C”+C, (b) “Si”+Si, (c) low-intensity Pb+Pb, and (d) high-intensity Pb+Pb systems.

error value, and we subsequently calculate the probability density function of weights for each studied system. Assignment of weights is a somewhat arbitrary process; a reasonable option, however, is to assign as weights the inverse products of the errors of the two fit parameters,  $w = \frac{1}{\delta C \delta \phi_2}$ . Weighted  $\phi_2$  distributions are shown in Fig. 5.12, whereas the corresponding confidence intervals  $\delta \phi_{2,Bw}$  are given in Table 5.2.

### 5.5.2 Simulation of the “Si”+Si system via the CMC and EPOS Monte Carlos

It is evident from the preceding discussion that the “Si”+Si system at maximum energy is the only candidate for critical behavior among the studied systems. Nevertheless, there are substantial uncertainties involved in the estimated intermittency index of “Si”+Si, and although the critical value  $\phi_{2,cr} = 5/6$  is within the range of possible values, we wish to understand the origin of the uncertainties, as well as examine the possibility of non-critical processes giving a false positive intermittency signal.

To this end, we have used the CMC code, adapted for critical proton generation, as described in Ch.4. The algorithm was set up to produce clusters of mass dimension  $\tilde{d}_F = 1/3$  in transverse momentum space, leading to an intermittency index of  $\phi_2 = 5/6$ , which is the theoretically expected value for critical protons. We produced 150k events, similar to the statistics of the “Si”+Si system, simulating the observed event multiplicities of the NA49 dataset. Consequently, we calculated the factorial moments  $F_2(M)$  of the produced dataset in the same manner as with the experimental datasets.

Results are shown in Fig.(5.13)(b) (open triangles). It can be seen that the SSFMs of the pure critical system attain very large values for  $M^2 \gg 1$ , much larger than anything observed in the experimental data sets. This is evidence that, if the “Si”+Si set contains a critical component, it is contaminated by a dominant random background, as in the case of  $\lambda \lesssim 1$  in Eq.(5.7), discussed in section (5.4.2). In order to simulate such behavior within CMC, we substituted, in the simulated events, critical proton tracks with random tracks following the one-particle distribution of transverse momenta observed in the “Si”+Si dataset. Each critical track was replaced with probability  $\lambda$ , and the value of  $\lambda$  was adjusted so that the baseline level of  $F_2(M)$  in the “noisy” CMC dataset is approximately equal to the observed level of  $F_2(M)$  in “Si”+Si. In Fig.(5.13)(a), the results for  $\lambda = 99\%$  are shown, versus the “Si”+Si moments. The levels and behavior for  $M^2 \gg 1$  are very similar. Thus, our approximation to the correlator, eq.(5.8), is justified in the case of “Si”+Si, since  $\lambda$  turns out to be very close to 1, the cross-term in eq.(5.7) can be neglected, and the background can be well approximated by mixed events. This is clearly illustrated in Fig.(5.13)(b): although the moments of the pure (open triangles) and the contaminated CMC sets (filled triangles) differ by orders of magnitude, the slopes of the power-law fits in the log-log plot are approximately equal, meaning that the correlator  $\Delta F_2^{(e)}(M)$  of the contaminated system correctly captures the critical behavior of the pure critical system, after subtraction of the mixed events.

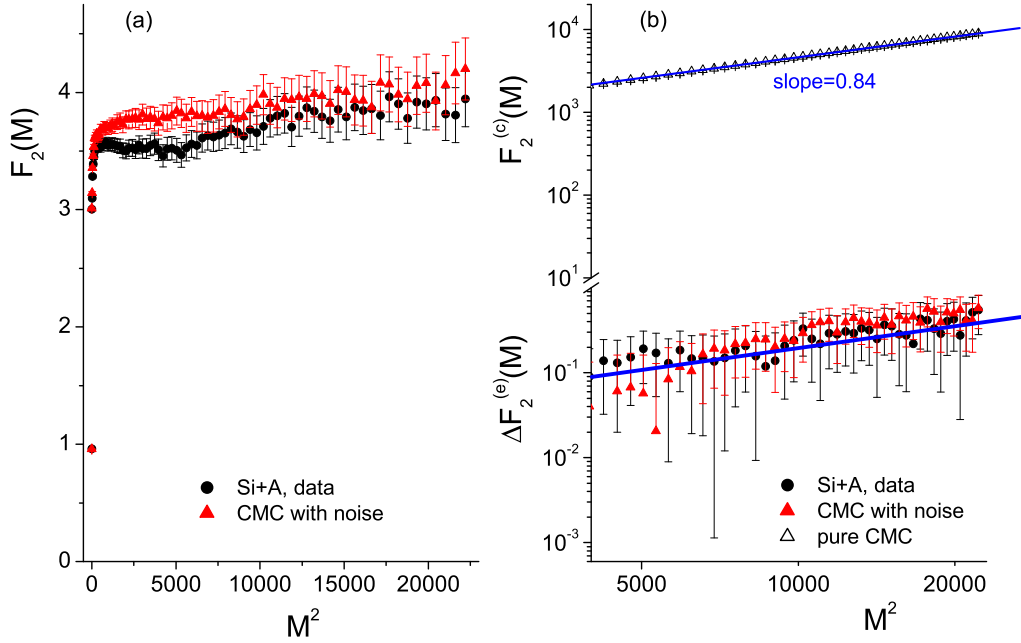


**Figure 5.13:** (a) SSFM of the proton density in transverse momentum space (filled triangles) for 150k events generated by the baryon CMC code to simulate central collisions of the “Si”+Si system at  $\sqrt{s_{NN}} = 17.3$  GeV. The critical system is contaminated with probability  $\lambda = 99\%$  with uncorrelated random tracks. For comparison, we also show the corresponding result for the SSFM obtained from the “Si”+Si data (filled circles), (b) The SSFM  $F_2(M)$  of the 150k baryon CMC events without contamination (open triangles) as well as the estimator  $\Delta F_2^{(e)}(M)$  for the contaminated ensemble (filled triangles) and the “Si”+Si system (filled circles) in double logarithmic scale. Power-law lines of slope  $\phi_2 = 0.84$  are plotted as a visual guide. Only the region  $M^2 > 1000$  is displayed in (b).

A	$M_{min}^2 = 6\ 000$				$M_{min}^2$ scan <sup>†</sup>
	$\phi_{2,PF}$	$\phi_{2,SB}$	$\phi_{2,B}^*$	$\phi_{2,Bw}^*$	$\phi_{2,M^2}$
<b>Pure CMC (“Si”+Si)</b>	0.8382(6)	0.8382(6)	0.8382(6)	0.8382(6)	0.833(3)
<b>Noisy CMC (“Si”+Si)</b>	0.795(24)	0.79(05)	$0.80^{+0.19}_{-0.15}$	$0.77^{+0.14}_{-0.13}$	0.78(03)

\* 67% C.I. †  $M_{min}^2 \in [6\ 000, 12\ 000]$

**Table 5.3:** Summary of intermittency analysis results for the Critical Monte Carlo (CMC) proton simulation of “Si”+Si (2D – transverse momentum only). Values of the intermittency index  $\phi_2$  are given for the case of uncorrelated fit to the original sample ( $\phi_{2,PF}$ ), for sparse binning ( $\phi_{2,SB}$ ) and confidence intervals via the bootstrap method ( $\phi_{2,B}$ ,  $\phi_{2,Bw}$ ). Finally, the range of values is shown for a threshold scan in  $M^2$ .

Table 5.3 summarizes the results of the CMC simulation for both the pure and contaminated (“noisy”) critical systems. We see that, for pure CMC, all estimations of  $\phi_2$  are essentially concentrated in a narrow peak around  $\phi_2 = 0.835$ , which is very close to the plug-in value of  $\phi_2 = 5/6$ . In contrast, we see in the noisy CMC results the effects of omitting the cross-term, eq.(5.7). There is a small shift in the median of  $\phi_2$ , but more importantly we see a spread of values and an increase in statistical uncertainty comparable to that of the NA49 “Si”+Si dataset. We note that the distance of the median from the expected value is much smaller than the spread of values, i.e. the median is almost unbiased. We therefore conclude that the use of the estimator (5.8) for the correlator allows us to determine with fair accuracy the intermittency index  $\phi_2$  in a noise dominated data set.

We also checked our experimental results against simulated events produced by the EPOS event generator [Werner et al., 2006; Drescher et al., 2001], which includes generating high- $p_T$  jets, in order to examine whether the presence of a small number of protons in these jets can produce an intermittency effect. To this end, we configured EPOS to generate a set of 630k events corresponding to a beam of Si nuclei on a Si target ( $Z=14$ ,  $A=28$ , for both beam and target), with a maximum impact parameter of  $b = 2.6$  fm, corresponding to the centrality (12%) of the “Si”+Si experimental dataset. The center of mass energy was set at  $\sqrt{s_{NN}} = 17.3$  GeV, whereas  $p_T$ ,  $p_{tot}$  and rapidity cuts were applied exactly as in the NA49 data. Finally, we performed intermittency analysis of transverse momenta of the protons in the simulated events, as well as the corresponding mixed events. Figure (5.14) compares the correlator  $\Delta F_2^{(e)}(M)$  of the EPOS events with that from the “Si”+Si data. It is evident that EPOS, including conventional sources of correlation, for example jet production and resonance decays, cannot account for the intermittency observed in “Si”+Si, since its correlator fluctuates around or below zero.

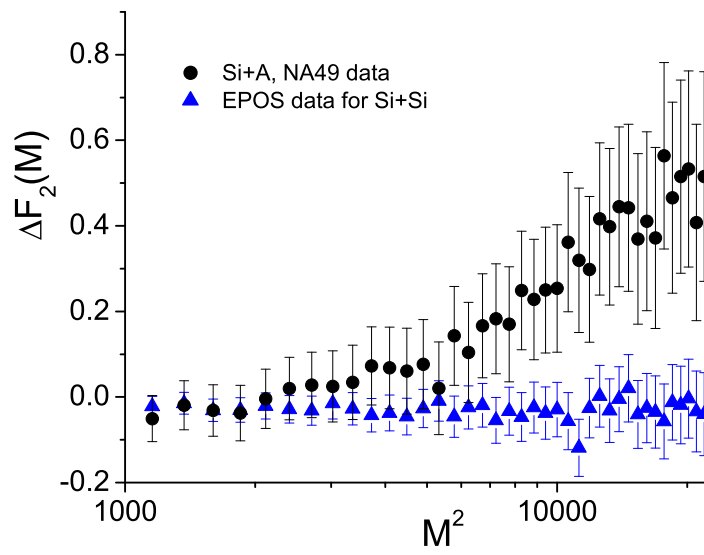


**Figure 5.14:** The estimated correlator  $\Delta F_2^{(e)}(M)$  of protons for the 12% most central collisions (a) from the EPOS event generator (blue triangles), and (b) from “Si”+Si data (black circles) at  $\sqrt{s_{NN}} = 17.3\text{ GeV}$ . Error bars were obtained by the bootstrapping method.

### 5.5.3 Fluctuations at $\sqrt{s_{NN}} = 8.8$ GeV (40A GeV)

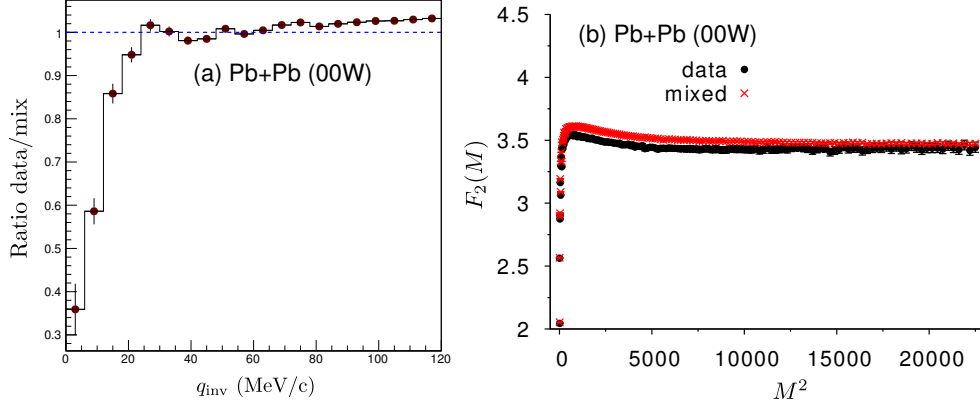


**Figure 5.15:** (a) The  $C(q_{inv})$  correlation function of proton pairs (ratio of pairs from real and mixed events) at midrapidity ( $-0.65 < y_{CM} < 0.65$ ) for the 12.5% most central collision of Pb+Pb at 40A GeV ( $\sqrt{s_{NN}} = 8.8$  GeV), (b) The SSFMs for protons in the same dataset. A cutoff of  $q_{inv} \geq 20$  MeV/c was applied. Plotted values correspond to the lattice average of  $F_2(M)$ . Error bars were obtained by the bootstrapping method.

Finally, we have checked for critical fluctuation at lower collision energies, by extracting proton tracks from the NA49 Pb+Pb (00W) dataset at 40A GeV ( $\sqrt{s_{NN}} = 8.8$  GeV) (last column in Table 5.1). In Fig.5.15(a), we show the  $C(q_{inv})$  correlation function for proton pairs in Pb+Pb (00W); the expected peak around 20 MeV/c, as well as the dip in low  $q_{inv}$ , are present. In Fig.5.15(b), we have plotted the SSFMs for Pb+Pb (00W) transverse proton momenta. It can be seen that the mixed event moments are above the data moments, and therefore no intermittency is present at 40A GeV.

This result is consistent with the claim of the NA49 collaboration that the freeze-out states in the phase diagram of Pb+Pb collisions at low energies (around 30A GeV) lie close to the onset of deconfinement, as evidenced by the energy dependence of yields of particles (e.g.  $K^+/\pi^+$ ) [Alt et al., 2008]. In particular, non-monotonic fluctuation measures, such as the relative strangeness  $E_s$  ratio [Alt et al., 2008] exhibit a peak around  $\sqrt{s_{NN}} \sim 7 - 9$  GeV (the ‘‘horn’’), a range which includes the 40A GeV Pb+Pb set collision energy. The freeze-out of Pb+Pb 40A GeV is estimated to occur around ( $T \sim 140$  MeV,  $\mu_B \sim 380$  MeV) [Becattini et al., 2006]. However, the peak could be an indication of a first order phase transition, as well as of a second order transition, and therefore it is quite possible that it would lie at a distance from the critical point. Absence of intermittency for the low-energy Pb+Pb set is indeed evidence that the freeze-out of the collision occurs at a distance from the critical point, along the first order transition line.

## CHAPTER 6

### CONCLUSIONS & FUTURE PROSPECTS

In the present work, we have attempted to shed some light on the large scale physical characteristics of the chiral phase transition of strongly interacting hadronic matter at the vicinity of the purported QCD critical point. Our approach has been a phenomenological one: we have used the predictions of the theory of critical phenomena to link the critical exponents of the singular part of observable macroscopic quantities (in particular, the order parameter and the corresponding correlation function) to the fractal structure of the chiral condensate. Specifically, the isothermal critical exponent  $\delta$  is linked to the fractal dimension of the chiral condensate clusters in transverse configuration and momentum space. Such a direct connection is feasible due to universality, which allows us to describe a critical system by means of an effective action belonging to a certain universality class. Based on the results of analytic field theory calculations and numerical lattice simulations, we have concluded that the QCD critical point belongs to the 3D-Ising universality class, and that the only relevant field near the critical point is the scalar  $\sigma$ -field, which becomes massless at the critical point. The net baryon density is also an order parameter, equivalent to the  $\sigma$ -condensate.

We have demonstrated that it is possible to simulate the fractal geometry of critical sigma and baryon clusters, using stochastic Lévy walks. We focus primarily on simulating transverse space in mid-rapidity, since it is a manifestly boost-invariant system. The fractal dimension of sets of events produced by such simulations can be approximately reconstructed by intermittency analysis employing scaled factorial moments, even in the presence of small multiplicities and significant background, although statistical uncertainties grow larger the more background is introduced, and the less structure is present (small multiplicities). The technique of statistical bootstrap (resampling) can be used to reliably estimate the statistical uncertainties in the value of the intermittency index.

Having gained insight through simulations of critical clusters, we applied our intermittency analysis technique to experimental data sets of the NA49 experiment. The main focus of the analysis were four datasets at the maximum collision energy of 158A GeV

( $\sqrt{s_{NN}} = 17.3$  GeV), namely, the most central “C”+C, “Si”+Si, and low and high-intensity Pb+Pb collisions, from which we extracted (candidate) proton tracks. A first indication of the presence of critical fluctuations in the protons of the “Si”+Si system was furnished by the distribution of relative transverse momenta  $\Delta p_T$  exhibiting a strong peak for  $\Delta p_T \rightarrow 0$  (see Fig.5.5), which is very similar to the behaviour of the corresponding CMC simulation. Based on this initial indication, we calculated the second scaled factorial moments of the proton density for all sets. Our analysis revealed the presence of non-Poissonian fluctuations in the “Si”+Si system only, albeit accompanied by significant statistical and systematic uncertainties. Such behaviour is consistent with a power-law scaling of the the proton density in the freeze-out of the “Si”+Si system, an indication of proximity to the chiral critical point. No traces of critical correlations were found in the freeze-out states of “C”+C and low-intensity Pb+Pb interactions at the same collision energy, whereas the intermittency found in the high-intensity Pb+Pb system is suspect due to an anomalous peak found in its  $q_{inv}$  distribution for low  $q_{inv}$ . The power-law exponent  $\phi_2 = 0.96^{+0.38}_{-0.25}$  (stat.)  $\pm 0.16$  (syst.) for the “Si”+Si system is within 15% of the QCD prediction,  $\phi_{2,B} = 5/6$ , and the theoretically predicted value is within a 67% confidence interval of the measured intermittency index; however, statistical and systematic errors are fairly large.

An analogous intermittency effect was found recently Anticic et al. [2010] in central “Si”+Si collisions at  $\sqrt{s_{NN}} = 17.3$  GeV for  $\pi^+\pi^-$  pairs with invariant mass close to twice the pion mass (the threshold for the decay of a  $\sigma$  into  $\pi^+\pi^-$ ). Thus, we have evidence from two independent channels in the same collision energy and system size, of sizeable power-law fluctuations.

The large statistical errors in “Si”+Si do not allow a conclusive statement concerning the location of the critical point. However, our intermittency analysis results favor the neighborhood of the “Si”+Si freeze-out state, which can be estimated by particle yields to be around ( $T \approx 160$  MeV,  $\mu_B \approx 250$  MeV) [Braun-Munzinger and Stachel, 2007; Becattini et al., 2006], for a further detailed search for the critical point.

Such a program is currently pursued by the NA61/SHINE (SPS Heavy Ion and Neutrino Experiment), studying hadron production in hadron-hadron, hadron-nucleus and nucleus-nucleus collisions with small and intermediate size nuclei at CERN SPS. The NA61/SHINE physics goals include the search for the onset of deconfinement and the critical point of strongly interacting matter [Abgrall et al., 2014]. The first physics data with hadron beams (p+p) were recorded in 2009, and with ion beams in 2011 (Be+Be), and in 2015 (Ar+Sc). In 2017, data taking for Xe+La collisions is planned. NA61/SHINE will thus probe a region of relatively light ions with energies in the range 13A – 158A GeV, which are likely to produce a system with freeze-out in the vicinity of the critical point. Compared to its predecessor NA49, NA61/SHINE has considerably lower background, which leads to better momentum resolution, particle identification (performed through measurements of energy loss  $dE/dx$ , as well as of particle masses

through time of flight (TOF) measurements), and better event statistics (number of recorded events), all of which are essential for reducing the statistical and systematic uncertainty of an intermittency analysis. Moreover, precise measurements of forward energy and identification of beam particles reduces biases due to fluctuations of system size.

In the event that the energy and system size scans performed by the NA61/SHINE experiment approach the critical point of QCD, it is very likely that the critical fluctuations induced in the proton density, as well as decay products of sigmas, such as pions, will survive through the freeze-out and be detectable through an improved intermittency analysis. It is to be hoped that such an analysis will narrow down the uncertainties of the estimated intermittency index, allowing a reliable comparison with the theoretically expected critical intermittency index, ideally for both proton density and  $\sigma$ -density. We will then possess an excellent signature of the approach to the critical point. The success of such an analysis will depend on the available statistics and quality of data (purity of selected particle species).

Even so, many challenges remain for intermittency analysis as a tool for the detection of critical fluctuations. In particular, subtraction of the uncorrelated background via the correlator,

$$\Delta F_2^{(e)}(M) = F_2^{(d)}(M) - F_2^{(m)}(M) \quad (6.1)$$

ignoring the cross-term, (5.7), is only realistic in the region  $\lambda \simeq 1$  of very large background. The region  $\lambda \simeq 0$  can also be handled by simply ignoring the background. However, intermediate cases would require the full use of (5.7), which is not possible due to the unknown value of the cross-term.

One possible approach in cases of suspected intermediate background would be to perform many Monte Carlo runs with different  $\lambda$  values, attempting to closely reproduce the shape  $F_2^{(d)}(M)$  of the data moments, then calculate the CMC correlator for the closest  $\lambda$  match (cross-term calculation is always possible in a simulation, where we know the origin of particles). This method requires a good statistical test for the similarity of two functions, (e.g., wavelets).

Another, more ambitious programme, would be to attempt to calculate the whole multifractal spectrum of the set of momenta in transverse momentum space. The union of critical tracks and uncorrelated background can be considered as a multifractal, i.e. a set of interwoven fractals of different dimensionalities. The primary contributions to the spectrum would be the critical dimension  $d_F$  and the dimensionality of embedding space. By calculating factorial moments of different orders  $q$ , eq.(4.65), we can reproduce the spectrum of Rényi dimensions  $D_q$ . Presumably, the critical dimension would show as a sharp peak in such a multifractal spectrum. However, this approach requires extraordinarily good statistics, and the computationally intense calculation of a dense set of (fractional)  $q$ -order scaled factorial moments, and there are possibly further

unpredictable challenges in its practical application.

The search for the chiral critical point of strongly interacting matter is ongoing. A close co-ordination of experimental probes of increasing resolution, intermittency analysis of experimental results and Monte Carlo modeling is in our opinion the best approach to its eventual detection and comprehension.

## APPENDIX A

# ANALYTICAL CALCULATION OF MIXED EVENTS USING THE 1-PARTICLE DISTRIBUTION OF TRANSVERSE MOMENTA

### A.1 The Problem

Calculating the expectation value of the *Horizontal Second Scaled Factorial Moments*, *HSSFM*:

$$F_2^H(M) \equiv \frac{\left\langle \frac{1}{M^2} \sum_{m=1}^{M^2} n_m(n_m - 1) \right\rangle}{\left\langle \frac{1}{M^2} \sum_{m=1}^{M^2} n_m \right\rangle^2} \quad (\text{A.1})$$

as a function of the number of cells  $M$  in 1-D, averaged over cells and events, in the case of *uncorrelated momenta*.

### A.2 Assumptions

1. Momentum tracks in an event are *independent* and *identically distributed* (i.i.d.) in transverse momentum space (Fig.A.1). I.e., the probability of finding a pair of points in a given cell is equal to the product of the probabilities of finding either point of the pair inside the cell.
2. Multiplicities  $L$  of events follow a *truncated Poisson* distribution (i.e., zero multi-

plicity events have been rejected):

$$P_{mul}\{L = k\} = (e^\ell - 1)^{-1} \frac{\ell^k}{k!}, \quad (\text{A.2})$$

where  $\ell$  is the mean multiplicity of events.

3. The probability  $p_i$  of finding a point in the  $i$ -th cell is independent of event multiplicity.
4. The order in which we take the average  $\langle n_i(n_i - 1) \rangle$  over cells  $i$  and over events is irrelevant to the result. In effect, this is equivalent to assuming that enough events have been accumulated in order for the expectation values to have converged. This allows us to take the average for pairs in a cell  $i$ , over many events, followed by averaging over cells unrestricted by the total number of tracks.

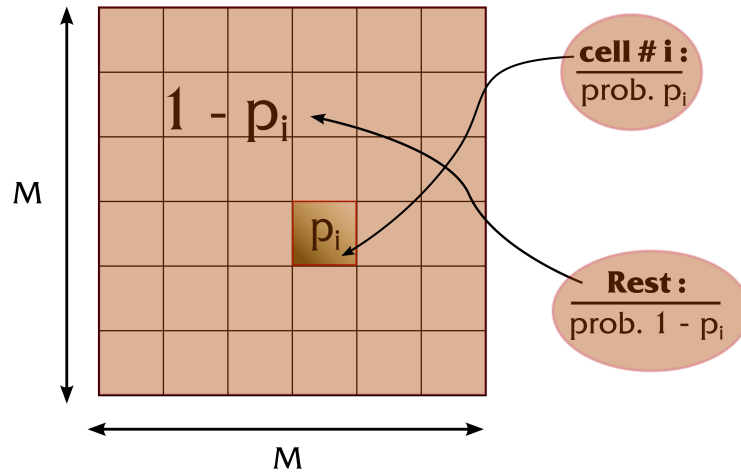


**Figure A.1:** Probability distribution function of momenta over the lattice. Momenta are independent and identically distributed, each having the same probability  $p_i$  of being found in the  $i$ -th cell.

### A.3 Expectation point and pair values for cell- $i$ , for constant multiplicity $L$

Let all events have the same multiplicity,  $L$ , then the probability of finding  $k$  points in the  $i$ -th cell (Fig.A.1) follows a *binomial distribution*:

$$P\{k \text{ points in } i\text{-th cell}\} \equiv P\{k, i; L\} = \binom{L}{k} p_i^k (1 - p_i)^{L-k}$$

Therefore, expected number of points per event equals:

$$\langle n_i \rangle_L = \sum_{k=0}^L P\{k, i; L\} k = L \cdot p_i \quad (\text{A.3})$$

Likewise, expected number of pairs equals:

$$\langle n_i(n_i - 1) \rangle_L = \sum_{k=0}^L P\{k, i; L\} k(k-1) = L(L-1) \cdot p_i^2 \quad (\text{A.4})$$

#### A.4 Expectation point and pair values per cell, for constant L

Averaging over cells, in the limit of infinite events,  $N_{ev} \rightarrow \infty$ , we get:

$$\langle n_M \rangle_L = \frac{1}{M^2} \sum_{i=1}^{M^2} \langle n_i \rangle_L = \frac{L}{M^2} \sum_{i=1}^{M^2} p_i = \frac{L}{M^2} \quad (\text{A.5})$$

$$\langle n_M(n_M - 1) \rangle_L = \frac{1}{M^2} \sum_{i=1}^{M^2} \langle n_i(n_i - 1) \rangle_L = \frac{L(L-1)}{M^2} \sum_{i=1}^{M^2} p_i^2 \quad (\text{A.6})$$

#### A.5 Weighing over event multiplicity distribution

Using eq.(A.2), we weigh the average number of points, eq.(A.5) and pairs, eq.(A.6), proportionally to event multiplicity frequencies. We find:

$$\langle n_M \rangle = \sum_{k=1}^{\infty} P_{mul}(k) \cdot \langle n_M \rangle_k = \ell \left( \frac{e^\ell}{e^\ell - 1} \right) \frac{1}{M^2} \quad (\text{A.7})$$

and:

$$\langle n_M(n_M - 1) \rangle = \sum_{k=1}^{\infty} P_{mul}(k) \cdot \langle n_M(n_M - 1) \rangle_k = \ell^2 \left( \frac{e^\ell}{e^\ell - 1} \right) \frac{1}{M^2} \sum_{i=1}^{M^2} p_i^2 \quad (\text{A.8})$$

Lastly, using eq.(A.1), the expected value  $F_2(M)$  over cells and events is found to be:

$$\langle F_{2,th}(M) \rangle = \frac{\langle n_M(n_M - 1) \rangle}{\langle n_M \rangle^2} = \left( \frac{e^\ell - 1}{e^\ell} \right) \cdot \underbrace{M^2 \sum_{i=1}^{M^2} p_i^2}_{\text{p.d.f. factor}} \quad (\text{A.9})$$

More generally, in the case of a non-poissonian multiplicity distribution, eq.(A.9) takes the form:

$$\langle F_{2,th}(M) \rangle = \frac{\langle n_M(n_M - 1) \rangle}{\langle n_M \rangle^2} = \left( \frac{\langle \ell(\ell - 1) \rangle}{\langle \ell \rangle^2} \right) \cdot \underbrace{M^2 \sum_{i=1}^{M^2} p_i^2}_{\text{p.d.f. factor}} \quad (\text{A.10})$$

where  $\langle \ell \rangle$  is the mean event multiplicity.

## A.6 General properties of $\langle F_{2,th}(M) \rangle$

1. The 1-particle momentum distribution *p.d.f. factor*, eq.(A.9, A.10), fluctuates considerably for large binnings (small  $M$ ), while for large enough  $M$ , it approaches asymptotically the limiting value:

$$(\text{area}) \times \int_{(\text{area})} \rho^2(p_x, p_y) dp_x dp_y$$

where  $\rho(p_x, p_y)$  is the probability density function (p.d.f.) of points in transverse momentum space.

2. When  $\rho(p_x, p_y)$  is a *smooth function*, the factorial moments for large  $M$  will always tend to *level out*, regardless of the specific form of  $\rho(p_x, p_y)$ .
3. The p.d.f. factor *attains its minimum* for a *uniform p.d.f.*  $\rho(p_x, p_y) = \text{const}$ , in which case, it is equal to 1, while  $F_2(M)$  are constant and equal to  $\left( \frac{\langle \ell(\ell - 1) \rangle}{\langle \ell \rangle^2} \right)$  for all  $M$ .

## A.7 Comparison of theoretical prediction to real mixed events

Using eq.(A.9), it is possible to estimate  $F_2(M)$  for a set of events without mixing, by simply plugging in the 1-particle momentum p.d.f., as well as the event multiplicity distribution. In what follows, we test this theoretical prediction, by first comparing it

to simulated mixed events drawn from a known p.d.f, and then to the actual mixed events of the “Si”+Si set.

### A.7.1 $F_{2,th}(M)$ of gaussian noise in $p_x, p_y$ (disjoint)

Using the univariate distributions of  $p_x$  and  $p_y$  of the “Si”+Si dataset (after the rapidity cut), we simulate proton tracks where the coordinates  $(p_x, p_y)$  follow i.i.d. gaussian p.d.f’s, with:

$$\mu_x = 1.173 \times 10^{-1} \text{ GeV}, \sigma_x = 5.121 \times 10^{-1} \text{ GeV}$$

$$\mu_y = -4.21 \times 10^{-2} \text{ GeV}, \sigma_y = 4.024 \times 10^{-1} \text{ GeV}$$

while event multiplicities follow a poisson distribution with  $\ell = 3.004$ . The resulting 2-D p.d.f. is shown in Fig.A.2.

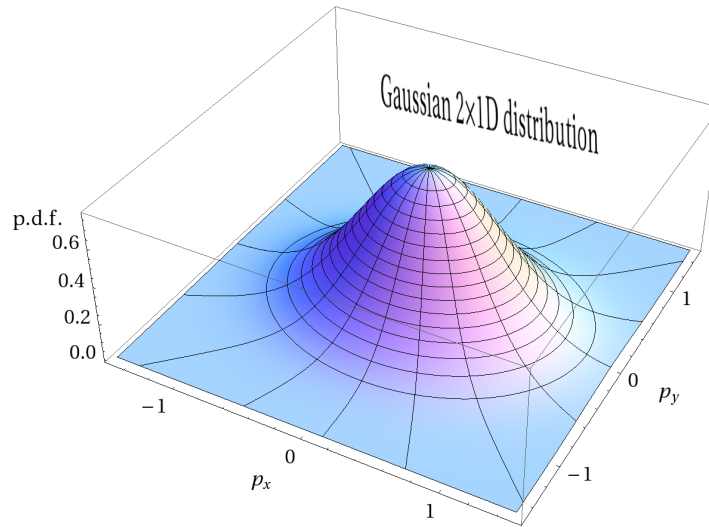


**Figure A.2:** Probability density function of transverse momenta for stochastic, normally distributed mixed events.

The moments  $F_2(M)$  of gaussian mixed events are shown in Fig.A.3, alongside the corresponding theoretical prediction. The data is in good agreement with the theoretically predicted values.

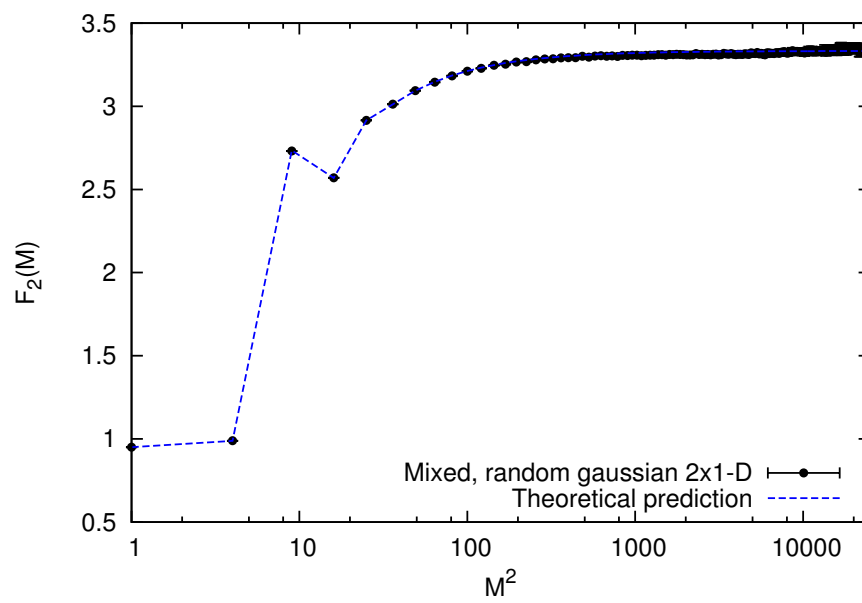


**Figure A.3:** The SSFMs  $F_2(M)$  of random (normally distributed) mixed events, compared to the theoretical curve.

### A.7.2 $F_{2,th}(M)$ for the actual mixed events in the “Si”+Si system

Next, we turn our attention to mixed events in the “Si”+Si dataset. Multiplicity distribution and  $\rho(p_x, p_y)$  p.d.f. (Fig.A.4) are extracted via a statistical analysis of the original “Si”+Si dataset.

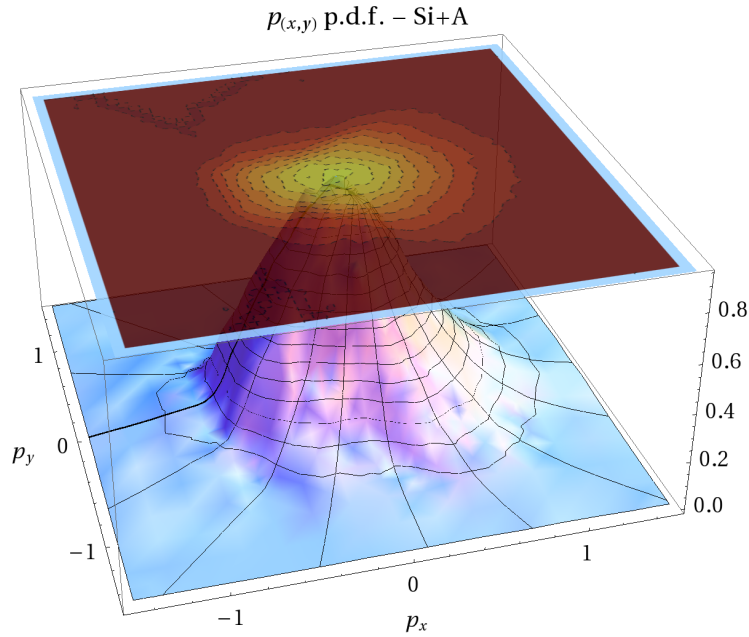


**Figure A.4:** Probability density function of transverse momenta for the “Si”+Si dataset.

In Fig.A.5, we show the SSFMs, alongside the theoretical prediction, for mixed events in the “Si”+Si system. We note that the level of mixed events is in good agreement with the theoretical prediction.

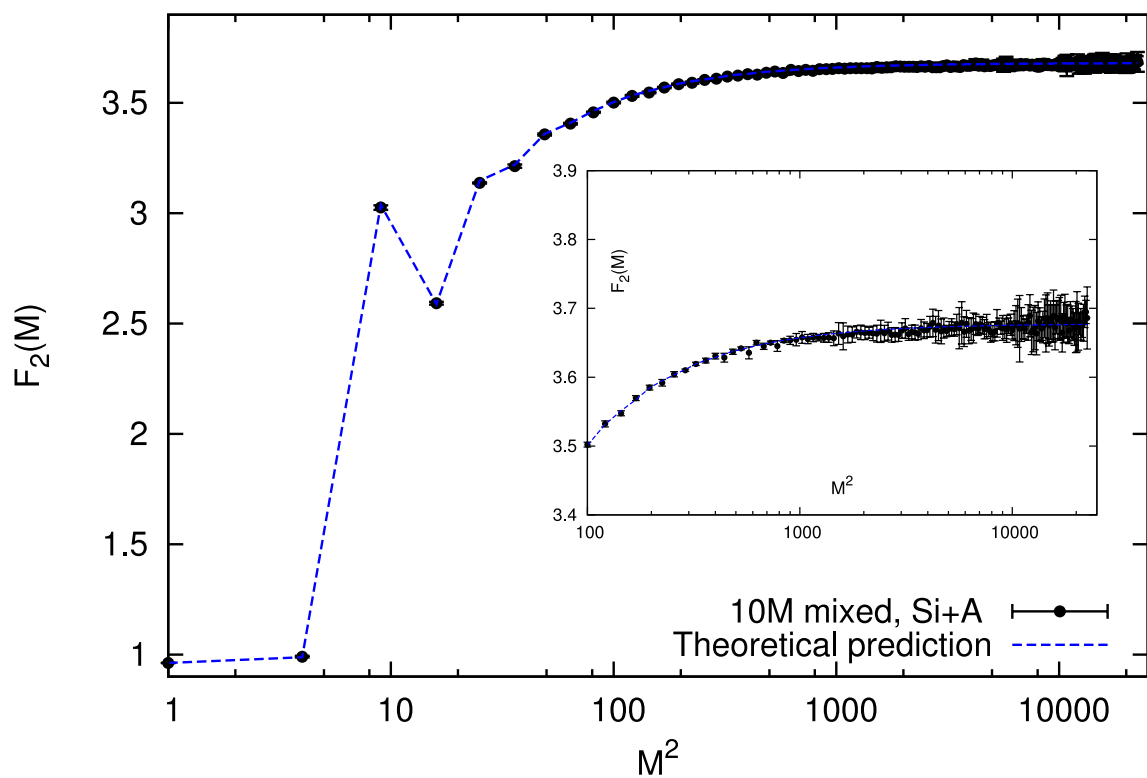


**Figure A.5:** The SSFMs  $F_2(M)$  of mixed events in the "Si"+Si system, compared to the theoretical curve.

## APPENDIX B

### CRITICAL MONTE CARLO CODE

#### B.1 CMC code for $\sigma$

The following code implements, in Fortran 90, the Critical Monte Carlo (CMC) algorithm for the simulation of critical  $\sigma$ -clusters in transverse momentum/rapidity space, presented in section 4.6.1<sup>1</sup>.

The code takes the form of a module, `mod_sigma`, consisting of the following routines:

1. Routine `set_sigma_params` reads input parameters (section 4.6.2) from the external `fname` file, and initializes the values of all derived parameters for the rest of the simulation. It should be called once at the beginning of a run of events.
2. Routine `get_sigma_event` produces a single  $\sigma$  event, and stores the table of 3-momenta of produced  $\sigma$ -particles in the array `sigtracks`. Event multiplicity is stored in integer variable `mult`.
3. Function `randpt` returns a random  $p_T$  value following an exponential distribution. It takes an input parameter `ptmean` – the mean  $p_T$  value.
4. Routine `random_permut` returns a random permutation of the range  $[1, \dots, n]$ .

---

<sup>1</sup>The latest copy of the code and documentation can be found in `lxplus:/afs/cern.ch/user/n/ndavis49/public/cmc/`

```

module mod_sigma
USE nrtype ! Portable precision
USE nrutil, ONLY : assert
USE nr, ONLY : sort
implicit none
private ! unless declared public
public :: set_sigma_params, get_sigma_event

!***** global parameters *****
REAL(SP), PARAMETER :: D_F = 2._sp/3._sp ! Fractal dimension (2/3)
REAL(SP), SAVE :: D, ptmean, pd, c, dc2
integer, SAVE :: nc_tr=1, nc_r=1, nt_cl=1, nt_tot=1, ntot=1
logical, SAVE :: read_params = .false. ! Has a parameter file
! ever been read?

contains

subroutine set_sigma_params(fname)
!*****
!** Reads an input file with **
!** initial parameters and **
!** calculates the simulation **
!** parameters, saved as module **
!** variables, until this sub **
!** is called again. **
!*****
character*(*), intent(in):: fname ! Input file name (parameters)
!***** local simulation parameters *****
integer :: n_c, mul_p
REAL(SP), parameter :: HBARC = 197.32858_sp ! hbar * c (MeV * fm)
REAL(SP) :: G, T_c, R_t, tau, &
           b_c, c_a, rdt, p_o, &
           gl2, gl6, V_o, V_c, &
           d_c, r_c, xm_cl

integer :: funit ! Input file unit number
logical :: UNITOK, UNITOP ! inquire about file units

    funit = 8 ! Safe starting unit number
    do while (funit < 100)
        inquire (unit=funit,exist=UNITOK,opened=UNITOP)
        if (UNITOK .and. .not. UNITOP) exit
        funit = funit + 1 ! Try next unit
    end do
    if (funit >= 100) stop "Can't find available file unit!"

```

```

open(funit,file=fname,STATUS="OLD",action="READ",ERR=999)
read(funit,*,ERR=999) G,T_c      ! coupling constant,
                                ! Critical Temperature (T_c,MeV)
read(funit,*,ERR=999) R_t,D,tau ! Transverse cross section (R_t,fm),
                                ! tot. rapidity interval (D),
                                ! proper time (tau,fm),
read(funit,*,ERR=999) pd        ! truncation parameter (pd, MeV)
                                ! -- pd: 0.85, 1.0,...

close(funit)
!*** Calculate secondary parameters ***
ptmean=2.d0*T_c
b_c=(HBARC/T_c)
c_a=tau/b_c
rdt=(4.d0*PI*c_a*D*G)**(0.1d0)*b_c
p_o=HBARC/rdt

g12=gamma(0.5d0)
g16=gamma(1.d0/6.d0)
V_o=dsqrt(2.d0*G*c_a)*b_c**2
d_c=0.5d0*dsqrt(PI)*(0.5d0*G)**(-0.25d0)*(R_t/tau)
r_c=PI*tau*D/(12.d0*dsqrt(6.d0*G))
V_c=PI*r_c**2*d_c
dc2=0.5d0*d_c

! **** print results ****
write (*,*) "radius of cluster in rap.=", dc2
write (*,*) "radius of cluster in tr. mom=", p_o

c=1.d0-(pd/(pd+p_o))**D_F ! ** Random walk normalization

!***** number of clusters in tr. space *****
nc_tr=int((R_t/r_c)**2)
!***** multiplicity in one 3-D cluster *****
xm_cl=(g12/g16)*(V_c/V_o)**(2.d0/3.d0)
!*****
!***** number of clusters in rapidity *****
nc_r=int((D/d_c))
!***** total number of clusters *****
n_c=nc_tr*nc_r
!***** total multiplicity *****
mul_p=int(xm_cl*dble(n_c))
!***** multiplicity per cluster *****
!***** in tr. mom. space *****
nt_cl=int(dble(nc_r)*xm_cl)

```

```

!***** total multiplicity in tr. space *****
  nt_tot=nc_tr*nt_cl
!***** maximum total multiplicity *****
  ntot=nc_r*nt_tot

  ! **** print results ****
  write (*,*) "mult./cluster in tr. mom.=", nt_cl
  write (*,*) "number of clusters in rap.=", nc_r
  write (*,*) "number of clusters in tr. mom=", nc_tr
  write (*,*) "total multiplicity=", mul_p
  ! **** set input file flag to true ****
  read_params = .true.
  return
  ! **** there was an error in the input file, abort ****
999 write (*,*) "Error reading params file! PARAMS NOT SET!"
return
end subroutine set_sigma_params

subroutine get_sigma_event(mult,sigtracks)
! ***** Parameters *****
integer, intent(out) :: mult          ! Sigma event multiplicity
REAL(SP), POINTER :: sigtracks(:,:) ! Sigma event tracks (OUT)
!***** Local variables *****
REAL(SP) :: xoutr,outr,outr1,outr2, ptr,fi, &
             meanpx,meanpy, xmean,ymean, &
             rtol, dlim,ulim, scl,pl,dey, ymax
REAL(SP) :: xco, yco, zco ! 3-momenta of sigma track
integer :: mulef, & ! Sigma event
             & ! multiplicity
             mi,ni,ml,npc, & ! Loop counters
             ipar,inear,nacl,mul_r,mulne
!integer :: ialloc ! Allocation error code
!***** Local array declarations *****
REAL(SP), DIMENSION(1:nc_tr) :: ctr_x,ctr_y
! List of cluster centers in pt
REAL(SP), DIMENSION(1:nt_cl) :: x_n, y_n
! List of particles in cluster
REAL(SP), DIMENSION(1:2*nt_cl) :: roxy, cxy
! Random vectors
REAL(SP), DIMENSION(1:nt_tot) :: partr_x, partr_y
! List of produced particles in pt
REAL(SP), DIMENSION(0:nc_r+1) :: crap
! Rapidity cluster centers
REAL(SP), DIMENSION(1:nc_r) :: rleft, rright, raplen, probra
REAL(SP), DIMENSION(1:ntot) :: rapi

```

```

REAL(SP), DIMENSION(1:nt_tot) :: rapid
REAL(SP), DIMENSION(1:nc_r,1:nt_tot) :: yrapc
INTEGER, DIMENSION(1:nc_r) :: npacr
INTEGER, DIMENSION(1:nt_tot) :: nmul

  if (.not. read_params) &
    stop "Simulation params not set! STOPPING"

  !cccccccccccccccccccccccccccccccccccccccccccccccccccccccc
  !cccc production of particles ccccc
  !cccc in p_t ccccc
  !cccccccccccccccccccccccccccccccccccccccccccccccccccccccc

  !*****
  !** Produce nc_tr clusters in **
  !** transverse momentum **
  !*****
  do ni=1,nc_tr
    ptr= randpt(ptmean) ! get random p_T value
    call random_number(outr)
    fi=2.d0*PI*dbble(outr)
    ctr_x(ni)= ptr * cos(fi)
    ctr_y(ni)= ptr * sin(fi)
  end do
  ! ** calculate mean momenta in x,y
  meanpx = sum(ctr_x)/dbble(nc_tr)
  meanpy = sum(ctr_y)/dbble(nc_tr)
  ! ** center clusters to 0 total momentum
  ctr_x = ctr_x - meanpx
  ctr_y = ctr_y - meanpy

  ipar=0 ! Counter for total number of particles
  do ni=1,nc_tr ! ** For every cluster...
    !*****
    !** Build random walks of D_F in x,y[nt_cl] **
    !*****
    call random_number(roxy) ! Random step sizes
    roxy=pd*(1.d0-c*roxy)**(-1.d0/D_F)
    call random_number(cxy) ! Random step directions
    where (cxy < 0.5d0) ! (+/-1)
      cxy = 1.d0
    elsewhere
      cxy = -1.d0
    end where
    roxy = cxy * roxy ! Steps with their sign
  end do

```

```

! *** Accumulate steps to build x,y random walks
x_n(1) = roxy(1)
y_n(1) = roxy(nt_cl+1)
do mi=2,nt_cl
  x_n(mi) = x_n(mi-1) + roxy(mi)
  y_n(mi) = y_n(mi-1) + roxy(mi + nt_cl)
end do ! mi
! *** Calculate mean momenta in x,y
xmean= sum(x_n)/dble(nt_cl)
ymean= sum(y_n)/dble(nt_cl)
! *** center walks around clusters
x_n = x_n - xmean + ctr_x(ni)
y_n = y_n - ymean + ctr_y(ni)

do mi=1,nt_cl
  ! find cluster index 'inear'
  ! where {x_n(mi),y_n(mi)} is closer
  inear = minloc( (x_n(mi) - ctr_x)**2 + &
                 (y_n(mi) - ctr_y)**2 , 1)
  ! if it's closer to THIS cluster,
  ! put it in the list-- partr_x,y
  if(inear == ni) then
    ipar=ipar+1
    partr_x(ipar)= x_n(mi)
    partr_y(ipar)= y_n(mi)
  end if
end do !mi
end do !ni

mulef=ipar ! Effective multiplicity

!cccccccccccccccccccccccccccccccccccccccccccccccccccccccc
!cccccc Events in rapidity ccccccc
!cccccccccccccccccccccccccccccccccccccccccccccccccccccccc
!*** Allocate random numbers [0,D) to crap
call random_number(crap)
crap = D*crap
crap(0)=0.d0 ! start at 0...
crap(nc_r+1)=D ! ...end at D
call sort(crap) ! sort in ascending order

!***** Calculate rapidity intervals
rleft(1) = min(dc2,crap(1)-crap(0))
rleft(2:nc_r) = min(dc2, 0.5d0*(crap(2:nc_r)-crap(1:nc_r-1)) )
rright(1:nc_r-1)= min(dc2, 0.5d0*(crap(2:nc_r)-crap(1:nc_r-1)) )

```

```

rright(nc_r) = min(dc2,crap(nc_r+1)-crap(nc_r))
raplen = rleft + rright
probra = raplen**D_F
rtole = sum(probra)
probra = probra/rtole

npacr = 0 ! Initialize npacr
do mul_r = 1,mulef
  call random_number(xoutr)
  dlim = 0.d0
  do ni=1,nc_r
    ulim = dlim + probra(ni)
    if(xoutr >= dlim .and. xoutr < ulim) then
      nacl = ni
      exit
    end if
    dlim = dlim + probra(ni) ! update dlim
  end do
  scl = rleft(nacl)**D_F + rright(nacl)**D_F
  pl = rleft(nacl)**D_F / scl
  call random_number(outr1)
  call random_number(outr2)
  dey = dble(outr2)**(-1.d0/D_F)
  if (dble(outr1) < pl) dey = -dey ! Flip sign
  npacr(nacl) = npacr(nacl) + 1
  yrapc(nacl,npacr(nacl)) = dey
end do ! mul_r

do ni=1,nc_r
  ymax = maxval( abs(yrapc(ni,1:npacr(ni))) )

  do npc=1,npacr(ni)
    yrapc(ni,npc)=crap(ni)+yrapc(ni,npc)*dc2/ymax
  end do
end do

mulne=0
do ni=1,nc_r
  do npc=1,npacr(ni)
    mulne=mulne+1
    rapi(mulne)=yrapc(ni,npc)
  end do
end do

call assert(mulne==mulef,'Error in rapidity clusters')

```

```

!cccccccccccccccccccccccccccccccccccccccccccccccccccccccc
!cccc Form the cartesian product cccc
!cccccccccccccccccccccccccccccccccccccccccccccccccccccccc
! * permute nmul = {1,2,...,mulef} *
call random_permut(nmul(1:mulef))
! * subtract D/2 from (permuted) *
! * rapi(1:mulef) *
rapi(nmul(1:mulef)) = rapi(nmul(1:mulef)) - 0.5_sp * D
rapid(1:mulef) = rapi(nmul(1:mulef))
! * Final rapidity vector *

!***** output sigma tracks *****
mult = mulef ! Output event multiplicity

if (associated(sigtracks)) deallocate(sigtracks)
allocate(sigtracks(1:mulef,1:3))

do ml=1,mulef
  xco=partr_x(ml)
  yco=partr_y(ml)
  zco=dsqrt(xco**2+yco**2)*sinh(rapid(ml))
  !**** Convert to GeV ****
  xco = xco/1000.d0
  yco = yco/1000.d0
  zco = zco/1000.d0
  !**** Fill sigma tracks ****
  sigtracks(ml,:) = (/xco,yco,zco/)
end do

return
end subroutine get_sigma_event

function randpt(ptmean)
!*****
!** Gives random pt value **
!** following the distribution **
!**  $g(pt) \sim pt \cdot \exp(-2pt/ptmean)$  **
!*****
!USE nrtype
!implicit none
REAL(SP), intent(in) :: ptmean
REAL(SP) :: randpt
REAL(SP) :: r, r2(2)

```

```

r = 0._sp
do while (r <= 0._sp .or. r > 1._sp)
  call random_number(r2)
  r = product(r2)
end do
randpt = -log(r) * ptmean/2._sp
end function randpt

subroutine random_permut(ind)
!*****
!** Fills vector ind (size n) **
!** with random permutation **
!** of the integers 1->n **
!*****
!USE nrtype
!implicit none
integer, intent(out) :: ind(:)
integer :: k, ns, ni, irnd, iswap
REAL(SP) :: xrand ! random number

ns = size(ind)
ind = (/ (k, k=1,ns) /) ! ind = {1->ns}
ni = ns
do k = 1, ns-1
  call random_number(xrand) ! Random number [0,1)
  irnd = int(REAL(ni,SP)*xrand) + 1 ! irnd: [1->ni]
  irnd = max(1, min(irnd,ni)) ! Just in case...
  iswap = ind(k) ! Swap ind(k)
  ind(k) = ind(k+irnd-1) ! with ind(k+irnd-1)
  ind(k+irnd-1) = iswap
  ni = ni-1 ! Decrease size left
end do !k

end subroutine random_permut

end module mod_sigma

```

## B.2 CMC code for protons

Next follows the modified CMC code used for critical proton cluster simulation. The function `randpt` from “vanilla” CMC code is re-used.

```

program cmc_proton
USE nrtype
implicit none
integer, parameter :: nevmax = 150000
REAL(SP), parameter :: Tc = 163.0e-3_SP, ptmean = 2*Tc
REAL(SP), parameter :: dF = 1._SP / 6._SP
REAL(SP), parameter :: rdF = 1._SP / dF, &
                    lmin = 5.0e-4_SP, &
                    lmax = 5.0e-1_SP, &
                    smin = lmin**(-dF), &
                    smax = lmax**(-dF)
REAL(SP) :: ctr_x, ctr_y, ptr, fi
REAL(SP) :: outr, skew, cskew, sskew
REAL(SP) :: rmul1 = 1._SP/3._SP, rmul9 = 0.98
integer :: mul, nev
integer :: k,m
!
REAL(SP), target :: dir(3,2), step(3,2)
REAL(SP), pointer, dimension(:,:) :: pdir, pstep

call init_random_seed()
open (unit=10, file="mcsisidf.dat",&
      status="REPLACE",action="WRITE")

do nev = 1, nevmax

!*****
!***          Put cluster center          ***
!*****
ptr = randpt(ptmean) ! get random p_T value
call random_number(outr)
fi=2.d0*PI*dble(outr)
ctr_x = ptr * cos(fi)
ctr_y = ptr * sin(fi)

!*****
!***          Select multiplicity          ***
!*****
call random_number(outr)
if (outr < rmul1) then
    mul = 1
else if (outr > rmul9) then
    mul = 3
else
    mul = 2

```

```

end if

write (10,"(2('\t',I0))") nev, mul**2

!*****
!***      Create random walk      ***
!*****
pdir => dir(1:mul,1:2)
pstep => step(1:mul,1:2)
call random_number(pdir)
where (pdir < 0.5_SP)
  pdir = 1._SP
elsewhere
  pdir = -1._SP
end where
call random_number(pstep)
pstep=(smin*(1._SP-pstep)+smax*pstep)**(-rdF)
pstep = pdir * pstep
call tally(pstep(:,1))
call tally(pstep(:,2))

call random_number(skew)
skew=2.d0*PI*dbble(skew)
cskew = cos(skew)
sskew = sin(skew)

!*****
!***      Write event to file      ***
!*****
do k = 1, mul
  do m = 1, mul
    write (10,66) &
      ctr_x + cskew * pstep(k,1) - &
        sskew * pstep(m,2), &
      ctr_y + sskew * pstep(k,1) + &
        cskew * pstep(m,2)
66      format (2('\t',F0.4))
  end do
end do

end do !nev

close (10)

contains

```

```

subroutine tally(arr,off)
REAL(SP), intent(inout) :: arr(:)
REAL(SP), intent(in), optional :: off
integer :: n

do n = 2, size(arr)
    arr(n) = arr(n-1) + arr(n)
end do
if (present(off)) arr = off + arr
return
end subroutine tally

SUBROUTINE init_random_seed()
    INTEGER :: i, n, clock
    INTEGER, DIMENSION(:), ALLOCATABLE :: seed

    CALL RANDOM_SEED(size = n)
    ALLOCATE(seed(n))

    CALL SYSTEM_CLOCK(COUNT=clock)

    seed = clock + 37 * (/ (i - 1, i = 1, n) /)
    CALL RANDOM_SEED(PUT = seed)

    DEALLOCATE(seed)
END SUBROUTINE

end program cmc_proton

```

### B.3 Numerical recipes auxiliary code

CMC code utilizes some auxiliary modules from *Numerical Recipes for Fortran 90* [Press et al., 1996]. Specifically:

1. `nrtype` defines portable floating point types, as well as basic mathematical constants.
2. `nrutil` is a collection of common utilities for various tasks, i.e. swapping variables and terminating execution with appropriate error messages.
3. `nr` is a list of routine interfaces.

```

MODULE nrtype
  !Symbolic names for kind types of 8-, 4-, 2-, and 1-byte integers:
  INTEGER, PARAMETER :: I8B = SELECTED_INT_KIND(15)
  INTEGER, PARAMETER :: I4B = SELECTED_INT_KIND(9)
  INTEGER, PARAMETER :: I2B = SELECTED_INT_KIND(4)
  INTEGER, PARAMETER :: I1B = SELECTED_INT_KIND(2)
  !Symbolic names for kind types of single- and double-precision reals:
  INTEGER, PARAMETER :: SP = KIND(1.0D0)
  INTEGER, PARAMETER :: DP = SELECTED_REAL_KIND(18,300)
  !Symbolic names for kind types of single- and double-precision complex:
  INTEGER, PARAMETER :: SPC = KIND((1.0D0,1.0D0))
  INTEGER, PARAMETER :: DPC = SELECTED_REAL_KIND(18,300)
  !Symbolic name for kind type of default logical:
  INTEGER, PARAMETER :: LGT = KIND(.true.)
  !Frequently used mathematical constants (with precision to spare):
  REAL(SP), PARAMETER :: PI=3.141592653589793238462643383279502884197_sp
  REAL(SP), PARAMETER :: PI02=1.57079632679489661923132169163975144209858_sp
  REAL(SP), PARAMETER :: TWOPI=6.283185307179586476925286766559005768394_sp
  REAL(SP), PARAMETER :: SQRT2=1.41421356237309504880168872420969807856967_sp
  REAL(SP), PARAMETER :: EULER=0.5772156649015328606065120900824024310422_sp
  REAL(DP), PARAMETER :: PI_D=3.141592653589793238462643383279502884197_dp
  REAL(DP), PARAMETER :: PI02_D=1.57079632679489661923132169163975144209858_dp
  REAL(DP), PARAMETER :: TWOPI_D=6.283185307179586476925286766559005768394_dp
  ! Derived data types for sparse matrices, single and double precision
  ! (see use in Chapter B2):
  TYPE sprs2_sp
    INTEGER(I4B) :: n,len
    REAL(SP), DIMENSION(:), POINTER :: val
    INTEGER(I4B), DIMENSION(:), POINTER :: irow
    INTEGER(I4B), DIMENSION(:), POINTER :: jcol
  END TYPE sprs2_sp
  TYPE sprs2_dp
    INTEGER(I4B) :: n,len
    REAL(DP), DIMENSION(:), POINTER :: val
    INTEGER(I4B), DIMENSION(:), POINTER :: irow
    INTEGER(I4B), DIMENSION(:), POINTER :: jcol
  END TYPE sprs2_dp
END MODULE nrtype

MODULE nrutil
  USE nrtype
  IMPLICIT NONE
  INTERFACE swap
    MODULE PROCEDURE swap_i,swap_r,swap_rv,swap_c, &
      swap_cv,swap_cm,swap_z,swap_zv,swap_zm
  END INTERFACE

```

**END INTERFACE**

**INTERFACE** assert

**MODULE PROCEDURE** assert1,assert2,assert3,assert4,assert\_v

**END INTERFACE**

**SUBROUTINE** nrerror(string)

    ! *Report a message, then die.*

**CHARACTER**(LEN=\*), **INTENT**(IN) :: string

**write** (\*,\*) 'nrerror: ',string

**STOP** 'program terminated by nrerror'

**END SUBROUTINE** nrerror

**SUBROUTINE** assert1(n1,string)

    ! *Report and die if any logical is false (used for arg range checking).*

**CHARACTER**(LEN=\*), **INTENT**(IN) :: string

**LOGICAL**, **INTENT**(IN) :: n1

**if** (.not. n1) **then**

**write** (\*,\*) 'nrerror: an assertion failed with this tag:', &  
            string

**STOP** 'program terminated by assert1'

**end if**

**END SUBROUTINE** assert1

**SUBROUTINE** assert2(n1,n2,string)

**CHARACTER**(LEN=\*), **INTENT**(IN) :: string

**LOGICAL**, **INTENT**(IN) :: n1,n2

**if** (.not. (n1 .and. n2)) **then**

**write** (\*,\*) 'nrerror: an assertion failed with this tag:', &  
            string

**STOP** 'program terminated by assert2'

**end if**

**END SUBROUTINE** assert2

**SUBROUTINE** assert3(n1,n2,n3,string)

**CHARACTER**(LEN=\*), **INTENT**(IN) :: string

**LOGICAL**, **INTENT**(IN) :: n1,n2,n3

**if** (.not. (n1 .and. n2 .and. n3)) **then**

**write** (\*,\*) 'nrerror: an assertion failed with this tag:', &  
            string

**STOP** 'program terminated by assert3'

**end if**

**END SUBROUTINE** assert3

**SUBROUTINE** assert4(n1,n2,n3,n4,string)

```
CHARACTER(LEN=*), INTENT(IN) :: string
LOGICAL, INTENT(IN) :: n1,n2,n3,n4
if (.not. (n1 .and. n2 .and. n3 .and. n4)) then
    write (*,*) 'nrerror: an assertion failed with this tag:', &
        string
    STOP 'program terminated by assert4'
end if
END SUBROUTINE assert4
```

```
SUBROUTINE assert_v(n,string)
CHARACTER(LEN=*), INTENT(IN) :: string
LOGICAL, DIMENSION(:), INTENT(IN) :: n
if (.not. all(n)) then
    write (*,*) 'nrerror: an assertion failed with this tag:', &
        string
    STOP 'program terminated by assert_v'
end if
END SUBROUTINE assert_v
```

```
SUBROUTINE swap_i(a,b)
!   Swap the contents of a and b.
INTEGER(I4B), INTENT(INOUT) :: a,b
INTEGER(I4B) :: dum
dum=a
a=b
b=dum
END SUBROUTINE swap_i
```

```
SUBROUTINE swap_r(a,b)
REAL(SP), INTENT(INOUT) :: a,b
REAL(SP) :: dum
dum=a
a=b
b=dum
END SUBROUTINE swap_r
```

```
SUBROUTINE swap_rv(a,b)
REAL(SP), DIMENSION(:), INTENT(INOUT) :: a,b
REAL(SP), DIMENSION(SIZE(a)) :: dum
dum=a
a=b
b=dum
END SUBROUTINE swap_rv
```

```
SUBROUTINE swap_c(a,b)
```

```
COMPLEX(SPC), INTENT(INOUT) :: a,b  
COMPLEX(SPC) :: dum  
dum=a  
a=b  
b=dum  
END SUBROUTINE swap_c
```

```
SUBROUTINE swap_cv(a,b)  
COMPLEX(SPC), DIMENSION(:), INTENT(INOUT) :: a,b  
COMPLEX(SPC), DIMENSION(SIZE(a)) :: dum  
dum=a  
a=b  
b=dum  
END SUBROUTINE swap_cv
```

```
SUBROUTINE swap_cm(a,b)  
COMPLEX(SPC), DIMENSION(:,:), INTENT(INOUT) :: a,b  
COMPLEX(SPC), DIMENSION(size(a,1),size(a,2)) :: dum  
dum=a  
a=b  
b=dum  
END SUBROUTINE swap_cm
```

```
SUBROUTINE swap_z(a,b)  
COMPLEX(DPC), INTENT(INOUT) :: a,b  
COMPLEX(DPC) :: dum  
dum=a  
a=b  
b=dum  
END SUBROUTINE swap_z
```

```
SUBROUTINE swap_zv(a,b)  
COMPLEX(DPC), DIMENSION(:), INTENT(INOUT) :: a,b  
COMPLEX(DPC), DIMENSION(SIZE(a)) :: dum  
dum=a  
a=b  
b=dum  
END SUBROUTINE swap_zv
```

```
SUBROUTINE swap_zm(a,b)  
COMPLEX(DPC), DIMENSION(:,:), INTENT(INOUT) :: a,b  
COMPLEX(DPC), DIMENSION(size(a,1),size(a,2)) :: dum  
dum=a  
a=b  
b=dum
```

```
END SUBROUTINE swap_zm
```

```
END MODULE nrutil
```

```
MODULE nr
```

```
INTERFACE
```

```
  SUBROUTINE sort(arr)
```

```
  USE nrtype
```

```
  REAL(SP), DIMENSION(:), INTENT(INOUT) :: arr
```

```
  END SUBROUTINE sort
```

```
END INTERFACE
```

```
END MODULE nr
```

```
SUBROUTINE sort(arr)
```

```
USE nrtype; USE nrutil, ONLY : swap,nrerror
```

```
IMPLICIT NONE
```

```
REAL(SP), DIMENSION(:), INTENT(INOUT) :: arr
```

```
INTEGER(I4B), PARAMETER :: NN=15, NSTACK=50
```

```
! Sorts an array arr into ascending numerical order
```

```
! using the Quicksort algorithm. arr is replaced on
```

```
! output by its sorted rearrangement.
```

```
! Parameters: NN is the size of subarrays sorted by
```

```
! straight insertion and NSTACK is the
```

```
! required auxiliary storage.
```

```
REAL(SP) :: a
```

```
INTEGER(I4B) :: n,k,i,j,jstack,l,r
```

```
INTEGER(I4B), DIMENSION(NSTACK) :: istack
```

```
n=size(arr)
```

```
jstack=0
```

```
l=1
```

```
r=n
```

```
do
```

```
  if (r-l < NN) then
```

```
    !Insertion sort when
```

```
    do j=l+1,r
```

```
    !subarray small enough.
```

```
      a=arr(j)
```

```
      do i=j-1,l,-1
```

```
        if (arr(i) <= a) exit
```

```
        arr(i+1)=arr(i)
```

```
      end do
```

```
      arr(i+1)=a
```

```
    end do
```

```
    if (jstack == 0) RETURN
```

```
    r=istack(jstack)
```

```
    !Pop stack and begin a
```

```
    l=istack(jstack-1)
```

```
    !new round of partitioning.
```

```

      jstack=jstack-2
    else
      k=(l+r)/2
      call swap(arr(k),arr(l+1))
      call swap(arr(l),arr(r),arr(l)>arr(r))
      call swap(arr(l+1),arr(r),arr(l+1)>arr(r))
      call swap(arr(l),arr(l+1),arr(l)>arr(l+1))
      i=l+1
      j=r
      a=arr(l+1)
      do
        do
          i=i+1
          if (arr(i) >= a) exit
        end do
        do
          j=j-1
          if (arr(j) <= a) exit
        end do
        if (j < i) exit
        call swap(arr(i),arr(j))
      end do
      arr(l+1)=arr(j)
      arr(j)=a
      jstack=jstack+2
      ! Push pointers to larger subarray on stack;
      ! process smaller subarray immediately.
      if (jstack > NSTACK) call nrerror('sort: NSTACK too small')
      if (r-i+1 >= j-l) then
        istack(jstack)=r
        istack(jstack-1)=i
        r=j-1
      else
        istack(jstack)=j-1
        istack(jstack-1)=l
        l=i
      end if
    end if
  end do
END SUBROUTINE sort

```

## APPENDIX C

### APPLIED CUTS FOR THE NA49 DATA SETS

#### C.1 “Si”+Si, 158A GeV

##### Event cuts

The primary event cuts imposed were removal of the tails in the distributions of vertex positions ( $V_x, V_y, V_z$ ), as well as quality cuts (iflag,  $\chi^2$ , ntf/nto). Veto calorimeter energy was used to select 12.5% most central events, i.e. the 1st and 2nd centrality bins:

- iflag = 1
- $\chi^2 > 0$
- $-0.4 \text{ cm} \leq V_x \leq 0.4 \text{ cm}$
- $-0.5 \text{ cm} \leq V_y \leq 0.5 \text{ cm}$
- $-580.3 \text{ cm} \leq V_z \leq -578.7 \text{ cm}$
- #Tracks fitted / #Tracks output (ntf/nto)  $\geq 0.15$
- Centrality  $\leq 12.5\%$  (1st, 2nd bin)

The “Si” beam is made up of Si, Al and P ions. During analysis, we extracted each beam component separately, by gaussian-fitting the peaks in the beam energy profile:

- Al+Si  $\rightarrow$  Beam Energy  $\in [1256, 1344]$
- Si+Si  $\rightarrow$  Beam Energy  $\in [1350, 1450]$
- P+Si  $\rightarrow$  Beam Energy  $\in [1460, 1546]$

Fig.C.1 shows a summary of the “Si”+Si dataset vertex cuts. Fig.C.2 shows the veto energy distribution for each beam component, and the divide between centrality bins.

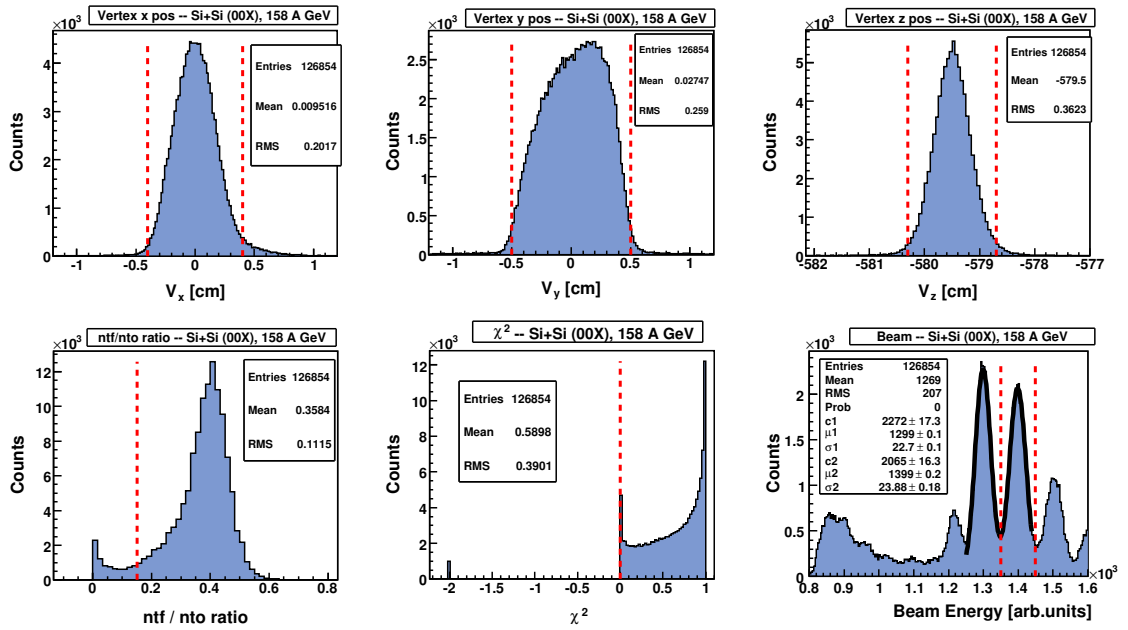


**Figure C.1:** Summary of the "Si"+Si vertex cuts. Top row: vertex position distributions (dotted red lines show selection cuts). Bottom row: Vertex quality cuts (left) and beam component selection (right). See text for details.

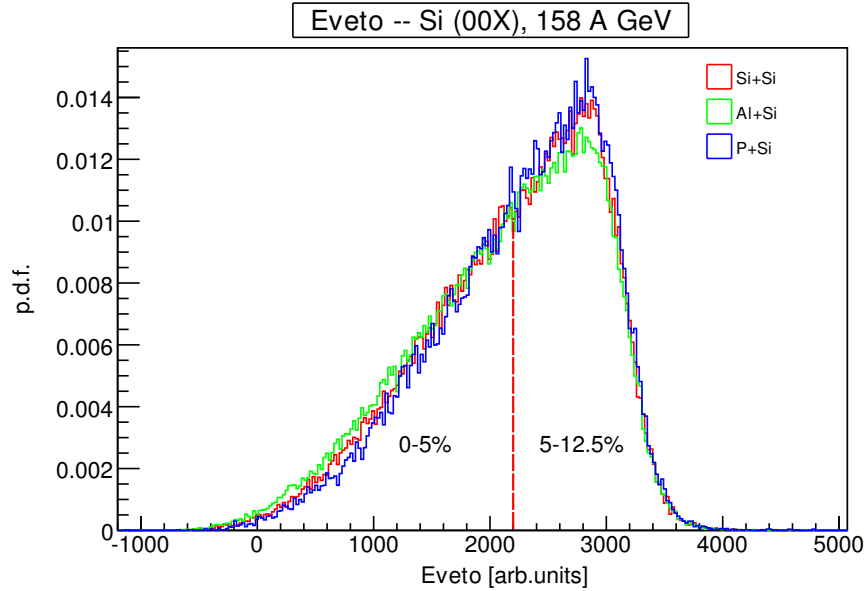


**Figure C.2:** Normalized veto energy distribution for "Si"+Si

### Track cuts

The primary track cuts were a restriction in the maximum impact parameter ( $B_x, B_y$ ), a cut on zFirst in order to ensure the track has points in the VTPCs, as well as requiring a minimum number of reconstructed points on each track and a minimum ratio of number of measured points to estimated maximum number of points (np/nmp):

- $|B_x| < 2$  cm
- $|B_y| < 1$  cm
- zFirst  $\leq 200$  cm
- #Maximum number of points (nmp)  $> 30$
- #Points / #Maximum number of points: np / nmp  $> 0.5$

### Particle ID, $p_{tot}$ cuts

Particle identification is performed via the particle energy loss  $dE/dx$ . In Fig.C.3,  $dE/dx$  is plotted vs the total momentum  $p_{tot}$ , along with the theoretical curves for each particle species, and the proton selection bands. We select candidate protons with purity above 80%, as described in section 5.3.2.  $p_{tot}$  is restricted to the region where the proton curve does not overlap with other species curves, and therefore we impose an indirect cut:

- $3 \leq p_{tot} \leq 50$  GeV/c

### Rapidity distributions

In Fig.C.4, we show the rapidity distributions of protons for all beam components of the “Si”+Si system. Our intermittency analysis is performed in the midrapidity region:

- $|y_{CM}| \leq 0.75 \iff 2.16 \leq y_{LAB} \leq 3.66$  ( $y_{beam} \approx 2.91$ ),

and therefore within the plateau of the rapidity distribution.

## C.2 “C”+C, 158A GeV

The “C”+C set consists of a 3mm and a 10mm target thickness set, which we have merged for the purposes of this analysis, in order to enhance event statistics.

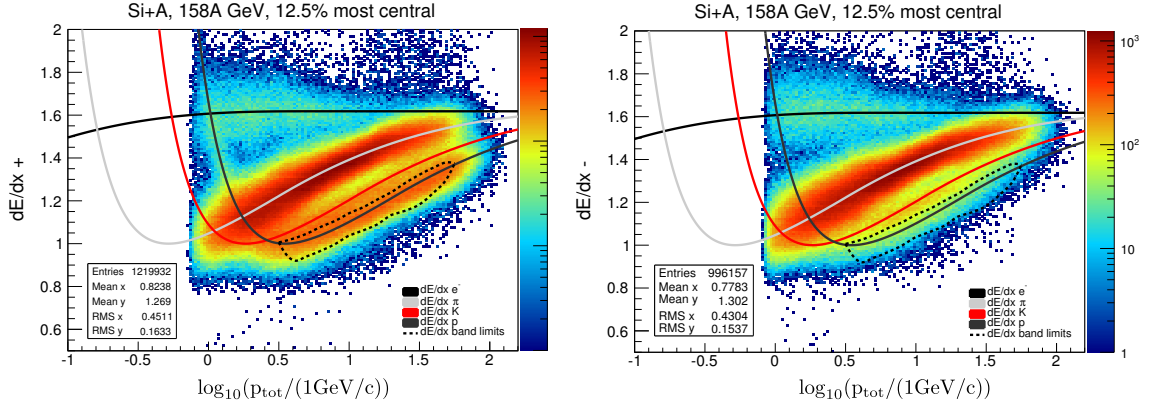


**Figure C.3:**  $dE/dx$  vs  $p_{tot}$  distributions for positive and negative charged particles in the “Si”+Si system. The dotted line contour delimits an 80% purity selection of candidate proton tracks

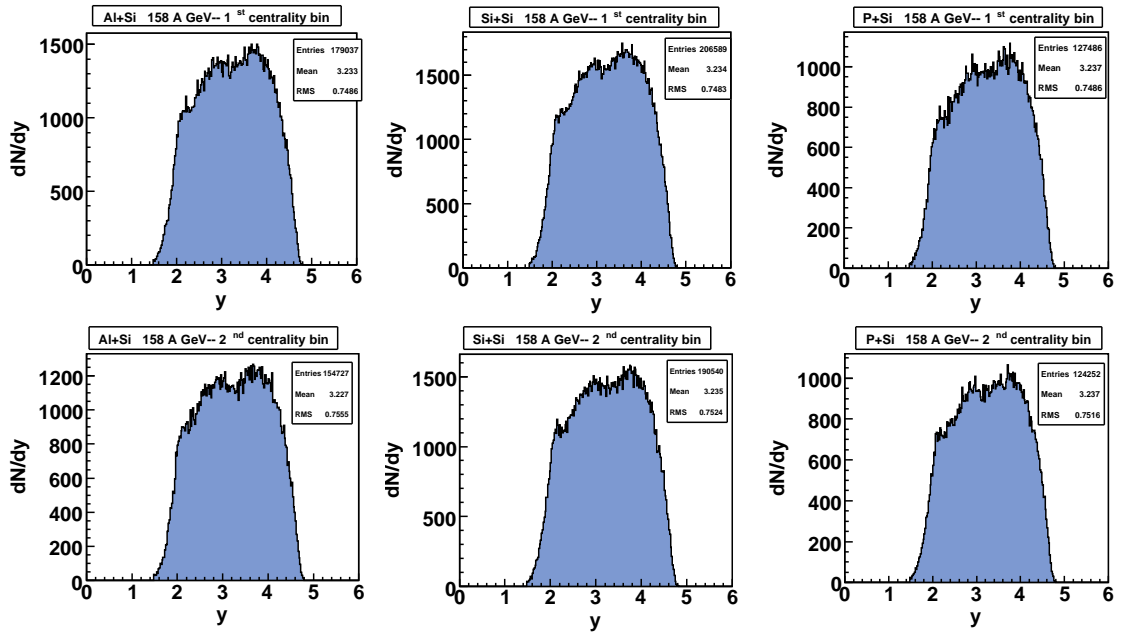


**Figure C.4:** Proton rapidity distributions for beam components in the “Si”+Si dataset

### Event cuts

Most event cuts are the same as in the “Si”+Si set. Vertex position cuts applied, in the 3mm target set, are:

- $-0.5 \text{ cm} \leq V_x \leq 0.7 \text{ cm}$
- $-0.6 \text{ cm} \leq V_y \leq 0.6 \text{ cm}$
- $-581.0 \text{ cm} \leq V_z \leq -578.0 \text{ cm}$

and, in the 10mm target set:

- $-0.5 \text{ cm} \leq V_x \leq 0.7 \text{ cm}$
- $-0.6 \text{ cm} \leq V_y \leq 0.6 \text{ cm}$
- $-580.5 \text{ cm} \leq V_z \leq -577.5 \text{ cm}$

The “C” beam is made up of C and N ions. During analysis, we extracted each beam component separately, by gaussian-fitting the peaks in the beam energy profile:

- C+C  $\rightarrow$  Beam Energy  $\in [570, 670]$
- C+N  $\rightarrow$  Beam Energy  $\in [670, 740]$

Figs.C.5,C.6 show a summary of the “C”+C 3mm and 10mm dataset vertex cuts, respectively. Fig.C.7 shows veto energy distributions and the divide between centrality bins.

### Track cuts

The same track cuts were applied as in the case of “Si”+Si.

### Particle ID, $p_{tot}$ cuts

Particle identification was performed in an identical manner as with “Si”+Si. The  $p_{tot}$  cut effected by  $dE/dx$  cuts was:

- $3 \leq p_{tot} \leq 56 \text{ GeV}/c$

### Rapidity distributions

Rapidity distribution of candidate protons was very similar to that of “Si”+Si, and we used the same midrapidity range,  $|y_{CM}| \leq 0.75$ .

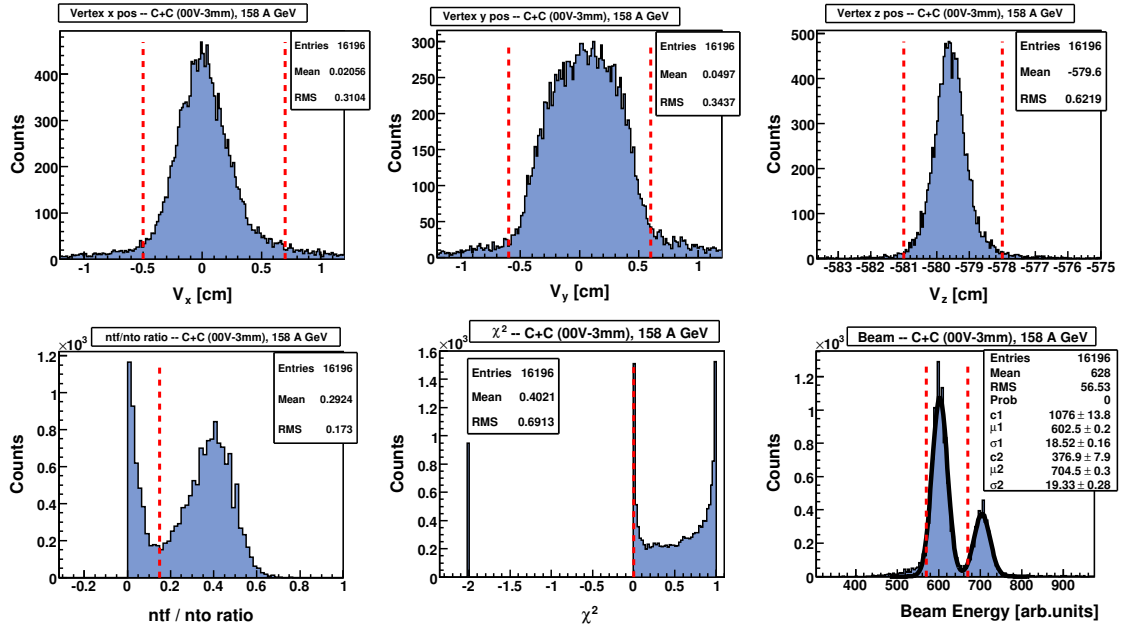


Figure C.5: Summary of the "C"+C 3mm vertex cuts

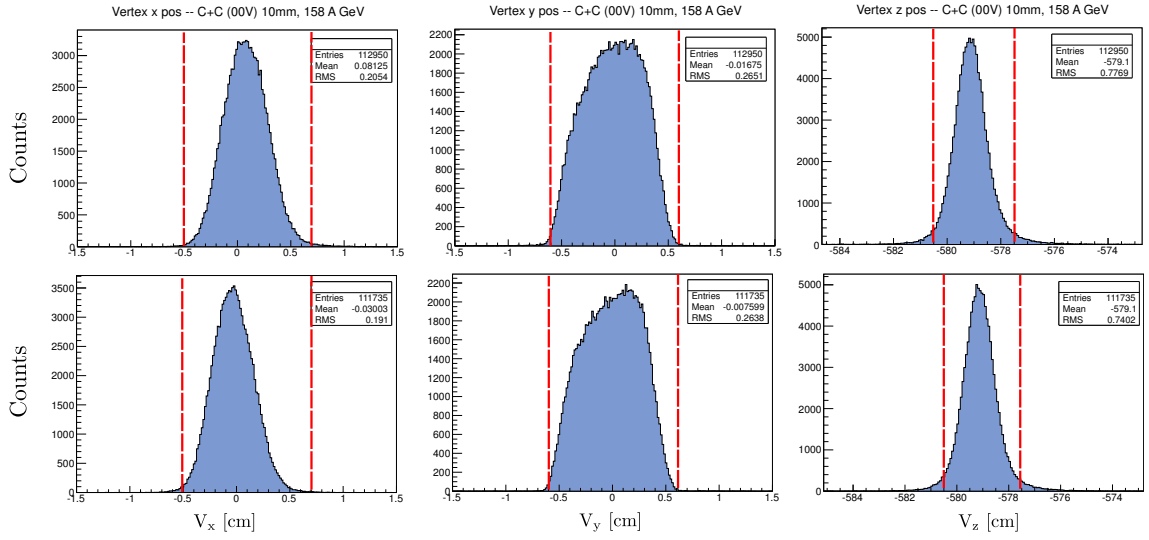


Figure C.6: Summary of the "C"+C 10mm vertex cuts

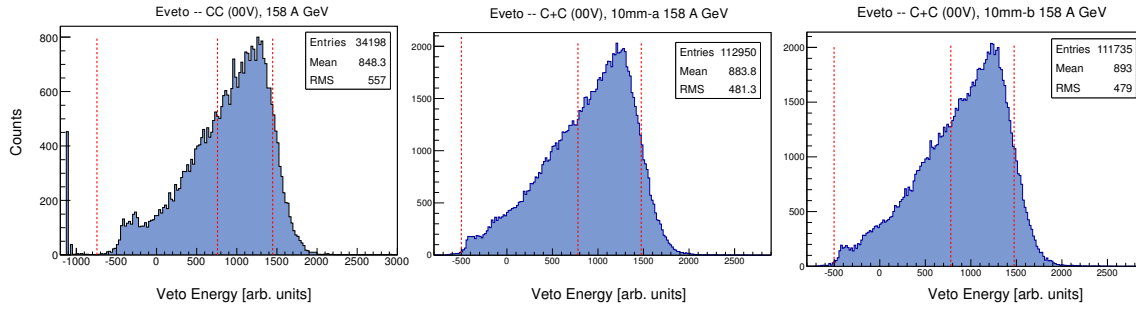


Figure C.7: Veto energy distributions for “C”+C

### C.3 Pb+Pb low-intensity (00B), 158A GeV

#### Event cuts

- iflag = 1
- $\chi^2 > 0$
- $-0.1 \text{ cm} \leq V_x \leq 0.04 \text{ cm}$
- $-0.1 \text{ cm} \leq V_y \leq 0.1 \text{ cm}$
- $-579.3 \text{ cm} \leq V_z \leq -578.6 \text{ cm}$
- #Tracks fitted, ntf  $\geq 400$
- #Tracks output, nto  $\leq 2800$
- Centrality  $\leq 10\%$  (1st, 2nd bin)

Fig.C.8 shows the vertex cuts applied in Pb+Pb. The ntf/nto cut is shown in Fig.C.9. Finally, the veto energy distribution and cut is shown in Fig.C.10.

#### Track cuts

In addition to the zFirst cut, a zLast cut was applied to the Pb+Pb tracks in order to ensure there are measured points in the MTPCs. Furthermore, we demanded a minimum number of points separately in the VTPCs and MTPCs.

Full list of cuts:

- $|B_x| < 5 \text{ cm}$
- $|B_y| < 2 \text{ cm}$

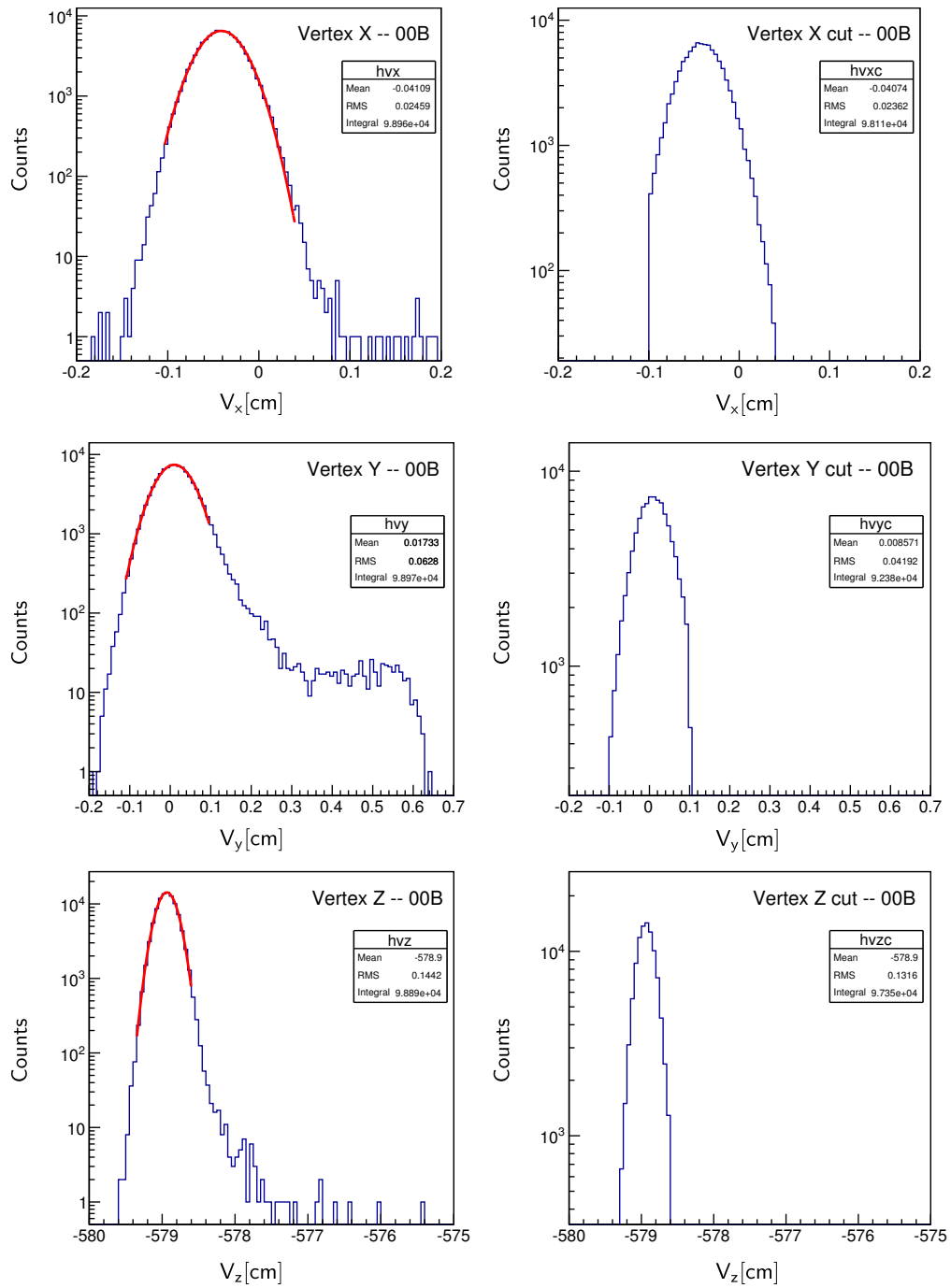


Figure C.8: Summary of the Pb+Pb vertex cuts

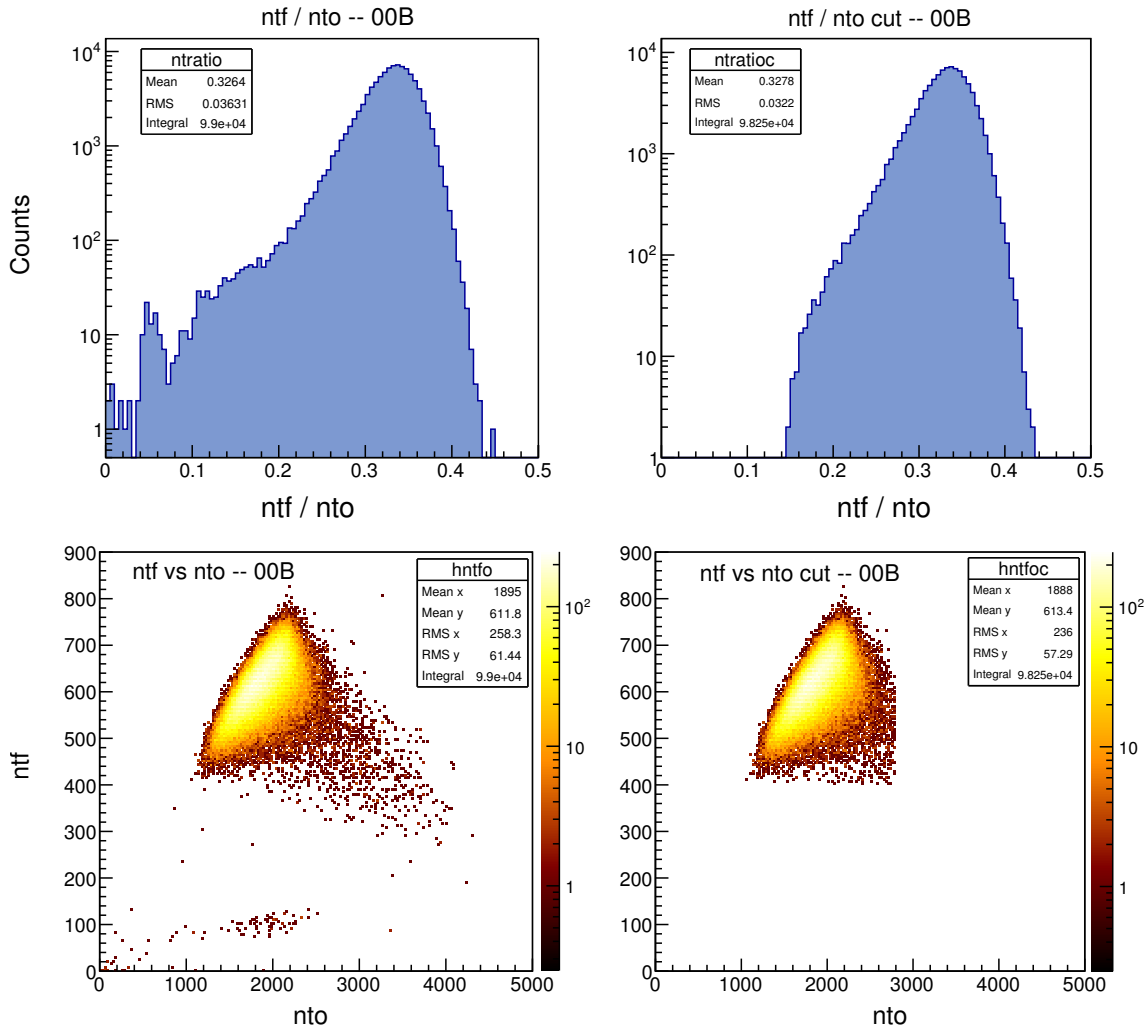
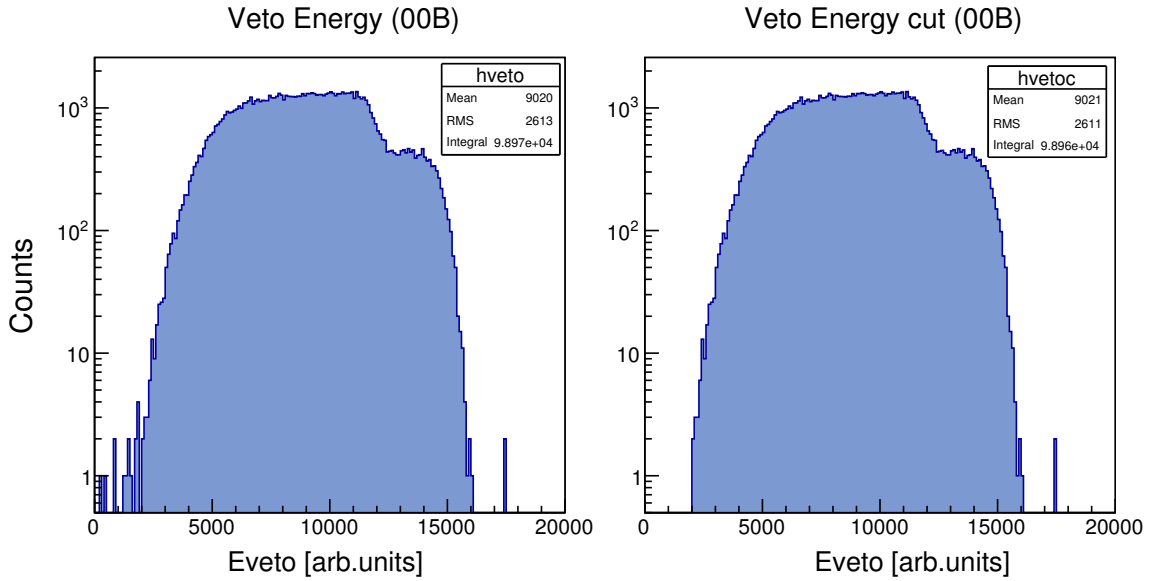


Figure C.9: Summary of the ntf-nto cuts in Pb+Pb



**Figure C.10:** Veto energy distribution for Pb+Pb

- $z_{\text{First}} \leq 200$  cm
- $z_{\text{Last}} \geq 400$  cm
- At least 30 recorded points in the MTPCs
- At least 10 recorded points in VTPC1 or VTPC2
- #Maximum number of points in MTPCs  $> 0$
- $n_p/n_{mp}$  in the MTPCs  $> 0.55$

The effect of the various track cuts is illustrated in Figs.C.11-C.14.

#### Particle ID, $p_{tot}$ cuts

Particle identification is again performed via particle energy loss  $dE/dx$ . In Fig.C.15,  $dE/dx$  is plotted vs the total momentum  $p_{tot}$ , along with the theoretical curves for each particle species, and the proton selection bands. We select candidate protons with purity above 90%, as described in section 5.3.2.  $p_{tot}$  is restricted by the  $dE/dx$  cut within the range:

- $4.4 \leq p_{tot} \leq 66$  GeV/c

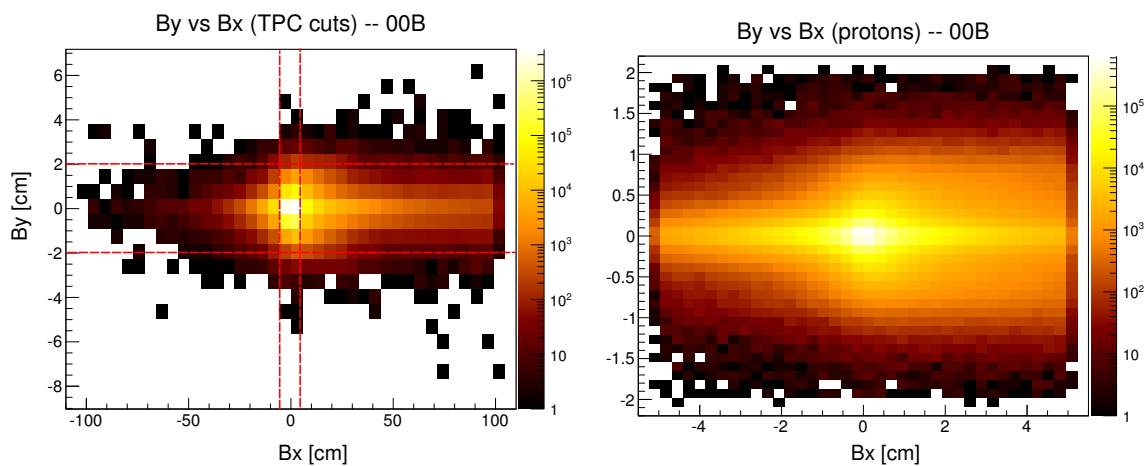


Figure C.11: Impact parameter ( $B_x, B_y$ ) cuts for Pb+Pb

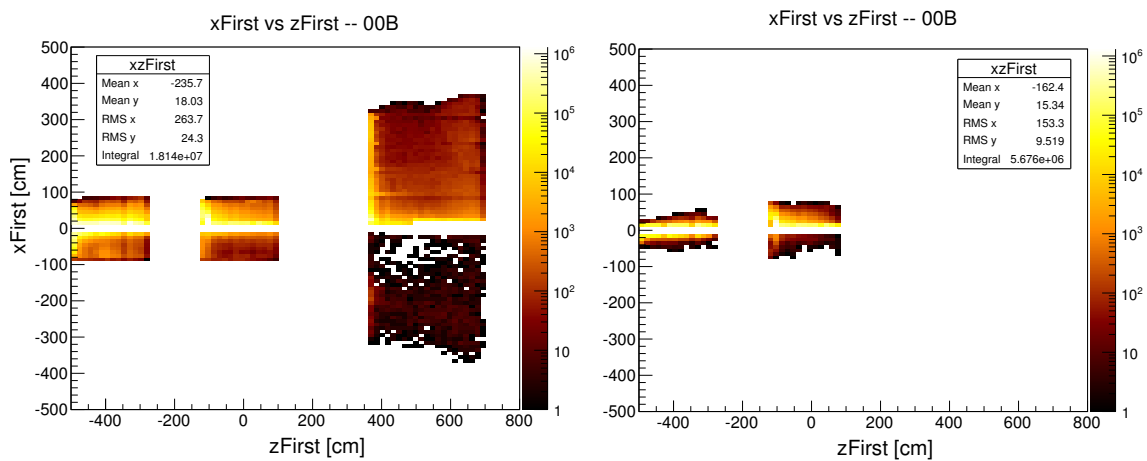


Figure C.12: Effect of the  $z_{\text{First}}$  cut on track selection in the  $X$ - $Z$  plane, for Pb+Pb

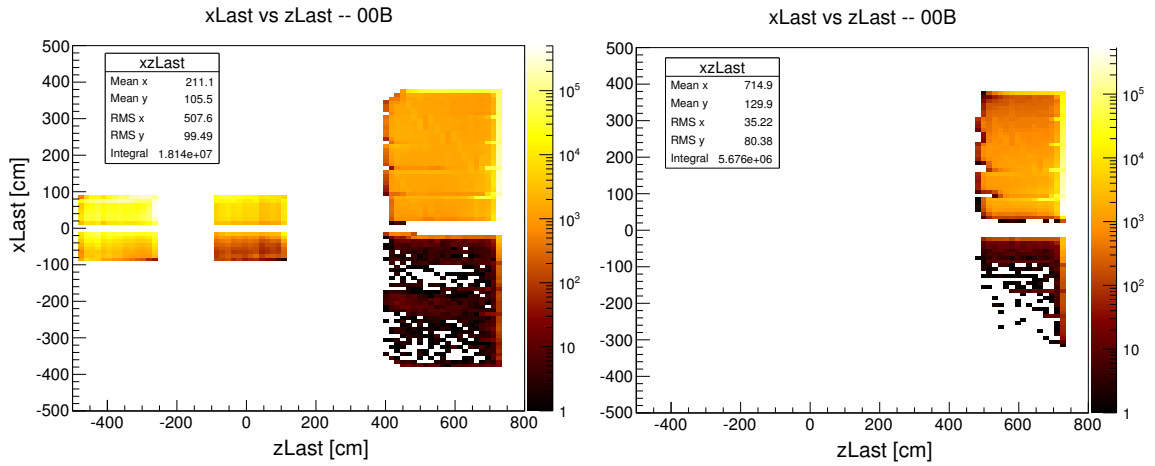


Figure C.13: Effect of the  $z_{\text{Last}}$  cut on track selection in the X-Z plane, for Pb+Pb

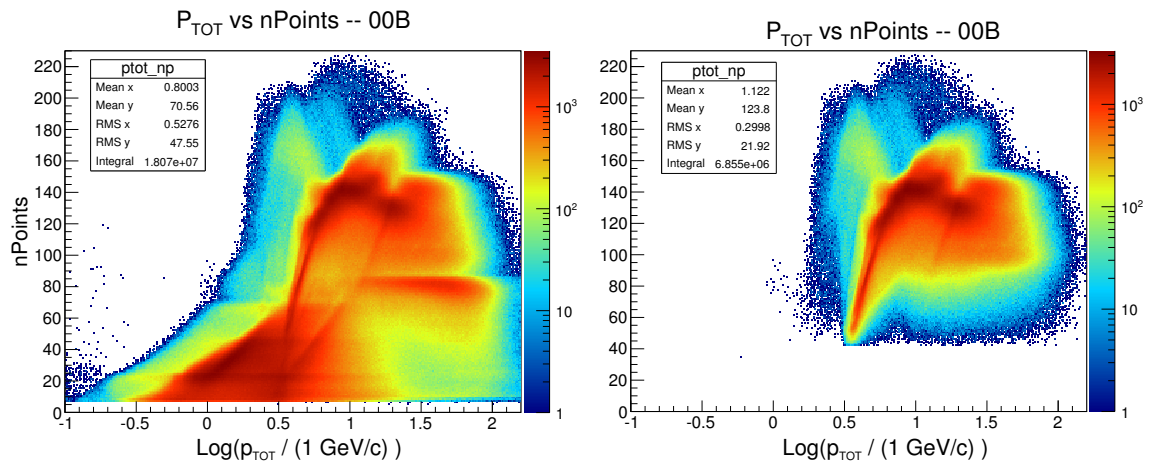
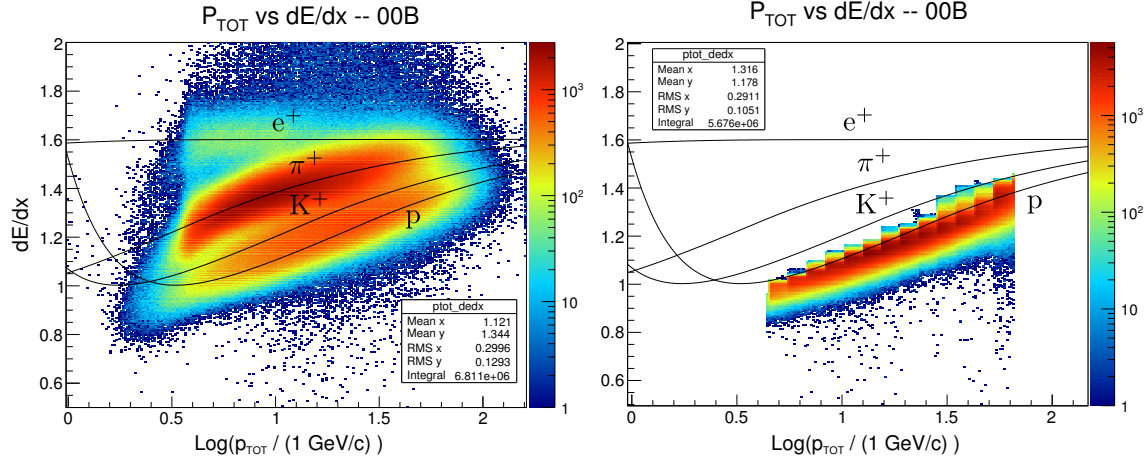


Figure C.14: Effect of the cut on number of points in the TPCs, as a function of total momentum  $p_{\text{tot}}$ , for Pb+Pb



**Figure C.15:**  $dE/dx$  vs  $p_{tot}$  distribution, before and after cuts, for positive charged particles in the Pb+Pb system. A 90% purity selection of candidate proton tracks is effected.

## C.4 Rapidity profiles and cuts for analyzed systems

In Fig.C.16, we plot the normalized rapidity distributions of protons for all analyzed systems, along with our selection range,  $|y_{CM}| < 0.75$ . We notice that, for the “C”+C and “Si”+Si systems, the midrapidity range approximately coincides with the plateau in  $dN/dy_{CM}$ , whereas for Pb+Pb there is a very narrow plateau that is only partially covered by the midrapidity selection. However, we are looking here at the rapidity distribution *after* event and track cuts; it is strongly expected that the corrected rapidity distribution, accounting for distortions due to the detector acceptance and cuts, would give a plateau around midrapidity. In order to have a better comparable set of analyzed systems, we chose to use the same midrapidity range for all analyzed systems.

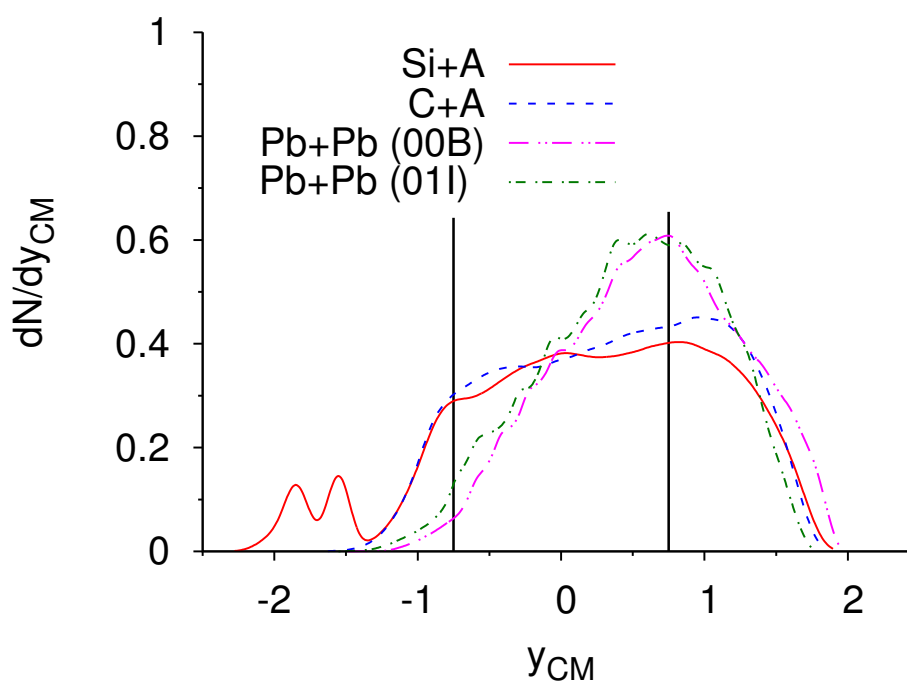


**Figure C.16:** Normalized rapidity distributions for “C”+C, “Si”+Si and Pb+Pb systems (protons). The rapidity  $y_{CM}$  is given in the C.M. frame.

# Bibliography

- N. Abgrall et al. NA61/SHINE facility at the CERN SPS: beams and detector system. *JINST*, 9:P06005, 2014. doi: 10.1088/1748-0221/9/06/P06005, 1401.4699.
- S. Abreu, et al. Heavy Ion Collisions at the LHC - Last Call for Predictions. *ArXiv e-prints*, November 2007, 0711.0974.
- Hiroaki Abuki, Tetsuo Hatsuda, and Kazunori Itakura. Structural change of Cooper pairs and momentum dependent gap in color superconductivity. *Phys.Rev.*, D65:074014, 2002. doi: 10.1103/PhysRevD.65.074014, hep-ph/0109013.
- S. Afanasiev, et al. The NA49 large acceptance hadron detector. *Nuclear Instruments and Methods in Physics Research Section A: Accelerators, Spectrometers, Detectors and Associated Equipment*, 430(2–3):210 – 244, 1999. ISSN 0168-9002. doi: [http://dx.doi.org/10.1016/S0168-9002\(99\)00239-9](http://dx.doi.org/10.1016/S0168-9002(99)00239-9). URL <http://www.sciencedirect.com/science/article/pii/S0168900299002399>.
- Mark G. Alford, Andreas Schmitt, Krishna Rajagopal, and Thomas Schäfer. Color superconductivity in dense quark matter. *Rev.Mod.Phys.*, 80:1455–1515, 2008. doi: 10.1103/RevModPhys.80.1455, 0709.4635.
- C. Alt et al. Pion and kaon production in central Pb + Pb collisions at 20-A and 30-A-GeV: Evidence for the onset of deconfinement. *Phys.Rev.*, C77:024903, 2008. doi: 10.1103/PhysRevC.77.024903, 0710.0118.
- T. Anticic, et al. Search for the QCD critical point in nuclear collisions at 158A GeV at the CERN Super Proton Synchrotron (SPS). *Phys. Rev. C*, 81(6):064907, June 2010. doi: 10.1103/PhysRevC.81.064907, 0912.4198.
- T. Anticic, et al.  $K^*(892)^0$  and  $K^{*-}(892)^0$  production in central Pb + Pb, Si + Si, C + C, and inelastic p + p collisions at 158A GeV. *Phys. Rev. C*, 84(6):064909, December 2011a. doi: 10.1103/PhysRevC.84.064909, 1105.3109.

- T. Anticic et al. Proton - Lambda Correlations in Central Pb+Pb Collisions at  $\sqrt{s_{NN}} = 17.3$  GeV. *Phys. Rev. C*, 83:054906, 2011b. doi: 10.1103/PhysRevC.83.054906, 1103.3395.
- N. G. Antoniou, F. K. Diakonou, and A. S. Kapoyannis. Net-baryon scaling near the QCD critical point. *ArXiv High Energy Physics - Phenomenology e-prints*, December 2000, hep-ph/0012163.
- N. G. Antoniou, Y. F. Contoyiannis, F. K. Diakonou, A. I. Karanikas, and C. N. Ktorides. Pion production from a critical QCD phase. *Nuclear Physics A*, 693:799–824, October 2001. doi: 10.1016/S0375-9474(01)00921-6, arXiv:hep-ph/0012164.
- N. G. Antoniou, Y. F. Contoyiannis, F. K. Diakonou, and G. Mavromanolakis. Critical QCD in nuclear collisions. *Nuclear Physics A*, 761:149–161, October 2005. doi: 10.1016/j.nuclphysa.2005.07.003, arXiv:hep-ph/0505185.
- N. G. Antoniou, F. K. Diakonou, and A. S. Kapoyannis. Indication of divergent baryon-number susceptibility in QCD matter. *Phys. Rev. C*, 81(1):011901, January 2010. doi: 10.1103/PhysRevC.81.011901, 0809.0685.
- N.G. Antoniou, Y.F. Contoyiannis, F.K. Diakonou, and C.G. Papadopoulos. Fractals at  $T = T(c)$  due to instanton - like configurations. *Phys.Rev.Lett.*, 81:4289–4292, 1998. doi: 10.1103/PhysRevLett.81.4289, hep-ph/9810383.
- N.G. Antoniou, F.K. Diakonou, A.S. Kapoyannis, and K.S. Kousouris. Critical Opalescence in Baryonic QCD Matter. *Phys. Rev. Lett.*, 97(3):032002, July 2006. doi: 10.1103/PhysRevLett.97.032002, arXiv:hep-ph/0602051.
- Y. Aoki, G. Endrodi, Z. Fodor, S.D. Katz, and K.K. Szabo. The Order of the quantum chromodynamics transition predicted by the standard model of particle physics. *Nature*, 443:675–678, 2006a. doi: 10.1038/nature05120, hep-lat/0611014.
- Y. Aoki, Z. Fodor, S.D. Katz, and K.K. Szabo. The QCD transition temperature: Results with physical masses in the continuum limit. *Phys.Lett.*, B643:46–54, 2006b. doi: 10.1016/j.physletb.2006.10.021, hep-lat/0609068.
- Y. Aoki, et al. The QCD transition temperature: results with physical masses in the continuum limit II. *JHEP*, 0906:088, 2009. doi: 10.1088/1126-6708/2009/06/088, 0903.4155.
- H. Appelshauser et al. Two proton correlations from 158-A-GeV Pb + Pb central collisions. *Phys.Lett.*, B467:21–28, 1999. doi: 10.1016/S0370-2693(99)01152-1, nucl-ex/9905001.

- Peter Brockway Arnold and Laurence G. Yaffe. The NonAbelian Debye screening length beyond leading order. *Phys.Rev.*, D52:7208–7219, 1995. doi: 10.1103/PhysRevD.52.7208, hep-ph/9508280.
- M. Asakawa and K. Yazaki. Chiral Restoration at Finite Density and Temperature. *Nucl.Phys.*, A504:668–684, 1989. doi: 10.1016/0375-9474(89)90002-X.
- C. Bagnuls, C. Bervillier, D.I. Meiron, and B.G. Nickel. Nonasymptotic Critical Behavior From Field Theory at  $D = 3$ . 2. The Ordered Phase Case. *Phys.Rev.*, B35:3585–3607, 1987. doi: 10.1103/PhysRevB.35.3585, hep-th/0006187.
- D. Bailin and A. Love. Superfluidity and Superconductivity in Relativistic Fermion Systems. *Phys.Rept.*, 107:325, 1984. doi: 10.1016/0370-1573(84)90145-5.
- A. Barducci, R. Casalbuoni, S. De Curtis, Raoul Gatto, and Giulio Pettini. Chiral Symmetry Breaking in QCD at Finite Temperature and Density. *Phys.Lett.*, B231:463, 1989. doi: 10.1016/0370-2693(89)90695-3.
- Bertrand C. Barrois. Superconducting Quark Matter. *Nucl.Phys.*, B129:390, 1977. doi: 10.1016/0550-3213(77)90123-7.
- G. Baym. Confinement of quarks in nuclear matter. *Physica A Statistical Mechanics and its Applications*, 96:131–135, April 1979. doi: 10.1016/0378-4371(79)90200-0.
- A. Bazavov, et al. Equation of state and QCD transition at finite temperature. *Phys.Rev.*, D80:014504, 2009. doi: 10.1103/PhysRevD.80.014504, 0903.4379.
- Alexei Bazavov and Peter Petreczky. Deconfinement and chiral transition with the highly improved staggered quark (HISQ) action. *J.Phys.Conf.Ser.*, 230:012014, 2010. doi: 10.1088/1742-6596/230/1/012014, 1005.1131.
- F. Becattini, J. Manninen, and M. Gazdzicki. Energy and system size dependence of chemical freeze-out in relativistic nuclear collisions. *Phys.Rev.*, C73:044905, 2006. doi: 10.1103/PhysRevC.73.044905, hep-ph/0511092.
- J. Berges, N. Tetradis, and C. Wetterich. Critical equation of state from the average action. *Phys.Rev.Lett.*, 77:873–876, 1996. doi: 10.1103/PhysRevLett.77.873, hep-th/9507159.
- Juergen Berges and Krishna Rajagopal. Color superconductivity and chiral symmetry restoration at nonzero baryon density and temperature. *Nucl.Phys.*, B538:215–232, 1999. doi: 10.1016/S0550-3213(98)00620-8, hep-ph/9804233.
- C. Bernard et al. QCD thermodynamics with three flavors of improved staggered quarks. *Phys.Rev.*, D71:034504, 2005. doi: 10.1103/PhysRevD.71.034504, hep-lat/0405029.

- A. Bialas and R. Peschanski. Moments of rapidity distributions as a measure of short-range fluctuations in high-energy collisions. *Nuclear Physics B*, 273:703–718, September 1986. doi: 10.1016/0550-3213(86)90386-X.
- A. Bialas and R. Peschanski. Intermittency in multiparticle production at high energy. *Nuclear Physics B*, 308:857–867, October 1988. doi: 10.1016/0550-3213(88)90131-9.
- V.G. Bornyakov, et al. Probing the finite temperature phase transition with  $N(f) = 2$  nonperturbatively improved Wilson fermions. *Phys.Rev.*, D82:014504, 2010. doi: 10.1103/PhysRevD.82.014504, 0910.2392.
- S. Borsányi, et al. Is there still any  $T_c$  mystery in lattice QCD? Results with physical masses in the continuum limit III. *Journal of High Energy Physics*, 9:73, September 2010. doi: 10.1007/JHEP09(2010)073, 1005.3508.
- Peter Braun-Munzinger and Johanna Stachel. The quest for the quark-gluon plasma. *Nature*, 448:302–309, 2007. doi: 10.1038/nature06080.
- Frank R. Brown, et al. On the existence of a phase transition for QCD with three light quarks. *Phys.Rev.Lett.*, 65:2491–2494, 1990. doi: 10.1103/PhysRevLett.65.2491.
- N. Cabibbo and G. Parisi. Exponential hadronic spectrum and quark liberation. *Physics Letters B*, 59:67–69, October 1975. doi: 10.1016/0370-2693(75)90158-6.
- M. Cheng, et al. The Transition temperature in QCD. *Phys.Rev.*, D74:054507, 2006. doi: 10.1103/PhysRevD.74.054507, hep-lat/0608013.
- Michael Cheng, et al. The finite temperature QCD using  $2 + 1$  flavors of domain wall fermions at  $N(t) = 8$ . *Phys.Rev.*, D81:054510, 2010. doi: 10.1103/PhysRevD.81.054510, 0911.3450.
- Philippe Chomaz. The Nuclear liquid gas phase transition and phase coexistence: A Review. 2004, nucl-ex/0410024.
- Thomas D. Cohen, R.J. Furnstahl, and David K. Griegel. Quark and gluon condensates in nuclear matter. *Phys.Rev.*, C45:1881–1893, 1992. doi: 10.1103/PhysRevC.45.1881.
- John C. Collins and M.J. Perry. Superdense Matter: Neutrons Or Asymptotically Free Quarks? *Phys.Rev.Lett.*, 34:1353, 1975. doi: 10.1103/PhysRevLett.34.1353.
- E. A. De Wolf, I. M. Dremin, and W. Kittel. Scaling laws for density correlations and fluctuations in multiparticle dynamics. *Phys.Rept.*, 270:1–141, 1996. doi: 10.1016/0370-1573(95)00069-0, hep-ph/9508325.

- C. DeTar and U.M. Heller. QCD Thermodynamics from the Lattice. *Eur.Phys.J.*, A41: 405–437, 2009. doi: 10.1140/epja/i2009-10825-3, 0905.2949.
- Carleton E. Detar. A Conjecture Concerning the Modes of Excitation of the Quark-Gluon Plasma. *Phys.Rev.*, D32:276, 1985. doi: 10.1103/PhysRevD.32.276.
- H.J. Drescher, M. Hladik, S. Ostapchenko, T. Pierog, and K. Werner. Parton based Gribov-Regge theory. *Phys.Rept.*, 350:93–289, 2001. doi: 10.1016/S0370-1573(00)00122-8, hep-ph/0007198.
- E.G. Drukarev and E.M. Levin. Structure of nuclear matter and QCD sum rules. *Prog.Part.Nucl.Phys.*, 27:77–134, 1991. doi: 10.1016/0146-6410(91)90003-7.
- B. Efron. Bootstrap methods: another look at the jackknife. *The annals of Statistics*, pages 1–26, 1979.
- Shinji Ejiri. Recent progress in lattice QCD at finite density. *PoS*, LATTICE2008:002, 2008, 0812.1534.
- H. Fujii. Scalar density fluctuation at the critical end point in the Nambu Jona-Lasinio model. *Phys. Rev. D*, 67(9):094018, May 2003. doi: 10.1103/PhysRevD.67.094018, hep-ph/0302167.
- Masataka Fukugita, Masanori Okawa, and Akira Ukawa. Finite Size Scaling Study of the Deconfining Phase Transition in Pure SU(3) Lattice Gauge Theory. *Nucl.Phys.*, B337:181, 1990. doi: 10.1016/0550-3213(90)90256-D.
- K. Fukushima and T. Hatsuda. The phase diagram of dense QCD. *Reports on Progress in Physics*, 74(1):014001, January 2011. doi: 10.1088/0034-4885/74/1/014001, 1005.4814.
- S. Gavin. Extraordinary Baryon Fluctuations and the QCD Tricritical Point. *ArXiv Nuclear Theory e-prints*, August 1999, arXiv:nucl-th/9908070.
- Sean Gavin, Andreas Gocksch, and Robert D. Pisarski. QCD and the chiral critical point. *Phys.Rev.*, D49:3079–3082, 1994. doi: 10.1103/PhysRevD.49.R3079, hep-ph/9311350.
- Marek Gazdzicki, Mark Gorenstein, and Peter Seyboth. Onset of deconfinement in nucleus-nucleus collisions: Review for pedestrians and experts. *Acta Phys.Polon.*, B42:307–351, 2011. doi: 10.5506/APhysPolB.42.307, 1006.1765.
- P. Gerber and H. Leutwyler. Hadrons Below the Chiral Phase Transition. *Nucl.Phys.*, B321:387, 1989. doi: 10.1016/0550-3213(89)90349-0.

- P. I. Good and J. W. Hardin. *Common errors in statistics (and how to avoid them)*. John Wiley & Sons, 2012.
- P. Grassberger and I. Procaccia. Measuring the strangeness of strange attractors. *Physica D Nonlinear Phenomena*, 9:189–208, October 1983. doi: 10.1016/0167-2789(83)90298-1.
- R. Hagedorn. Statistical thermodynamics of strong interactions at high-energies. *Nuovo Cim.Suppl.*, 3:147–186, 1965.
- R. Hagedorn. How We Got to QCD Matter From the Hadron Side by Trial and Error. *Lect.Notes Phys.*, 221:53–76, 1985.
- A. Hart, M. Laine, and O. Philipsen. Static correlation lengths in QCD at high temperatures and finite densities. *Nucl.Phys.*, B586:443–474, 2000. doi: 10.1016/S0550-3213(00)00418-1, hep-ph/0004060.
- T. Hatsuda and T. Kunihiro. Fluctuation Effects in Hot Quark Matter: Precursors of Chiral Transition at Finite Temperature. *Phys.Rev.Lett.*, 55:158–161, 1985. doi: 10.1103/PhysRevLett.55.158.
- Tetsuo Hatsuda and Su Hounng Lee. QCD sum rules for vector mesons in nuclear medium. *Phys.Rev.*, C46:34–38, 1992. doi: 10.1103/PhysRevC.46.34.
- Y. Hatta and T. Ikeda. Universality, the QCD critical and tricritical point, and the quark number susceptibility. *Phys. Rev. D*, 67(1):014028, January 2003. doi: 10.1103/PhysRevD.67.014028, hep-ph/0210284.
- Y. Hatta and M. A. Stephanov. Proton number fluctuation as a signal of the QCD critical endpoint. *Phys. Rev. Lett.*, 91:102003, 2003. doi: 10.1103/PhysRevLett.91.102003, hep-ph/0302002.
- H. Heiselberg and M. Hjorth-Jensen. Phases of dense matter in neutron stars. *Physics Reports*, 328:237–327, May 2000. doi: 10.1016/S0370-1573(99)00110-6, nucl-th/9902033.
- T. Hesterberg, D. S. Moore, S. Monaghan, A. Clipson, and R. Epstein. Bootstrap methods and permutation tests. *Introduction to the Practice of Statistics*, 5:1–70, 2005.
- K. Huang. *Statistical mechanics*. Wiley, 1987. ISBN 9780471815181. URL <https://books.google.co.uk/books?id=M8PvAAAAMAJ>.
- Mei Huang. QCD Phase Diagram at High Temperature and Density. 2010, 1001.3216.

- C. Itzykson and J.B. Zuber. *Quantum Field Theory*. International series in pure and applied physics. McGraw-Hill, 1985. ISBN 9780070663534. URL <https://books.google.gr/books?id=46m8QgAACAAJ>.
- M. Kitazawa, T. Koide, T. Kunihiro, and Y. Nemoto. Precursor of color superconductivity in hot quark matter. *Phys.Rev.*, D65:091504, 2002. doi: 10.1103/PhysRevD.65.091504, nucl-th/0111022.
- M. Kobayashi and T. Maskawa. Chiral symmetry and eta-x mixing. *Prog.Theor.Phys.*, 44:1422–1424, 1970. doi: 10.1143/PTP.44.1422.
- M. Kobayashi, H. Kondo, and T. Maskawa. Symmetry breaking of the chiral  $u(3) \times u(3)$  and the quark model. *Prog.Theor.Phys.*, 45:1955–1959, 1971. doi: 10.1143/PTP.45.1955.
- S. E. Koonin. Proton pictures of high-energy nuclear collisions. *Physics Letters B*, 70: 43–47, September 1977. doi: 10.1016/0370-2693(77)90340-9.
- M.P. Lombardo, K. Splittorff, and J.J.M. Verbaarschot. Lattice QCD and dense quark matter. 2009, 0912.4410.
- Y. Maezawa, et al. Thermodynamics of two-flavor lattice QCD with an improved Wilson quark action at non-zero temperature and density. *J.Phys.*, G34:S651–654, 2007. doi: 10.1088/0954-3899/34/8/S65, hep-lat/0702005.
- Y. Maezawa et al. Electric and Magnetic Screening Masses at Finite Temperature from Generalized Polyakov-Line Correlations in Two-flavor Lattice QCD. *Phys.Rev.*, D81: 091501, 2010. doi: 10.1103/PhysRevD.81.091501, 1003.1361.
- B. B. Mandelbrot. *The fractal geometry of nature*. W.H. Freeman, San Francisco, 1982. ISBN 0716711869.
- Larry D. McLerran and Benjamin Svetitsky. Quark Liberation at High Temperature: A Monte Carlo Study of SU(2) Gauge Theory. *Phys.Rev.*, D24:450, 1981. doi: 10.1103/PhysRevD.24.450.
- W. J. Metzger. Estimating the uncertainties of factorial moments. Technical Report HEN-455, Experimental High Energy Physics Group, University of Nijmegen, Nijmegen, The Netherlands, June 2004.
- C. Michael. Fitting correlated data. *Phys. Rev. D*, 49:2616–2619, March 1994. doi: 10.1103/PhysRevD.49.2616, hep-lat/9310026.

- Shin Muroya, Atsushi Nakamura, Chiho Nonaka, and Tetsuya Takaishi. Lattice QCD at finite density: An Introductory review. *Prog.Theor.Phys.*, 110:615–668, 2003. doi: 10.1143/PTP.110.615, hep-lat/0306031.
- Sudhir Nadkarni. Nonabelian Debye Screening. 2. The Singlet Potential. *Phys.Rev.*, D34:3904, 1986a. doi: 10.1103/PhysRevD.34.3904.
- Sudhir Nadkarni. Nonabelian Debye Screening. 1. The Color Averaged Potential. *Phys.Rev.*, D33:3738, 1986b. doi: 10.1103/PhysRevD.33.3738.
- Yusuke Nishida and Hiroaki Abuki. BCS-BEC crossover in a relativistic superfluid and its significance to quark matter. *Phys.Rev.*, D72:096004, 2005. doi: 10.1103/PhysRevD.72.096004, hep-ph/0504083.
- Robert D. Pisarski and Frank Wilczek. Remarks on the Chiral Phase Transition in Chromodynamics. *Phys.Rev.*, D29:338–341, 1984. doi: 10.1103/PhysRevD.29.338.
- Alexander M. Polyakov. Thermal Properties of Gauge Fields and Quark Liberation. *Phys.Lett.*, B72:477–480, 1978. doi: 10.1016/0370-2693(78)90737-2.
- William H. Press, Saul A. Teukolsky, William T. Vetterling, and Brian P. Flannery. *Numerical Recipes in Fortran 90 (2Nd Ed.): The Art of Parallel Scientific Computing*. Cambridge University Press, New York, NY, USA, 1996. ISBN 0-521-57439-0.
- Krishna Rajagopal and Frank Wilczek. Static and dynamic critical phenomena at a second order QCD phase transition. *Nucl.Phys.*, B399:395–425, 1993. doi: 10.1016/0550-3213(93)90502-G, hep-ph/9210253.
- Krishna Rajagopal and Frank Wilczek. The Condensed matter physics of QCD. 2000, hep-ph/0011333.
- M. Reuter, N. Tetradis, and C. Wetterich. The Large N limit and the high temperature phase transition for the  $\phi^4$  theory. *Nucl.Phys.*, B401:567–590, 1993. doi: 10.1016/0550-3213(93)90314-F, hep-ph/9301271.
- E. K. Riedel and F. J. Wegner. Tricritical Exponents and Scaling Fields. *Physical Review Letters*, 29:349–352, August 1972. doi: 10.1103/PhysRevLett.29.349.
- Helmut Satz. Deconfinement and percolation. *Nucl.Phys.*, A642:130–142, 1998. doi: 10.1016/S0375-9474(98)00508-9, hep-ph/9805418.
- Bernd-Jochen Schaefer and Jochen Wambach. Susceptibilities near the QCD (tri)critical point. *Phys.Rev.*, D75:085015, 2007. doi: 10.1103/PhysRevD.75.085015, hep-ph/0603256.

- Andreas Schmitt. Dense matter in compact stars: A pedagogical introduction. *Lect. Notes Phys.*, 811:1–111, 2010. doi: 10.1007/978-3-642-12866-0, 1001.3294.
- M. F. Shlesinger, G. M. Zaslavsky, and U. Frisch, editors. *Lévy Flights and Related Topics in Physics*, volume 450 of *Lecture Notes in Physics*, Berlin Springer Verlag, 1995. doi: 10.1007/3-540-59222-9.
- Paul Stankus, David Silvermyr, Soren Sorensen, and Victoria Greene. Proceedings, 21st International Conference on Ultra-Relativistic nucleus nucleus collisions (Quark matter 2009). *Nucl. Phys.*, A830:pp.1c–968c, 2009.
- M. Stephanov. QCD Phase Diagram and the Critical Point. *Progress of Theoretical Physics Supplement*, 153:139–156, 2004. doi: 10.1143/PTPS.153.139.
- M. Stephanov, K. Rajagopal, and E. Shuryak. Signatures of the Tricritical Point in QCD. *Phys. Rev. Lett.*, 81:4816–4819, November 1998. doi: 10.1103/PhysRevLett.81.4816, arXiv:hep-ph/9806219.
- M. Stephanov, K. Rajagopal, and E. Shuryak. Event-by-event fluctuations in heavy ion collisions and the QCD critical point. *Phys. Rev. D*, 60(11):114028, December 1999. doi: 10.1103/PhysRevD.60.114028, hep-ph/9903292.
- M. A. Stephanov. QCD Phase Diagram and the Critical Point. *International Journal of Modern Physics A*, 20:4387–4392, 2005. doi: 10.1142/S0217751X05027965, hep-ph/0402115.
- M. A. Stephanov. Non-Gaussian Fluctuations near the QCD Critical Point. *Physical Review Letters*, 102(3):032301, January 2009. doi: 10.1103/PhysRevLett.102.032301, 0809.3450.
- R.B. Stinchcombe. Phase transitions. In Stig Lundqvist, Norman H. March, and Mario P. Tosi, editors, *Order and Chaos in Nonlinear Physical Systems*, Physics of Solids and Liquids, pages 295–340. Springer US, 1988. ISBN 978-1-4899-2060-7. doi: 10.1007/978-1-4899-2058-4\_10. URL [http://dx.doi.org/10.1007/978-1-4899-2058-4\\_10](http://dx.doi.org/10.1007/978-1-4899-2058-4_10).
- Leonard Susskind. Lattice Models of Quark Confinement at High Temperature. *Phys. Rev.*, D20:2610–2618, 1979. doi: 10.1103/PhysRevD.20.2610.
- Benjamin Svetitsky. Symmetry Aspects of Finite Temperature Confinement Transitions. *Phys. Rept.*, 132:1–53, 1986. doi: 10.1016/0370-1573(86)90014-1.
- Benjamin Svetitsky and Laurence G. Yaffe. Critical Behavior at Finite Temperature Confinement Transitions. *Nucl. Phys.*, B210:423, 1982. doi: 10.1016/0550-3213(82)90172-9.

- Gerard 't Hooft. Computation of the Quantum Effects Due to a Four-Dimensional Pseudoparticle. *Phys.Rev.*, D14:3432–3450, 1976a. doi: 10.1103/PhysRevD.18.2199, 3,10.1103/PhysRevD.14.3432.
- Gerard 't Hooft. Symmetry Breaking Through Bell-Jackiw Anomalies. *Phys.Rev.Lett.*, 37:8–11, 1976b. doi: 10.1103/PhysRevLett.37.8.
- Milton Toy. Net Proton and Negatively-Charged Hadron Spectra from the NA49 Experiment. In *Advances in Nuclear Dynamics 3*, pages 61–65. Springer, 1997.
- M.M. Tsypin. Universal effective potential for scalar field theory in three-dimensions by Monte Carlo computation. *Phys.Rev.Lett.*, 73:2015–2018, 1994. doi: 10.1103/PhysRevLett.73.2015.
- Tamás Vicsek. *Fractal growth phenomena*. World Scientific, Singapore New Jersey, 1989. ISBN 9971-50-830-3.
- Klaus Werner, Fu-Ming Liu, and Tanguy Pierog. Parton ladder splitting and the rapidity dependence of transverse momentum spectra in deuteron-gold collisions at RHIC. *Phys.Rev.*, C74:044902, 2006. doi: 10.1103/PhysRevC.74.044902, hep-ph/0506232.
- F. Wilczek. QCD In Extreme Conditions. *ArXiv High Energy Physics - Phenomenology e-prints*, March 2000, hep-ph/0003183.
- Frank Wilczek. Application of the renormalization group to a second order QCD phase transition. *Int.J.Mod.Phys.*, A7:3911–3925, 1992. doi: 10.1142/S0217751X92001757.